LOS ANGELES PUBLIC LIBRARY

MAY 26 1960

SCIENCE & TECHNOLOGY

ARS JOURNAL

A PUBLICATION OF THE AMERICAN ROCKET SOCIETY

VOLUME 30 NUMBER 5 MAY 1960

BIND

SURVEY ARTICLE

Recent Progress in Rarefied Gasdynamics . . . . . S. A. Schaaf 443

CONTRIBUTED ARTICLES

Fluorescent Technique for Determining the Cross-Sectional Drop Size Distributions of Liquid Sprays . . . . . G. M. Benson, M. M. El-Wakil, P. S. Myers and O. A. Uyehara 447

Hypersonic Shock Wave-Boundary Layer Interaction and Leading Edge Slip . . . . . H. T. Nagamatsu and R. E. Sheer Jr. 454

Numerical Comparison Between Exact and Approximate Theories of Hypersonic Inviscid Flow Past Slender Blunt Nosed Bodies . . . . . Saul Feldman 463

Aerodynamic Instability of Supersonic Inlet Diffusers . . . . . Chieh-Chien Chang and Cheng-Ting Hsu 468

Satellite Pressure Losses Caused by Meteoroid Impacts . . . . . M. Kornhauser 475

Solar Heating of a Rotating Cylindrical Space Vehicle . . . . . A. Charnes and S. Raynor 479

TECHNICAL NOTES

Solar-Lunar Perturbations of the Orbit of an Earth Satellite . . . . . Mildred M. Moe 486

Jet Flows With Shocks . . . . . Mildred M. Moe and B. Andreas Troesch 487

Specific Impulse Nomograph . . . . . William L. Jenn Jr. and Ronald V. Repetti 489

Initial Azimuths and Times for Ballistic Lunar Impact Trajectories . . . . . W. C. Riddell 491

Evaluation of Preflight Risks by Means of Very High Speed Digital System Simulation . . . . . Jesse R. Brinkerhoff 493

Prediction of Peak Temperature for Satellite Entries With Lift . . . . . R. H. Edwards and G. S. Campbell 496

Polymerization of Solid Propellants . . . . . W. H. Grootzinger III 498

Real-Time Analysis, New Approach in Flight Testing . . . . . Guenther Hintze 500

Ballistic Effect of Pyrolyzed Liner in Solid Propellant Motor Firings . . . . . L. J. Gordon 502

Heating Penalty Associated With Modulated Entry into Earth's Atmosphere . . . . . John V. Becker 504

Electrically Charged Missile in Vertical Descent . . . . . Marvin H. Hewitt 505

DEPARTMENTS

New Patents 507

Book Reviews 508

Technical Literature Digest 511

TAKE A GIANT STEP

. . . into your future and seek out the professional opportunities awaiting creative engineers and scientists at Martin-Denver . . . For here exists the most challenging problems in space and human engineering. Join with us and communicate with N. M. Pagan, Director of Technical and Scientific Staffing (Dept. 4C), The Martin Company, P. O. Box 179, Denver 1, Colorado.

MARTIN
DENVER DIVISION

The eight divisions of the Martin Company are Activation, Baltimore, Cocoa, Denver, Nuclear, Orlando, RIAS, and Space Flight.

The nation's largest industrial computational facility

. . . important part of a unique research environment that can multiply your scientific accomplishments

Wherever you are carrying on scientific investigations, we doubt if you can call on advanced facilities and complementary scientific skills equal to those available at the Research Laboratories.

Here, leaders in a variety of scientific disciplines provide assistance in many areas that relate to your primary field of research. In addition, the nation's largest industrial computational facility can take over the routine of solving difficult calculations — routine that might otherwise burden you for months.

The Research Laboratories are organized to respect the time and abilities of men working in advanced scientific areas. If you appreciate an environment where a scientist can focus full mental power on scientific accomplishment, we would like to hear from you.

ATTRACTIVE OPENINGS
in many areas . . .

Chemical Kinetics
Fuel and Combustion Analysis
Thermodynamic Cycle Analysis
Space Mechanics
Electrical Propulsion
Plasma Physics
Gaseous Electronics
Vehicle Trajectory and Performance Analysis
High Temperature Materials
Direct Conversion
Surface Chemistry
Nuclear Engineering

Please write to Mr. W. F. Walsh, or phone Hartford, Conn., JAckson 8-4811, Ext. 7145

RESEARCH LABORATORIES
UNITED AIRCRAFT CORPORATION
400 Main Street, East Hartford 8, Conn.

UAC RESEARCH
. . . symbol of creative research

ARS JOURNAL

A PUBLICATION OF THE AMERICAN ROCKET SOCIETY

EDITOR	Martin Summerfield
ASSOCIATE TECHNICAL EDITOR	Irvin Glassman
MANAGING EDITOR	Barbara Nowak
ART EDITOR	John Culin
CONTRIBUTOR	George F. McLaughlin

ASSOCIATE EDITORS

J. George Adashko, *Russian Supplement;* **Ali Bulent Cambel,** *Northwestern University, Book Reviews;* **Igor Jurkevich,** *G. E. Space Sciences Laboratory, Russian Articles;* **Charles J. Mundo Jr.,** *Raytheon Manufacturing Co., Guidance;* **Bernard H. Paiewonsky,** *Aeronautical Research Associates of Princeton, Flight Mechanics;* **M. H. Smith,** *Princeton University, Technical Literature Digest*

ASSISTANT EDITORS

Julie Hight, Carol Rubenstein, Estelle Viertel

ADVERTISING AND PROMOTION MANAGER

William Chenoweth

ADVERTISING PRODUCTION MANAGER

Walter Brunke

ADVERTISING REPRESENTATIVES

New York
D. C. Emery and Associates
400 Madison Ave., New York, N. Y.
Telephone: Plaza 9-7460

Los Angeles
James C. Galloway and Co.
6535 Wilshire Blvd., Los Angeles, Calif.
Telephone: Olive 3-3223

Chicago
Jim Summers and Associates
35 E. Wacker Dr., Chicago, Ill.
Telephone: Andover 3-1154

Detroit
R. F. Pickrell and Vincent Purcell
318 Stephenson Bldg., Detroit, Mich.
Telephone: Trinity 1-0790

Boston
Robert G. Melendy
17 Maugus Ave., Wellesley Hills, Mass.
Telephone: Cedar 5-6503

Pittsburgh
John W. Foster
239 4th Ave., Pittsburgh, Pa.
Telephone: Atlantic 1-2977

American Rocket Society

500 Fifth Avenue, New York 36, N. Y.

Founded 1930

OFFICERS

President	Howard S. Seifert
Vice-President	Harold W. Ritchey
Executive Secretary	James J. Harford
Treasurer	Robert M. Lawrence
Secretary and Asst. Treasurer	A. C. Slade
General Counsel	Andrew G. Haley
Director of Publications	Irwin Hersey

BOARD OF DIRECTORS

Terms expiring on dates indicated

Ali B. Cambel	1962	William H. Pickering	1961
Richard B. Canright	1962	Simon Ramo	1960
James R. Dempsey	1961	William L. Rogers	1960
Herbert Friedman	1962	David G. Simons	1961
Robert A. Gross	1962	John L. Sloop	1961
Samuel K. Hoffman	1960	Martin Summerfield	1962
A. K. Oppenheim	1961	Wernher von Braun	1960

Maurice J. Zucrow 1960

TECHNICAL COMMITTEE CHAIRMEN

Ali B. Cambel, Magnetohydrodynamics
William H. Dorrance, Hypersonics
James S. Farrior, Guidance and Navigation
Herbert Friedman, Physics of the Atmosphere and Space
George Gerard, Structures and Materials
Martin Goldsmith, Liquid Rockets
Andrew G. Haley, Space Law and Sociology
Samuel Herrick, Astrodynamics
Maxwell W. Hunter, Missiles and Space Vehicles
David B. Langmuir, Ion and Plasma Propulsion
Max A. Lowy, Communications
Irving Michelson, Education
Peter L. Nichols Jr., Propellants and Combustion
Eugene Perchonok, Ramjets
Richard A. Schmidt, Test, Operations and Support
John I. Shafer, Solid Rockets
C. J. Wang, Nuclear Propulsion
Stanley C. White, Human Factors and Bioastronautics
George F. Wislicenus, Underwater Propulsion
John E. Witherspoon, Instrumentation and Control
Abe M. Zarem, Power Systems

Scope of ARS JOURNAL

This Journal is devoted to the advancement of astronautics through the dissemination of original papers disclosing new scientific knowledge and basic applications of such knowledge. The sciences of astronautics are understood here to embrace selected aspects of jet and rocket propulsion, spaceflight mechanics, high speed aerodynamics, flight guidance, space communications, atmospheric and outer space physics, materials and structures, human engineering, overall system analysis, and possibly certain other scientific areas. The selection of papers to be printed will be governed by the pertinence of the topic to the field of astronautics, by the current or probable future significance of the research, and by the importance of distributing the information to the members of the Society and to the profession at large.

Information for Authors

Manuscripts must be as brief as the proper presentation of the ideas will allow. Exclusion of dispensable material and conciseness of expression will influence the Editors' acceptance of a manuscript. In terms of standard-size double-spaced typed pages, a typical maximum length is 22 pages of text (including equations), 1 page of references, 1 page of abstract and 12 illustrations. Fewer illustrations permit more text, and vice versa. Greater length will be acceptable only in exceptional cases.

Short manuscripts, not more than one quarter of the maximum length stated for full articles, may qualify for publication as Technical Notes or Technical Comments. They may be devoted to new developments requiring prompt disclosure or to comments on previously published papers. Such manuscripts are published within a few months of the date of receipt.

Sponsored manuscripts are published occasionally as an ARS service to the industry. A manuscript that does not qualify for publication, according to the above-stated requirements as to subject, scope or length, but which nevertheless deserves widespread distribution among jet propulsion engineers, may be printed as an extra part of the Journal or as a special supplement, if the author or his sponsor will reimburse the Society for actual publication costs. Estimates are available on request. Acknowledgment of such financial sponsorship appears as a footnote on the first page of the article. Publication is prompt since such papers are not in the ordinary backlog.

Manuscripts must be double spaced on one side of paper only with wide margins to allow for instructions to printer. Include a 100 to 200 word abstract. State the authors' positions and affiliations in a footnote on the first page. Equations and symbols may be handwritten or typewritten; clarity for the printer is essential. Greek letters and unusual symbols should be identified in the margin. If handwritten, distinguish between capital and lower case letters, and indicate subscripts and superscripts. References are to be grouped at the end of the manuscript and are to be given as follows. For journal articles: Authors first, then title, journal, volume, year, page numbers; for books: Authors first, then title, publisher, city, edition and page or chapter numbers. Line drawings must be clear and sharp to make clear engravings. Use black ink on white paper or tracing cloth. Lettering should be large enough to be legible after reduction. Photographs should be glossy prints, not matte or semi-matte. Each illustration must have a legend; legends should be listed in order on a separate sheet.

Manuscripts must be accompanied by written assurance as to security clearance in the event the subject matter lies in a classified area or if the paper originates under government sponsorship. Full responsibility rests with the author.

Preprints of papers presented at ARS meetings are automatically considered for publication.

Submit manuscripts in duplicate (original plus first carbon, with two sets of illustrations) to the Managing Editor, ARS JOURNAL, 500 Fifth Avenue, New York 36, N.Y.

ARS JOURNAL is published monthly by the American Rocket Society, Inc. and the American Interplanetary Society at 20th & Northampton Sts., Easton, Pa., U. S. A. Editorial offices: 500 Fifth Ave., New York 36, N. Y. Price: $12.50 per year, $2.00 per single copy. Second-class mail privileges authorized at Easton, Pa. This publication is authorized to be mailed at the special rates of postage prescribed by Section 132.122. Notice of change of address should be sent to the Secretary, ARS, at least 30 days prior to publication. Opinions expressed herein are the authors' and do not necessarily reflect the views of the Editors or of the Society.
© Copyright 1960 by the American Rocket Society, Inc.

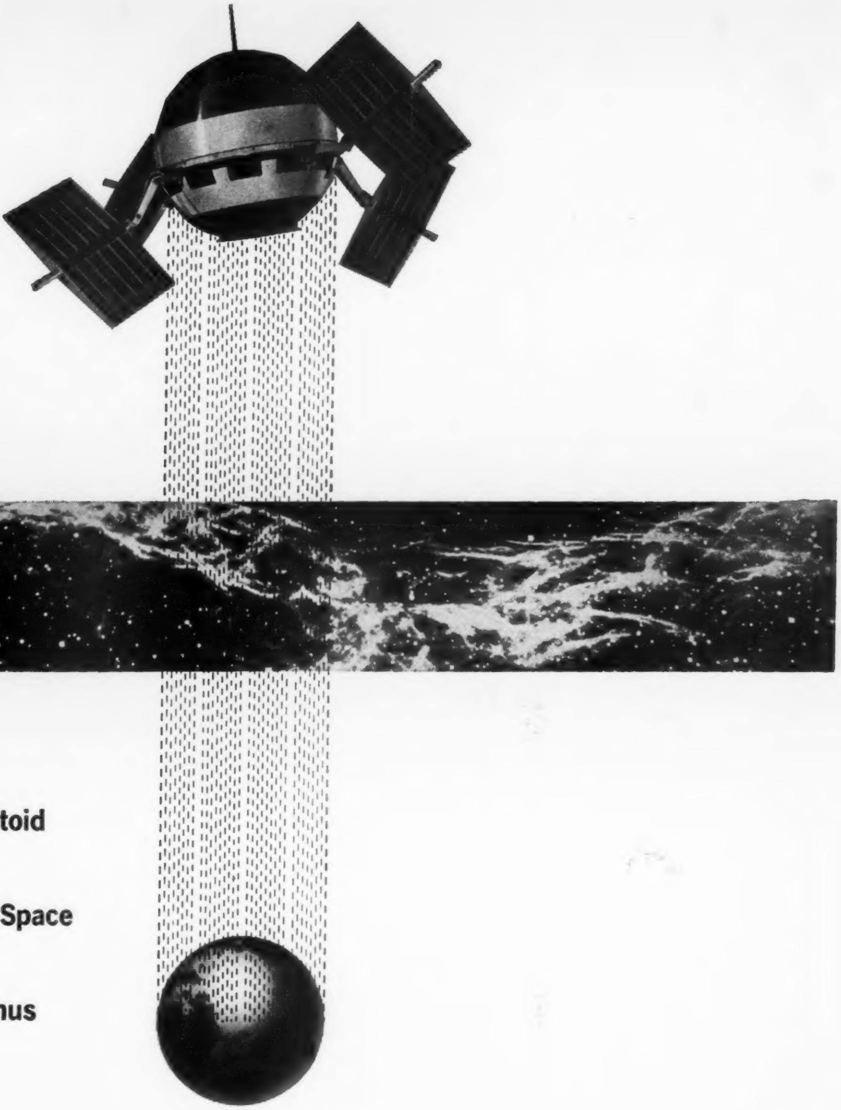

Pioneer V
Paddlewheel Planetoid
Is Vaulting
Through Unexplored Space
Toward The
Orbital Path of Venus

At this moment Pioneer V, one of the most advanced space probe vehicles ever launched, is on a course toward the path of Venus—26 million miles from earth. Blasted aloft March 11 by a Thor Able-4 rocket booster, this miniature space laboratory will reach its destination in about 130 days.

The project, carried out by Space Technology Laboratories for the National Aeronautics and Space Administration under the direction of the Air Force Ballistic Missile Division, may confirm or disprove long-standing theories of the fundamental nature of the solar system and space itself.

Energy from the sun—captured by almost 5,000 cells mounted in the four paddles—is used to supply all of the electrical power to operate the sophisticated array of instrumentation packed into the 94-pound spacecraft which measures only 26" in diameter.

By combining a phenomenal digital electronic brain (telebit) with a powerful radio transmitter inside the satellite, STL scientists and engineers expect to receive communications from Pioneer V at their command over interplanetary distances up to 50 million miles.

STL's technical staff brings to this space research the same talents which have provided over-all systems engineering and technical direction since 1954 to the Air Force missile programs including Atlas, Thor, Titan, Minuteman, and related space programs.

Important positions in connection with these activities are now available for scientists and engineers with outstanding capabilities. Inquiries and resumes are invited.

SPACE TECHNOLOGY LABORATORIES, INC.

Los Angeles • Santa Maria • Edwards Rocket Base • Cheyenne
Cape Canaveral • Manchester, England • Singapore • Hawaii

P. O. Box 95004, Los Angeles 45, California

THIOKOL's Utah Division is fully staffed and equipped to produce solid rocket motors of unprecedented size . . . of ICBM and even satellite proportions.

Why THIOKOL subcontracts to Industry, U.S.A. in the production of rocket powerplants of unprecedented reliability.

In development of advanced powerplants for missiles like Minuteman, Nike-Zeus, Subroc, and for research vehicles like Little Joe and X-17 . . . THIOKOL draws on its own vast propulsion know-how plus the advanced technological background of scores of industrial organizations.

The Allison Division of General Motors, Scaife Company, Goodyear, General Electric, Heintz Mfg. Co., Curtiss-Wright, RCA, Solar Aircraft, Borg-Warner Corp. . . . these are but a few of the many companies, large and small, to whom THIOKOL has subcontracted in producing dependable propulsion systems.

We have called upon the pressure vessel industry to whom metals for strength are second nature to get rocket casings combining light weight and high tensile strength.

We have called upon the electronics industry whose art is instrumentation for the delicate devices required for precise testing and production controls.

We have turned to the transportation and construction industries for development of specialized equipment such as monorail systems and movable cranes needed to process giant rocket motors with unfailing precision on an assembly line basis.

Many industrial technologies are met in a rocket propulsion system. Recognizing this, THIOKOL calls on specialists to achieve highest reliability, to meet the critical rocket power requirements of national defense and space research.

Thiokol® Chemical Corporation

BRISTOL, PENNA.

Plants in: TRENTON, N. J.; MOSS POINT, MISS.; DENVILLE, N. J.; ELKTON, MD.; HUNTSVILLE, ALA.; MARSHALL, TEXAS; BRIGHAM CITY, UTAH.

®Registered trademark of the Thiokol Chemical Corporation for its liquid polymers, rocket propellants, plasticizers, and other chemical products.

At The Ramo-Wooldridge Laboratories...
integrated programs of research & development
of electronic systems and components.

The new Ramo-Wooldridge Laboratories in Canoga Park provide an environment for creative work in an academic setting. Here, scientists and engineers seek solutions to the technological problems of today. The Ramo-Wooldridge research and development philosophy places major emphasis on the imaginative contributions of the members of the technical staff. ■ There are outstanding opportunities for scientists and engineers. *Write* Dr. Richard C. Potter, Head, Technical Staff Development, Department 11-E.

THE RAMO-WOOLDRIDGE LABORATORIES
8433 FALLBROOK AVENUE, CANOGA PARK, CALIFORNIA

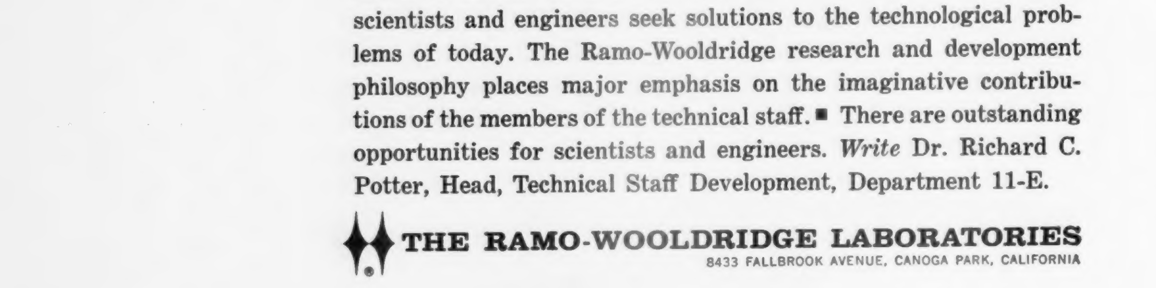

An electron device permits scientists to study the behavior of charged dust particles held in suspension.

Recent Progress in Rarefied Gasdynamics[1]

S. A. SCHAAF

University of California
Berkeley, Calif.

SUMMARIES of research developments in the mechanics of rarefied gases through 1956 are contained in (1 and 2).[2] The present paper thus will concentrate mostly on work in the field since that date, except for a few brief introductory remarks.

The general field of rarefied gasdynamics is concerned with phenomena related to the molecular or noncontinuum nature of a gas flow which may occur at sufficiently low densities. The relative importance of such effects is determined by the ratio of the molecular mean free path λ to a characteristic dimension l of the flow field. It has been found convenient to distinguish between flows which are slightly rarefied ($\lambda/l \sim 0.01 - 0.1$), moderately rarefied ($\lambda/l \sim 0.1 - 10$) and highly rarefied ($\lambda/l > 10$). These are usually referred to as "slip flow," "transition flow" and "free molecule flow," respectively.

There is by now a rather extensive literature—mostly, but not entirely, experimental—dealing with aerodynamic force and heat characteristics of a variety of geometrical shapes immersed in a low density flow. Geometries so far investigated include: Flat plates, spheres, cylinders, cones, wedges, cone-cylinders, sphere-nosed cones, and some special developmental configurations. The data of this type available in 1956 are summarized in (3); more recent data are included in the third section of the present report.

A number of additional experimental investigations have been carried out for flow situations of basic scientific interest, such as Couette flow, shock structure, and the dispersion and absorption of ultrasonic sound waves. This type of investigation is summarized in (2,4,5 and 6). The general conclusions to be drawn from these investigations are:

1 The "slip flow" regime is dominated by continuum viscous effects describable in terms of the normal Navier-Stokes formulation. The only important noncontinuum effect appears to be a slight modification in the boundary conditions for the gas flow past a solid surface, where slip velocity and temperature jump phenomena occur. These generally result in relatively small correction terms to be applied to standard continuum viscous results.

2 The "free molecule flow" regime seems to be quite satisfactorily understood in terms of the kinetic theory of gases. The prediction of heat transfer and aerodynamic force characteristics for convex bodies may be carried out in a quite straightforward way (except for the question of molecule-surface interaction, which will be discussed in some more detail further on). Experimental measurements appear to provide quite good agreement with the theoretical predictions.

3 No simple, generally applicable, analytic method has yet been developed for treating the "transition flow" regime. Experiments as well as linearized kinetic theory, however, suggest that a simple interpolation between "free molecule flow" and "slip flow" results is usually possible.

With these general remarks we now turn to a more detailed discussion of recent developments in the field.

Limits of Continuum Flow

There has been much discussion recently [see (7,8 and 9)] of the correct limits on the gas density to insure that a flow is essentially continuum. The original demarcation between slip flow and continuum flow was suggested by Tsien (10) as corresponding to a value of $\lambda/\delta \sim 0.01$, where λ is the molecular mean free path and δ is the boundary layer thickness. (For very low Reynolds number flows, the boundary layer disappears and only the characteristic dimension l of the flow field itself appears; the discussion in the present paper is directed toward the higher Reynolds number case.) For low speed flow past a flat plate $\delta/l \sim 1/\sqrt{Re}$, where Re is the Reynolds number and λ is essentially constant everywhere. Hence, using the relationship that $\lambda/l \sim M/Re$, one finds that $\lambda/\delta \sim M/\sqrt{Re}$. The original Tsien definition of the demarcation between slip and continuum flow was accordingly expressed in terms of the Mach number M and the Reynolds number Re by $M/\sqrt{Re} \sim 0.01$. Most of the recent discussion referred to previously has been concerned with the extension of this basic notion to the high speed case. For very large M, the situation becomes more complicated, due to the dependence of both λ_w the wall mean free path, and δ_* the displacement thickness, or θ the boundary layer momentum thickness, on M body geometry and the heat transfer conditions at the body surface. It seems reasonable to suspect that slip effects on induced pressure are governed by the parameter λ_w/δ_* [see, for example, (11)], whereas slip effects on skin friction are determined by λ_w/θ (2). Stagnation regions on blunt bodies will have different expressions for λ_w/δ_* and for λ_w/θ in terms of

---

Received March 11, 1960.

[1] This article is a modification and extension of a paper presented at the Sixth Midwestern Conference on Fluid Mechanics, Austin, Texas, Sept. 1959.

[2] Numbers in parentheses indicate References at end of paper.

Dr. Schaaf, a graduate in mathematics of the University of California, Berkeley, is now Professor and Chairman of the Division of Aeronautical Sciences there. He has made many notable contributions in the field of fluid mechanics, particularly on the subject of rarefied gas flow. He is the author of the section on this subject in the Princeton Series volume "Fundamentals of Gas Dynamics." Dr. Schaaf has served as chairman of the Fluid Dynamics Division of the American Physical Society, in an advisory capacity to numerous government agencies and as a consultant for various industrial organizations.

Mach and Reynolds number than will the downstream side of slender objects. Also, adiabatic boundary layers—frequently the wind tunnel case—will, in general, have expressions for λ_w/δ_* and for λ_w/θ in terms of Mach and Reynolds number which differ considerably from highly cooled boundary layers—usually the high speed free flight case. Thus a large variety of criteria for determining the onset of slip flow effects may be established at high M. In every case, however, the suggested modifications in a demarcation between slip and continuum flow are given in terms of an appropriate value for λ_w/δ_* or for λ_w/θ, and it turns out that all of these cases result in a demarcation between the slip flow and continuum regimes at *lower* densities than the corresponding Tsien criterion. No experimental disagreement with the basic ideas has yet been noted.

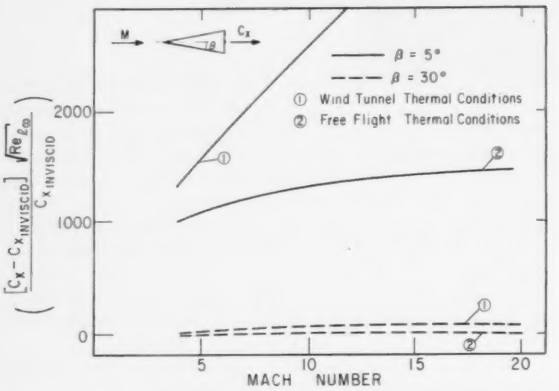

Fig. 1 Viscous effect on the axial forces of a wedge at zero angle of attack

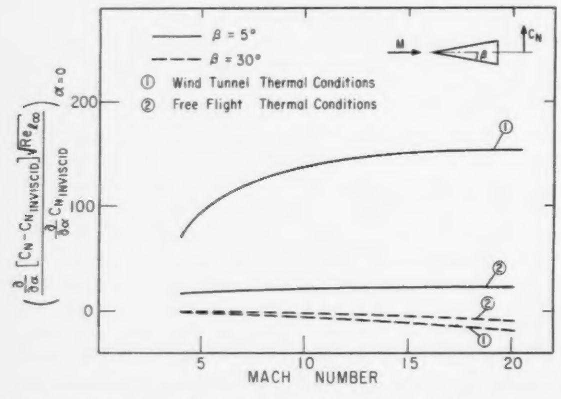

Fig. 2 Viscous effect on the normal forces of a wedge at zero angle of attack

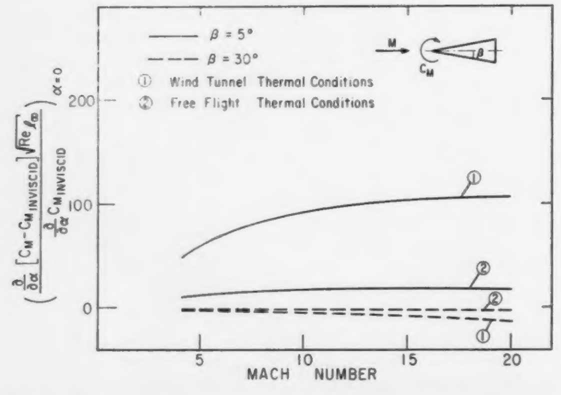

Fig. 3 Viscous effect on the moment coefficent of a wedge at zero angle of attack

The emphasis on the presence of noncontinuum effects, such as slip and temperature jump as the defining characteristic of the slip flow regime has perhaps been somewhat unfortunate, in that it has tended to obscure the very important fact that the *dominant* fluid mechanic effects in the slip flow regime are not these noncontinuum effects at all. The dominant effects are associated with the presence of the very thick laminar boundary layers which occur and which give rise to skin friction of the same order as the pressure, and which, through the displacement effect, disturb the surface pressure from its inviscid value, oftentimes manyfold. These are completely continuum effects and are basically well understood, although their application to determination of aerodynamic coefficients presents considerable computational difficulty. A simple example will serve to illustrate the point. Consider the skin friction on a wedge in low speed flow. The boundary layer for the no-slip case is that considered by Falkner and Skan (12), and leads to an expression for the skin friction coefficient in the form

$$C_f \sim a/\sqrt{Re}$$

Modifying the boundary layer analysis to include the effect of slip (2, 13), one obtains

$$C_f \sim \frac{a}{\sqrt{Re}}\left(1 - \frac{bM}{\sqrt{Re}}\cdots\right)$$

The slip correction is thus seen to be of the order of $M/\sqrt{Re}$, as expected. More important, however, is the fact that for this term to amount to a correction of the order of a few per cent, it is necessary that Re be very small indeed, i.e., of the order of 10^2 or so. Under these conditions, the skin friction—with or without a slip correction amounting to only a few per cent or so—will be orders of magnitude larger than at normal density. Most of the experimental results so far obtained in the slip flow range have reflected these continuum viscous effects, rather than noncontinuum slip flow effects. The more recent of these are summarized in the next section.

If slip corrections to boundary layer effects are significant, then other corrections, for example departure from strict boundary layer theory itself, must be considered. For the flat plate case this is apparently very difficult [see, for example, (14)]; for the blunt body case in highly cooled flow the correction to boundary layer theory due to the vorticity generated behind the detached shock wave (15) appears to dominate the slip effect, so that even lower densities are necessary for this case before any sizable departure from continuum flow will become of importance. However, a calculation of the "shock layer" heat transfer with and without a modification in the boundary condition to include the temperature jump effect has been carried out by Hoshizaki (16). He finds a substantial effect due to slip which serves to illustrate the point that noncontinuum effects are often of importance when considering *modifications* of boundary layer theory. In connection with the foregoing discussion, it is appropriate to emphasize the importance of both geometry and heat transfer effects on the viscous modifications to aerodynamic coefficients in a low density continuum flow. These coefficients depend not only on Mach and Reynolds numbers, but also on the heat transfer conditions at the model or prototype surface. Lift, drag and moment characteristics of simple wedge-shaped airfoils calculated on the basis of a no-slip laminar boundary layer and Newtonian flow are presented in Figs. 1, 2 and 3 for two different heat transfer conditions, one corresponding more or less to wind tunnel test conditions, and the other to the free flight case. The very great difference between the two, particularly for the slender wedge airfoils, is quite striking. It is also apparent that viscous effects become of importance at higher Reynolds numbers on slender objects than on blunt objects.

Recent Investigations

A number of experimental investigations have been completed during the past 3 years in the slip flow and transition regimes. These will be summarized briefly here.

Lift and drag forces on a slender, sharp cone-cylinder configuration have been measured (17) at $M = 4$ and $Re = 4 \times 10^3$. It was found that the measured drag coefficient was approximately 10 times the inviscid drag coefficient. However, the simplest laminar boundary layer correction, including both skin friction and displacement pressure effects, leads to good agreement with the experimental data (see Fig. 4).

Pressure distributions on sharp leading edge flat plates have been measured by a number of different investigators. The experiments which have penetrated farthest into the slip and transition regimes are reported in (18). These and other results published in available publications will not be reproduced here. It was observed that the data followed continuum theory until rather high values of the interaction parameter, $X \sim M^3/\sqrt{Re}$, but departed at a point corresponding to $\lambda_w/\delta_* \sim 0.35$ (18). This was presumably due to the effect of slip near the leading edge (11).

Pressure distributions on sphere-nosed cones (19) have been determined at $M \sim 4$ and $M \sim 6$ at low Reynolds numbers. It was observed that—in contrast to the sharp leading edge configuration of the cone-cylinder and the flat plate—neither induced pressure nor slip effects were present, due to the bluntness of the geometry investigated.

Heat transfer to cross-stream cylinders has been investigated by several groups (20,21,22). The results obtained in (20) extend farthest into the slip flow regime. Here again, it was noted that the bluntness of the configuration insured that the results were within the scope of applicability of ordinary boundary layer theory.

Drag coefficients for cross-stream cylinders have been measured and reported in (23). The results are presented in Fig. 5, which serves to illustrate the applicability of the interpolation process for transition regime results.

A study of the flow in the vicinity of a very short flat plate utilizing a "free molecule pressure probe" has been carried out in (24). The results were in reasonably good agreement with a simple diffuse reflection model for the flow in the vicinity of the plate, and constituted the nearest approach yet made to the direct observation of a slip velocity.

The flow field in the vicinity of the leading edge of a long flat plate has been studied (25), utilizing a "free molecule flow heat transfer probe." Various features of the flow, including the interaction between the shock and the growing viscous layer, were revealed in a qualitative manner.

In addition to these experimental investigations, a number of theoretical calculations have been made for rarefied flows. These are mostly based on the Navier-Stokes equations and on slip and temperature jump boundary conditions. The results of most interest are listed in (26 to 32).

Kinetic Theory Developments

Several new methods have been developed recently for dealing with basic flow situations, particularly in the transition flow regime, in terms of the fundamental Maxwell-Boltzmann equation of kinetic theory. An excellent summary of these methods is given in (33). Gross et al. (34,35,36) and Uhlenbeck and Chang (37,38), have developed methods for solving the linearized Maxwell-Boltzmann equation, i.e., the kinetic theory of infinitesimal disturbances in a gas, but with no restrictions as to the gas density. The essential difference between the two methods is in the use of "full range" expansions, i.e., expansions of the molecular velocity distribution function in terms of a set of eigen functions of the linearized collision operator taken over the entire range of molecular velocities, or in "half range" expansions, i.e., expansions of the distribution function which explicitly distinguish between molecular velocities directed toward or away from surface elements. Most of the simple basic problems, such as Couette flow, the impulsive flat plate, heat transfer between parallel plates, shear flow near a wall and the dispersion and absorption of sound waves, have been investigated along these lines. Perhaps the most important conclusions from these studies have been:

1 There are no unexpected phenomena in transition flow. The results usually constitute reasonable interpolations between the free molecule flow and continuum or slip flow limits.

2 Slip flow and temperature jump boundary conditions along with the full Navier-Stokes equations seem to be valid for predicting macroscopic flow conditions in the slip flow regime.

3 The mathematical dependence of the solutions on λ seems to be nonanalytic in both λ and $1/\lambda$, so that simple perturbation expansion procedures for modifying either continuum or free molecule flow results appear questionable.

A somewhat more powerful method has been suggested by Lees (39). This involves solution of the Maxwell transport equations with suitable parameterized forms for the molecular distribution function. The method is in the spirit of the well-known momentum-integral boundary layer method, and also to some extent follows the earlier work of Mott-Smith. An entirely different approach to low density

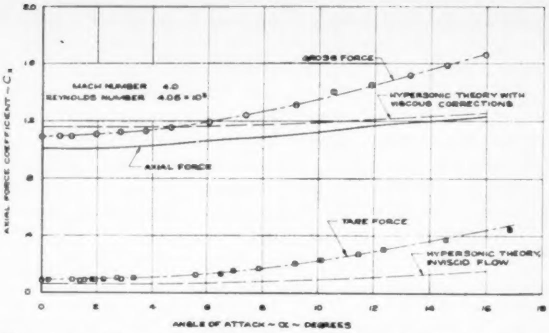

Fig. 4 Axial force coefficient at a nominal Mach number of 4.0

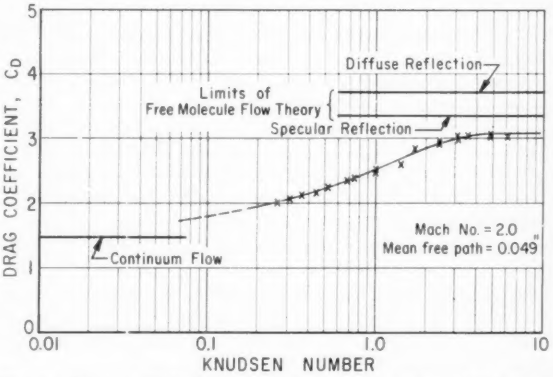

Fig. 5 Drag coefficient of a cylinder as a function of Knudsen number, measured by Sreekanth (23)

kinetic theory has been formulated by Bhatnager, Gross and Krook (40). They suggest replacing the momentum collision integral term in the Maxwell-Boltzmann equation by a relaxation expression which requires the distribution function to decay toward local Maxwellian equilibrium at a rate proportional to its instantaneous departure from it. This modified Boltzmann equation (sometimes called the "Krooked Boltzmann equation") is more tractable for analytical work. Solutions for typical problems have been in good agreement with results of the more exact methods (40,41).

Near Free Molecule Flow

The flow regime at densities which are just beginning to depart from strict free molecule flow has been the subject of a number of recent studies. The case of a sphere in very high speed flow, for example, has been investigated by Charwat and Baker (42) among others (43,44,45). Molecules re-emitted from the upstream surface occasionally deflect free stream molecules away from the surface which they would otherwise have struck, as well as occasionally deflecting free stream molecules into the surface which they would otherwise have passed by. It appears that the former effect is the dominant one, so that there is a net "shielding effect" which reduces drag and heat transfer coefficients if the density increases. The effect begins at surprisingly low densities for the high speed flow case. At a Mach number of 20, for example, the free stream mean free path must be a hundred times the sphere diameter to insure strictly free molecule flow. This result is thus in line with the preceding discussion, which indicates that high speed noncontinuum effects for blunt bodies begin at lower densities than had been originally supposed.

Free Molecule Flow

The aerodynamics of free molecule flow, i.e., flow at such low pressures that the molecules re-emitted from the surface have no effect on the incident flow, had been regarded as pretty well understood [see (2) for example] until very recently. However, the importance of and the consequent need to learn more about the exchange of momentum and energy between gas molecules and surfaces has only lately been realized, mostly in connection with the problem of predicting drag forces on artificial satellites. The classical free molecule flow analyses obtain expressions for heat transfer and aerodynamic force characteristics in terms of momentum and energy exchange "accommodation coefficients" which range from the limiting condition of completely diffuse reflection for which the exchange is complete, to the case of specular reflection for which there is no exchange. For some applications, particularly at very high velocities, it develops that the actual physical interaction is probably such as to give gross aerodynamic characteristics which are *not* intermediate to these two supposedly limiting types of interaction. The theoretical drag coefficient of a sphere, for example, in high velocity free molecule flow is exactly 2.00 for both the ideal specular and diffuse types of surface interaction. The theoretical drag coefficient for a more reasonable model for the surface interaction now appears (46) instead to be in the range 2.2 to 2.6, depending primarily on the degree of dissociation experienced by incident nitrogen molecules upon collision with the surface. The need for more information, particularly in the satellite range of velocities, had led to the development of new experimental equipment in the form of high energy ion and molecular beams. No experimental data of aerodynamic use are yet available, however, in the case of satellite energies. At Berkeley, molecular beam (47,48) and rotating cylinder (49) investigations of surface-molecule interactions have been carried out. These studies have suggested a new approach to the "accommodation coefficient" method of free molecule flow analysis. The new method (50) involves the use of three empirical constants to describe the surface interaction, but should be more in accord with the underlying physical reality than the older method.

Symposia

The rapid growth of the field of rarefied gasdynamics as a research area has given rise to a series of international symposia. The first of these was held in Nice in the summer of 1958; the proceedings of this meeting will be published shortly. The second symposium will be held **Aug. 3–6, 1960**, at the University of California, Berkeley. It will be preceded by a short course in Rarefied Gas Dynamics, conducted by Dr. Schaaf, to be held July 18–29.

References

1 Schaaf, S. A., "Rarefied Gas Dynamics," *Appl. Mech. Rev.*, vol. 9, Oct. 1956, pp. 413–415.

2 Schaaf, S. A. and Chambré, P. L., "Flow of Rarefied Gases," Vol. III, Part H, in "High Speed Aerodynamics and Jet Propulsion Series," Princeton University Press, 1958.

3 Schaaf, S. A. and Talbot, L., "Mechanics of Rarefied Gases," Vol. 5, Section 16, in "Handbook of Supersonic Aerodynamics," NavOrd Rep. 1488, Feb. 1959.

4 Bowyer, J. M. and Talbot, L., "Near-Free-Molecule Couette Flow Between Concentric Cylinders," University of California, Berkeley, Engineering Project Rep. HE-150-139, June 1956.

5 Talbot, L. and Sherman, F. S., "Structure of Weak Shock Waves in Monatomic Gases," NASA Memo 12-14-58W, 1959.

6 Talbot, L. and Sherman, F. S., "Experiment vs. the Kinetic Theory for Rarefied Gases," Proc. First International Symposium on Rarefied Gas Dynamics, Pergamon Press, London, 1960.

7 Adams, M. C. and Probstein, R. F., "On the Validity of Continuum Theory for Satellite and Hypersonic Flight Problems at High Altitudes," JET PROPULSION, vol. 28, no. 2, 1958, pp. 86–89.

8 Herman, R., "Hypersonic Flow Regimes at the Re-Entry of Satellite Vehicles," Proc. Sixth Tech. Conf. of Rosemount Aero. Labs., University of Minnesota, Rep. no. 165, Oct. 1959.

9 Devienne, F. M., "On Similitude in Rarefied Gas Aerothermodynamics," *J. Aeron. Sci.*, vol. 26, 1959, p. 183.

10 Tsien, H. S., "Superaerodynamics, Mechanics of Rarefied Gases," *J. Aeron. Sci.*, vol. 13, no. 12, 1946, pp. 643–664.

11 Laurmann, J. A., "The Effect of Slip on Induced Pressures," *J. Aero/Space Sci.*, vol. 26, 1959, p. 53.

12 Falkner, J. M. and Skan, S. W., "Some Approximate Solutions of the Boundary Layer Equations," British Aero. Res. Council Rep. and Memo. 1314, London, April 1930.

13 Lin, T. C. and Schaaf, S. A., "Effect of Slip on Flow near a Stagnation Point and in a Boundary Layer," NACA TN 2568, 1951.

14 Goldstein, S., "Summary Interim Report—Flow of an Incompressible Viscous Fluid Along a Semi-Infinite Flat Plate," University of California, Berkeley, Engineering Project Rep. HE-150-144, Dec. 1956.

15 Probstein, R. F. and Kemp, N. H., "Viscous Aerodynamic Characteristics in Hypersonic Rarefied Gas Flow," Avco Res. Lab. Rep. 48, Everett, Mass., March 1959.

16 Hoshizaki, H., "Effect of Slip on the Vorticity Correction to Stagnation Point Heat Transfer," *J. Aeron. Sci.* (in publication).

17 Schaaf, S. A. and Nark, T., "Lift and Drag Forces in Cone-Cylinder Bodies in a Rarefied Gas," Proc. Conf. on High-Speed Aerodynamics and Structures, ARDC Tech. Rep. 57-46, 1957, pp. 109–115.

18 Schaaf, S. A., Hurlbut, F. C., Talbot, L. and Aroesty, J., "Induced Pressures on Flat Plates in Low Density Supersonic Flow," ARS JOURNAL, vol. 29, no. 7, 1959, pp. 527–528.

19 Talbot, L., Schaaf, S. A. and Hurlbut, F. C., "Pressure Distributions on Blunt-Nosed Cones in Low Density Hypersonic Flow," JET PROPULSION, vol. 28, no. 12, 1958, pp. 832–834.

20 Tewfik, O. K. and Giedt, W. H., "Heat Transfer, Recovery Factor and Pressure Distributions Around a Circular Cylinder Normal to a Subsonic Rarefied Air Stream," IAS Preprint no. 60-46, Jan. 1960.

21 Bomelburg, H. J., "Heat Loss From Very Thin Heated Wires in Rarefied Gases," *Phys. Fluids*, vol. 2, 1959, p. 717.

22 Baldwin, L. V., "Slip Flow Heat Transfer from Cylinders in Subsonic Airstreams," NACA TN-4369, Sept. 1958.

23 Sreekanth, A. R., "Aerodynamic Force Measurements in a Highly Rarefied Gas Flow," Inst. Aero. (Univ. Toronto) Bulletin, Oct. 1959, pp. 11–12.

24 Harris, E. L., "Investigation of Free Molecule and Transition Flows Near the Leading Edge of a Flat Plate," Inst. Aero. (Univ. Toronto) Rep. no. 53.

25 Laurmann, J. A., "The Free Molecule Probe and Its Use for the Study of Leading Edge Flows," *Phys. Fluids*, vol. 1, 1958, p. 469.

26 Mirels, H., "Flat Plate Laminar Skin Friction and Heat Transfer in the Free Molecule to Continuum Flow Regimes," JET PROPULSION, vol. 28, no. 10, 1958, pp. 689–690.

27 Reeves, B. L. and van Camp, W. M., "Aerodynamic Heating of Simple Geometries in the Slip and Intermediate Flow Regimes," *J. Aeron. Sci.*, vol. 26, 1959, p. 838.

28 Oman, R. H. and Schewing, R. A., "On Slip Flow Heat Transfer to a Flat Plate," *J. Aeron. Sci.*, vol. 26, 1959, p. 126.

29 Charwat, A. F., "On the Contribution of Thermal Creep to the Skin Friction in Slip Flow," *J. Aeron. Sci.*, vol. 26, 1959, p. 120.

30 Hasmito, H., "Boundary Layer Slip Solutions for a Flat Plate," *J. Aeron. Sci.*, vol. 25, 1958, p. 68.

31 Maslen, S. H., "On Heat Transfer in Slip Flow," *J. Aeron. Sci.*, vol. 25, 1958, p. 400.

32 Tan, H. S., "Nose Drag in Free Molecule Flow and Its Minimization," *J. Aeron. Sci.*, vol. 26, 1959, p. 360.

33 Grad, H., "Principles of the Kinetic Theory of Gases," in "Handbuch der Physik," vol. XII, Springer-Verlag, Berlin, 1958, pp. 205–294.

34 Gross, E. P. and Jackson, E. A., "Kinetic Theory of the Impulsive Motion of an Infinite Plane," *Phys. Fluids*, vol. 1, 1958, p. 318.

35 Gross,, E. P. and Ziering, S., "Kinetic Theory of Linear Shear Flow," *Phys. Fluids*, vol. 1, 1958, p. 215.

36 Gross, E. P. and Ziering, S., "Heat Flow Between Parallel Plates," *Phys. Fluids*, vol. 2, 1959, p. 701.

37 Uhlenbeck, G. E. and Chang, C. S. W., "The Couette Flow Between Two Parallel Plates as a Function of the Knudsen Number," University of Michigan Engineering Research Institute Rep. 1999-1-T, June 1954.

38 Chang, C. S. W. and Uhlenbeck, G. E., "On the Behavior of a Gas Near a Wall," University of Michigan Engineering Research Institute Rep. 2457, Aug. 1956.

39 Lees, L., "A Kinetic Theory Description of Rarefied Gas Flows," Proc. 1959 Heat Transfer and Fluid Mechanics Institute, Stanford University Press.

40 Bhatnager, P. N., Gross E. P. and Krook, M., "Model for Collision Processes in Gases," *Phys. Rev.*, vol. 94, 1954, p. 511.

41 Gross, E. P. and Jackson, E. A., "Kinetic Models and the Linearized Boltzmann Equation," *Phys. Fluids*, vol. 2, 1959, p. 432.

42 Baker, R. M. L. and Charwat, A. F., "Transitional Correction to the Drag of a Sphere in Free Molecule Flow," *Phys. Fluids*, vol. 1, 1958, p. 73.

43 Hammerling, P. and Kivel, B., "Heat Transfer to a Sphere at the Transition From Free Molecule Flow," *Phys. Fluids*, vol. 1, 1958, p. 357.

44 Willis, D. R., "A Study of Nearly Free Molecule Flow," Rand Rep. 339, Santa Monica, Calif., June 1959.

45 Lin, V. C., "On Pitot Pressure in an Almost Free Molecule Flow," *J. Aeron. Sci.*, vol. 25, 1958, p. 779.

46 Schaaf, S. A., "Aerodynamics of Satellites," Rand Rep. 339, June 1959.

47 Hurlbut, F. C., "Studies of Molecular Scattering at Solid Surfaces," *J. Appl. Phys.*, vol. 28, no. 8, 1957, pp. 844–850.

48 Hurlbut, F. C., "Molecular Scattering at the Solid Surface," in "Recent Research in Molecular Beams," Academic Press, N. Y., 1958, chap. 8.

49 Merlic, E., "An Experimental Determination of Reflection Coefficients for Air on Aluminum," University of California, Berkeley, Engineering Project Rep. HE-150-141, Aug. 1956.

50 Schamberg, R., "A New Analytic Representation of Surface Interaction for Hyper Thermal Free Molecule Flow with Application to Satellite Drag," Proc. 1959 Heat Transfer and Fluid Mechanics Institute, pp. 1–16.

Fluorescent Technique for Determining the Cross-Sectional Drop Size Distributions of Liquid Sprays

G. M. BENSON[1]

University of California
Livermore, Calif.

M. M. EL-WAKIL,[2]
P. S. MYERS[2] **and**
O. A. UYEHARA[2]

University of Wisconsin
Madison, Wisc.

The development of a unique laboratory instrument which measures cross-sectional drop sizes in dynamic liquid sprays by a fluorescent technique is described. This technique consists of focusing a short duration, high intensity radiation flash into a thin sheet of radiation which intersects the spray nearly perpendicularly to the spray axis. The spray drops within this sheet, acting as primary radiators due to a fluorescent dye additive, are photographed and subsequently measured. The error in the measurement of the drop size was estimated from actual camera calibration data through the use of a specially made reticle to be less than 10 per cent for 10-micron diameter drops, and was found to decrease sharply for larger diameter drops. The fluorescent, optical and photographic problems encountered in the development are discussed. Drop size distribution data and spray photographs showing drop sizes are presented.

EFFICIENT power generation by fuel oxidation demands high rates of heat release within efficient combustion reactors, often of limited volume. In combustion reactors where fuel, or propellants, are originally present in the liquid phase, information on the rate and mechanism of the atomization and vaporization of these materials is of interest, particularly in reaction propulsion when liquid fuels are used (1–4).[3] Consequently many studies of the atomization and vaporization processes have been conducted. In spite of these numerous studies the state of our knowledge is such that it is still difficult to predict rates of vaporization of sprays for a particular nozzle, fuel and set of operating conditions because of incomplete information on drop size distributions from nozzles and rates of vaporization in sprays.

With the feeling that a basic understanding of drop size distributions and rates of vaporization from liquid sprays was essential to the understanding of heterogeneous combustion, a research program intended to furnish information on these points has been in progress for some time (5–9) in the

---

Presented at the ARS 13th Annual Meeting, New York, N. Y., Nov. 17–21, 1958.

[1] Research Scientist, Radiation Laboratory.

[2] Professor of Mechanical Engineering.

[3] Numbers in parentheses indicate References at end of paper.

Mechanical Engineering Department at the University of Wisconsin. These studies have resulted in the experimental confirmation of theoretical relations that predict the life history of single drops of various liquids, subjected to an atmosphere at various temperatures, pressures and velocities. The accuracy of the predictions, for the sizes studied, was nearly as great as the accuracy with which the physical properties are known. The application of these techniques to densely populated sprays (10) indicated that the assumption of a single drop surrounded by an infinite volume of air, unaffected by the vaporization of the other drops, does not agree with the experimental facts. In order to develop a correction factor for the effect of one drop on another, experimental drop size distributions in vaporizing sprays at cross sections normal to the spray axis and located at various distances downstream from the nozzle are needed.

Techniques previously used to measure drop size distributions in sprays may be classified into six major groups: Collecting drops on slides or in cells and microscopic size determination, freezing of drops and mechanical sieving, direct photographic techniques, scattering or light absorption techniques (including Tyndall and Mie scattering, and other optical methods), electronic or radiographic techniques, and selective impaction. Reference (4) has a bibliography of 120 papers written on these techniques, and discusses their advantages and disadvantages in detail. All of these techniques may be criticized because the functional relation with drop size is either complicated, or based upon conjectural and tenuous assumptions, the accuracy of the method cannot be determined, an undesirable physical disturbance of the spray is produced by the measuring technique, the physical phenomena of the measuring characteristic is inadequately understood, or the practical difficulties have seemed insurmountable. In addition, rigorous direct methods of calibration under operational conditions are in most cases unavailable.

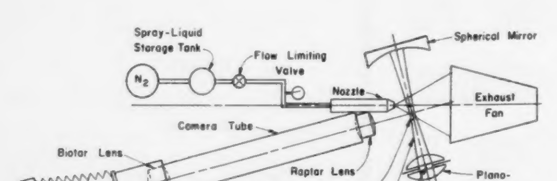

Fig. 1 Apparatus layout (top view)

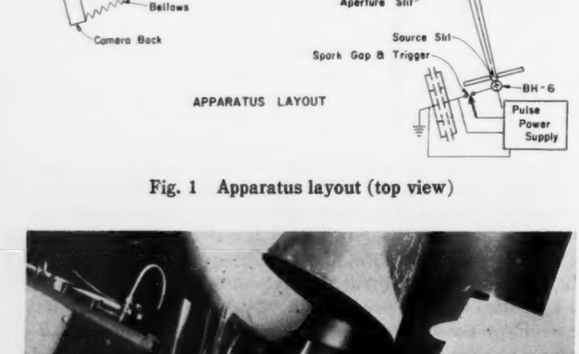

Fig. 2 Photograph of apparatus showing radiation sheet in spray (top view)

Of the methods indicated, direct photography shows the most promise. However the methods used to date obtained cross sections of portions of the spray that were parallel rather than perpendicular to the spray axis. They all suffered from inherent uncertainties as to uncertain depths of field and image blur because of drop motion perpendicular to the cameras' lens axis.

The technique that was developed and is being reported herein is believed capable of determining, with good accuracy, cross-sectional drop sizes in vaporizing sprays. It is not completely free of all the mentioned criticisms, but it does offer the following advantages over previously used techniques: It is capable of direct and fairly accurate calibration for drop sizes under actual spray conditions; it produces minimum interference with the spray; it does not influence drop size distribution; it has the sampling plane perpendicular to the spray axis; it permits only a well-defined volume within the spray to be analyzed at one particular setting; and it produces little or negligible drop motion-blur.

Technique

The apparatus, which utilizes the fluorescent characteristic of certain liquids or liquid dye mixtures, is shown schematically in Fig. 1. A fluid pressurized by nitrogen is ejected from a nozzle, forming a conical spray which, further downstream, is drawn, together with entrained air, into a duct and fan assembly and subsequently discharged from the test area. A high pressure capillary mercury-arc lamp is flashed by capacitor discharge. The resulting radiation is focused into a thin sheet by two plano-parabolic quartz lenses having a rectangular midstop aperture. At a predetermined location between the nozzle and the duct, this sheet intersects the spray nearly perpendicularly to the spray nozzle axis and irradiates a narrow cross section of the spray. The spray drops within this sheet act as primary radiators due to a minute quantity of a fluorescent dye additive.

This dye partially absorbs the radiation and reradiates it. The images of the fluorescent drops are enlarged and photographed by a high resolution camera whose optical axis is perpendicular to the sheet of radiation and centered upon the spray area to be photographed.

The apparatus is rigidly fixed in space with the exception of the nozzle, which can be positioned accurately upon machined ways by three micrometers in three mutually perpendicular directions. This construction insures nearly perfect optical alignment, since the spray can be completely photographed by simply moving the nozzle, while the optical systems remain fixed in space.

Fig. 2 is a photograph of the apparatus showing the radiation sheet intersecting the spray.

If satisfactory drop images are to be obtained, only the half of the spray on the camera side should be photographed. Reference (11) presents the details of this problem. If it is not desired to assume symmetry in the spray, the nozzle can be rotated and the other half of the spray studied.

The brightness (power per unit solid angle per unit projected area) that a given fluorescing drop exhibits is directly proportional to the product of the brightness in the sheet of radiation and the solid angle of radiation convergent upon the drop. The excitation brightness must, of course, lie within the absorption band of the fluorescent dye. In addition, the sheet of radiation illuminating the spray should be quite thin and have a thickness no greater than the depth of focus of the camera lens. The radiation sheet should also be carefully positioned so that it will fall within the depth of focus.

These objectives were met in the present apparatus by using a plano-parabolic lens with a rectangular midstop, plus a reflecting spherical mirror, by using a source of high effective brightness, and by maximizing the pulse-light circuit parameters so that electrical energy is supplied to the radiation source at a maximum rate.

Fluorescence

The radiation falling on the drops is absorbed and re-emitted because of the added fluorescent dye. The use of this dye causes the drop to act as a primary light source and thus enables better drop images to be obtained than if reflected light had been used. In addition, calibration of the optical system in place and under actual conditions is possible.

Inasmuch as the drops are to receive radiation from a small solid angle and to emit over a solid angle of 4π, it is necessary to conserve radiation in all ways possible. It is obvious that the fluorescent dye must efficiently convert the radiation from the illuminating source to fluorescent radiation. In addition, the dye must absorb at the wave lengths present in the illuminating source and, because of the unavailability of suitable lenses, emit in the visible region. Also, the fluorescent induction and decay times should be very short (10^{-7} sec or less), so that the drops will not be still fluorescing when they have passed out of the "depth-of-focus" of the camera lens. Finally, if a dye additive is used, it must have a high solubility in the fluids of interest.

Fig. 3, taken primarily from data given in (12), indicates how well an aqueous uranin solution meets these requirements. It will be noted that the relative quantum yield (Q_r) is very high throughout the whole absorption band; the absorption and fluorescent spectra (relative intensity I_r not to common scale) are strong, and the fluorescence is in the visible spectrum. Further, the induction and decay times are approximately 5×10^{-9} sec, and this dye is highly soluble in glycerine, water, alcohol and alcohol-ether mixtures (which represent a tremendous range of liquid properties). Other fluorescent dyes, such as rubrene (tetraphenylnaphthacene), are soluble in many fuels and exhibit characteristics that are as favorable to this technique as those of uranin (11).

It should be noted that in spray fluids composed of fluorescent dyes (solutes) in solution with nonfluorescent spray liquids (solvents), the fluorescent brightness of the spray vapor is usually negligible, since the fluorescent dyes usually have much less volatile than the solvents; i.e., the boiling point of rubrene is much higher than that of benzene. Therefore, the spray vapor usually is not photographable. Further, due to the great difference in boiling points, the dye concentration in the liquid drop may increase as the drop vaporizes. As an example, if a drop is reduced in diameter by a factor of 10 through vaporization, and if high internal circulation (7) exists within the drop, the dye concentration would increase roughly by a factor of 1000. In that case, if the initial concentration were close to its saturation value, the liquid properties of the drop would change as the drop vaporizes, with a resulting tendency for the drop to gel. In the data taken to date, the initial dye concentration by weight has been less than 1 per cent and usually about 10^{-2} mols per liter of spray liquid, and the diameter change was much less than 10. Of course, any system improvement which further increases or conserves radiation would permit the use of smaller dye concentrations.

Fig. 4 shows the relative effect of dye concentration on brightness. C_c and B_{fc} are reference concentrations and brightness, respectively. Curves similar in shape to those shown in Fig. 4 but having different coordinate values are obtained for different liquids and dyes. Thus it is important to select the proper concentration for a given dye and liquid.

Table 1 presents data on the effect of a 5-gm per liter uranin dye concentration on selected properties of different fluids.

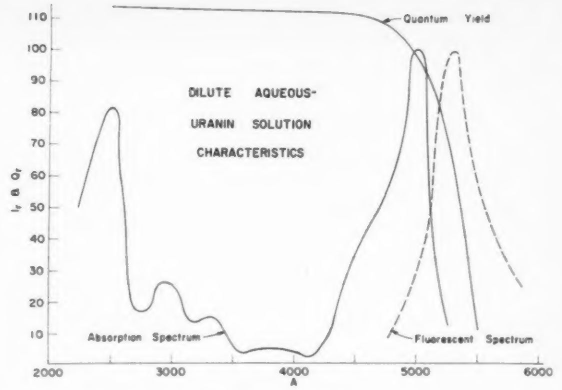

Fig. 3 Dilute aqueous uranin solution spectral characteristics

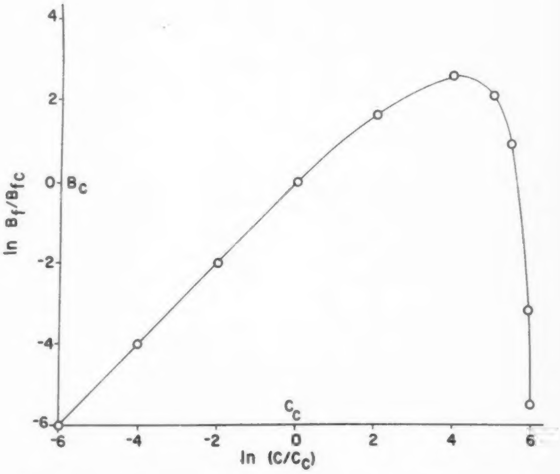

Fig. 4 Relative fluorescent brightness vs. dye concentration

Photographing the Drops

The quality of a photograph of the drops depends upon the radiation from and the motion of the drop, the camera lens and the film.

Speaking of the camera lens, a low *f*-number is desired to gather the maximum amount of radiation. At the same time a long focal length lens is desired so that the lens does not interfere with or be wetted by the spray. Most readily available lenses having small *f*-numbers also have a short focal length. Also, equal manufacturing precision will result in less optical errors in short focal length lenses. The lens must also have high resolving power if small drops are to be faithfully recorded. Fig. 5, taken using a high priced camera lens operated under reasonable photographic conditions, indicates that the problem is not simple.

A sensitive film is desired, since the radiation from the drop is very low. For the same reason, not much enlargement of the drop image is desired. However, if the drop image is not enlarged, grain size and defects in the film will become important. The problem in photographing the drops then is to maximize several conflicting requirements and characteristics (11).

Since the technique demands both a true size and shape record of spray drops, and since a number of lenses did not product such images (see Fig. 5), an extensive lens testing program was conducted to optimize the camera optical system. In order to both test and calibrate the optical system, an annular reticle having increasing concentric radii from 5 to 250 μ, accurate within a 1 per cent error (relative to a ruled stage micrometer of accuracy within 100 Å) was used upon high resolution spectroscopic plate emulsion and a high resolution microscope objective. Such a reticle is a very critical test for a well-corrected optical system (11). The image of this reticle formed by an aerial camera lens is shown in Fig. 6. For comparison, the image of the same reticle produced by the finally adopted camera optical system is shown in Fig. 7.

Table 1 Effect of dye additives on spray liquid properties

Viscosity

Fluid, 20 C	Measured viscosity[a] (c.p.)	Referenced viscosity, 29 (c.p.)
ethyl alcohol	1.2	1.200
ethyl alcohol (dyed)	1.2	
water	1.0	1.005
water (dyed)	1.0	
glycerine	1.5×10^3	1.490×10^3
glycerine (dyed)	1.5×10^3	

Surface tension

Fluid, 20 C	Measured surface tension,[b] dynes/cm	Referenced values, 29 dynes/cm
ethyl alcohol	23	22.3
ethyl alcohol (dyed)	23	
water	73	72.75
water (dyed)	73	
glycerine	64	63.4
glycerine (dyed)	64	

Specific gravity

Fluid, 20 C	Measured specific gravity	Referenced values, 29
ethyl alcohol	100° (alcoholometer)	100°
ethyl alcohol (dyed)	99° (alcoholmeter)	
water	0° (alcoholmeter)	0°
water (dyed)	0° (alcoholmeter)	
glycerine	29.9° (Baumé)	29.92°
glycerine (dyed)	29.9° (Baumé)	

[a] Determined by Saybolt viscometer using a Universal tube.

[b] Determined by open-to-air capillary tube.

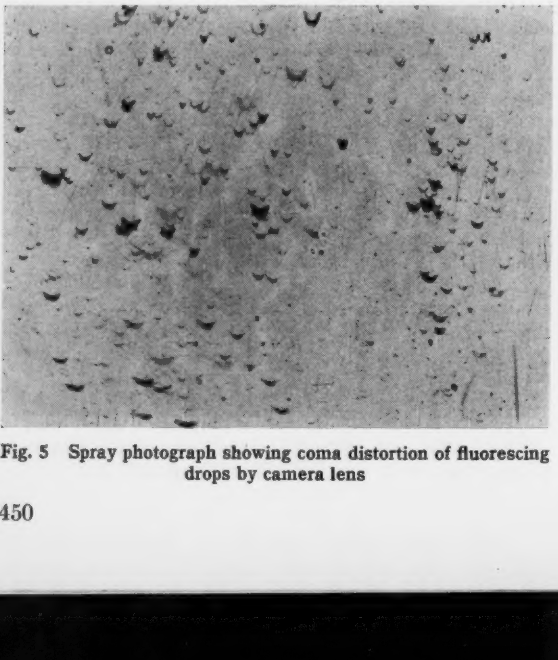

Fig. 5 Spray photograph showing coma distortion of fluorescing drops by camera lens

It is obvious that any system which records an optical image must be precisely calibrated under actual data sampling conditions over the entire operating range, if the recorded data are to be reliable. This apparatus was calibrated by determining the relation between the true drop size and the apparent drop size recorded on a film produced by this reticle. In this test the reticle was successfully positioned throughout the optical field volume (that spray volume determined by the camera's field of view superimposed upon the thickness of the radiation sheet). The same type of film was used as is used in recording spray drop sizes. The negatives were then developed, processed and visually measured from their magnified images using the same procedures as used for spray photographs. Since the size of the reticle was known and the camera and read-out magnifications were determined independently, the error could then be determined. A graph of apparent size vs. actual size of the diameters of the concentric circles in the reticle was plotted from this data and is shown in Fig. 8. The region between the two solid lines in the graph indicates the spread or indeterminancy of the experimental data for any given actual diameter. It may be noted that, since the curve as a whole is linear, diffraction effects are undetectable even at 10 μ diameters. From this graph it is evident that, percentagewise, the size indeterminancies are largest for the smallest drops, and that this indeterminancy decreases rapidly for larger drops. The indeterminancy at 10 μ is about 10 per cent. However, it should be cautioned that extrapolation of this linear curve to smaller sizes is not at all possible, since both aberration and diffraction effects would cause the curve to swing upward. Part of the indeterminancy may be attributed to human error in averaging the edge gradient in the film image during read-out. The same statement, in general, may be made for drop counting and measuring.

Unfortunately, fluorescing spray drops within the radiation sheet apparently fail to fluoresce with uniform emittance (emitted radiant flux per unit cross-sectional area) both across the cross section of any given drop and between drops. The nonuniformity across the cross section is attributed to both a fluorescent trapping effect and the variation in the optical thickness of a drop throughout its cross section, with consequent production of an emissivity gradient across the drop. The nonuniformity between drops is attributed, among other

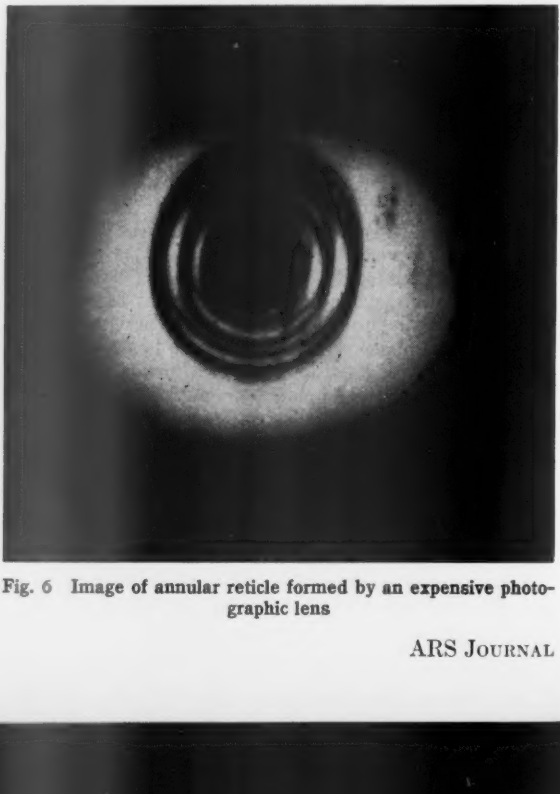

Fig. 6 Image of annular reticle formed by an expensive photographic lens

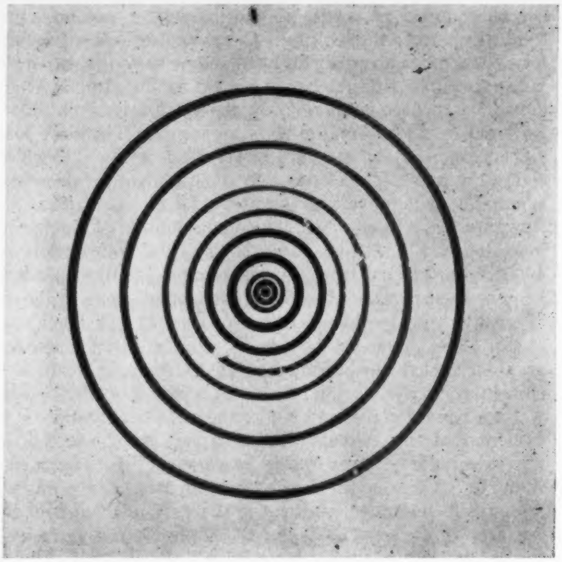

Fig. 7 Image of annular reticle formed by camera of apparatus

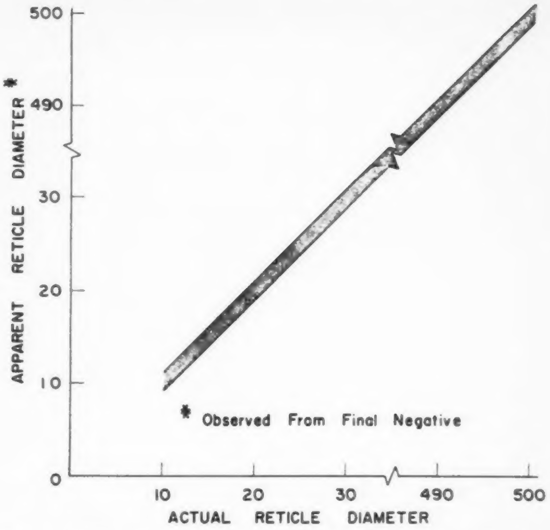

Fig. 8 Calibration curve for camera of apparatus showing apparent reticle diameter vs. actual reticle diameter

things, to the light source producing a nonuniform brightness across its cross section due to electron temperature gradients in the source's plasma, and to the excitation optical system producing an imperfect image of the source, thus producing a nonuniform radiation field.

This random variation in intensity of radiation from the drops produces images of varying intensity on the film with consequent "edge effects." These edge effects (which are further increased by "graininess" in the film) cause some uncertainty in determining drop sizes from the original negative, and are magnified when a reproduction of the negative is made. Since no way of calibrating these edge effects is available, the original negatives are used for drop counting purposes.

The foregoing discussion indicates that all data must be taken under the same conditions at which the apparatus was calibrated. If not, then not only are the spray drop size and size distribution data relative, but they can be varied for given spray conditions by simply changing the camera aperture, camera lens, film exposure, film developing and processing (including printing), or by a variable discrimination of the optical density value that represents the spray drop image boundary (edge gradient effect).

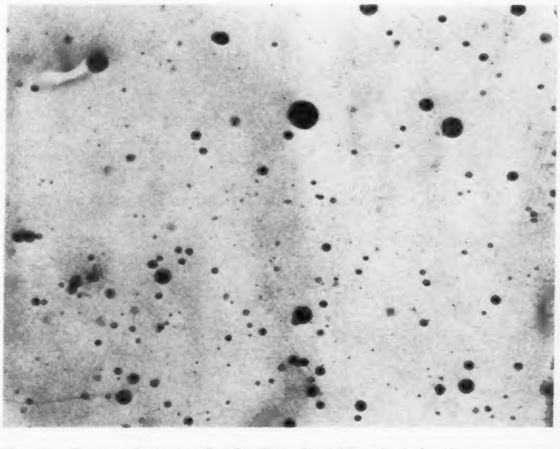

Fig. 9 Spray photograph of ethanol at 10-psig injection pressure with five flashes superimposed

Data

Fig. 9 is an unretouched photograph of an ethyl-alcohol spray injected at 10 psig into static ambient air, taken at a location on the spray axis 3 in. downstream from the nozzle. The other operating conditions are listed in Table 2. The photograph is the result of five successive exposures (flashes) on the same film. Multiple exposure is desirable from a statistical point of view. It may be noted that some drops are not completely within the radiation sheet and consequently appear out-of-focus, whereas the grainy appearance is caused by the negative emulsion material. What at first may be interpreted to be spray breakup, represented by the somewhat superimposed drops in Fig. 9, is probably due to the multiple exposures on this photograph, since the location is thought sufficiently downstream to avoid such phenomena. Fig. 10 is a photograph having five exposures of a 100-psig alcohol spray taken under the same spray conditions.

To date, spray drop photographs of similar quality have

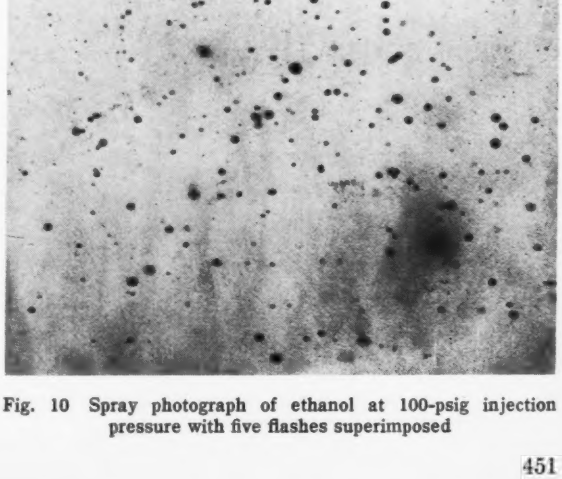

Fig. 10 Spray photograph of ethanol at 100-psig injection pressure with five flashes superimposed

been obtained by this technique for glycerine, water, ethyl alcohol, and isobutyl alcohol-diethyl ether liquids with uranin as the fluorescent additive. In addition, benzene, kerosene, diethyl ether, and petroleum lubricating oil with rubrene as the fluorescent additive have been successfully photographed. Such fluids give a wide range of viscosity, surface tension, vapor pressure and density. Further, all of the fluids in which one dye is soluble are mutually soluble and therefore permit a continuous alteration of the above properties, if desired.

In presenting drop size distribution data it is convenient to use a reduced temporal drop size number represented by

$$\frac{{}^{t}\overline{dN/dD}}{N}$$

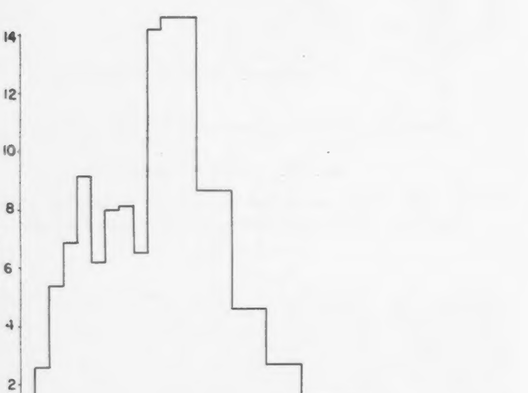

Fig. 11 Drop size distribution for ethanol spray at 10-psig injection pressure

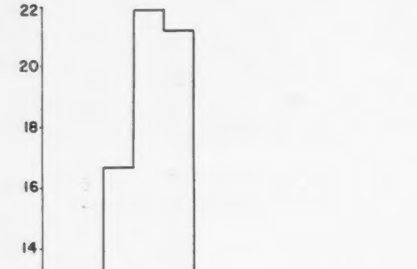

Fig. 12 Drop size distribution for ethanol spray at 100-psig injection pressure

i.e., the number of drops (dN) in diameter range (dD) per total number of sampled drops (N) averaged over a time interval (t) sufficiently long to average out spray fluctuations. When this drop size number is plotted against drop size (diameter), a reduced temporal drop size distribution is obtained. In practice, these infinitesimals are finite. The drop size classification so obtained are represented in Fig. 11, which shows the percentage of drops in a particular size classification. The data for this bar-graph type drop size distribution curve were obtained for ethyl alcohol atomized at conditions indicated in Fig. 11 and Table 2. The size distribution for 4000 drops, plotted here, represents over 1000 independent exposures—a number of exposures felt large enough to average out any temporal spray fluctuations.

Fig. 12 is a reduced temporal drop size distribution bar graph for ethyl alcohol injected at 100 psig. Fig. 13 is a similar graph for an equal concentration of glycerine and water atomized at 100 psig under the same conditions. It is evident that this last distribution is very similar to that of ethyl alcohol injected at 10 psig, as shown in Fig. 14 by curves A and C. These continuous curves were obtained by drawing a relatively smooth curve through the midpoint values of the bar graphs of Figs. 11, 12 and 13. It is interesting to note that each curve has three peaks with those of curve B being reversed in order of magnitude to those of curves A and C. Since most naturally occurring distribution curves are smooth curves if a sufficient number are considered, this may indicate that 4000 drops are an insufficient number to give a completely accurate distribution curve.

In the data presented herein, all of the counted drops that appeared to be smaller than 10 μ in diameter were measured to be greater than about 5 μ, but it is believed that even in this 5–10 μ range a high percentage was missed. The many unknowns in this problem might be circumvented by not including any population values in the 0–5 μ range, since these values are, at best, in very great error and therefore could be misleading to spray atomization and vaporization studies.

It is self-evident that unless a certain minimum number of drops are measured the drop size distribution obtained is a function of the number of drops measured. In order to esti-

Table 2 Operating conditions for spray data

capacitor voltage	8–10 kv
capacitance	0.15 μf
spark gap setting	such as to cause self-breakdown at 11 kv when in series with cold tube (around 0.10 in.)
source	BH-6, nonpre-ionized
BH slit width	800 μ
radiation sheet thickness	200 μ
radiation sheet, location	3 in. downstream from nozzle, 15 deg off normal from spray axis
radiation sheet area	5 × 5 mm
spray fluid temperature (upstream from nozzle)	70 F
nozzle	Monarch "F-80" 30-deg solid cone, 0.60 gal/hr at 200 psig for fuel oil
camera magnification	20.00 ± 0.05
photographic film	Royal-X Pan (Kodak)
development	12 min at 68 F, DK-60a, continuous agitation
intensification	chromium intensifier followed by Monckhoven's intensifier

Visual size classification is made from measuring film image projected at 28.2 × upon a white low-gloss plane screen (12).

mate if this certain minimum number were included in the foregoing data the following analysis was made. The first 100 drops sampled were classified into their k predetermined size classification with the result that n_{1_i} drops would occur in the ith size classification for this first group of 100 drops, represented by subscript 1 (i ranges from 1 to k). Therefore the summation of n_{1_i} from 1 to k will yield 100. Each n_{1_i} is the percentage of drops in the ith size classification for this first group of 100 drops. This, divided by 100, is the reduced temporal drop size number for the ith size classification based upon 100 drops sampled. Let this be denoted by M_{1_i}. M_{0_i} for any size classification is zero. Denote $(M_{1_i} - M_{0_i})/M_{1_i}$ as percentage change in W_{1_i} for the first 100 drops sampled, which is 100 per cent. Now 100 additional drops are classified into the same k classifications. Consider again the ith classification, which has n_{2_i} drops in it. The sum of n_{1_i} and n_{2_i} is the number of drops in the ith classification for 200 drops sampled. This sum is divided by 200, and this percentage is called M_{2_i}. Then $(M_{2_i} - M_{1_i})/M_{2_i}$, the percentage change in W_{2_i} in the ith size classification for 100 additional drops sampled, is calculated.

In general then, the following procedure can be used. Consider a given ith drop size classification obtained for a given total number $(N-j)$ of sampled drops and the percentage of total drops contained therein. Count j additional drops, which in the case noted was 100, and calculate the new percentage in this given ith drop size classification based upon all drops counted so far, i.e., N drops. It is evident that if any comparison in the rate of convergence of W_{N_i} with N is to be made for various total numbers (N) of drops counted, the value of j must be fixed. Calculate the absolute value of the difference between these two percentages and divide by the new percentage. This ratio is termed percentage change in W_{N_i} for this given ith drop size classification for N drops sampled, and serves as the ordinate for the graph shown in Fig. 15. As is evident, the percentage change in W_{N_i} is different and converges differently for each drop size classification, as illustrated for the ith groups of 10, 50 and 250μ for this alcohol spray injected at 10 psig. The low value of percentage change in W_{N_i} occurring at 1200 drops is misleading, since other size (ith) groups had a relatively high value at this point.

It can be seen, therefore, that in determining the cutoff point for the number of drops to be included in the analysis, the envelope of least upper bound for all size classifications should be considered; whereas, due to fluctuations in the rate of convergence between size groups, it is incorrect to state that the ith drop size classification that approaches zero most slowly determines the required minimum number. It may be stated that the values of W_{N_i} for all drop size classifications were approximately within these curves given in Fig. 15 at cutoff; i.e., the curves shown there serve as least upper bound envelopes at cutoff.

Acknowledgment

The generous financial grants given by the National Science Foundation, the National Aeronautics and Space Administration, General Electric Company's Aircraft Gas Turbine Division, the Wisconsin Alumni Research Foundation and the College of Engineering, University of Wisconsin, not only made this study possible, but were instrumental in helping to perfect and modify this technique into an analytical laboratory instrument.

References

1 Priem, R. J. and Heidmann, M. F., "Vaporization of Propellants in Rocket Engines," ARS Journal, vol. 29, no. 11, Nov. 1959, p. 836.

2 Weisenberg, I. J., "A Rational Approach to High Performance Rocket Injector Design," ARS preprint 674–58, Nov. 1958.

3 Mayer, E., "Vaporization Rate Limited Combustion in Bipropellant Rocket Chambers," ARS preprint 676–58, Nov. 1958.

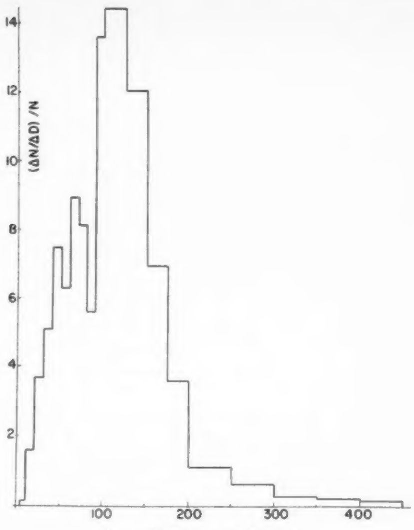

Fig. 13 Drop size distribution for aqueous glycerin spray at 100-psig injection pressure

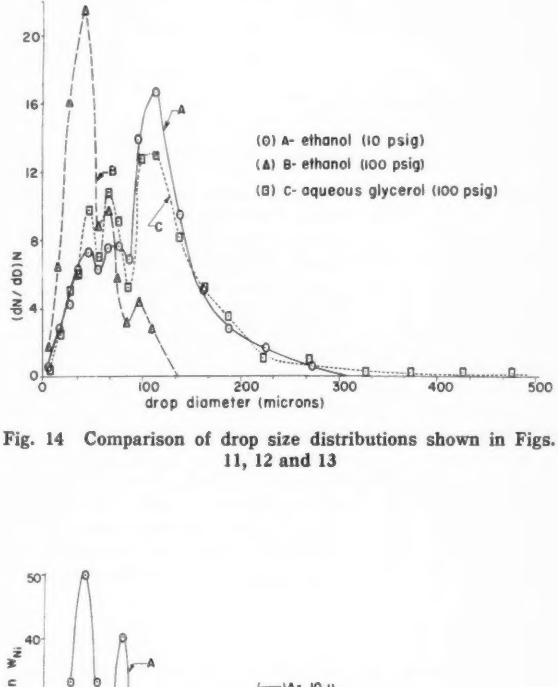

Fig. 14 Comparison of drop size distributions shown in Figs. 11, 12 and 13

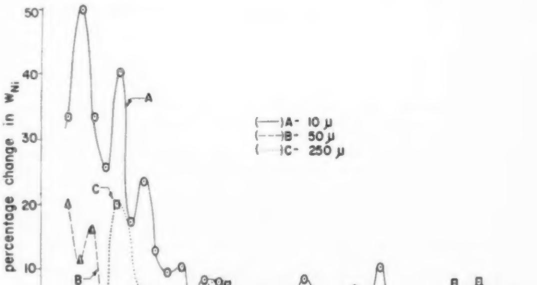

Fig. 15 Drop size distribution convergency vs. number of drops sampled for 10-psig ethanol spray

4 Putnam, A. A. et al., "Injection and Combustion of Liquid Fuels," WADC T. R. 56-344, Office of Technical Service, U. S. Dept. of Comm., Washington, D. C., 1957.

5 El-Wakil, M. M., Uyehara, O. A. and Meyers, P. S., "A Theoretical Investigation of the Heating-Up Period of Injector Fuel Droplets Vaporizing in Air," NACA TN 3179, 1954.

6 El-Wakil, M. M., Priem, R. J., Brikowski, H. J., Myers, P. S. and Uyehara, O. A., "Experimental and Calculated Temperature and Mass Histories of Vaporizing Fuel Drops," NACA TN 3490, 1956.

7 Priem, R. J., Borman, G. L., El-Wakil, M. M., Uyehara, O. A. and Myers, P. S., "Experimental and Calculated Histories of Vaporizing Fuel Drops," NACA TN 3988, 1957.

8 Borman, G. L., El-Wakil, M. M., Uyehara, O. A. and Myers, P. S., "Reduced Graphs for Computing Histories of Vaporizing Fuel Drops and Drop Histories under Pressure," NACA TN 4338.

9 Priem, R. J.,"Vaporization of Fuel Drops Including the Heating-Up Period," Ph.D. Thesis, Univ. of Wisconsin, 1955.

10 El-Wakil, M. M., Myers, P. S. and Uyehara, O. A., "Fuel Vaporization and Ignition Lag in Diesel Combustion," 1956 SAE Trans., vol. 64, pp. 713–729.

11 Benson, G. M., "The Determination of Cross-Sectional Drop-Size Distributions of Liquid Sprays by a Fluorescent Technique," Ph.D. Thesis, Univ. of Wisconsin, 1960.

12 Pringsheim, P., "Fluorescence and Phosphorescence," Interscience Publishers. N. Y., 1949.

Hypersonic Shock Wave-Boundary Layer Interaction and Leading Edge Slip[1]

H. T. NAGAMATSU[2] and
R. E. SHEER Jr.[3]

General Electric Co.
Schenectady, N. Y.

An investigation was conducted on the flow over a flat plate with a sharp leading edge in a hypersonic shock tunnel. A flow Mach number range of 9.77 to 19.6 with a reflected stagnation temperature of 2500 R, and a flow Mach number of 7.8 at 7200 R were used. For these flow conditions the static pressure in the test section varied from 20 microns to 1 mm of mercury, and the Knudsen number based on the leading edge radius varied from about 0.3 to 2.9. Slip flow effects at the sharp leading edge were observed showing that the strong shock wave and the boundary layer were delayed in forming on the plate. The slip region increased with the free stream flow Mach number and with the mean free path of the air ahead of the model. In the strong interaction region near the leading edge, the viscous region extended from the plate surface to the shock wave, and there was no apparent inviscid region between the shock wave and the boundary layer. The induced pressure on the plate varied inversely as the square root of the distance from the leading edge as originally predicted theoretically by Li and Nagamatsu. The strong interaction parameter $M_1^3/\sqrt{Re_X}$ varied from 2 to approximately 140, and at the highest flow Mach number tested, the maximum induced pressure near the leading edge was nearly 29 times the free stream static pressure. Cooling of the boundary layer by the plate surface greatly affected the magnitude of the induced pressure at high flow Mach numbers. Even for a reflected stagnation temperature of 7200 R, with appreciable real gas effects, the strong interaction between the shock wave and the boundary layer was present.

RECENT advances in rocket and missile technology have made possible the development of intercontinental ballistic missiles, satellites and space vehicles. The flight Mach numbers for these vehicles range from about 20 to 35. The calculated equilibrium stagnation temperature for a blunt body during re-entry at 100,000 ft for Mach 35 is 20,000 R. With manned hypersonic vehicles the deceleration and the control problems will be important, so that a glide-type vehicle looks most promising. Also, to decrease the dispersion of long range ballistic missiles, the nose cones can be equipped with fins for terminal guidance. Thus, there is a great need for fundamental knowledge regarding the aerodynamic characteristics of lifting surfaces at high flow Mach numbers and correspondingly high stagnation temperatures.

For a flat plate with a sharp leading edge in a hypersonic flow, a shock wave and a viscous boundary layer will be formed at the leading edge. Recent experimental results (1–3)[4] for a flat plate at hypersonic Mach numbers have indicated a delay in the formation of the strong shock wave, where the boundary layer was merged with the shock wave for

---

Presented at the ARS Semi-Annual Meeting, San Diego, Calif., June 8–11, 1959.

[1] This research was sponsored jointly by the General Electric Co. and Ballistic Missile Division, ARDC, U. S. Air Force under Contract AF 04-647-269.

[2] Research Associate; also, Adjunct Professor, Rensselaer Polytechnic Institute, Troy, N. Y. Member ARS.

[3] Gas Dynamics Division.

[4] Numbers in parentheses indicate References at end of paper.

some distance back of the leading edge before separating. For a given Reynolds number with insulated wall conditions, the boundary layer thickness is approximately proportional to the square of the Mach number. At hypersonic Mach numbers the large boundary layer growth causes a strong interaction between the leading edge shock wave and the boundary layer. Since the pressure across a shock wave is proportional to the square of the flow deflection angle and the Mach number, the induced pressures due to the interaction of the shock wave and the boundary layer on a flat plate can be much greater than the free stream pressure at high Mach numbers. This increase in the surface pressure for a flat plate will increase the skin friction as well as the heat transfer. For lower supersonic flow conditions these induced pressure effects are small, and at low subsonic speeds the classical laminar boundary layer theory applies, which predicts no pressure increase.

The case of hypersonic flow over a flat plate with a thick leading edge, where the thickness is much greater than the mean free path of the gas in the free stream, is entirely different from that of the sharp leading edge. With a blunt leading edge, a detached shock wave is produced ahead of the plate and the flow Mach number after the shock is subsonic with high pressures. For this condition the viscous effects become small and the inviscid flow over the blunt leading edge predominates as discussed in (4 through 6.) Since the flow is subsonic ahead of the leading edge, there is no possibility of the existence of slip flow for a reasonably dense gas, as in the case of a sharp leading edge at hypersonic Mach numbers.

A number of theoretical papers (7–13) for a flat plate with infinitely thin leading edge at hypersonic Mach numbers have been prepared in recent years. At the high flow Mach numbers, the induced pressure near the leading edge caused by the interaction of shock wave and boundary layer will be large. This is usually referred to as the strong interaction regime. Two general approaches have been utilized in developing the strong interaction theories. In (8 and 9) the boundary layer is assumed to extend from the plate surface to the shock wave. It was originally shown in (9) that for a strong interaction region the induced pressure varies as $X^{-1/2}$, where X is the distance from the leading edge, and the important parameter was $M_1{}^3/\sqrt{Re_X}$, where M_1 is the free stream Mach number and Re_X is the Reynolds number based on the distance X. The other solutions (10–12) were derived on the assumption that the boundary layer and the shock wave were distinctly separated, even in the vicinity of the leading edge. A theoretical result for the hypersonic viscous flow over a noninsulated flat plate has been derived in (13). Recent experimental results (1,2) for a flat plate with a sharp leading edge have indicated that the shock wave and the boundary layer are merged for some distance back of the leading edge before separating. The shock wave-boundary layer interaction induced pressure results obtained at very high flow Mach numbers (to be presented in this paper), indicate the existence of the slip flow, and the merged region of the shock wave, and the boundary layer for large values of the interaction parameter $M_1{}^3/\sqrt{Re_X}$.

Some experiments have been conducted in air to determine the magnitude and nature of the shock wave-boundary layer interaction phenomena in hypersonic wind tunnels (14,15). In (14) a careful investigation of the flow between the shock wave and the flat plate surface has been conducted at Mach 5.8. The interaction parameter was only of the order of 3, so that the induced pressure due to the interaction at the leading edge was quite small. By heating the air to 1360 R, a hypersonic flow over a flat plate was investigated at Mach 9.6 by measuring the surface pressure (15). The highest interaction parameter for these investigations was about 10, and the maximum measured induced pressure ratio near the leading edge was about 9. A similar flat plate with a sharp leading edge was studied in the University of California Low Density Tunnel over Mach range 2 to 5.8 for rarefied conditions. The flow field between the shock wave and the plate surface was surveyed by means of a free molecular probe (1). These results indicated the possible existence of the slip flow and the merged region between the shock wave and the boundary layer in the vicinity of the leading edge. The other method of investigating the flow over a flat plate was to measure the induced pressure on the surfaces of a number of flat plates with orifices located at different distances from the leading edge. Induced pressure results (3,16) have also indicated the existence of the slip flow at the leading edge, with the largest interaction parameter being about 10 and a corresponding induced pressure ratio of 8 at flow Mach 5.8. An experimental investigation of a flat plate with a sharp leading edge in a helium tunnel has been conducted, and the induced pressure results are presented in (17). For helium, the ratio of specific heats γ is 1.67, which is greater than the value for air, $\gamma = 1.4$.

The present investigation was conducted in order to extend the available knowledge in the literature regarding the slip flow at the leading edge of a sharp flat plate, the shock wave-boundary layer interaction phenomenon at higher flow Mach numbers and the interaction parameters. A study was made to determine the existence of the leading edge slip, and the nature of the shock wave-boundary layer interaction at high stagnation temperatures where the real gas effects for air are appreciable. A brief description of the hypersonic shock tunnel facility and the instrumentation used to obtain surface pressures, and Schlieren photographs of the shock wave and the viscous region will be presented. The leading edge slip flow phenomenon for a flat plate with a sharp leading edge was investigated by measuring the surface pressure near the leading edge, and obtaining Schlieren photographs of the delay in formation of the strong shock wave and boundary layer at the leading edge. Shock wave-boundary layer interaction results over flow Mach range 9.77 to 19.6 and an interaction parameter range of 2 to 140 will be discussed for conditions of nearly perfect gas flow. The real gas effects at high stagnation temperatures upon the induced pressures on a flat plate will be presented.

Facility, Instrumentation, Model and Test Conditions

Hypersonic Shock Tunnel

The investigation was conducted in the hypersonic shock tunnel with different throat diameters, for a conical nozzle with a 24-in. exit diameter, to obtain the various hypersonic flow Mach numbers in the test section. A detailed description of this facility is presented in (18). Fig. 1 shows the nozzle and the dump tank with windows located at the test section of the nozzle. Under perfect gas conditions for air ($\gamma = 1.4$), the nominal nozzle Mach numbers of 10, 16 and 20 had throat diameters of 1.0, 0.33 and 0.19 in., respectively. This conical nozzle was attached to the end of the 4-in. ID, 103-ft long constant area driven tube. The shock wave was reflected at the entrance to the nozzle, for the present investigation, to increase the pressure and temperature after the reflected shock and to minimize the attenuation effects due to the boundary layer in the driven tube.

At the entrance to the nozzle a scored aluminum diaphragm is used to permit the shock tube and dump tank to be evacuated to different pressures. Usually the dump tank and the nozzle are evacuated to very low pressures, often as low as 4 μ of mercury, to facilitate the flow establishment in the test section and to minimize the strength of the starting shock wave. This diaphragm opens upon the arrival of the incident shock wave, with the bursting pressure controlled by using different material thicknesses and cut depths.

Observation windows are located at the exit of the nozzle to permit optical investigations of the flow fields around models. The windows are optically selected thick plate glass. A sting, which holds the model in the test section, was mounted separately to the floor and vibration isolated from the dump tank and floor by the use of Teflon bushings. This hollow sting was also used to carry the electrical leads from the pressure gages mounted in the model to the oscilloscopes.

Instrumentation

All the static and impact pressures were measured by piezoelectric pressure gages (18,19). The standard Kistler SLM quartz pressure pickups were used to measure the reflected stagnation pressure at the entrance to the nozzle, and the impact pressure in the test section. These gages, large in size and with a small output of about 5 mv per psi, cannot be used to measure the very low pressures on the surface of a flat plate. Small barium-titanate pressure pickups have been developed to meet the requirements of small size and high output. These gages were mounted in the flat plate model and were dynamically calibrated by placing the model at the end of the constant area driven section, and using the pressure jump across a weak incident shock wave. Both the Kistler and the barium-titanate pressure pickups are sensitive to their position and type of mounting in the models.

A modified Tektronix 535 oscilloscope (18) was used to determine the shock wave position as a function of time in the 103-ft long driven tube. Heat and ionization gages are used as time of arrival pickups, and the output from these gages are fed into the Tektronix scope. For the normal operation of the shock tunnel, the shock velocity measurements are supplemented by a Berkeley counter which measures the shock wave traversal time over the last $6\frac{1}{4}$ ft of the driven tube with 1-microsec accuracy.

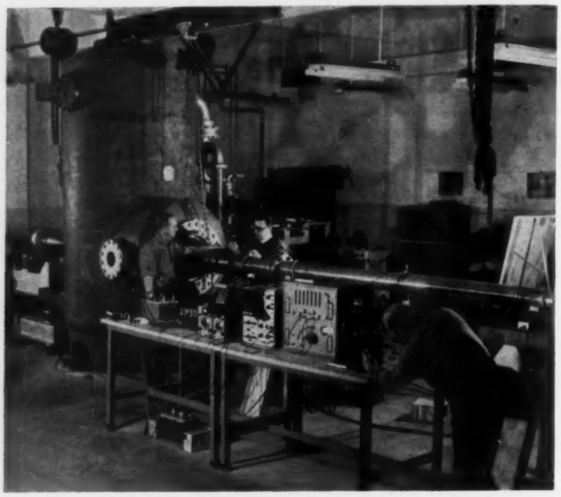
Fig. 1 Shock tunnel nozzle and dump tank

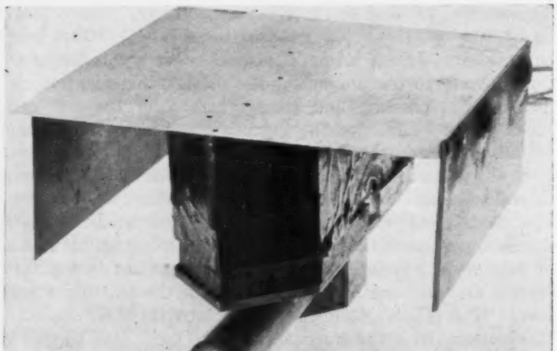
Fig. 2 Flat plate model

A single pass Schlieren system with parabolic mirrors is used to obtain the Schlieren photographs of the flow field for the flat plate model. The light source is provided by a suitably timed spark of 10,000-v capacitor discharge, with a duration of the order of 0.4 microsec.

Model

The steel flat plate model shown in Fig. 2 was of 5-in. width and 11-in. length, of which the last 5 in. was a lucite extension mounted flush with the top surface. This extension was used to minimize the trailing edge effects upon the induced pressure measurements. The bottom of the leading edge was beveled 15 deg. By observing the leading edge under a high power microscope, the leading edge thickness was estimated to be 0.001 in. over the central part of the plate. Thin side plates were attached to the flat plate, as shown in Fig. 2, to prevent the strong shock wave, produced by the wedge housing the pressure gages, from disturbing the flow on the top surface. Since the boundary layer at hypersonic Mach numbers is very thick, it is necessary to use great caution to minimize any disturbances that may affect the boundary layer.

For the measurements of the pressure induced by the interaction of the shock wave and the viscous layer, there were five orifices in the top surface located between $X = 0.193$ and 3.90 in. The shielded electrical leads from the pressure gages were all housed within the wedge and in the hollow sting, both of which were maintained at the same low pressure as the dump tank. Each pressure gage was carefully shock mounted with rubber and also insulated electrically from the model. A separate cylindrical housing with a hemispherical nose (see Fig. 2) was used to hold the Kistler gage for measuring the impact pressure at the leading edge location. All the gages were dynamically calibrated in the model at the end of the driven tube before and after each series of induced pressure measurements in the test section. The output from each pressure gage was amplified and then fed into a Tektronix 535 oscilloscope equipped with a Polaroid attachment for recording the induced pressure.

Test Conditions

The flow conditions in the test section (20) at the exit of the conical nozzle are essentially determined by the area ratio for the nozzle, and the conditions behind the reflected shock at the downstream end of the driven tube. The equilibrium stagnation temperature behind the reflected shock wave is controlled by the strength of the incident shock wave, which is produced by the combustion driver, and the initial temperature and pressure in the driven tube. Thus for a hypersonic shock tunnel the stagnation temperature at the entrance to the nozzle can be varied over an extreme range, without difficulty, for any given area ratio for the nozzle.

Pressures behind the reflected shock wave at the entrance to the nozzle are measured directly with the standard Kistler quartz pickups, whereas the reflected temperatures are calculated values based on the shock Mach number at the end of the driven tube and the equilibrium thermodynamic data for air (21–25). All reflected equilibrium stagnation temperatures referred to in this paper are determined in this manner.

To determine the flow Mach number in the test section with the conical nozzle, an axial survey was conducted with static and impact pressure probes. For the condition of a reflected stagnation temperature of 2500 R at the entrance to the nozzle, the slight variation in the ratio of specific heats was considered in the determination of the flow Mach number for a measured static pressure in the test section. Even at this relatively low reflected temperature, the slight real gas effects caused the flow Mach number to lower slightly, and increased the static temperature and the static pressure compared with the perfect gas expansion with constant $\gamma = 1.4$. By this method the flow Mach numbers in nozzles of nominal Mach number 10, 16 and 20 were determined to be respectively 9.77, 15.6 and 19.6 for a reflected stagnation temperature of approximately 2500 R.

At an elevated reflected stagnation temperature of 7200 R for the nominal Mach 10 nozzle with a 1-in. throat diameter and 24-in. exit diameter, the static and impact pressures were measured along the axis of the nozzle. Again, by assuming thermodynamic equilibrium during the expansion process in the nozzle, the flow conditions in the nozzle were calculated for isentropic expansion of a source flow. The measured static and impact pressures agreed very closely with calculated values for an equilibrium flow (20). By this method the flow Mach number in the test section was determined to be 7.8, with a static temperature of 810 R for a reflected stagnation temperature of 7200 R with a corresponding reflected pressure of 500 psi. Hence, it is apparent from this result that the real gas effects decrease the flow Mach number in the test section for a given area ratio, and the static temperature is then higher due to the energy release from the recombination of the plasma during the expansion process. A more detailed investigation is being conducted to determine the state of the hot plasma as it expands in the nozzle, for various reflected stagnation temperatures and pressures.

Leading Edge Slip Flow for a Flat Plate

Mach Number, Reynolds Number, Mean Free Path and Knudsen Number in the Test Section

The flow Mach numbers in the test section of the nozzle were determined by measuring the static and impact pressures on the axis, and correlating these pressure results for air (21–25) with the assumption of equilibrium flow. In order to minimize the real gas effects, one series of investigations for the flat plate was conducted at a reflected stagnation temperature T_5 of approximately 2500 R, with nozzle area ratios for nominal Mach numbers of 10, 16 and 20.

Calculation of the Reynolds number for the different test conditions was based on the free stream condition existing in the test section. For low static temperature ranges, the viscosity coefficient was obtained from results presented in (16). The Sutherland equation was used to determine the viscosity for a static temperature in the range of 810 R. These values of viscosity coefficients were used in calculating the mean free path of the gas from the equation based on the kinetic theory for gases (26)

$$\mu = 0.499\, \rho \bar{v} \lambda$$

where

ρ = density
$\bar{v}$ = average molecular velocity
λ = mean free path

All of these quantities are for the ambient condition in the test section. To determine the effective sharpness of the leading edge, the Knudsen number $K_n = \lambda/t$, based on the ratio of mean free path to thickness of the leading edge, was calculated for each test condition.

By taking a Schlieren photograph of the flow over the flat plate at different delay times, it could be seen that the boundary layer on the plate required approximately 200 microsec to become fully established after arrival of the starting shock wave at the plate leading edge. Approximately the same time interval was required for establishment of the detached shock wave at the impact probe, which is mounted on the bottom of the flat plate. For these investigations the flow duration after flow establishment is approximately 2.5 millisec. The shock wave and the boundary layer require only a small part of the total testing time to be fully established. Response time of the static pressure gages in the model is approximately 100 microsec, and, thus, the surface pressure measurements should be very close to a steady flow condition.

Surface Pressure Distribution Near the Leading Edge

In Figs. 3 and 6 the ratios of surface pressure to free stream pressure for different Mach numbers are plotted as functions of $X^{-1/2}$, which is the variation originally derived in (9) for the strong shock wave-boundary layer interaction region on a flat plate with a sharp leading edge. For both of these figures the pressure ratio varies nearly linearly with the forementioned parameters for X greater than the second pressure orifice located 0.712 in. from the leading edge. There is a sharp drop off in the increase rate of pressure ratio from the $X^{-1/2}$ variation as the leading edge is approached. The first pressure orifice is located at $X = 0.193$ from the leading edge. This deviation from linear variation becomes greater with

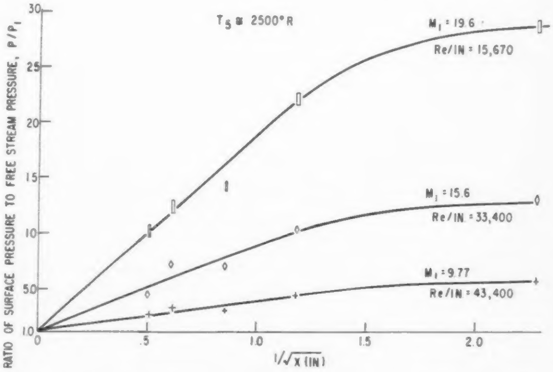

Fig. 3 Ratio of surface pressure to free stream pressure vs. the inverse of the square root of distance from the leading edge, $T_5 \cong 2500$ R

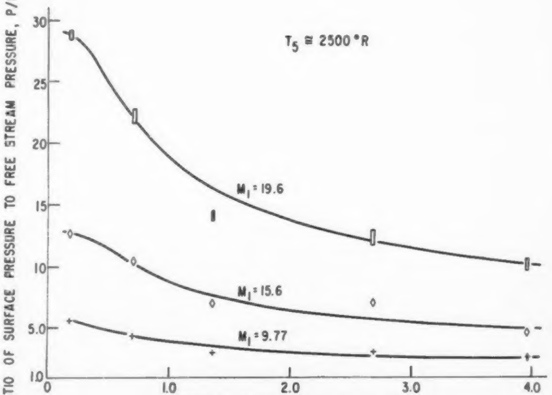

Fig. 4 Ratio of surface pressure to free stream pressure vs. distance from the leading edge, $T_5 \cong 2500$ R

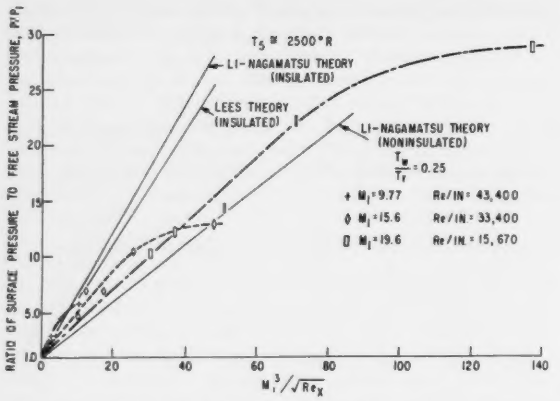

Fig. 5 Ratio of surface pressure to free stream pressure vs. the interaction parameter, $T_5 \cong 2500$ R

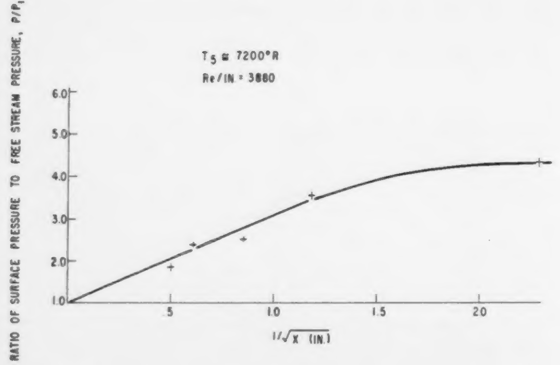

Fig. 6 Ratio of surface pressure to free stream pressure vs. the inverse of the square root of distance from the leading edge, $T_5 \cong 7200$ R

increasing flow Mach number for nearly perfect gas conditions, as indicated in Fig. 3. Also the asymptotic value for the pressure ratio near the leading edge increases approximately as the square of the flow Mach number. At the higher stagnation temperature of nearly 7200 R, where appreciable real gas effects are present, the induced pressure ratio near the leading edge also approaches an asymptotic value for a flow Mach number of 7.8. (See Fig. 6.)

In Figs. 5 and 8 the induced pressure ratios are plotted in terms of the hypersonic parameter $M_1^3/\sqrt{Re_X}$ for reflected stagnation temperatures of approximately 2500 and 7200 R. Plotted in this manner, the tapering off of the induced pressure as the leading edge is approached is quite evident, and the magnitude of departure from the straight line for a given Mach number is much greater at the highest flow Mach number investigated. The asymptotic value for the induced pressure at the leading edge increased with the flow Mach number. At the higher stagnation temperature of approximately 7200 R the curvature of the induced pressure ratio, in terms of the interaction parameter near the leading edge, is well defined because of the lower free stream Reynolds number.

This drop off in the increase rate of the induced pressure and the approach to an asymptotic value at the leading edge could be caused by the slip flow existing at the front part of the plate (3,16) at low density conditions for flow Mach numbers up to 5.8, theoretically postulated in (7).

Schlieren Photographs of the Flow

The Schlieren photographs presented in Figs. 9–12 of the flow over a flat plate were obtained with a spark light source of 0.4 microsec duration. Figs. 9–11 are for the flow with a reflected stagnation temperature of approximately 2500 R for flow Mach 9.77, 15.6 and 19.6. For these test conditions the air can be considered a nearly perfect gas with $\gamma = 1.4$, and the real gas effects are small. In these figures the strong shock wave and the boundary layer are delayed in forming at the leading edge. The maximum shock wave angles are located downstream rather than at the leading edge $X = 0$, as predicted by the classical boundary layer theory with no slip at the surface. Also, the shock wave and boundary layer are merged together before becoming separated. The merged region increased with the flow Mach number as indicated by the Schlieren photographs. In hypersonic flow, the outer edge of the boundary layer has a large density gradient (14,27), so it appears in the photograph as a light region. The location of the reverse curvature in shock wave and boundary layer also moved downstream from the leading edge with increasing flow Mach number.

Because of the low density and Reynolds number at a reflected stagnation temperature of approximately 7200 R and flow Mach 7.8, the boundary layer is not distinct in the Schlieren photograph presented in Fig. 12. Again, the shock wave and boundary layer are delayed in forming and the

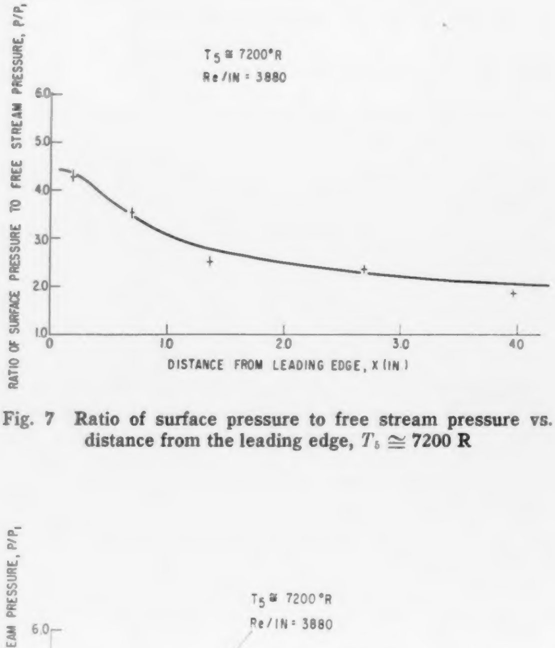

Fig. 7 Ratio of surface pressure to free stream pressure vs. distance from the leading edge, $T_5 \cong 7200$ R

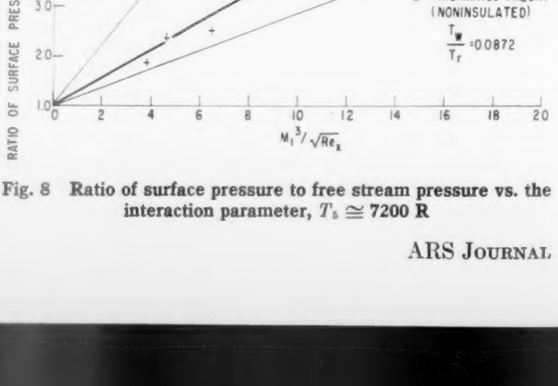

Fig. 8 Ratio of surface pressure to free stream pressure vs. the interaction parameter, $T_5 \cong 7200$ R

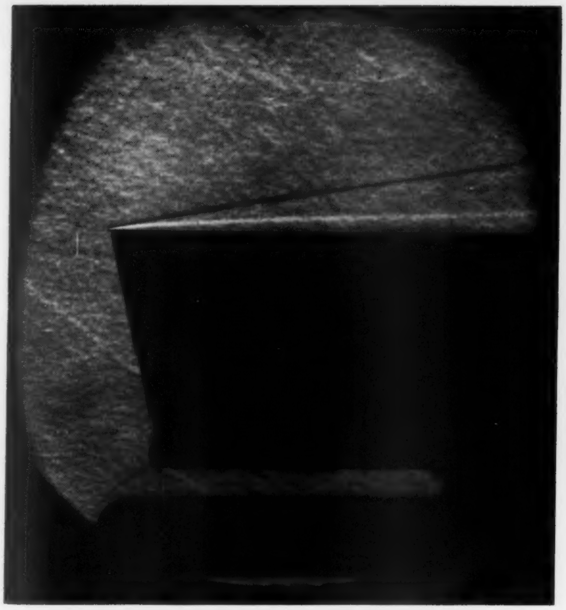

Fig. 9 Schlieren photograph of flow over a flat plate at Mach 9.77, $T_5 \cong 2500$ R

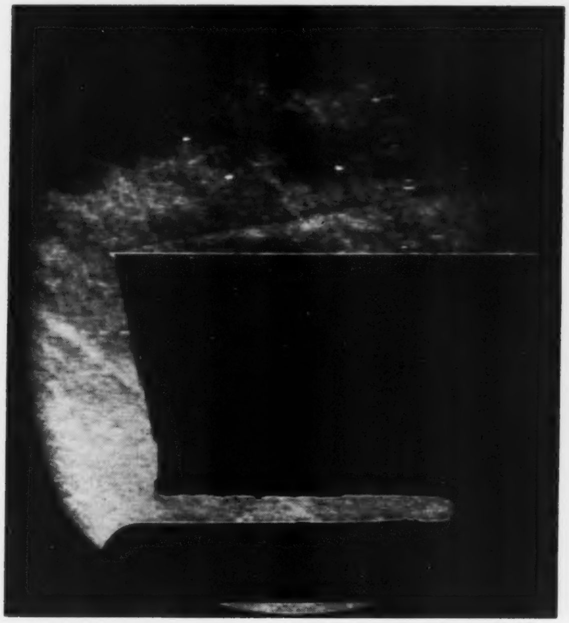

Fig. 11 Schlieren photograph of flow over a flat plate at Mach 19.6, $T_5 \cong 2500$ R

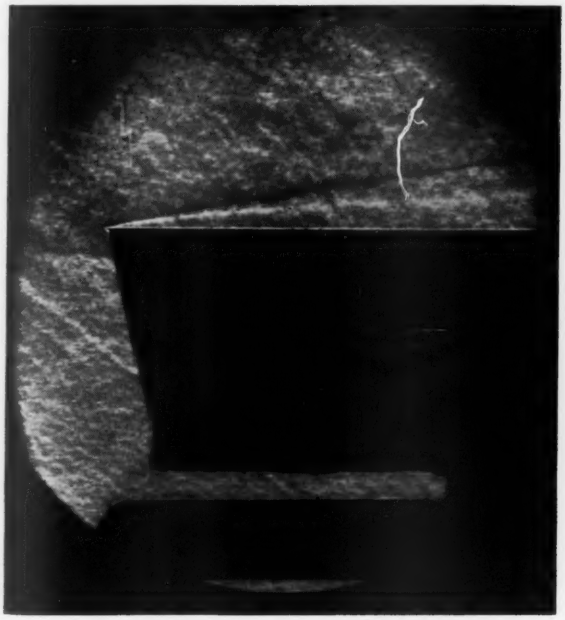

Fig. 10 Schlieren photograph of flow over a flat plate at Mach 15.6, $T_5 \cong 2500$ R

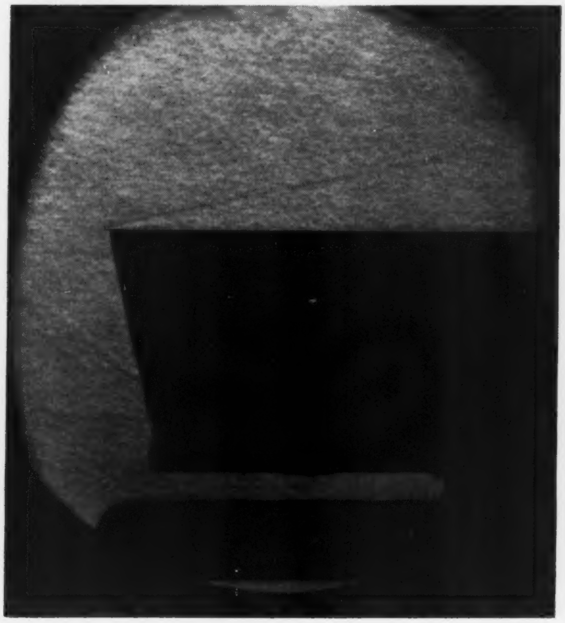

Fig. 12 Schlieren photograph of flow over a flat plate at Mach 7.80, $T_5 \cong 7200$ R

maximum shock angle location is downstream of the leading edge. This location at this temperature condition was greater than that of the case of a reflected temperature of 2500 R and flow Mach 9.77. The primary cause for this difference in the location of the maximum shock wave angle (7) must be due to the larger mean free path in the test section. See Table 1.

All the Schlieren photographs of the flow over the present flat plate with a sharp leading edge have exhibited the delay in formation of strong shock wave and boundary layer at the leading edge, for both the nearly perfect gas condition $\gamma = 1.4$ and the higher temperature case with appreciable real gas effects. The shock wave and boundary layer were merged together before becoming separated. The location of the maximum shock wave angle and the merged shock wave and boundary layer region increased with the flow Mach number and the mean free path in the test section of the nozzle. The shock wave angle at the leading edge was always appreciably lower than the maximum shock angle slightly downstream. This delay in the strong shock wave and boundary layer

Table 1 Some representative test conditions for different flow Mach numbers in the test section

M_1	T_5,[a] R	p_1, mm Hg	$Re/\dot{m}$	λ, in.	K_n
9.77	2375	0.765	43,400	0.335×10^{-3}	0.335
15.6	2385	0.104	33,400	0.695×10^{-3}	0.695
19.6	2475	0.020	15,670	1.85×10^{-3}	1.85
7.80	7130	1.128	3,880	2.99×10^{-3}	2.99

[a] T_5 is the reflected equilibrium stagnation temperature at the entrance to the nozzle.

formation could be caused by the existence of slip flow on the surface. A free molecular probe survey of the leading edge region, at flow Mach 5.8 and with rarefied flow conditions, has indicated a similar delay in the formation of a strong shock wave, and the existence of a merged shock wave and boundary layer (1).

By measuring the shock wave angle from the Schlieren photograph as a function of the distance from the leading edge, the pressure ratio across the shock can be calculated by using the oblique shock wave relationship for perfect gas, as well as for real gas with thermodynamic equilibrium (28). From the leading edge the pressure ratio across the shock wave increased with X up to a peak value corresponding to the maximum shock wave angle. After this maximum value the pressure ratio continuously decreased as the shock wave angle became smaller. For flow Mach 19.6 the pressure ratio near the leading edge was approximately one-half the maximum pressure ratio value, slightly farther downstream from the leading edge. The result for the stagnation temperature of approximately 7200 R and flow Mach 7.8 has indicated a much lower pressure ratio at the leading edge compared to the peak pressure ratio.

This increase in the pressure ratio behind the shock wave to a maximum pressure ratio could be caused by the slip flow existing in the leading edge region (2,3,16). As the slip velocity at the surface is brought to rest from the free stream value in the slip distance ζ (7), the pressure ratio must increase from a finite value to a maximum value at the end of the slip distance. Beyond this value of X the velocity at the surface will be equal to zero, which is the case for the conventional boundary layer in a continuum flow.

Slip Flow Theory

In the vicinity of the leading edge of the flat plate, the surface pressures and the Schlieren photographs at various flow Mach numbers and stagnation temperatures have indicated the possible existence of the slip flow region, as discussed previously. A first-order slip flow theory has been developed (7) to estimate the slip distance, the delay in the formation of the strong shock wave and boundary layer, and the possible variation of the slip flow region. The slip distance based upon the kinetic theory of gases is

$$\zeta \sim NM_1\lambda$$

where N is the number of collisions required to bring the molecules to rest on the surface. It has been found experimentally that the value of N is approximately five collisions; M_1 is the free stream Mach number, and λ is the mean free path in the test section. For a Reynolds number based on the free stream conditions and the slip distance ζ, the no slip regime is defined as

$$Re_\zeta/M_1^2 \geq N$$

Slip flow exists when

$$Re_\zeta/M_1^2 < N$$

as indicated in Fig. 13.

In the slip distance ζ where the velocity at the surface is brought to rest, the pressure ratio must increase from a finite value at the leading edge to a maximum value at $X = \zeta$ where the velocity of the gas at the wall is equal to zero. Also, in the slip region the strength of the shock wave must increase from a finite value at the leading edge to a maximum shock angle at the end of the slip region. The shock wave and the boundary layer are both merged and delayed in forming in the slip region. The present experimental results for a flat plate with a sharp leading edge have indicated the existence of the slip flow region at high flow Mach numbers and reasonably large mean free path. Rarefied flow results for a flat plate up to flow Mach 5.8 have also indicated the existence of slip flow (1,16).

Shock Wave-Boundary Layer Interaction

Induced Pressure Distribution for Reflected Stagnation Temperature of Approximately 2500 R

The actual measured static pressure ratios, surface pressure to the free stream pressure, are plotted as a function of $1/\sqrt{X}$, X and $M_1^3/\sqrt{Re_X}$, in Figs. 3–5, respectively, for a reflected stagnation temperature of 2500 R. For these investigations the flat plate surface temperature was close to room temperature throughout the test duration. By assuming a laminar boundary layer and a recovery factor of 0.85, the ratio of the wall temperature to the recovery temperature is approximately 0.25 for Mach range 9.77 to 19.6 at the previously noted reflected stagnation temperature. Thus, the cooling effects of the plate surface upon the induced pressures caused by the shock wave boundary layer must be considered. A theoretical result for the effects of a noninsulated flat plate, for both cooling and heating of the boundary layer, is presented in (13). The real gas effects upon the induced pressure are small for this particular stagnation temperature compared to the cooling effects.

It is evident from Figs. 3–5 that the maximum pressure ratio near the leading edge increases approximately as the square of the free stream Mach number. For the present flat plate, the first static pressure orifice is located at 0.193 in. from the leading edge. At this location the induced pressure ratios are close the asymptotic value and have deviated appreciably from the $X^{-1/2}$ variation which seems to apply in the strong interaction region. This similar variation of the induced pressure at flow Mach range 3.5 to 6 has been observed in the low density tunnel (3,16). For all the Mach numbers that were investigated, the induced pressure ratio from the second static pressure orifice, located at 0.712 in. back from the leading edge, does vary inversely as the square root of the distance (see Figs. 3 and 5) as originally predicted in (9). The asymptotic values of the induced pressure ratio, as X becomes large, approach unity for all the Mach numbers investigated. These results also indicate that the lucite extension at the end of the flat plate and the fins at the sides of the plate, as in Fig. 2, were effective in reducing the external disturbances on the boundary layer growth.

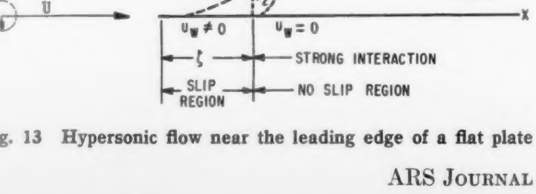

Fig. 13 Hypersonic flow near the leading edge of a flat plate

The induced pressure ratios have been plotted as a function of the distance X from the leading edge for the different Mach numbers in Fig. 4. For flow Mach 9.77 the peak pressure ratio near the leading edge is nearly 6, and at 4 in. back from the leading edge the pressure ratio is approximately 2.5. Thus, at even this relatively low hypersonic Mach number, the effect of the shock wave-boundary layer interaction is appreciable. For flow Mach 19.6 the maximum pressure ratio near the leading edge is nearly 29, and for $X = 4.0$ in. the induced pressure is 10 times the free stream value ahead of the flat plate. The skin friction and heat transfer (13) for the plate will be much higher for this flow condition compared with values determined by the compressible boundary layer without pressure gradient. The results for flow Mach 15.6 lie between the induced pressure results for flow Mach 9.77 and 19.6.

In Fig. 5 the induced pressure ratio for the different Mach numbers are plotted as functions of the interaction parameter $M_1^3/\sqrt{Re_X}$, where M_1 is the free stream Mach number and Re_X is the Reynolds number based on the free stream condition and the distance X from the leading edge. For each flow Mach number the induced pressure ratio approaches an asymptotic value of different magnitude, indicating the existence of the slip phenomenon near the leading edge for the present plate with a sharp leading edge. After the leading edge slip region, the induced pressure ratios for all the Mach numbers vary linearly with the strong interaction parameter. The slope of the straight portion of the induced pressure ratio in Fig. 5 decreases as the Mach number increases. The theoretical slopes predicted for the insulated case (9,10) are plotted in Fig. 5. At flow Mach 9.77 the analytical slopes for insulated conditions are reasonably close to the observed experimental results for noninsulated conditions. The results obtained in the low density tunnel (3,16) for induced pressures on a flat plate agree reasonably well with the present Mach 9.77 results.

In (13) the effects of noninsulated conditions on the induced pressure, skin friction and heat transfer have been determined analytically for a sharp flat plate with perfect gas assumptions. For a stagnation temperature of 2500 R, the gas can be considered nearly perfect without an appreciable error. The theoretical slope for the induced pressure ratio as a function of the interaction parameter is plotted in Fig. 5 for the actual temperature ratio for the plate surface. It is interesting to note that the result for the highest flow Mach number, 19.6, has the closest agreement with the analytical prediction for a noninsulated surface. At high flow Mach number, the surface cooling of the boundary layer decreases the induced pressures produced by the shock wave-boundary layer interaction. But at the lower flow Mach 9.77, the cooling effects of the plate surface does not seem to be appreciable. For flow Mach 15.6 the slope of the induced pressure ratio curve in the strong interaction region is approximately in the middle of the slopes for Mach 9.77 and 19.6, as indicated in Fig. 5. Hence for this flow Mach number of 15.6 the surface cooling effects are noticeable. Also, the induced pressures are decreased in comparison with the insulated plate values, but the slope is appreciably higher than the theoretical value for the noninsulated flat plate.

Real Gas Effects on Shock Wave-Boundary Layer Interaction

For a reflected stagnation temperature of 7200 R and pressure of 500 psi, the flow Mach number in the test section was 7.8 with a static temperature of 810 R. Behind a normal shock wave in the test section, for this condition, the density ratio is increased approximately 50 per cent over the perfect gas case $\gamma = 1.4$, due to the real gas effects (20). By assuming the boundary layer to be laminar and with a recovery factor of 0.85, the ratio of the wall to the recovery temperature is 0.0872. The boundary layer is relatively cool because of the high stagnation temperature for the free stream. In Table 1 the other physical parameters in the test section for this temperature are presented. Because of the high stagnation temperature, the free stream Reynolds number per inch is quite small compared with the results for the lower temperature.

Even at this relatively high temperature and with, comparatively, very cooled surface, the induced pressure caused by the interaction of the leading edge shock wave with the boundary layer is present, as indicated in Figs. 6–8. The pressure ratio near the leading edge again approached an asymptotic value, and in the strong interaction region behind the leading edge slip phenomenon, the induced pressure ratio varied as a function of $X^{-1/2}$, as indicated in Figs. 6 and 8. The observed pressure ratio varied from approximately 4.4 to 2 over the front 4 in. of the flat plate. Since the Reynolds number per inch is relatively low compared with its value at lower stagnation temperatures, the pressure over the surface did not vary as much as for flow Mach 9.77 (see Fig. 4). In Fig. 8 the induced pressure result has been plotted as a function of the interaction parameter $M_1^3/\sqrt{Re_X}$. Near the leading edge the surface pressure was obtained for the value of the interaction parameter of 17.3. The leading edge slip phenomenon existed down to values for the interaction parameter of 10. Below this value the induced pressure ratio varied linearly with the strong interaction parameter. The theoretical value of the slope of the induced pressure ratio has been calculated by using the results of (13) and assuming, as an approximation, the ratio of specific heats equal to 1.4. In the free stream this assumption is reasonable because the static temperature is only 810 R. For this test condition the theoretical value of the induced pressure is less than the experimental results as shown in Fig. 8. In comparison, the theoretical insulated plate slope (9) has been plotted in that figure. The low ratio of wall to recovery temperature has a great effect on the induced pressure, even with an appreciable amount of real gas effects present in the boundary layer.

Pressure Ratio Across the Shock Wave

The pressure across the shock wave was determined from the Schlieren photographs, Figs. 9–12, of the flow over the flat plate at various flow Mach numbers and stagnation temperatures. In these photographs the shock wave can be observed as a sharp discontinuity in the density gradient, and the outer edge of the boundary layer appears as a light region where the density gradient is large for a hypersonic laminar boundary layer. The shock angle was measured from the Schlieren photographs. The free stream Mach number and the ratio of specific heats $\gamma = 1.4$ were used to calculate the pressure ratio across the shock wave from an oblique shock relationship. Since the free stream temperature in the test section is 810 R for a reflected stagnation temperature of 7200 R, the ratio of specific heats of 1.4 is valid as long as the shock wave angle is not large (28).

All the Schlieren results have indicated that the pressure ratio at the leading edge based upon the shock wave angle is appreciably lower than the pressure ratio calculated for the maximum shock wave angle located slightly downstream of the leading edge. After the maximum shock wave angle, the shock wave becomes weaker as the distance from the leading edge increases. The shock wave and the boundary layer seem to be merged before separating into a distinct shock wave and boundary layer. As the flow Mach number was increased, the merged region extended over a larger portion of the plate, as in Figs. 9–12. Thus, the pressure ratio increased to a maximum value and then decreased in a manner similar to the surface pressure ratio. Similar results were observed for the pressure ratio determined from the shock wave angle obtained from Fig. 12, where the stagnation temperature is 7200 R. Again, the calculated pressure ratio at the leading edge was less than slightly downstream where the maximum shock wave angle was located.

In the region where the shock wave and the boundary layer were merged, the pressure calculated from the shock wave angle and the surface pressure was approximately the same. This indicates that the pressure in the strong shock wave-boundary layer interaction region is nearly constant from the surface to the shock wave. This assumption was utilized in the analysis of the strong interaction between the shock wave and the boundary layer in (9). When the shock wave became separated, the pressure ratio across the shock wave was greater than that measured at the surface for a given distance from the leading edge, as previously observed at lower Mach numbers (14).

Conclusions

The flow over a flat plate with a sharp leading edge has been investigated in a hypersonic shock tunnel with air at flow Mach 9.77, 15.6 and 19.6 for nearly perfect gas conditions. At flow Mach 7.8 the reflected stagnation temperature of 7200 R was utilized to determine the real gas effects on the shock wave-boundary layer interaction. Schlieren photographs and surface pressure distributions for the flat plate were obtained for each test condition, and the interaction parameter $M_1^3/\sqrt{Re_X}$ has been extended to 140.

Slip flow phenomenon was observed at the leading edge of the flat plate. The strong shock wave and the boundary layer were delayed in forming, and the surface pressure near the front deviated from the strong interaction variation. The important parameters governing the slip distance are the free stream Mach number, mean free path and the number of collisions required to slow the velocity at the wall to zero.

In the region of the strong interaction between the shock wave and the boundary layer, the induced pressure on the flat plate for nearly perfect gas condition $\gamma = 1.4$ varies inversely as the square root of the distance from the leading edge, as originally predicted by Li and Nagamatsu. At higher flow Mach numbers the surface cooling effects upon the induced pressure become appreciable and the results agree reasonably well with the noninsulated theory for the strong interaction phenomenon. For flow Mach 9.77 the cooling effects were not large and the results did not agree with the calculated value. The maximum induced pressure ratio near the leading edge increased approximately as the square of the Mach number for the present test conditions.

Even for a reflected stagnation temperature of 7200 R, with appreciable real gas effects, the strong shock wave-boundary layer interaction was observed. The variation of the induced pressure on the plate was predicted reasonably well with the noninsulated theory, using the ratio of the wall temperature to the recovery temperature.

The pressure ratios determined from the shock wave angle and the free stream Mach number have indicated the increase in pressure ratio from the leading edge to a maximum value slightly downstream. Beyond the location of the maximum value, the pressure ratio decreased similarly to the surface pressure variation. When the shock wave and the boundary layer were merged, the pressure from the shock wave to the surface for a given location from the leading edge was approximately constant. After the shock wave became separated from the boundary layer, the pressure behind the shock wave was greater than the surface pressure at the same location from the leading edge.

Higher induced pressures at high flow Mach numbers, caused by the interaction of the shock wave and the boundary layer, will increase the skin friction, heat transfer and force on a lifting surface, as compared with the values calculated by the compressible laminar boundary layer theory with no pressure gradient.

Acknowledgment

The contribution of A. J. Nerad assisted greatly in the attainment of the results presented in this paper. J. R. Schmid and R. P. McCabe assisted in the operation and reduction of data. J. B. Workman assisted in the analysis of the state of the plasma in the nozzle. L. A. Osburg and K. H. Cary assisted with the mechanical design and instrumentation.

References

1 Laurmann, J. A., "The Free Molecule Probe and Its Use for the Study of Leading Edge Flows," *Phys. Fluids*, vol. 1, no. 6, 1958, pp. 469–477.

2 Nagamatsu, H. T. and Sheer, R. E., Jr., "Leading Edge Slip Flow and Shock Wave-Boundary Layer Interaction on a Flat Plate in Hypersonic Flow," *Bull. Amer. Phys. Soc.*, vol. 4, Series II, 1958. Abstract.

3 Laurmann, J. A., "The Effect of Slip on Induced Pressures," *J. Aero/Space Sci.*, vol. 26, no. 1, 1959, pp. 53–54.

4 Hammitt, A. G., "The Hypersonic Viscous Effect on a Flat Plate with Finite Leading Edge," *J. Fluid Mech.*, vol. 5, no. 2 1959, pp. 242–256.

5 Bertram, M. H., "Viscous and Leading-Edge Thickness Effects on the Pressures on the Surface of a Flat Plate in Hypersonic Flow," *J. Aeron. Sci.*, vol. 21, no. 6, 1954, pp. 430–431.

6 Lees, L. and Kubota, T., "Inviscid Hypersonic Flow Over Blunt-Nosed Slender Bodies," *J. Aeron. Sci.*, vol. 24, no. 3, 1957, pp. 195–202.

7 Nagamatsu, H. T. and Li, T. Y., "On Hypersonic Flow Near the Leading Edge of a Flat Plate," submitted for publication in *Phys. Fluids*.

8 Shen, S. F., "An Estimate of Viscosity Effect on Hypersonic Flow Over an Insulated Wedge," *J. Math. Phys.*, vol. 31, no. 3, 1952, pp. 192–205.

9 Li, T. Y. and Nagamatsu, H. T., "Shock Wave Effects on the Laminar Skin Friction of an Insulated Flat Plate at Hypersonic Speeds," *J. Aeron. Sci.*, vol. 20, no. 5, 1953, pp. 345–355.

10 Lees, L., "On the Boundary Layer Equations in Hypersonic Flow and Their Approximate Solutions," *J. Aeron. Sci.*, vol. 20, no. 2, 1953, pp. 143–145.

11 Stewartson, K., "On the Motion of a Flat Plate at High Speeds in a Viscous Compressible Fluid—II Steady Motion," *J. Aeron. Sci.*, vol. 22, no. 5, 1955, pp. 303–309.

12 Bertram, M. H., "An Approximate Method for Determining the Displacement Effects and Viscous Drag of Laminar Boundary Layers in Two-Dimensional Hypersonic Flow," NACA TN 2773, 1952.

13 Li, T. Y. and Nagamatsu, H. T., "Hypersonic Viscous Flow on Non-Insulated Flat Plate," Proc. Fourth Midwestern Conference on Fluid Mech., Purdue Engineering Research Series no. 128, pp. 273–287.

14 Kendall, J. M., Jr., "An Experimental Investigation of Leading-Edge Shock Wave-Boundary Layer Interaction at Mach 5.8," *J. Aeron. Sci.*, vol. 24, no. 1, 1957, pp. 47–56.

15 Bertram, M. H. and Henderson, A., Jr., "Effects of Boundary-Layer Displacement and Leading-Edge Bluntness on Pressure Distribution, Skin Friction, and Heat Transfer of Bodies at Hypersonic Speeds," NACA TN 4301, 1958.

16 Schaaf, S. A., Hurlbut, F. C., Talbot, L. and Aroesty, J., "Viscous Interaction Experiments at Low Reynolds Numbers," ARS JOURNAL, vol. 29, no. 7, July 1959, pp. 527–528.

17 Bogdonoff, S. M. and Hammitt, A. G., "Fluid Dynamic Effects at Speeds from $M = 11$ to 15," *J. Aeron. Sci.*, vol. 23, no. 2, 1956, pp. 108–116.

18 Nagamatsu, H. T., Geiger, R. E. and Sheer, R. E., Jr., "Hypersonic Shock Tunnel," ARS JOURNAL, vol. 29, no. 5, May 1959, pp. 332–340.

19 Yoler, Y. A. and Nagamatsu, H. T., "A Study of Piezoelectric Elements for the Measurements of Transient Forces," Calif. Inst. of Tech., GALCIT Hypersonic Wind Tunnel Memo 13, 1954.

20 Nagamatsu, H. T., Geiger, R. E. and Sheer, R. E., Jr., "Real Gas Effects in Flow Over Blunt Bodies at Hypersonic Speeds," *J. Aero/Space Sci.* (in press).

21 Gilmore, F. R., "Equilibrium Composition and Thermodynamic Properties of Air to 24,000°K," Rand Rep. RM-1543, 1953.

22 Hilsenrath, J. and Beckett, C. W., "Tables of Thermodynamic Properties of Argon-Free Air to 15,000°K," Arnold Engng. Devel. Ctr., TN 56-12, 1956.

23 Treanor, C. E. and Logan, J. G., Jr., "Tables of Thermodynamic Properties of Air from 3000°K to 10,000°K," Cornell Aero. Lab. Rep. AD-1052-A-2, 1956.

24 Hirschfelder, J. D. and Curtiss, C. F., "Thermodynamic Properties of Air," Univ. of Wisconsin, CM-518; Navy Bur. Ord. Contract no. 9938, 1948.

25 Feldman, S., "Hypersonic Gas Dynamic Charts for Equilibrium Air," Avco Res. Lab. Rep., Jan. 1957.

26 Kennard, E. H., "Kinetic Theory of Gases," McGraw-Hill Book Co., Inc., N. Y., 1938.

27 Von Kármán, T. and Tsien, H. S., "Boundary Layer in Compressible Fluids," *J. Aeron. Sci.*, vol. 4, no. 5, 1938, pp. 227–232.

28 Nagamatsu, H. T., Workman, J. B. and Sheer, R. E., Jr., "Oblique Shock Relations for Air at Mach Number 7.8 and 7200°R Stagnation Temperature," submitted for publication in ARS JOURNAL.

Numerical Comparison Between Exact and Approximate Theories of Hypersonic Inviscid Flow Past Slender Blunt Nosed Bodies[1]

SAUL FELDMAN[2]

Avco-Everett Research Laboratory
Everett, Mass.

This paper presents numerical results of exact calculations of the inviscid equilibrium flow about a long hemisphere-cylinder in motion at hypersonic velocity. A comparison is made with blast wave as well as free layer theories of hypersonic flow. As a result of the comparison, it is concluded that the second-order blast wave theory can be used for the purpose of finding the shock shape and the body pressure distribution. However, this procedure is definitely empirical and cannot be justified on rational or theoretical grounds. We show that the presently calculated radial distribution of energy is radically different than that given by blast wave theory. If body shapes other than those considered here are of interest, the only reliable approach at the present time is to carry out numerical calculations. It was found that for certain flight velocities the pressure on the body does not decay to free stream pressure monotonically but overexpands.

THE INTEREST in hypersonic flow around blunt bodies has been stimulated in the last few years by the intercontinental ballistic missile and satellite programs. Meteor physicists have been interested for many years in the trails left by meteors (1).[3] Recently, interest in the wakes left in the atmosphere by a body moving at hypersonic speed has also been stimulated by the desire to monitor objects entering from space. Among effects that can be observed during atmospheric entry are the radiation emitted by the hot gas left in the trail and the reflection of microwaves by the ionized material. In order to design adequate detectors of these effects, an estimate is required of the flow field surrounding a blunt object.

Although a survey of the present status of inviscid hypersonic flow theory has been made by Hayes and Probstein (2), it should be mentioned that numerical calculations of the entire flow field about slender blunt nosed bodies at hypersonic speeds in equilibrium air have never been reported in the literature. Ferri (3) and Casaccio (4) have given results for the pressure distribution on a hemisphere-cylinder at $M_\infty = 20$ in a perfect gas to a position on the cylinder about 15 nose-radii away from the nose. Numerical calculations are deemed necessary for evaluating the merits of approximate theories suggested in the literature for determining the flow field away from the blunt nose.

For the purpose of carrying out this evaluation, we will consider the features of the equilibrium flow about a hemisphere-cylinder about 75-radii long flying through the atmosphere at 60,000-ft altitude at 17,500 fps. The reason for choosing this particular slender body is that it is plausible to assume that the features of the gas flow far away from the nose of the body chosen here will not be too different from the inviscid flow surrounding the viscous wake of a short blunt body (since the viscous wake core could probably be assumed to be replaced by a solid body without introducing very large errors). At sufficiently high altitudes the flow will not be in thermodynamic equilibrium. However, this effect will not be considered here.

Some Results of Existing Theories

Theories for the overall features of the flow have been proposed by Lin (5), Lees and Kubota (6), Lighthill (7), and Hayes and Probstein [(2), pp. 81–92]. Earlier Russian work has been summarized by Sedov (8). These researchers attempt to determine the general features of the flow field by using constant energy solutions or Newtonian theory. Lin (5) solved the problem of a strong cylindrical blast wave for a perfect gas of constant specific heat and used his results, together with Hayes' equivalence principle, for determining the shape of the strong portion of the shock in front of a body moving steadily at hypersonic velocity. The basic assumption was that the gas energy, in a plane normal to the body axis, per unit length in the axial direction, is a constant. This was equated to the product of body drag force and flight velocity. The blast wave theory is valid for a body of zero thickness and is of asymptotic nature, its results being invalid locally near the nose.

The shock shape for an axial symmetric body obtained from the "blast wave" theory is a parabola. Sakurai (9,10) also solved the problem of the axisymmetric blast wave and, in addition, analyzed the two-dimensional blast wave case. He used values for the specific heat ratio γ of 1.2, 1.4 and 1.67. He also solved higher order approximations that account for the free stream pressure being finite instead of zero. A summary of the results for different specific heats γ is given in Table 1, where r is the radial ordinate of the shock, R denotes

---

Received Aug. 17, 1959.

[1] This work was sponsored by Army Rocket and Guided Missile Agency, Huntsville, Ala., under Contract no. DA-19-020-ORD-4765.

[2] Principal Research Scientist. Member ARS.

[3] Numbers in parentheses indicate References at end of paper.

Table 1 Summary of first-order blast wave results for axisymmetric flow

γ	p_{axis}/p_∞	$p_{\text{shock}}/p_{\text{axis}}$	r/R
1.20	$0.0925\,M_\infty^2/(x/R)$	3.32	$0.920\,(x/R)^{1/2}$
1.40	$0.133\,M_\infty^2/(x/R)$	2.68	$1.104\,(x/R)^{1/2}$
1.667	$0.177\,M_\infty^2/(x/R)$	2.19	$1.273\,(x/R)^{1/2}$

the nose radius, M_∞ the free stream Mach number and x the axial distance measured from the stagnation point. The results presented are:

1 The ratio of the pressure along the axis of symmetry of the flow p_{axis} to the free stream pressure p_∞.

2 The pressure ratio $p_{\text{shock}}/p_{\text{axis}}$, where p_{shock} denotes the pressure behind the shock at the axial position given by the x/R coordinate.

3 The shock ordinate r nondimensionalized with respect to the nose radius R.

For the purpose of evaluating the merits of the blast wave theory, we will now make a comparison between some of its results with some results from a characteristic calculation. We will compare the ratio of pressure behind the shock to the pressure at the axis of symmetry (as obtained from blast wave theory) and a characteristic calculation. Ferri and Pallone (11) calculated the flow around a double wedge with a leading wedge half-angle of 45 deg and trailing wedge of 12 deg in a free stream Mach number of 20. They used a specific heat ratio γ of 1.4 and carried out the calculation to about 35 body thicknesses downstream of the leading edge. A comparison of the pressure ratio mentioned previously, as a function of position, with the pressure ratio of 2.56 that one can obtain from the two-dimensional blast wave results of Sakurai (9,10) (with $\gamma = 1.4$), shows that the agreement improves when away from the nose region (Fig. 1). From blast wave theory one would expect worse agreement, since the shock is not strong there. Thus, blast wave theory is unsatisfactory in this case. Lees and Kubota (6) used the work of Sakurai (9,10) in order to improve Lin's results by accounting for the fact that the free stream pressure is finite and not zero. Their results for $\gamma = 1.4$ are

$$\frac{p_{\text{axis}}}{p} = \frac{0.133\,M_\infty^2}{x/R} + 0.405$$

$$\frac{r}{R} = 1.104\left(\frac{x}{R}\right)^{1/2}\left(1 + 0.81\,\frac{x/R}{M_\infty^2}\right)$$

Lighthill (7) and Hayes and Probstein [(2), p. 85] determine the pressure distribution on the blunt portion of a body by assuming Newtonian flow with a centrifugal correction. For a hemisphere, this assumption leads to vanishing pressure at a point on the surface whose normal makes an angle of 60 deg with respect to the flight direction. Within the Newtonian framework the shock is, of course, parallel to the body up to the same point. In order to determine the shock shape beyond 60 deg, these authors make the assumption that the pressure downstream is zero. The physical meaning of the assumption is that the mass of the gas that goes through the shock moves parallel to it after crossing it, and that the centrifugal force on the shock layer permits the pressure to drop from the value that it had behind the shock to a value of zero behind the shock layer. It should be noted that the free layer theory is strictly valid in the limit obtained when γ approaches unity. The shape of the shock layer that one obtains when using this so-called "free shock layer" theory is cubic. This should be compared with the parabolic shock shape obtained from first-order blast theory.

The results of numerical calculations about a hemisphere-cylinder flying through the atmosphere at an altitude of 60,000 ft and at a velocity of 17,500 fps will be discussed next.

Results of Numerical Calculation for the Flow Field and Comparison With Approximate Theories

In order to calculate the supersonic flow field around the body it was necessary to first determine the subsonic flow field. This was done using a method first suggested by Dorodnitsyn and then applied to the blunt body problem by Belotserkovskii [(2), pp. 214–226]. This numerical calculation was carried out for a hemisphere to first approximation only, for an ideal gas with a ratio of specific heats γ of 1.2; this value of γ was chosen as being reasonable for a simplified calculation representing the behavior of air at the high flight velocity of interest here. Although this calculation was not very accurate, that is probably of no consequence here. The output of the calculation downstream of the sonic "line" and limiting characteristic was used as the input to a characteristic calculation (12) using the properties of dissociated air in thermodynamic equilibrium. The important features of the flow field are given in Figs. 2 through 5.

Streamlines (Fig. 2)

One interesting observation that can be made from the streamline pattern is that the gas that crosses the shock between the axis of symmetry and a point on the shock intersected by the perpendicular to the body at the sonic point, occupies about half the shock layer thickness when the gas expands around the body to free stream condition. The rest of the shock layer is occupied by the gas that goes through the remaining portion of the shock. It is interesting to note that the gas close to the body at the sonic point expands so drastically as it flows around the body, that, for example, a streamline at a distance of 0.012 nose-radii away from the surface ends up 2 nose-radii away from the body when far away from the nose region where the pressure is near free stream.

The calculated flow field has left, as may be expected, only vestiges of the results of the "free layer" theory of Lighthill (7) and Hayes and Probstein [(2), p. 85].

Density (Fig. 3)

It should be noted that near the hemisphere-cylinder tangency point (Fig. 3 top), the density across the shock layer increases by a factor of about 3½ or 4 when going from the body to the shock in a direction perpendicular to the axis. However, at distances far from the nose region (Fig. 3 bottom) this factor becomes 20 or 30.

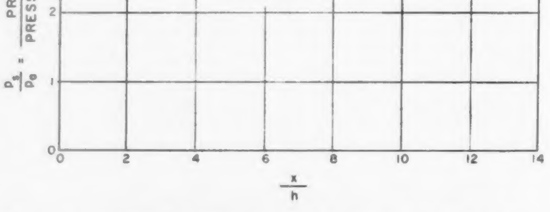

Fig. 1 Comparison of pressure distribution on a wedge ($\gamma = 1.4$, $M_\infty = 20$) as obtained from a characteristic calculation (11) with two-dimensional blast wave theory

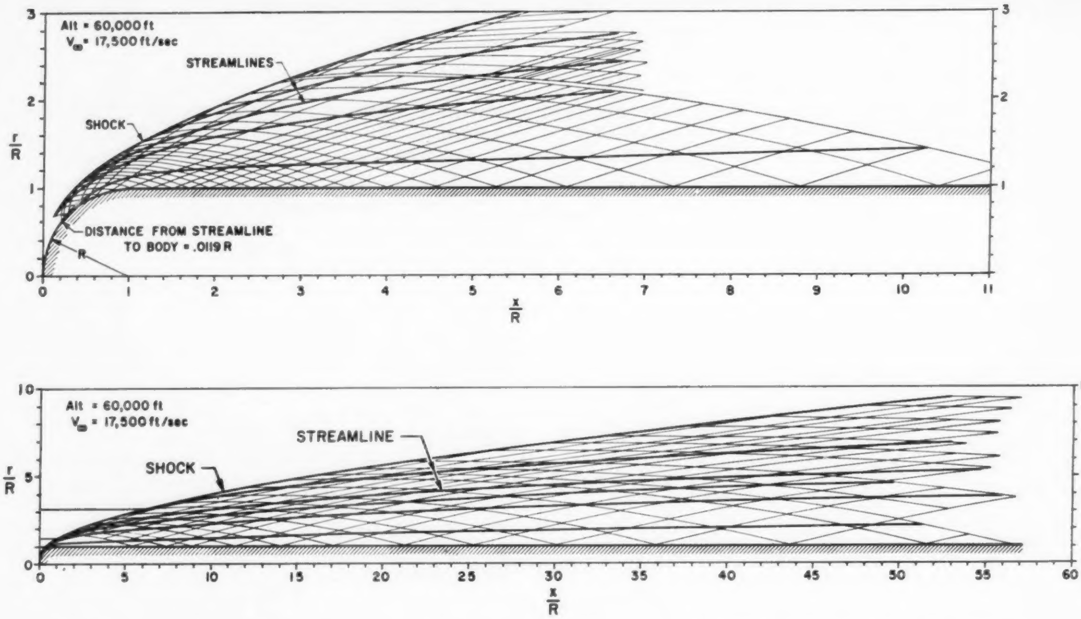

Fig. 2 Streamlines and characteristics. Top: In the neighborhood of the nose. Bottom: Far from the nose

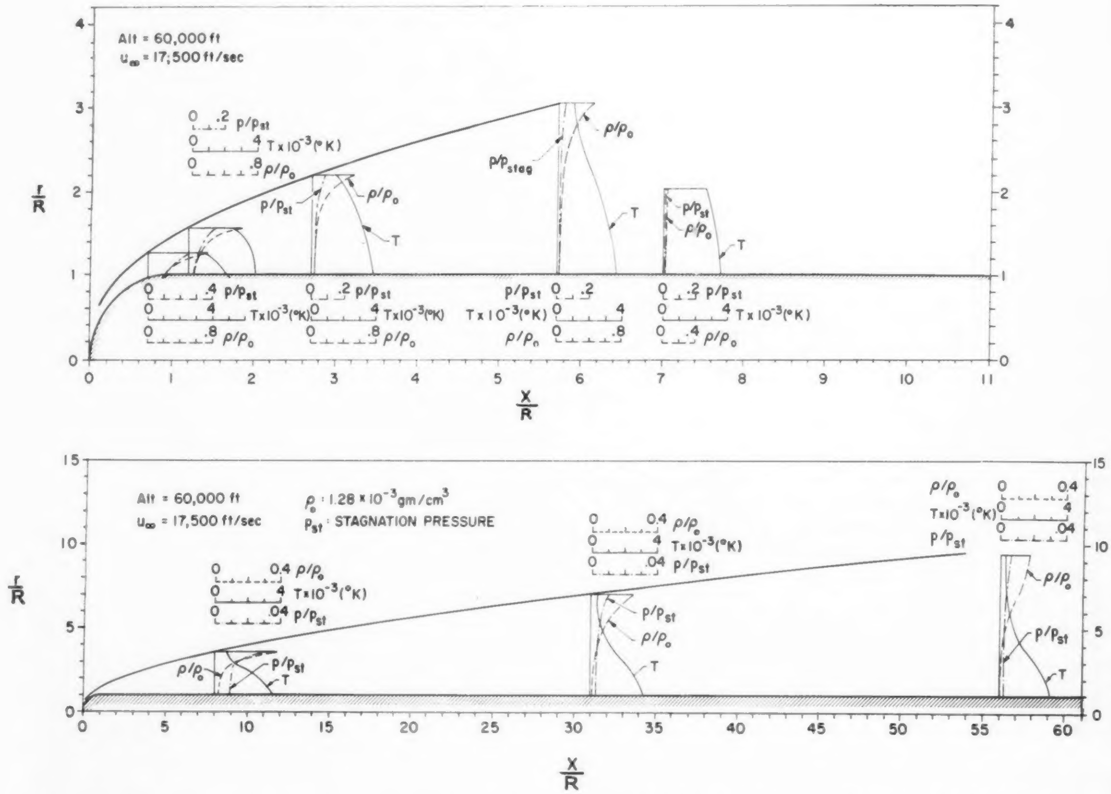

Fig. 3 Density, temperature and pressure profiles. Top: In the neighborhood of the nose. Bottom: Far from the nose

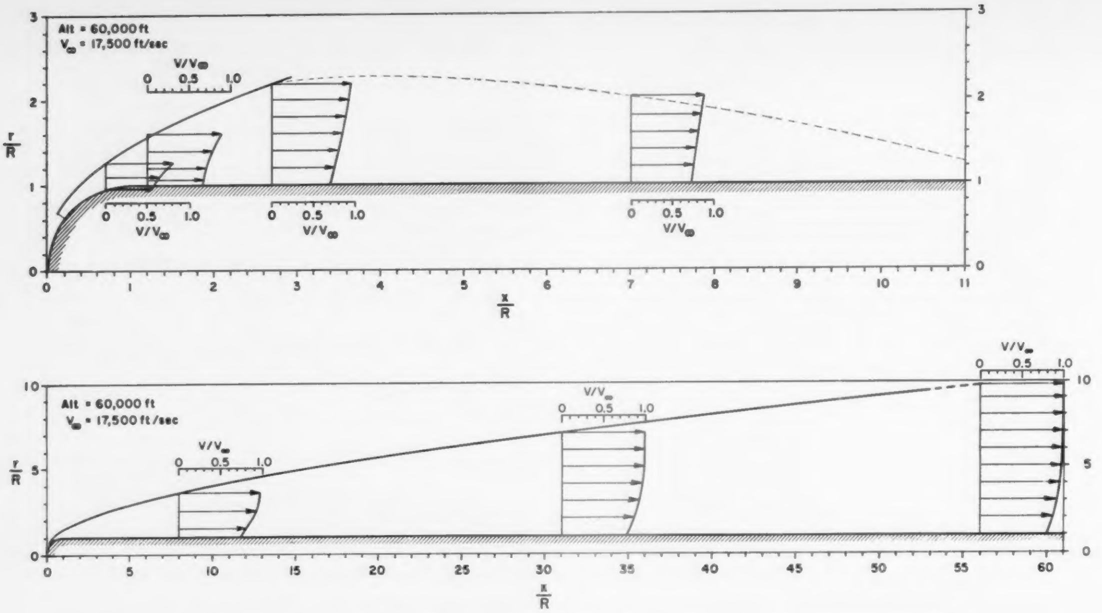

Fig. 4 Velocity profiles. Top: In the neighborhood of the nose. Bottom: Far from the nose

Temperature (Fig. 3)

The temperature is nearly constant across the shock layer in the neighborhood of the nose region (Fig. 3 top). Far away from the nose (Fig. 3 bottom) the temperature is nearly constant near the shock for about one half the shock layer thickness and then rises to a high value as the body is approached. The temperature along the cylindrical portion decays at a rather slow rate. It should be noted that the high temperature region occurs where the density is low. Fig. 3 (top) also shows the entropy profile across the shock layer at a point not far from the hemispherical nose. It should be noted that the entropy gradient has a very slow variation across the shock layer; the entropy changes across the shock layer only by about 30 per cent. Reference is often made to the large entropy gradients that exist in connection with curved shocks at hypersonic speeds. We here conclude from Fig. 3 (top) that a far more physically significant thermodynamic variable than the entropy gradient is the density gradient, since large density gradients can exist when a gas goes through a curved shock at hypersonic velocity.

Pressure (Fig. 3)

The pressure increases across the shock layer when going from the body to the shock by a factor whose value becomes a maximum of about 6 when near the hemisphere-cylinder tangency region; this factor changes to about 2 when 55 nose-radii away, and from there on it decreases further.

Velocity (Fig. 4)

The velocity profiles (Fig. 4) change curvature from concave to convex at about 3 nose-radii away from stagnation point. Beyond 10 nose-radii the velocity at the body is about 80 per cent of free stream, and in about half a shock layer it increases to just about the free stream value. This means that a body flying through the atmosphere at a velocity of 17,500 fps would leave a jet of gas whose velocity could change from about 20 per cent of the flight velocity when near the axis to zero velocity when the gas is 5 or 10 body-radii away from the jet axis. Of course, the velocity on the axis, where viscous effects are important, would be larger than 20 per cent of free stream velocity; thus, due to mixing, the velocity of the inviscid wake mentioned previously could be increased.

Body Pressure Distribution

Fig. 5 shows the pressure distribution along the body as determined by the characteristics calculation. Free stream pressure is reached at about 80 nose-radii from the stagnation point. From there downstream, the flow overexpands. The manner in which the pressure recovers to the free stream value was not computed. For the purpose of comparison, the pressure distribution obtained by using first- and second-order blast wave theory is also given. In the region away from the nose the second-order blast wave theory with $\gamma = 1.4$ seems to disagree at most by 25 per cent. From Fig. 5 the limitation of the constant γ assumption in the blast wave theory, when applied to the present problem, is quite clear, since in the actual flow γ varies approximately between about 1.2 and 1.4.

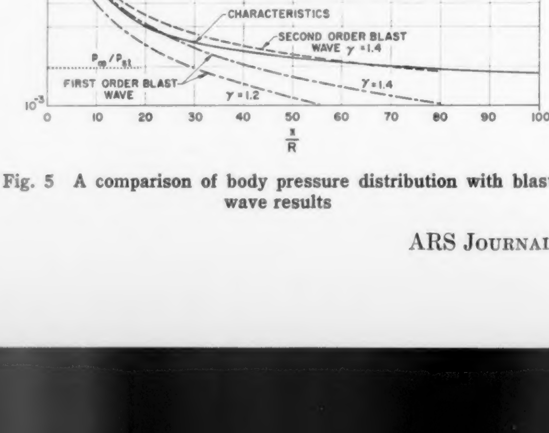

Fig. 5 A comparison of body pressure distribution with blast wave results

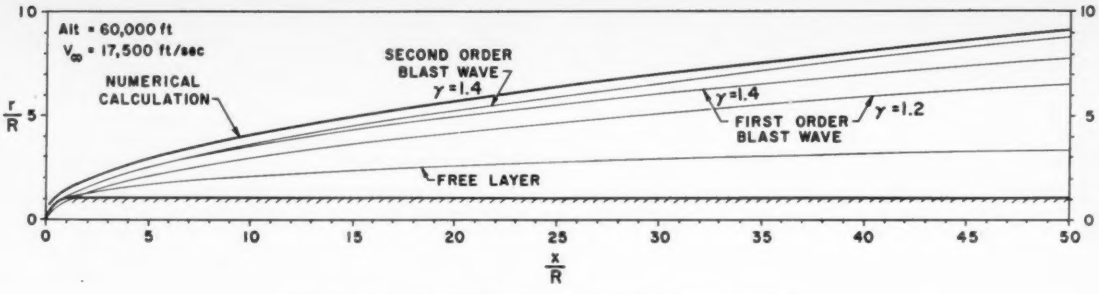

Fig. 6 A comparison of shock shapes from several theories

Shock Shape

A comparison was made of the results of the characteristic calculation and a least square fit for the shock shape downstream of the sonic region, using a quadratic and a cubic equation; the cubic equation gave a shape which was indistinguishable from the characteristics results. Fig. 6 shows the shock shapes obtained from first- and second-order blast wave theory with $\gamma = 1.4$, and from the free layer theory of Lighthill (7) and Hayes and Probstein [(2), p. 85]. When using the free layer theory, an infinite density ratio was assumed across the bow wave. Thus, the shock is parallel to the body up to 60 deg where the theory yields a vanishing value for the pressure. The free layer theory yields a shock shape which disagrees radically with the characteristic calculation. The principal reason for the large disagreement is the assumption of zero pressure behind the shock layer beyond 60 deg. However, the free layer shape could be improved further by using a finite instead of zero pressure behind the shock layer.

Although the general shock shape obtained from the second-order blast wave is nearly parallel to the numerically calculated shape, there is no valid reason for using a value of 1.4 for γ except when about 20 radii away from the stagnation point, where the gas temperature is sufficiently low. In order to coincide with the calculated shock shape, the blast wave shock would have to be displaced outward by about 0.4 R.

One reason for the inadequacy of blast wave theory is that it assumes that the energy per unit length, in a plane normal to the body axis, is a constant. Fig. 7 shows this energy distribution as obtained from the characteristics calculation nondimensionalized with respect to the blast wave first-order result. Two curves are given: Curve (a) represents the sum

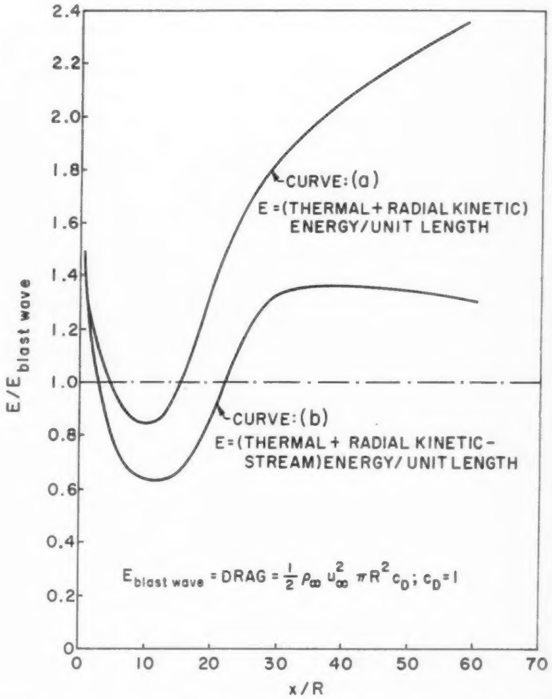

Fig. 7 Energy per unit length between the body and the shock in a plane normal to the body axis

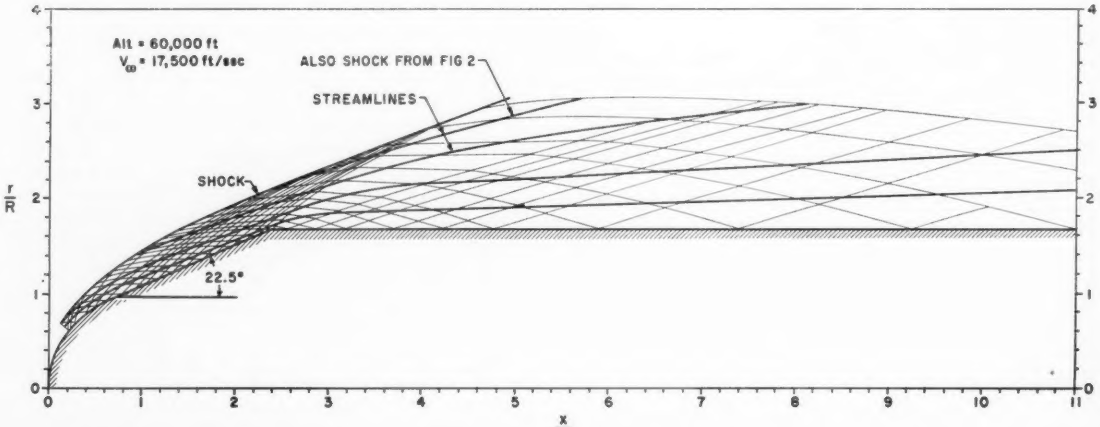

Fig. 8 Comparison of shock shape for hemisphere-cylinder and hemisphere-cone-cylinder

of the thermal and radial kinetic energy (based on velocities relative to a coordinate system fixed on the body) per unit length within the shock envelope; and curve (b) corrects for the fact that the free stream energy is not negligible when away from the nose. The energy level is not only incorrect but also is not constant. (A discussion of the fallacy involved when assuming in blast wave theory that the energy per unit length is equal to the drag will be given in a future paper.) However, since the radius of the shock wave and the pressure depend on the $\frac{1}{4}$ and $\frac{1}{2}$ powers, respectively, of the energy, the errors in these quantities due to evaluating the energy incorrectly are partly concealed.

One would conclude that blast wave theory might be used more as an empirical result rather than a justifiable theory.

Concluding Remarks

In view of the fact that the density is low in the neighborhood of the body as compared to regions closer to the shock, it seems reasonable to assume that a certain amount of change in the body shape will not affect the general features of the flow field about the hemisphere-cylinder. In order to check this assumption, the shock shape around a hemisphere-cone-cylinder (a fairly short cone) is presented in Fig. 8 together with the shock wave shape of Fig. 1. It can be seen that the shock shape is not affected much by the change in nose shape and cylinder radius.

As a result of the comparison made between the results that different theories yield for the flow about a long hemisphere-cylinder, we conclude that the second-order blast wave theory could be used for the purpose of finding the shock shape and the body pressure distribution. With this information and conservation of mass consideration [(2), pp. 210–214], one could find approximate values of the remaining quantities of interest in the flow field. This procedure is definitely empirical and cannot be justified theoretically.

If body shapes other than those considered here are of interest, the only reliable approach at the present time is to carry out numerical calculations. These are not too difficult using the presently available high speed computers.

Acknowledgment

The author is indebted to Dr. A. D. Wood of the Avco Research and Advanced Development Division, Avco Corp., for making available the computing procedure for the characteristics calculation, and to N. W. Brodeur for setting up and carrying out the machine calculations.

References

1 Öpik, E. J., "Physics of Meteor Flight in the Atmosphere," Interscience Publishers, Inc., N. Y., 1958.

2 Hayes, W. D. and Probstein, R. F., "Hypersonic Flow Theory," Academic Press, N. Y., 1959.

3 Ferri, A., "A Review of Some Recent Developments in Hypersonic Flow," Polytechnic Institute of Brooklyn, Sept. 1958 (ASTIA Document no. AD 155 822).

4 Casaccio, A., "Theoretical Pressure Distribution on a Hemisphere-Cylinder Combination," *J. Aero/Space Sci.*, vol. 26, 1959, pp. 63–64.

5 Lin, S. C., "Cylindrical Shock Waves Produced by Instantaneous Energy Release," *J. Appl. Phys.*, vol. 25, 1954, pp. 54–57.

6 Lees, L. and Kubota, T., "Inviscid Hypersonic Flow Over Blunt Nosed Slender Bodies," *J. Aero/Space Sci.*, vol. 24, 1957, pp. 195–202.

7 Lighthill, M. J., "Dynamics of a Dissociating Gas, Part I, Equilibrium Flow," *J. Fluid Mech.*, vol. 2, 1957, pp. 1–32.

8 Sedov, L. I., "Similarity and Dimensional Methods in Mechanics," Gostekhizdat, SSSR, fourth ed., 1957. English translation, M. Holt, Ed., Academic Press, N. Y., 1959.

9 Sakurai, A., "On the Propagation and Structure of the Blast Wave, I," *J. Phys. Soc. Japan*, vol. 8, 1953, pp. 662–669.

10 Sakurai, A., "On the Propagation and Structure of the Blast Wave, II," *J. Phys. Soc. Japan*, vol. 9, 1954, pp. 256–266.

11 Ferri, A. and Pallone, A., "Note on the Flow Fields on the Rear Part of Blunt Bodies in Hypersonic Flow," WADC TN 560294, 1956.

12 Sears, W., Ed., "High Speed Aerodynamics of Jet Propulsion," Vol. VI; and Ferri, A., "Several Theories of High Speed Aerodynamics," Princeton University Press, Princeton, 1954.

Aerodynamic Instability of Supersonic Inlet Diffusers[1]

CHIEH-CHIEN CHANG[2] and CHENG-TING HSU[3]

University of Minnesota
Minneapolis, Minn.

The stability problem of supersonic inlet diffusers is first reduced to find the acoustic impedance at the inlet of the plenum chamber. The inlet acoustic impedance is then obtained by solving the linearized viscous compressible flow equations in the entire subsonic diffusion regimes with assumptions of one-dimensional quasi-steady flow and linear velocity distribution. It is found that the self-excited shock oscillation is not possible in absence of viscous dissipation. Flow instability is found to be due to further entropy generated by viscous dissipation in addition to shock oscillation. Neutral stability boundaries are obtained in terms of the ratio of perturbation entropy to the corresponding shock velocity and are in agreement with Stoolman's experimental data. The present analysis confirms Trimpi's theory of instability and also justifies the Sterbentz-Evvard theory in the range of "steady" subcritical operation.

Received April 21, 1959.

[1] This investigation was part of a project sponsored by the Office of Scientific Research, Air Research and Development Command, USAF, under Contract no. AF 18 (600)-1553. The present research is under the sponsorship of the National Science Foundation.

[2] Professor of Fluid Mechanics, Aeronautical Engineering Dept. Member ARS.

[3] Formerly, Research Associate, University of Minnesota. Now, Associate Professor, Aeronautical Engineering Dept., Iowa State University. Member ARS.

Literature Review

THE PROBLEM of instability of supersonic inlet diffusers (commonly known as ramjet buzz) was first observed by Oswatitsch (1)[4] in 1944, and has received extensive attention during the recent years. Experimental research on this subject has been carried out by many investigators for the purpose of explaining the causes and nature of the instability. Ferri and Nucci (2) found that the vortex sheet generated at the three-shock intersection impinging on the cowling lip caused the choking of the entering flow to initiate buzz. Trimpi (3) observed that the flow separation on the central body is another factor contributing to the instability. Trimpi (4) proposed that the stability of flow is dependent upon the instantaneous ratio of the increase of entropy to the decrease of mass flow, and that it is not necessary in general to block or even to choke the inlet. Dailey (5) still emphasized that the instability is caused by a strong interaction of the subcritical shock with the boundary layer on the central body, and that this interaction blocks or chokes the inlet. Controversy in opinions between Trimpi (6) and Dailey (7) indicates that further investigation is needed.

Theoretical analyses have also been carried out extensively concerning the buzz frequency, amplitude and stability limit. Sterbentz, Evvard and Davids (8,9) applied the Helmholtz resonator approximation to determine the buzz frequency and amplitude. These authors concluded that the instability would occur if the curve of diffuser pressure recovery vs. captured mass flow has a positive slope of sufficient magnitude. Trimpi (4) improved that analysis by using quasi one-dimensional unsteady flow, and proposed his forementioned theory for instability. In fact, the instantaneous entropy generated should be contributed by both viscous dissipation and shock oscillation. Stoolman (10) first raised the interesting question of whether a self-excited shock oscillation can exist in the absence of viscous dissipation. Stoolman [and later Mirels (11)] formulated a stability criterion in terms of the acoustic impedance at the inlet of the plenum chamber. The acoustic impedance of the external diffusion regime for a normal shock inlet diffuser in the quasi-steady flow was obtained from numerical integration by Stoolman. Analytical solutions for Stoolman's original equations were presented by Chang and Hsu (12) and Edwards (13) with an additional assumption of linear axial velocity distribution. It was also indicated (12), contrary to Stoolman's conclusion (10), that a self-excited shock oscillation is not possible without introducing viscous dissipation.

Present Problem and General Approach

The main purpose of this paper is to show that the instability of a supersonic inlet diffuser is essentially dependent on the viscous dissipation of the flow, and to justify and unify the various existing theories of instability for supersonic inlet diffusers.

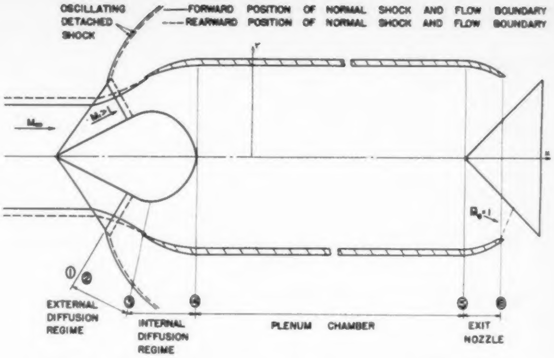
OSCILLATING DETACHED SHOCK
FORWARD POSITION OF NORMAL SHOCK AND FLOW BOUNDARY
REARWARD POSITION OF NORMAL SHOCK AND FLOW BOUNDARY
r
x
M_∞
$M_1>1$
$\bar{M}_e=1$
①
②
③
④
⑤
⑥
EXTERNAL DIFFUSION REGIME
INTERNAL DIFFUSION REGIME
PLENUM CHAMBER
EXIT NOZZLE

Fig. 1 Subcritical operation of a supersonic inlet diffuser

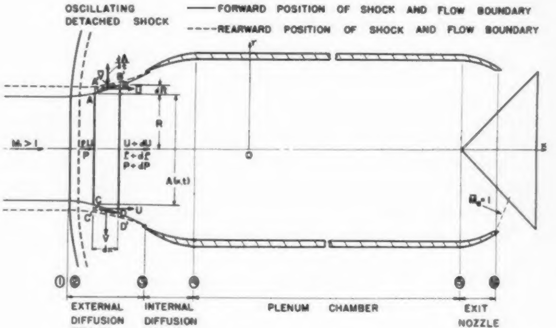
OSCILLATING DETACHED SHOCK
FORWARD POSITION OF SHOCK AND FLOW BOUNDARY
REARWARD POSITION OF SHOCK AND FLOW BOUNDARY
A
A'
B
B'
C
C'
D
D'
dR
R
$M_1>1$
ρ,U
P
U+dU
ρ+dρ
P+dP
A(x,t)
U
dx
r
0
x
$\bar{M}_e=1$
①
②
③
④
⑤
⑥
EXTERNAL DIFFUSION REGIME
INTERNAL DIFFUSION REGIME
PLENUM CHAMBER
EXIT NOZZLE

Fig. 2 Normal shock inlet diffuser at subcritical operation (simplified model)

The subcritical operation of a typical supersonic inlet diffuser is shown in Fig. 1, where, for a small disturbance generated downstream of the shock system, the instantaneous shock positions and captured flow boundaries are shown with solid and dotted lines, respectively. Assume the free stream captured flow area to be always inside the circle of triple-shock intersection. The Mach number M_1 immediately before the normal shock may be considered approximately uniform by averaging the Mach number distribution in the conical flow field because the variation is rather small. Therefore, the diffuser model under consideration can be simplified to a normal shock inlet diffuser as shown in Fig. 2. The viscous force acting on the surface of the central body and the free stream boundaries in the external diffusion regime are still retained in the present analysis. The length of the plenum chamber is assumed much longer than the portion of inlet and the exit nozzle. Therefore, the flow in the inlet and exit nozzle can be assumed to be operating quasi-steadily (11). The neutral stability criterion obtained by Stoolman (10) and Mirels (11) for small Mach number in the plenum chamber is

$$\left|\left[\frac{1+(\gamma-1)/2\bar{M}_c}{1-(\gamma-1)/2\bar{M}_c}\right]\left[\frac{1-\zeta_4}{1+\zeta_4}\right]\right| = 1 \qquad [1]$$

This criterion indicates that the particular mechanism leading to instability is actually the amplification of acoustic waves in the plenum chamber after successive reflections from the inlet and exit sections. In the first bracket of Equation [1] is the amplitude ratio of the reflected wave to the impinging wave at the exit nozzle; it is always less than 1. The second bracket contains the amplitude ratio of the reflected wave to the impinging wave at the inlet of the plenum chamber. This ratio is possibly greater than 1 if the viscous term is considered in the equation of motion. Obviously instability may occur if $|\zeta_4| > [(\gamma-1)/2]\bar{M}_c$. Therefore, the stability problem simply reduces to finding the acoustic impedance in the inlet of the plenum chamber. In order to obtain the inlet acoustic impedance, it is necessary to solve the viscous compressible flow equations in the external and internal diffusion regimes.

---

[4] Numbers in parentheses indicate References at end of paper.

Analysis of External Diffusion Regime

Fundamental Flow Equations

In the quasi one-dimensional unsteady and viscous compressible flow,[5] the equations of motion in the external diffusion regime are taken, respectively, as follows:

Continuity

$$\frac{\partial}{\partial t}(\rho A) + \frac{\partial}{\partial x}(\rho u A) = 0 \qquad [2]$$

Motion

$$\rho\frac{\partial u}{\partial t} + \rho u\frac{\partial u}{\partial x} = -\frac{\partial p}{\partial x} - \frac{4c_f}{D}\frac{\rho u^2}{2} \qquad [3]$$

Entropy

$$\left(\frac{\partial}{\partial t} + u\frac{\partial}{\partial x}\right)\frac{S}{c_v} = \frac{4c_f}{2D}(\gamma - 1)\frac{\rho u^3}{p} \qquad [4]$$

The conventional equation of continuity (3) in one-dimensional unsteady flow is used here.[6] The change of flow area with respect to time is taken into consideration as a flexible wall tube to account for the mass spillage over the cowling. The transient effect of viscous dissipation, such as flow separation, shock boundary layer interaction, etc., will be taken approximately into account by $c_f(x, t)$. Equation [4] expresses that the Eulerian derivative of entropy is contributed essentially by those viscous dissipations (14).

Assume the flow to be slightly perturbed from the steady state and represent the small perturbations as

$$\begin{aligned} \rho &= \bar{\rho}(x) + \rho'(x, t) \\ u &= \bar{u}(x) + u'(x, t) \\ p &= \bar{p}(x) + p'(x, t) \\ S &= \bar{S}(x) + S'(x, t) \\ c_f &= \bar{c}_f(x) + c_f'(x, t) \\ A &= \bar{A}(x) + A'(x, t) \\ D &= \bar{D}(x) + D'(x, t) \end{aligned}$$

$$\ldots\ldots\ldots\ldots\ldots\ldots\ldots\ldots\ldots\ldots\ldots\ldots\ldots\ldots [5]$$

and

$$\frac{\rho'}{\bar{\rho}}, \frac{u'}{\bar{u}}, \frac{p'}{\bar{p}}, \frac{A'}{\bar{A}}, \frac{D'}{\bar{D}}, \frac{c_f'}{\bar{c}_f}, \frac{S'}{\bar{S}} \ll 1 \qquad [6]$$

Equations [2, 3 and 4] together with Equations [5 and 6] can be reduced, respectively, to the following forms by retaining only the first-order terms in perturbations

$$\frac{\partial}{\partial t}\left(\frac{\rho'}{\bar{\rho}} + \frac{A'}{\bar{A}}\right) + \bar{u}\frac{\partial}{\partial x}\left(\frac{\rho'}{\bar{\rho}} + \frac{u'}{\bar{u}} + \frac{A'}{\bar{A}}\right) = 0 \qquad [7]$$

$$\frac{\partial}{\partial t}\left(\frac{u'}{\bar{u}}\right) + \bar{u}\frac{\partial}{\partial x}\left(\frac{u'}{\bar{u}}\right) + \left(\frac{\rho'}{\bar{\rho}} - \frac{p'}{\bar{p}} + 2\frac{u'}{\bar{u}}\right)\frac{d\bar{u}}{dx} = -\frac{\bar{p}}{\bar{\rho}\bar{u}}\frac{\partial}{\partial x}\left(\frac{p'}{\bar{p}}\right) + \frac{4c_f}{2\bar{D}}\bar{u}\left(\frac{p'}{\bar{p}} + \frac{D'}{\bar{D}} - \frac{\rho'}{\bar{\rho}} - \frac{2u'}{\bar{u}} - \frac{c_f'}{\bar{c}_f}\right) \qquad [8]$$

$$\left(\frac{\partial}{\partial t} + \bar{u}\frac{\partial}{\partial x}\right)\frac{S'}{c_v} = -\frac{4(\gamma - 1)\bar{c}_f}{2\bar{D}}\frac{\bar{\rho}\bar{u}^3}{\bar{p}} \times \left(\frac{p'}{\bar{p}} + \frac{D'}{\bar{D}} - \frac{\rho'}{\bar{\rho}} - \frac{2u'}{\bar{u}} - \frac{c_f'}{\bar{c}_f}\right) \qquad [9]$$

where

$$\frac{S'}{c_v} = \frac{p'}{\bar{p}} - \gamma\frac{\rho'}{\bar{\rho}} \qquad [10]$$

Eliminating the terms involving $\bar{c}_f$ between Equations [8 and 9] and replacing $p'/\bar{p}$ through Equation [10], Equation [8] becomes

$$\frac{\partial}{\partial t}\left(\frac{u'}{\bar{u}}\right) + \bar{u}\frac{\partial}{\partial x}\left(\frac{u'}{\bar{u}}\right) + \frac{\bar{a}^2}{\bar{u}}\frac{\partial}{\partial x}\left(\frac{\rho'}{\bar{\rho}}\right) - \left[(\gamma - 1)\frac{\rho'}{\bar{\rho}} - 2\frac{u'}{\bar{u}}\right]\frac{d\bar{u}}{dx} = \frac{S'}{c_v}\frac{d\bar{u}}{dx} - \frac{\bar{a}^2}{(\gamma - 1)\bar{u}}\frac{\partial}{\partial x}\left(\frac{S'}{c_v}\right) - \frac{\bar{a}^2}{\gamma(\gamma - 1)\bar{u}^2}\frac{\partial}{\partial t}\left(\frac{S'}{c_v}\right) \qquad [11]$$

where $\bar{a}^2 = \gamma\bar{p}/\bar{\rho}$. Equations [7 and 11] are the two first-order differential equations with two dependent variables $u'/\bar{u}$ and $\rho'/\bar{\rho}$ if S'/c_v and $A'/\bar{A}$ are given. Because of linearity of the previous equations and the conditions of Equation [5], the harmonic form of oscillatory time dependence can be chosen

$$\rho'/\bar{\rho} = \sigma(x)e^{i\omega t} \qquad u'/\bar{u} = \nu(x)e^{i\omega t} \qquad [12]$$

$$p'/\bar{p} = \varphi(x)e^{i\omega t} \qquad S'/c_v = \epsilon(x)e^{i\omega t} = [\varphi(x) - \gamma\sigma(x)]e^{i\omega t} \qquad [13]$$

and

$$A'/\bar{A} = \delta(x)e^{i\omega t} \qquad [14]$$

where σ, ν, φ, ϵ and δ are, in general, complex functions of x and ω. Making use of Equations [12, 13 and 14], Equations [7 and 11] can be reduced to the following system of ordinary differential equations with dependent variables in σ and ν

$$\bar{u}\left(\frac{d\sigma}{dx} + \frac{d\nu}{dx} + \frac{d\delta}{dx}\right) + i\omega(\sigma + \delta) = 0 \qquad [15]$$

$$\frac{\bar{a}^2}{\bar{u}}\frac{d\sigma}{dx} - (\gamma - 1)\frac{d\bar{u}}{dx}\sigma + \bar{u}\frac{d\nu}{dx} + \left(2\frac{d\bar{u}}{dx} + i\omega\right)\nu = \left(\frac{d\bar{u}}{dx} - \frac{i\omega\bar{a}^2}{\gamma(\gamma - 1)\bar{u}^2}\right)\epsilon - \frac{\bar{a}^2}{(\gamma - 1)\bar{u}}\frac{d\epsilon}{dx} \qquad [16]$$

where δ and ϵ are assumed to be given functions, as is shown later.

Linear Velocity Distribution

In view of Stoolman's experiments [Fig. 10 of (10)], the axial velocity gradient is known to be usually very large in the external diffusion regime just preceding the flow instability. It is probably reasonable to assume that $\bar{u}$ decreases linearly with x. Therefore, we choose

$$\frac{d\bar{u}}{dx} = \frac{\bar{u}}{x} = \frac{\bar{a}^*}{x^*} \qquad [17]$$

Moreover, we introduce a new independent variable z

$$0 \leq z = \left(\frac{x}{x^*}\right)^2 = \left(\frac{\bar{u}}{\bar{a}^*}\right)^2 = \bar{M}^{*2} \leq 1 \qquad [18]$$

in terms of which we have

$$\bar{a}^2 = \bar{a}^{*2}\left[\frac{1}{2}\left(\gamma + 1\right) - \frac{1}{2}(\gamma - 1)z\right] \qquad [19]$$

---

[5] The justification of quasi one-dimensional assumption has been discussed by Trimpi (6) in his reply to Dailey's comment (1957).

[6] The mass flux term $\rho[v - u(d\bar{R}/dx)]2\pi\bar{R}$ in Stoolman's equation of continuity (10) is equivalent to $\rho(\partial A/\partial t)$ in Equation [2]. The approximation of the mass flux term made later by Stoolman is equivalent to the neglect of v with respect to $u(\partial\bar{R}/dx)$. It seems too far from the realistic model. Consequently, the solution of ν in Stoolman's original equation retains a singularity (10,12) at $\lambda = 0$.

also we shall define a reduced angular frequency

$$\beta = -\frac{\omega x^*}{\bar{a}^*} = -\frac{\omega}{d\bar{u}/dx} \geq 0 \qquad [20]$$

Substituting Equations [17–20] into Equations [15 and 16] we obtain, respectively

$$2z\left(\frac{d\sigma}{dz} + \frac{d\nu}{dz} + \frac{d\delta}{dz}\right) - i\beta(\sigma + \delta) = 0 \qquad [21]$$

$$\frac{2(1 - bz)}{1 - b}\frac{d\sigma}{dz} + 2z\frac{d\nu}{dz} - \frac{2b\sigma}{1 - b} + (2 - i\beta)\nu = \left[1 + \frac{i\beta(1 - b)(1 - bz)}{2b(1 + b)z}\right]\epsilon - \frac{1 - bz}{b}\frac{d\epsilon}{dz} \qquad [22]$$

where $b = (\gamma - 1)/(\gamma + 1)$. Eliminating ν in Equations [21 and 22], we have a second-order differential equation in σ

$$z(1 - z)\frac{d^2\sigma}{dz^2} - [2 - i\beta(1 - b)]z\frac{d\sigma}{dz} + \frac{i\beta}{4}(2 - i\beta)(1 - b)\sigma = -\frac{i\beta(1 - b)^2}{4b(1 + b)z}\epsilon + \left[(1 - b)z + \frac{i\beta(1 - b)^2(1 - bz)}{4b(1 + b)}\right]\frac{d\epsilon}{dz} - \frac{(1 - b)(1 - bz)}{2b}z\frac{d^2\epsilon}{dz^2} - \frac{i\beta}{4}(2 - i\beta)(1 - b)\delta + (1 - b)(2 - i\beta)z\frac{d\delta}{dz} + (1 - b)z^2\frac{d^2\delta}{dz^2} \qquad [23]$$

Equation [23] is a nonhomogeneous complex hypergeometric equation, with singularities at $z = 0$, 1 and ∞ which correspond to $\bar{M} = 0$ and 1 in the actual flow field.

Quasi-Steady Flow and Constant δ

It may be possible to solve Equation [23] when $\epsilon(z)$ and $\delta(z)$ are given. However, in this paper, only the simple case of quasi-steady flow is treated. In other words, β is considered so small that at each instant those nonsteady perturbation ratios $\rho'/\bar{\rho}$ and $u'/\bar{u}$ may be represented approximately as their amplitudes σ and ν, respectively. Equation [23] then reduces to

$$(1 - z)\frac{d^2\sigma}{dz^2} - 2\frac{d\sigma}{dz} = (1 - b)\left[\frac{d\epsilon}{dz} - \frac{1 - bz}{2b}\frac{d^2\epsilon}{dz^2} + 2\frac{d\delta}{dz} + z\frac{d^2\delta}{dz^2}\right] \qquad [24]$$

The area fluctuation function $\delta(z)$ is rather difficult and complicated to impose. However, in view of Stoolman's experimental results [Fig. 7 of (10)] showing that the effect of external diffusion on the flow instability is about the same as internal diffusion, we may assume $d\delta/dz = 0$ for a first approximation. Equation [24] then reduces to

$$(1 - z)\frac{d^2\sigma}{dz^2} - 2\frac{d\sigma}{dz} = (1 - b)\left[\frac{d\epsilon}{dz} - \frac{1 - bz}{2b}\frac{d^2\epsilon}{dz^2}\right] \qquad [25]$$

The significance, and the consequence, of this assumption should be examined. The more realistic fluctuating model has the boundary streamlines swinging about a pivoted point near the cowling lip as shown in Fig. 2. Thus, $d\delta/dz$ is a positive quantity, whereas $d\epsilon/dz$ must be a negative quantity in order to produce flow instability, as will be shown later. Assume that the second derivatives of δ and ϵ are much smaller than those first derivatives and can be neglected in Equation [24]. Therefore the flow area fluctuation in the external diffusion regime has, in fact, a damping effect on the flow instability. For this reason the assumption of constant amplitude will not deteriorate our qualitative investigation of the viscous induced instability. It should be noted, however, that the present result will lead to a smaller value of ϵ for neutral stabilities.

Linear Entropy Perturbation $\epsilon(z)$

For a qualitative analysis, the perturbation entropy distribution is assumed to be linear with z, primarily for mathematical simplicity

$$\frac{d}{dz}\left(\frac{\epsilon}{\xi/\bar{u}_2}\right) = -m < 0 \qquad [26]$$

where $\xi/\bar{u}_2$ and m are constants. Integrating Equation [26] and inserting the boundary condition immediately behind the oscillating shock that $\epsilon = \epsilon_2$ for $z = z_2$, we obtain

$$\frac{\epsilon}{\xi/\bar{u}_2} = \frac{\epsilon_2}{\xi/\bar{u}_2} + m(z_2 - z) \qquad [27]$$

for $z < z_2$.

The first term on the right-hand side of Equation [27] is the perturbation entropy due to shock oscillation, which remains constant with fluid particles moving downstream. The second term on the right-hand side is the perturbation entropy due to viscous dissipation, which is assumed to increase linearly with the decrease of z.

Solutions and Boundary Conditions

Substituting Equation [26] or [27] into Equation [25], we have

$$(1 - z)\frac{d^2\sigma}{dz^2} - 2\frac{d\sigma}{dz} = -\frac{2}{\gamma + 1}m\frac{\xi}{\bar{u}_2} \qquad [28]$$

Solution for σ can be easily obtained in terms of M^* by using Equation [18] and Prandtl's shock relation $M_1{}^*\bar{M}_2{}^* = 1$

$$\sigma = \frac{BM_1{}^{*2}}{M_1{}^{*2} - \lambda^2} + C + \frac{\lambda^2}{(\gamma + 1)M_1{}^{*2}}m\frac{\xi}{\bar{u}_2} \qquad [29]$$

where

$$\lambda = \frac{\bar{M}^*}{\bar{M}_2{}^*} = \frac{\bar{u}}{\bar{u}_2}$$

Solution for ν may be obtained by substituting Equation [29] into Equation [22] in which β is taken to be zero

$$\nu = -\frac{BM_1{}^{*2}}{M_1{}^{*2} - \lambda^2} + \frac{\gamma - 1}{2}C + \frac{\epsilon_2}{2} + \left[\frac{1}{\gamma - 1} + \frac{\gamma + 1 - 2\lambda^3}{2(\gamma + 1)M_1{}^{*2}}\right]m\frac{\xi}{\bar{u}_2} \qquad [30]$$

The arbitrary constants B and C can be determined from the boundary conditions immediately behind the oscillating normal shock. Consider a normal shock oscillating slightly. The upstream flow conditions remain constant except for the magnitude of the relative velocity, whereas the flow conditions behind the shock are disturbed and vary with the shock velocity ratio $w/\bar{u}_2$. Assuming $w/\bar{u}_2 \ll 1$ and using Equation [6], Stoolman (10) obtained the following relations from Burgers' general expressions (15) by retaining only the first-order terms in perturbations (12)

$$\frac{(u'/\bar{u})_2}{w/\bar{u}_2} = \frac{\nu_2}{\xi/\bar{u}_2} = -\frac{2}{\gamma+1}\left(1+\frac{1}{M_1^2}\right) \qquad [31a]$$

$$\frac{(\rho'/\bar{\rho})_2}{w/\bar{u}_2} = \frac{\sigma_2}{\xi/\bar{u}_2} = \frac{4}{(\gamma+1)M_1^2} \qquad [31b]$$

$$\frac{(S'/c_v)_2}{w/\bar{u}_2} = \frac{\epsilon_2}{\xi/\bar{u}_2} = \frac{4\gamma}{\gamma+1}\,\frac{(\gamma-1)M_1^2(M_1^2-2)+(\gamma-1)}{(2\gamma M_1^2-\gamma+1\,M_1^2)} \qquad [31c]$$

$$\frac{(p'/\bar{p})_2}{w/\bar{u}_2} = \frac{\varphi_2}{\xi/\bar{u}_2} = \frac{4\gamma}{\gamma+1}\,\frac{2+(\gamma-1)\,M_1^2}{2\gamma M_1^2-\gamma+1} \qquad [31d]$$

where w is the shock oscillating velocity, positive toward upstream.[7] It is important to note that entropy will increase if the normal shock is moving upstream due to any disturbance, such as isentropic compression waves originating from the plenum chamber.

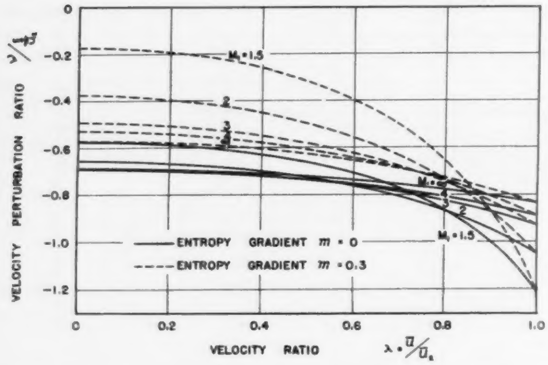

Fig. 3 Velocity perturbations in the subsonic diffusion regime (quasi-steady)

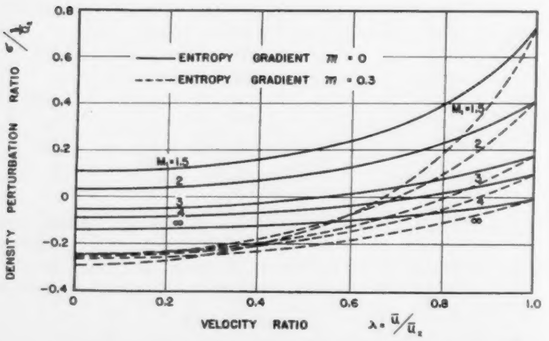

Fig. 4 Density perturbations in the subsonic diffusion regime (quasi-steady)

With the boundary conditions given in Equations [31], the arbitrary constants B and C can be determined. Therefore, the complete solutions for ν and σ can be expressed as

$$\nu = \frac{M_1^{*2}-1}{M_1^{*2}-\lambda_2}\,\nu_2 + \frac{1-\lambda^2}{M_1^{*2}-\lambda^2}\left\{\frac{\gamma-1}{\gamma+1}(\sigma_2+\nu_2) + \frac{\epsilon_2}{\gamma+1} + \frac{1}{\gamma-1}\left[1-\frac{(\gamma-1)\lambda^2}{(\gamma+1)M_1^{*2}}\right]m\frac{\xi}{\bar{u}_2}\right\} \qquad [32]$$

$$\sigma = \sigma_2 - \frac{1-\lambda^2}{M_1^{*2}-\lambda^2}\left\{\frac{\gamma-1}{\gamma+1}\sigma_2 - \frac{1}{\gamma+1}(2\nu_2-\epsilon_2) + \frac{1}{\gamma-1}\left[1-\frac{\gamma-1}{\gamma+1}\,\frac{\lambda^2}{M_1^{*2}}\right]m\frac{\xi}{\bar{u}_2}\right\} \qquad [33]$$

with the relation given in Equation [13], we obtain

$$\varphi = \gamma\sigma_2 + \epsilon_2 - \frac{1-\lambda^2}{M_1^{*2}-\lambda^2}\left\{\frac{\gamma(\gamma-1)}{\gamma+1}\sigma_2 - \frac{\gamma}{\gamma+1}(2\nu_2-\epsilon_2) + \frac{1}{\gamma-1}\left[1+\frac{\gamma-1}{\gamma+1}\,\frac{\lambda^2}{M_1^{*2}}\right]m\frac{\xi}{\bar{u}_2}\right\} \qquad [34]$$

Equations [32 and 33] are plotted in Figs. 3 and 4, respectively, against velocity ratio λ with M_1 and m as the parameters. Also φ/ν is plotted in Fig. 5. Since the inlet acoustic impedance can be expressed in terms of ν and φ

$$\zeta_4 = \left(\frac{\bar{a}}{\gamma\bar{p}}\right)_4\left(\frac{p'}{u'}\right)_4 = \frac{1}{\gamma\bar{M}_e}\left(\frac{\varphi}{\nu}\right)_4 \qquad [35]$$

it is clearly indicated in Fig. 5 that flow instability will not occur for a nonviscous fluid, since $\zeta < 0$ for $m = 0$, and that instability may occur if m is sufficiently large.

Internal Diffusion Regime

It was noted in Equation [25] that the terms involving the flow area fluctuation disappear when the assumptions of quasi-steady flow and constant δ are made. In other words, the flow equation in the external diffusion regime becomes exactly the same as in the internal diffusion regime. Therefore, the solutions in Equations [32, 33 and 34] can be directly extended into the internal diffusion regime, provided the assumptions of linear velocity variation and parabolic perturbation entropy distribution, with respect to the distance, are also used.

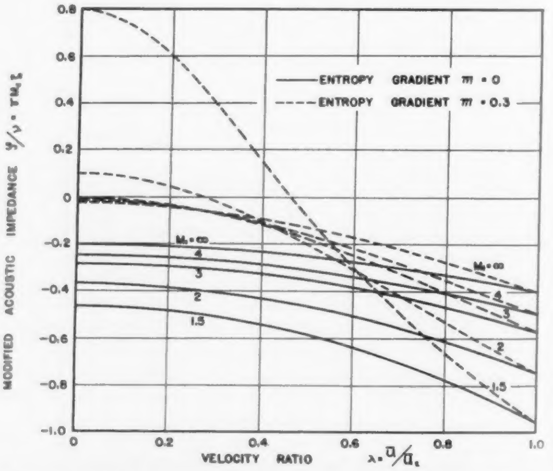

Fig. 5 Modified acoustic impedance in the subsonic diffusion regime (quasi-steady)

---

[7] It is equivalent in that the free stream velocity is accelerated to $u_1 + w$ with respect to a stationary shock. Therefore, it is in accordance with our coordinate system that flow velocity is positive toward downstream. In this way, $\epsilon/(\xi/\bar{u}_2)$ is expressed as a positive quantity. The present sign convention differs from that in (10 and 12).

Final Results

Equation of Neutral Stability Limit

The stability criterion in Equation [1] can be further expressed as follows, by using Equation [35] and $\bar{M}_c^*$ instead of $\bar{M}_c$

$$\frac{\varphi_4}{\nu_4} = \frac{\gamma(\gamma - 1)\lambda_c^2}{(\gamma + 1)M_1^{*2} - (\gamma - 1)\lambda_c^2} \qquad [36]$$

The perturbation entropy generated due to viscous dissipation at the inlet of plenum chamber is taken directly from the last term in Equation [27] and may be expressed as

$$\frac{\epsilon_\mu}{\xi/\bar{u}_2} = \frac{m}{M_1^{*2}}(1 - \lambda_c^2) \qquad [37]$$

Substituting Equations [32 and 34] into Equation [36] and using Equation [37], we obtain the equation of neutral stability limit in terms of λ_c and $\epsilon_\mu/(\xi/\bar{u}_2)$

$$\left[\left(M_1^{*2} - \frac{\gamma - 1}{\gamma + 1}\lambda_c^2\right)(M_1^{*2} - \lambda_c^2) - \frac{\gamma - 1}{\gamma + 1}M_1^{*2}(1 - \lambda_c^2)\right]\frac{\sigma_2}{\xi/\bar{u}_2} + \left[M_1^{*2}(1 - \lambda_c^2) - \frac{\gamma - 1}{\gamma + 1}(M_1^{*2} - \lambda_c^4)\right]\frac{\nu_2}{\xi/\bar{u}_2} +$$

$$\left[\frac{1}{\gamma}(M_1^{*2} - \lambda_c^2)\left(M_1^{*2} - \frac{\gamma - 1}{\gamma + 1}\lambda_c^2\right) - \frac{M_1^{*2}}{\gamma + 1}(1 - \lambda_c^2)\right]\frac{\epsilon_2}{\xi/\bar{u}_2} - \left[\frac{M_1^{*4}}{\gamma(\gamma - 1)} + \frac{\lambda_c^2 M_1^{*2}}{\gamma + 1} - \frac{(\gamma - 1)\lambda_c^4}{\gamma(\gamma + 1)}\right]\frac{\epsilon_\mu}{\xi/\bar{u}_2} = 0 \qquad [38]$$

For a given free stream Mach number $\nu_2/(\xi/\bar{u}_2)$, $\sigma_2/(\xi/\bar{u}_2)$ and $\epsilon_2/(\xi/\bar{u}_2)$ are known quantities in Equation [31]. Thus the critical plenum chamber velocity ratio λ_c can be solved in Equation [38] for any given values of $\epsilon_\mu/(\xi/\bar{u}_2)$ or vice versa.

Stability Boundaries

From Equation [38], we plot the critical values of $\epsilon_\mu/(\xi/\bar{u}_2)$ against λ_c for neutral stability in Fig. 6. Also, stability boundaries are replotted in Fig. 7 as lines of constant $\epsilon_\mu/(\xi/\bar{u}_2)$ with $\bar{M}_c^*$ and M_1^* as the ordinate and abscissa, respectively. The value of $\epsilon_\mu/(\xi/\bar{u}_2)$ on each curve may be considered as the sensitivity of a diffuser for neutral stable operation. In other words, the described value indicates a certain shock velocity which has to spill a certain amount of mass flow, due to a small entropy generated by viscous dissipation, so that a neutral stability can still be maintained. The neutral conditions previously mentioned can only be achieved if the diffuser operating conditions $(M_1^*, \bar{M}_c^*)$ lie on those curves of Fig. 7. Stable or unstable conditions will be obtained if the diffuser operating conditions are above or below those curves respectively. It should be noted that all the stability boundaries in Figs. 6 and 7 are valid only for small $\bar{M}_c$ according to Equation [1]. For a further understanding of the stability boundaries, we plot $[\epsilon_\mu/(\xi/\bar{u}_2)]\lambda_c = 0$, $\epsilon_s/(\xi/\bar{u}_2)$ and also their sums vs. M_1^* in Fig. 8 for the particular case of zero mass flow. The main purpose is to show that the entropy generated due to shock oscillation alone is insufficient to cause instability. It also indicates that the maximum value of $[\epsilon_\mu/(\xi/\bar{u}_2)]\lambda_c = 0$ required for instability occurs near $M_1^* = 1.36$ or $(M_1 = 1.5)$.

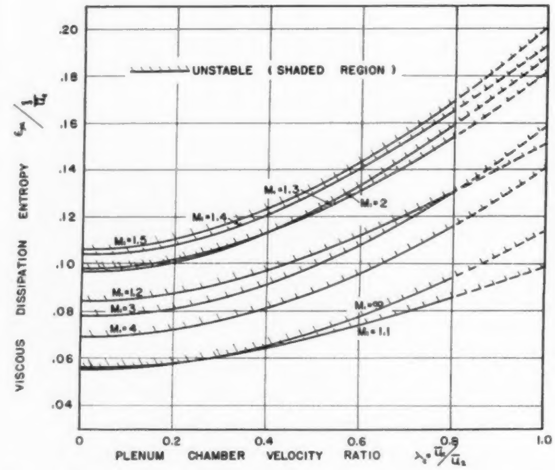

Fig. 6 Stability boundaries of viscous dissipation entropy with plenum chamber velocity ratio

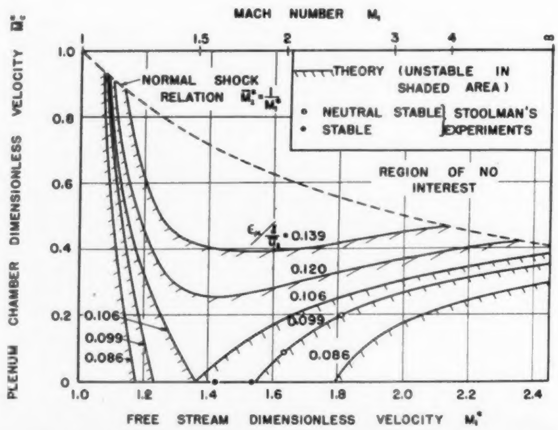

Fig. 7 Stability boundaries with viscous dissipation entropies

Discussion

Comparison With Stoolman's Experimental Data

Stoolman (10) tested four normal shock diffuser models with various internal contraction ratios ($A_3/A_4 = 0.28$ to 1.0) at $M_1 = 1.6$ (reported at 1.8), 2.0 and 2.45. The Reynolds numbers based on diffuser length are all about in the order of 10^5. Comparisons of Stoolman's data with the present analysis are made in the following discussion.

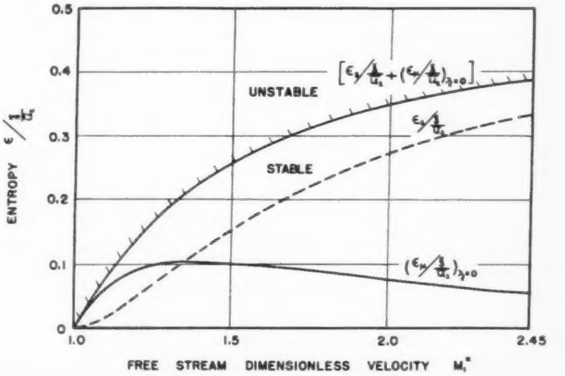

Fig. 8 Stability boundary of total entropy generation for zero mass flow

No significant effect of diffuser geometric contraction ratios on stability limit

For a given free stream Mach number and captured mass flow, Stoolman's result does not reveal any significant effect of diffuser geometric contraction ratios on the stability limit [Fig. 7 of (10)]. It immediately confirms a few of our important assumptions: Stoolman's result indicates that the effect of external diffusion on stability limit is approximately the same as internal diffusion. In other words, the assumptions of quasi-steady flow and constant amplitude of flow area fluctuation are quite close to the actual flow conditions; also, Stoolman's result shows that the velocity distribution in the external and internal diffusion regimes is not very significant to the stability limit. Therefore a simple linear velocity distribution may be chosen for qualitative investigation.

Agreement with Stoolman's data on neutral stability boundary

Stoolman's experimental data of the neutral stability limits for $M_1 = 2$ and 2.45 are also plotted in our Fig. 7. It is interesting to note that the previously mentioned data fall exactly on the curve of $\epsilon_\mu/(\xi/\bar{u}_2) = 0.099$. If we assume that the diffuser sensitivity $\epsilon_\mu/(\xi/\bar{u}_2)$ for Stoolman's model is close to this value, then Stoolman's observation of stable operation at $M_1 = 1.6$ or 1.8 with zero mass flow (Fig. 7) indeed confirms the present analytical result.

Comparison With Stability Theories of Trimpi and Sterbentz-Evvard

The present result may also be interpreted as follows: For a given free stream Mach number and captured mass flow, the flow stability is dependent on the instantaneous ratio of the total perturbation entropy generated by viscous dissipation and shock oscillation, to the corresponding shock velocity. Since the shock velocity is directly related to the instantaneous captured mass flow, the present analysis indeed confirms Trimpi's proposed theory of instability (4).

In the Sterbentz-Evvard analysis, a ratio $dp_{oc}/d\dot{m}$ was introduced which, as stated in their paper, represents the pressure change in the ramjet due to the diffuser shock position which changes during the "unsteady" operation of the diffuser. It has to be justified whether this ratio should be interpreted as the ratios between the "instantaneous" or the "time averaged" values of them in an unsteady flow with fixed exit throat area, or between their "steady" values with small changes of exit throat area. In order to answer this we explore the meaning of the inlet acoustic impedance, which is shown in Equation [35] to be independent of time. The acoustic impedance actually represents the magnitude of the amplitude ratio of the perturbation quantities φ and ν either in an "unsteady" state, or in a "steady" state with a small change of exit throat area. For this reason Mirels (11) can further express the stability criterion in terms of the "steady" diffuser characteristic curve $(\bar{\dot{m}}/\bar{p}_{oc})\ (d\bar{p}_{oc}/d\bar{\dot{m}})$ directly from the relation with the inlet acoustic impedance. However, it is not true when the stability criterion is measured by the slopes of "time average" diffuser characteristic curve during an "unsteady" operation. Therefore, it is clear that the original sense of $dp_{oc}/d\dot{m}$ in Sterbentz-Evvard's analysis is exactly the same as Trimpi's idea, but the interpretation of this ratio as the slope of diffuser characteristic is only applicable in the "steady" range of subcritical operation. The arguments noted also explain why some experimental results (5,16) have shown diffuser instability at zero or negative slopes of the "time average" diffuser characteristics, and why some others may have intermittent buzz in the subcritical range. This is because the instantaneous total pressure recovery with respect to its corresponding mass flow cannot be expressed on a time average scale of the diffuser characteristic curve.

Conclusions

1 The determination of the self-excited shock oscillation of a supersonic inlet diffuser is not possible without consideration of viscous dissipation. The entropy generated due to the shock oscillation alone is not sufficiently large to cause flow instability.

2 Instability is found to be due to further entropy generated by viscous dissipation. The present stability parameter (or diffuser sensitivity) expressed as $\epsilon_\mu/(\xi/\bar{u}_2)$ is the amplitude ratio of the perturbation entropy generated by viscous dissipation, to the corresponding shock velocity.

3 Neutral stability boundaries are obtained in terms of the diffuser sensitivity $\epsilon_\mu/(\xi/\bar{u}_2)$ for the entire range of free stream Mach numbers, and are in agreement with Stoolman's experimental data.

4 The free stream Mach number, which is rather insensitive to instability, is in the neighborhood of 1.5.

5 The present analysis confirms Trimpi's theory of instability and also unifies the Sterbentz-Evvard theory with that of Trimpi. However, the interpretation of Sterbentz-Evvard's theory as the slope of diffuser characteristic is only applicable in the "steady" range of subcritical operation, but is not applicable in the range of the time averaged values of an unsteady state.

Nomenclature

$A(x, t)$ = instantaneous flow area captured by the inlet diffuser
a = local sound velocity
B, C = arbitrary constants
b = $(\gamma - 1)/(\gamma + 1)$, constant for gas property ($b = \frac{1}{6}$ for air)
$c_f(x, t)$ = $\tau/\rho(u^2/2)$, coefficient of friction
c_p, c_v = specific heat at constant pressure and volume, respectively
$D(x, t)$ = $4A/P$, hydraulic diameter of flow area
M = u/a, Mach number
M^* = u/a^*, dimensionless velocity
m = slope of $\epsilon/(\xi/\bar{u}_2)$ vs. z curve, $m > 0$
$\dot{m}(t)$ = instantaneous captured mass flow
$P(x, t)$ = perimeter of $A(x, t)$
$p(x, t)$ = instantaneous pressure
$R(x, t)$ = radius of mean flow area $A(x, t)$
r = radial coordinate normal to diffuser axis
$S(x, t)$ = entropy
t = time
$u(x, t), v(x, t)$ = instantaneous velocity components in x, r directions, respectively
w = $\xi e^{i\omega t}$, shock oscillating velocity (positive toward upstream)
x = coordinate along the diffuser axis (positive toward downstream)
z = $(x/x^*)^2 = (\bar{u}/a^*)^2 = \bar{M}^{*2}$, new independent variable
β = $-\omega x^*/\bar{a}^* > 0$, reduced angular frequency
γ = c_p/c_v, ratio of gas specific heats; $\gamma = 1.40$ for air
$\nu(x), \sigma(x), \varphi(x)$ = time independent parts of $u'/\bar{u}$, ρ'/ρ and p'/p, respectively. See Equations [12, 13]
$\epsilon(x$ = $\varphi(x) - \gamma\sigma(x)$, time independent part of S'/c_v. See Equation [13]
$\delta(x)$ = time independent parts of $A'/\bar{A}$. See Equation [14]
ζ = $(\bar{a}/\gamma\bar{p})(p'/u')$, acoustic impedance
$\rho(x, t)$ = instantaneous density
$\tau(x, t)$ = shear stress
λ = $\bar{M}^*/\bar{M}_2^* = \bar{u}/\bar{u}_2$, velocity ratio
ω = angular frequency
ξ = amplitude of shock velocity

Subscripts

$*$ = sonic condition
$-$ = time average value, function of x only

$'$ = nonsteady small perturbation, function of x and t

1–6 = sections refer to different locations in the diffuser. See Figs. 1 or 2

c = plenum or combustion chamber

o = local stagnation condition

s = due to shock oscillation

μ = due to viscous dissipation

References

1 Oswatitsch, K. L., "Pressure Recovery for Missiles with Reaction Propulsion at High Supersonic Speeds (The Efficiency of Shock Diffusers)," NACA TM 1140, June 1947.

2 Ferri, A. and Nucci, L. M., "The Origin of Aerodynamic Instability of Supersonic Inlets at Subcritical Conditions," NACA RM L 50 K30, 1951.

3 Trimpi, R. L., "An Analysis of Buzzing in Supersonic Ram-Jets by a Modified One-Dimensional Non-Stationary Wave Theory," NACA RM L52A18, 1952; *see also* TN 3695, 1956.

4 Trimpi, R. L., "A Theory for Stability and Buzz Pulsation Amplitude in Ramjets and an Experimental Investigation Including Scale Effects," NACA RM L 53028, 1953. Superseded by NACA TR1265, 1956.

5 Dailey, C. L., "Supersonic Diffuser Instability," *J. Aeron. Sci.*, vol. 22, no. 11, Nov. 1955, pp. 733–749.

6 Trimpi, R. L., "Comments on 'Supersonic Diffuser Instability'," Readers' Forum, *J. Aeron. Sci.*, June 1956. Reply to "Further Comments on 'Supersonic Diffuser Instability'," *J. Aeron. Sci.*, Nov. 1957.

7 Dailey, C. L., "Further Comments on 'Supersonic Diffuser Instability'," Readers' Forum, *J. Aeron. Sci.*, Jan. 1957. Also "Reply," *J. Aeron. Sci.*, Nov. 1957.

8 Sterbentz, W. H. and Evvard, J. C., "Criteria for Prediction and Control of Ram-Jet Flow Pulsations," NACA TN 3506, 1955.

9 Sterbentz, W. H. and Davids, J., "Amplitude of Supersonic Diffuser Flow Pulsations," NACA TN 3572, 1955.

10 Stoolman, L., "Investigation of an Instability Phenomena Occurring in Supersonic Diffusers," Ph.D. Thesis, Cal. Tech., 1953.

11 Mirels, H., "Acoustic Analysis of Ram-Jet Buzz," NACA TN 3574, 1955.

12 Chang, C. C. and Hsu, C. T., "Solutions to Stoolman's External Diffusion Equations for Instability of a Normal Shock Inlet-Diffuser," JET PROPULSION, vol. 28, no. 7, July 1958, pp. 457–460.

13 Edwards, R. H., "Solution to the Linearized Quasi-Stationary External Diffuser Equations," ARS JOURNAL, vol. 29, no. 1, 1959, p. 54.

14 Shapiro, A. H., "The Dynamics and Thermodynamics of Compressible Fluid Flow," vol. 2, Ronald Press Co., N. Y., 1954, pp. 972–974.

15 Burgers, J. M., "On the Transmission of Sound Waves Through a Shock Wave," *Koninklijke Nederlandsche Akademie Van Wetnschappen*, vol. XLIS, 1946.

16 Hermann, R. and Hsu, C. T., "Free-Flight Simulation of the Testing of Supersonic Inlet-Diffusers in a Free-Jet Wind Tunnel with 50% Area Ratio in the Mach Number Range from 1.5 to 3," Fig. 39, Research Rep. 117, Rosemount Research Lab., Univ. of Minn., 1955.

Satellite Pressure Losses Caused by Meteoroid Impacts

M. KORNHAUSER[1]

General Electric Co.
Philadelphia, Pa.

In order to predict the frequency of hull penetration of a satellite capsule by meteoroids, estimates are made of the frequency of encounters with meteoroids, and the cratering effect of each impact. The cratering effects are based on the correlation of recent laboratory experimentation using hypervelocity particles, and very conservative estimates of impact frequency are employed. The resulting calculations of percentage of hull area covered by holes, and loss of internal pressure vs. time, are expected to be conservative for design purposes. Application of this method to a manned satellite capsule having a given surface area and time of exposure to meteoroids results in predictions of: Probability of penetration of several hull designs, time required for air pressure to drop to $\frac{1}{3}$ atm, and weight of reserve air needed to replace leakage and maintain internal pressure at 1 atm.

ALTHOUGH estimates have been made of the effects of meteoroids on satellites and space vehicles (1),[2] it is of current interest to reassess these estimates in the light of recent information on meteoroid cratering. A considerable volume of experimental data has been obtained on the cratering effects of hypervelocity particles, and the results of these empirical data are combined with meteoroid distribution estimates to yield conservative figures for the probability of penetrating the skin of a satellite.

Manned space vehicles pose the problem of maintaining air pressure within the hull. This problem is examined from the following standpoints:

Thickness of hull sufficient to withstand meteoroid bombardment for the duration of the mission of the space vehicle.

Weight of air needed to replace leakage when this does occur.

Time required for air pressure to drop below a tolerable level.

This last item is of practical interest to the passenger, who must decide whether he has time to complete his mission, or whether he must return to Earth immediately.

Received Sept. 2, 1959.

[1] Systems Project Engineer, Advance Space Vehicle Engineering Dept. Member ARS.

[2] Numbers in parentheses indicate References at end of paper.

Calculation of Hull Penetration

Laboratory data on hypervelocity cratering (2) present the empirical formulas[3]

$$\frac{VE}{U} = 17.5\left(\frac{E}{E_0}\right)^{0.28} \quad [1]$$

$$h = 2\left(\frac{U}{E}\right)^{1/3}\left(\frac{E}{E_0}\right)^{0.09} \quad [2]$$

The assumptions and extrapolations (velocity and size) necessary in order to arrive at Equations [1 and 2] are considered in (2). Note that the expression for depth of crater is expected to be correct within a factor of 2 or 3 for untested materials. A further assumption is that the skin of the satellite behaves as a semi-infinite medium, i.e., craters on a thin skin are the same as on a thick plate, and the skin is penetrated when h exceeds the thickness of the skin.

The meteor bumper configuration proposed by Whipple and others, consisting of a bumper shield placed some distance from the main pressure hull, is known to be quite advantageous on a weight basis. The thin bumper shield serves to shatter the hypervelocity particle, so that the material sprays out from the hole in the bumper and covers a large area on the main hull. The loss in concentration of energy permits the use of thin hulls, so that a saving of total weight is effected. Unfortunately, there is virtually no experimental performance data for double wall construction at present, and the following estimates must be based on solid hull construction.

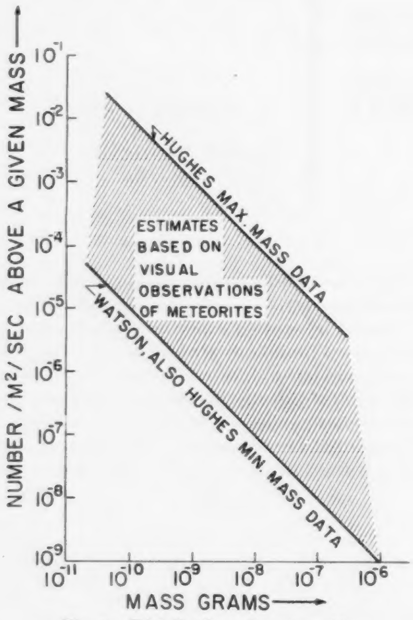

Fig. 1 Distribution of meteoroids

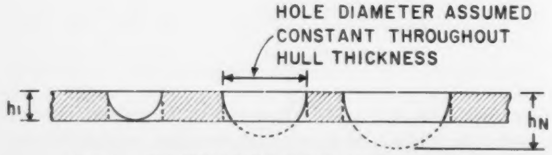

Fig. 2 Simplified holes in hull of space vehicle

Probability of Encounters With Meteoroids

The estimates of frequency of encountering meteoroids at each kinetic energy level have a spread of about three orders of magnitude, depending on the source of the estimate [see (3, 4); note that the figures in (1) fall near the average of the highest and lowest estimates]. Fig. 1 presents these estimates. Although the recent rocket and satellite meteoroid impact data (which fall in the meteoroid size range below that which may be expected to penetrate satellite hulls) show high impact frequencies, authoritative expectations place the larger meteoroids near the lowest curve (Watson curve). Noting, however, that meteor showers may increase impact frequency considerably (5), the most conservative estimates of Fig. 1 are used, on the kinetic energy basis

$$N_i = 1/U \quad [3]$$

where N_i is the number of impacts having kinetic energy *greater* than U (in.-lb) per 10 m² of exposed area per hr. No correction for satellite attitude appears to be warranted at this time.

Combining Equations [2 and 3]

$$N_h = \frac{8}{Eh^3}\left(\frac{E}{E_0}\right)^{0.27} \quad [4]$$

where N_h is the number of holes per hr in a 10-m² hull of thickness h.

Area Covered by Holes

For purposes of calculating the loss of air within the space vehicle, each meteoroid crater of depth greater than hull thickness h_1 is assumed to be a sharp edged orifice of area $\pi h^2 (h > h_1)$. Fig. 2 illustrates this assumption, which is estimated to be conservative; i.e., it should lead to high estimates of air leakage. The total area covered by holes larger than h_1 is

$$a = \int_{N_{h_1}}^{N_h} \pi h^2 dN \quad [5]$$

Substituting Equation [4]

$$a = \frac{24\pi}{E}\left(\frac{E}{E_0}\right)^{0.27}\int_{h_1}^{h_N}\frac{dh}{h^2} \quad [6]$$

Since a is in units of in.², and the original area A was taken as 10 m² or 15,500 in.²

$$\frac{a}{A} = \frac{24\pi}{15{,}500E}\left(\frac{E}{E_0}\right)^{0.27}\left(\frac{1}{h_1} - \frac{1}{h_N}\right) \quad [7]$$

per hour. Expressing the hole production rate

$$\frac{a}{A} = C_1 t \quad [8]$$

with t in hours, the penetration constant is

$$C_1 = 4.86 \times 10^{-9}\left(\frac{E_0}{E}\right)^{0.73}\left(\frac{1}{h_1} - \frac{1}{h_N}\right) \text{ in.}^2/\text{in.}^2 \text{ per hr}$$

Thickness h_N must be taken as infinity if all meteoroids are to be considered. Cutting off the calculation at probability level N_h as in Equation [4]

$$h_N = \frac{2}{(N_h E)^{1/3}}\left(\frac{E}{E_0}\right)^{0.09} \quad [9]$$

Values of h_N are shown in Table 1 for several values of N_h and E, and Fig. 3 presents penetration constant C_1, as in Equation [8]. N_h is shown for a 28-hr mission.

---

[3] Equations [1 and 2] are valid with any consistent set of units. The dimensions given in the Nomenclature apply to subsequent calculations.

Table 1 Values of h_N

N, 28 hr	E, psi × 10^{-6} 1	5	10	15	30	45
0.001	0.614	0.415	0.351	0.318	0.268	0.244
0.01	0.285	0.193	0.163	0.148	0.125	0.113
0.1	0.132	0.0900	0.0760	0.0684	0.0581	0.0528

Pressure Decay

For an infinite pressure ratio across a nozzle of area a

$$\frac{dW}{dt} = -aP\left(\frac{2}{\gamma+1}\right)^{1/(\gamma-1)}\sqrt{\frac{2g\gamma}{RT(\gamma+1)}} \qquad [10]$$

for $\gamma = 1.4$

$$\frac{dW}{dt} = -0.578\sqrt{\frac{g\gamma}{RT}}\,AP_0\left(\frac{a}{A}\,\frac{P}{P_0}\right) \qquad [11]$$

Assuming the expansion to be a throttling (Joule-Thomson) process, the internal temperature remains constant

$$\frac{1}{P_0}\frac{dP}{dt} = \frac{1}{W_0}\frac{dW}{dt} \qquad [12]$$

Combining Equations [11 and 12]

$$\frac{dP}{P} = -0.578\sqrt{\frac{g\gamma}{RT}}\left(\frac{AP_0}{W_0}\right)\left(\frac{a}{A}\right)dt \qquad [13]$$

Using the convenient spherical shape

$$\left.\begin{aligned} W_0 &= \frac{4}{3}\pi\left(\frac{P_0}{RT}\right)r^3 \\ A &= 4\pi r^2 \end{aligned}\right\} \frac{AP_0}{W_0} = \frac{3}{r}RT$$

Equation [13] now becomes

$$\frac{dP}{P} = -0.578\left(\frac{3}{r}\right)\sqrt{\gamma gRT}\,\frac{a}{A}\,dt \qquad [14]$$

Noting that $\sqrt{\gamma gRT} = C_0$ is equal to the speed of sound in air at temperature T, and introducing C_1t equal to a/A from Equation [8], Equation [14] becomes

$$\frac{dP}{P} = -1.734\,\frac{C_0C_1}{r}\,tdt \qquad [15]$$

Integrating, we arrive at

$$\frac{P}{P_0} = e^{-0.867C_0C_1t^2/r} \qquad [16]$$

Fig. 4 consists of plots of P/P_0 vs. time, for various values of C_0C_1/r, as in Equation [16]. Note the interesting feature of Equation [16]; the larger the space vehicle, the slower the pressure drops. This behavior is occasioned by the geometric fact that surface area to volume ratio decreases as size increases.

Of practical interest is the time for internal pressure to drop from 1 atm (at zero time) to $\frac{1}{3}$ atm

$$\begin{aligned} 0.867\,C_0C_1t^2/r &= \log 3 = 1.10 \\ t_{1/3} &= 0.969C_2^{-1/2} \end{aligned} \qquad \ldots\ldots\ldots [17]$$

where $C_2 = 0.74\ C_0C_1/r$ in units of $(\text{hr})^{-2}$, ($C_2 = 10^6C_1$ for 70 F and $r = 3^1$). Equation [17] is plotted in Fig. 5.

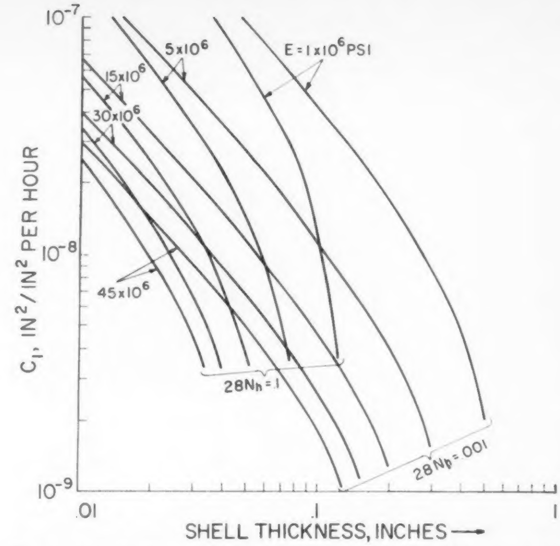

Fig. 3 Penetration constant C_1 for various shell thicknesses, E and N_h

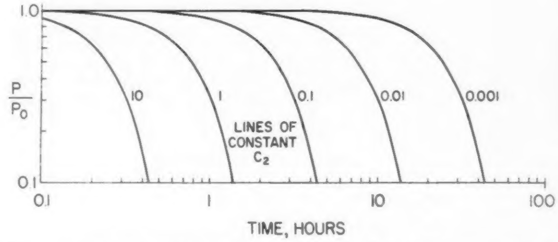

Fig. 4 Decompression of a spherical shell being punctured by meteoroids in space ($\gamma = 1.4$)

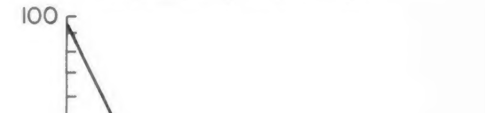

Fig. 5 Penetration constant C_2 vs. time for pressure to drop to $P_0/3$

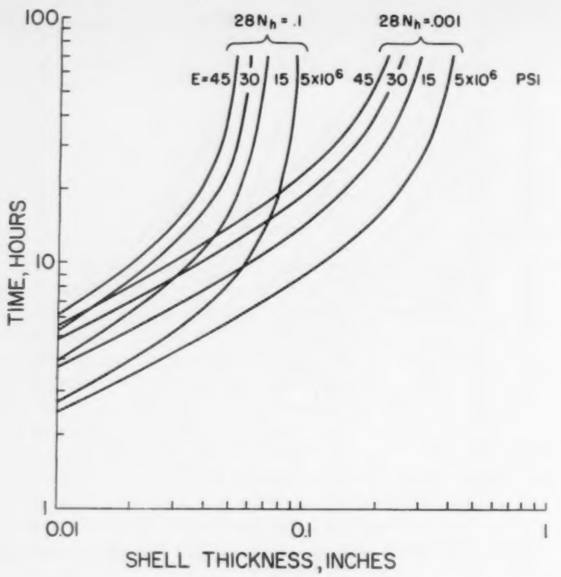

Fig. 6 Time to drop to $\frac{1}{3}$ P_o

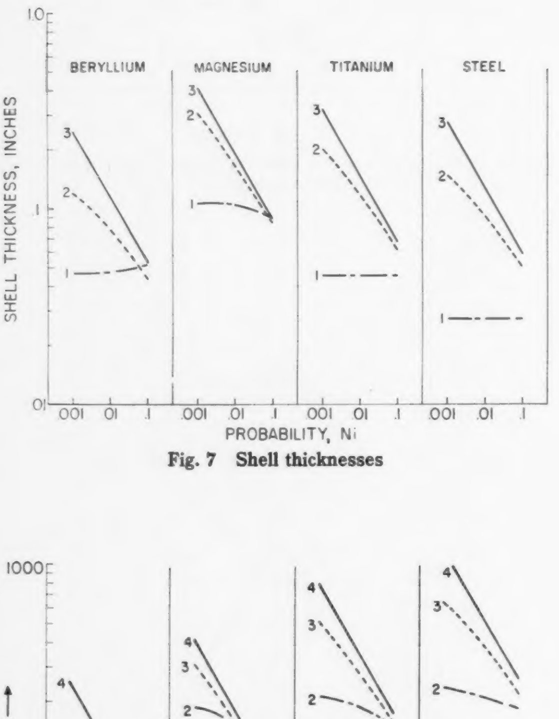

Fig. 7 Shell thicknesses

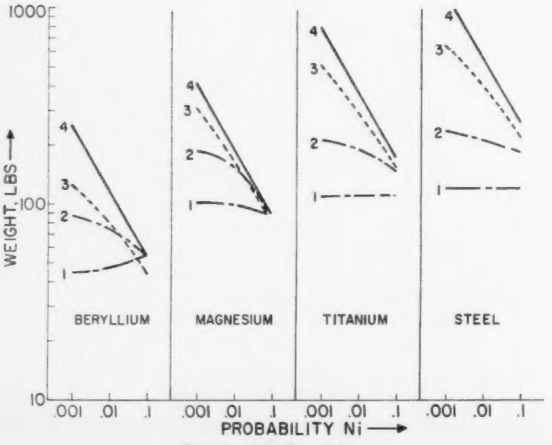

Fig. 8 Shell weights

Estimates for a Manned Satellite Capsule

It is of primary practical interest to the passenger of a manned satellite capsule to learn the time required for the pressure to drop below a tolerable level. Fig. 6 is obtained by taking $\frac{1}{3}$ atm as the tolerable pressure level, using the values of penetration constant C_1 obtained from Fig. 3 for various values of h_1, E and N_h (see Eq. [9]), using $C_2 = 10^6 C_1$ which implies that $T = 70$ F and $r = 3$ ft; and, finally, calculating time from Equation [17]. Note, in Fig. 6, that even the very thin hulls (e.g., 0.010 in.) permit ample time for return to Earth.

In order to compare heavy hulls (with no penetrations) with light hulls permitting pressure drops, we compute the weight of air needed to replace leakage and maintain pressure at 1 atm. Equation [11] at constant pressure becomes

$$\frac{dW}{dt} = -0.578\sqrt{\frac{g\gamma}{RT}}\,AP_0\frac{a}{A} = -0.578\sqrt{\frac{g\gamma}{RT}}\,AP_0C_1t$$

Integrating, we have

$$\Delta W = 0.289\sqrt{g\gamma/RT}\cdot AP_0C_1t^2 \qquad [18]$$

Expressing weight loss as a fraction of W_0 and adopting the spherical shape such that $AP_0/W_0 = 3RT/r$, Equation [18] becomes

$$\frac{\Delta W}{W_0} = 0.867\sqrt{\gamma gRT}\,\frac{C_1t^2}{r} = 0.867\,\frac{C_0C_1t^2}{r} \qquad [19]$$

For $C_0 =$ (1128) (3600) ft per hr, $r = 3$ ft, $t = 28$ hr

$$\Delta W/W_0 = 9.19 \times 10^8\, C_1 \qquad [20]$$

Using Equation [20] and Fig. 3 for C_1, one may rapidly estimate air weights ΔW (noting that $W_0 = 8.50$ lb for $r = 3$ ft, $P_0 = 1$ atm, $T = 70$ F) for various values of shell thickness E and probability N_h.

When the sum of weight of replacement air plus hull weight (10-m² area) is plotted vs. hull thickness, it is found that there is a hull thickness which represents minimum total weight. The dashed lines (no. 1) in Fig. 7 represent those hull thicknesses, with elasticity moduli of beryllium, steel, titanium and magnesium having been taken as 45 × 10⁶ psi, 30 × 10⁶ psi, 15 × 10⁶ psi and 5 × 10⁶ psi, respectively. Dotted lines (no. 2) represent thicknesses for P dropping to $\frac{1}{3}$ P_0 in 28 hr, and solid lines (no. 3) represent hull thicknesses for no penetrations in 28 hr.

Fig. 8 shows the corresponding weights, with curves numbered:

1 Shell weight for minimum total weight (shell plus air), which is attained by replacing leakage to maintain $P = P_0$.

2 Total of shell plus air weight for condition 1.

3 Allowing P to drop to $\frac{1}{3}$ P_0 in 28 hr with no air replacement.

4 No penetrations in 28 hr.

Conclusions

Calculations of pressure loss vs. time, as well as satellite capsule hull weights required for several types of protection against pressure loss, have been based on the most conservative estimates available for impact frequencies. Besides being conservative on impact frequency, the calculations do not reflect the expected advantages of the meteor bumper configuration, nor do they account for schemes such as self-sealing walls which should provide tremendous advantages in saving weight. On the other hand, much more empirical data on impact probabilities are required in order to place confidence levels on the estimates. It is anticipated that impact frequency data will be forthcoming in the next years of satellite research, as well as performance data on meteor bumpers and self-sealing double hull construction.

Even with the most conservative calculations, an examination of Fig. 6 shows that "explosive decompression" is not properly descriptive of the slow leakage process. Only if the pressure hull has too high a design stress will there be danger of catastrophic loss of pressure on meteoroid impact for any reasonable probability level.

The thickness and weight estimates of Figs. 7 and 8 show that weight saving is achieved by allowing meteoroids to puncture the hull, and by replacing the leakage, at least for the example of $A = 10$ m², $r = 3$ ft, $T = 70$ F with a 28-hr mission. Whether it will be considered practical to permit hull penetration is questionable. Also, that other capsule geometries and missions may lead to other conclusions on weight is not considered. General conclusions on capsule design will be possible after extensive design studies are made, using such methods as have been described.

Nomenclature

a = total area, holes produced by meteoroid impacts
A = surface area exposed to meteoric bombardment
c_0 = speed of sound in air
C_1 = penetration constant, $(\Delta a/A)/\text{hr}$
C_2 = leakage constant, $0.74\ C_0C_1/r$, hr^{-2} (70F, $C_2 = 10^6C_1$ for $r = 3^1$)
E = modulus of elasticity of hull material, psi
E_0 = reference modulus, 10^6 psi
g = acceleration of gravity at Earth surface, 32.2 fps²
h = depth of crater, see Equation [2]
h_1 = hull thickness
h_N = hull thickness which would have been penetrated by largest meteoroid (defined by impact probability N_t)
N_t = number of impacts with meteoroids larger than a given size
N_h = number of impacts with meteoroids larger than that just able to penetrate thickness h
P = internal pressure, any time
P_0 = initial pressure, time zero
r = radius, spherical capsule
R = gas constant
t = time, hr
T = air temperature inside capsule
U = kinetic energy of impacting particle, in.-lb
V = volume of crater, in.³
W = weight of air inside capsule
W_0 = initial weight of air inside capsule
γ = ratio of specific heats, taken as 1.4

References

1 Singer, S. F., "The Effect of Meteoric Particles on a Satellite," Jet Propulsion, vol. 26, no. 12, Dec. 1956, pp. 1071–1075, 1087, 1090.

2 Kornhauser, M., "Prediction of Cratering Caused by Meteoroid Impacts," *J. Astron. Sci.*, vol. V, nos. 3–4, Autumn-Winter 1958.

3 Gyllenhaal, P. R., "Correlation of Presently Available Information on the Impact of Meteoroids with Space Vehicles," General Electric Co., MSVD Rep. no. GE R56SD152, Aug. 31, 1956.

4 Hughes, R. F., "Meteoroid Impacts and Their Effects on Ballistic Missiles," General Electric Co., MSVD GE Real Gas Tech. Memo. no. 13, July 23, 1956.

5 Rinehart, J. S., "Meteor Distribution and Cratering," Smithsonian Astrophysical Observatory Tech. Rep. no. 3, Oct. 28, 1957, presented at Hypervelocity and Impact Effects Symposium, Naval Research Laboratory, May 22–24, 1957.

Solar Heating of a Rotating Cylindrical Space Vehicle

A. CHARNES[1] **and**
S. RAYNOR[2]

Northwestern University
Evanston, Ill.

Solar heating in a space vehicle idealized as a thin walled circular cylinder rotating with uniform velocity about its geometric axis is studied for a situation in which heat transfer by convection and heat exchange within the cylinder is negligible. The nonlinear problem is approximated through a perturbation analysis and detailed estimates are made of the parameters of interest for various ranges of speed of rotation. An estimate of the error between the exact and perturbational approach is made in the case of an illustrative example which might be expected to entail an extreme deviation.

THE TEMPERATURE distribution on the surface of an Earth satellite or space vehicle is receiving considerable attention. Schmidt and Hanawalt (1)[3] discussed the case of a nonrotating cylindrical shell exposed to solar and Earth radiation. They pointed out the importance of the ratio of absorptivity to emissivity on the temperature of the shell. Seavery (2) and Hibbs (3) studied the temperature problem of orbiting satellites; Haas and Drummeter (4), Drummeter and Schach (5), Hanel (6) and Sandorff and Prigge (7) investigated the problem of temperature control of satellites and space vehicles.

The problem considered here is that of a thin walled circular cylinder rotating with uniform velocity about its geometric axis and exposed to solar radiation. When steady state is achieved, the heat received by the rotating body is equal to

---

Received May 25, 1959.
[1] Professor of Applied Mathematics.
[2] Professor of Mechanical Engineering.
[3] Numbers in parentheses indicate References at end of paper.

the amount of heat reradiated into space. On an application of this analysis to a space vehicle, the heat transfer by convection can be neglected as soon as the vehicle leaves Earth's atmosphere. Furthermore, it is assumed that no heat exchange takes place inside the cylinder.

Simple physical considerations indicate that the part of the cylinder receiving the radiation will be hotter than the "shadow side." This temperature difference will be largest for the nonrotating cylinder and will decrease for higher rotational speeds. There should also be a displacement in the location of the line of the highest and lowest temperature on the surface of the cylinder due to rotation. For the stationary cylinder, the highest and lowest temperatures should be located at points that are closest and farthest from the heat source. In the case of a rotating cylinder, these positions should be shifted in the direction of the rotation. An analysis of the problem confirms these predictions and gives quantitatively the temperature distribution along the circumference of the cylinder.

The parameters defining the problems are:

r = radius of the cylinder, ft
s = wall thickness (assumed to be small compared with the radius), ft
k = heat conductivity of the wall material, Btu/ft hr R
c = specific heat of the wall material, Btu/lbm R
ρ = density of the wall material, lbm/ft^3
α = thermal diffusivity of the wall material, ft^2/hr

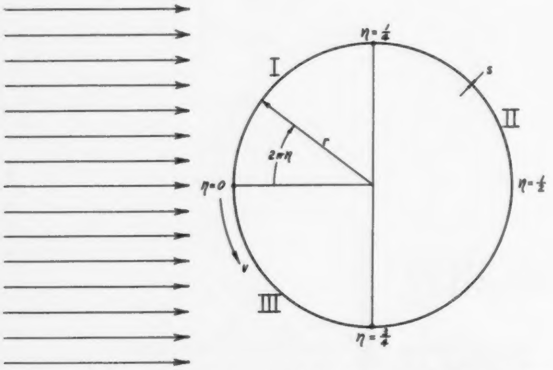

Fig. 1 Thin walled cylinder receiving solar radiation. Solar coordinate system v, η stationary in space

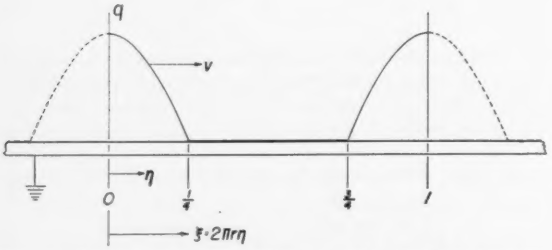

Fig. 2 Heat flux (per unit cylinder length) traveling along the developed stationary cylinder surface

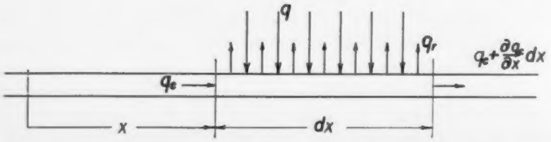

Fig. 3 Heat balance for a volume element of the cylinder wall

a = average (with respect to wave length and angle of incidence) absorptivity of the wall material
e = average total hemispherical emissivity of the wall material for the spectrum of wave length radiated by the cylinder
K_s = energy received from the radiating source by a plane perpendicular to the "line of vision," Btu/ft^2 hr
v = circumferential velocity, ft/hr

It is assumed that the cylinder axis is perpendicular to the line connecting the center of the cylinder cross section with the heat source, and that the cylinder length is large compared with the radius and small compared with the distance between the cylinder and the heat source. It is further assumed that no heat flow takes place in the axial direction, and therefore all calculations are made per unit length of the cylinder.

Differential Equation of the Temperature Distribution

In steady state, the temperature at every point on the circumference of the cylinder, as determined by the angle $2\pi\eta$ in a coordinate system that is stationary in space, remains constant (Fig. 1).

The problem can be visualized advantageously by unrolling the surface of the cylinder, as shown in Fig. 2, considering the surface stationary and allowing the heat source to travel in space, in the direction opposite to the cylinder rotation, in a manner that there is no change in the heat input. Fig. 2 illustrates the heat received (per unit area and unit time) q at any time, as a function of the position parameter η.

Consider the heat balance during the time element dt for a small volume element represented in Fig. 3. The position of the element is determined by the coordinate x attached to the cylinder. The heat received from the radiating heat source is $qdx\ dt$. The heat outflow from the volume element due to heat conduction is

$$\left(\frac{\partial q_c}{\partial x}\right) dx\ dt$$

where

$q_c = -ks(\partial\tau/\partial x)$
τ = temperature

The heat lost by radiation is

$$q_r = \sigma e \tau^4 dx\ dt$$

where σ is the Stefan Boltzmann constant.

The heat stored in the volume element during the time dt is

$$\rho s\ dx\ c(\partial\tau/\partial t)\ dt$$

The energy balance yields

$$q\ dx\ dt - \frac{\partial q_c}{\partial x}\ dx\ dt - \sigma e \tau^4 dx\ dt = \rho\ s\ c\ \frac{\partial \tau}{\partial t}\ dx\ dt$$

or

$$\frac{\partial^2 \tau}{\partial x^2} - \frac{\rho c}{k}\frac{\partial \tau}{\partial t} - \frac{\sigma e}{sk}\tau^4 = -\frac{q}{sk} \qquad [1]$$

It should be noted that the heat input due to radiation is moving along the circumference without "change in shape" and that at steady state, the temperature distribution is also moving along the circumference with no shape change. These observations can be expressed mathematically as

$$q = q(x - vt) \qquad \tau = \tau(x - vt)$$

It becomes apparent that a change of coordinates following a method described by Rosenthal (8)

$$x - vt = \xi \qquad (\xi = 2\pi r\eta) \qquad t = t' \qquad [2]$$

should be useful. It follows that

$$\frac{\partial\tau}{\partial x} = \frac{\partial\tau}{\partial\xi}\frac{\partial\xi}{\partial x} + \frac{\partial\tau}{\partial t'}\frac{\partial t'}{\partial x} = \frac{\partial\tau}{\partial\xi}$$

$$\frac{\partial^2\tau}{\partial x^2} = \frac{\partial^2\tau}{\partial\xi^2}$$

$$\frac{\partial\tau}{\partial t} = \frac{\partial\tau}{\partial\xi}\frac{\partial\xi}{\partial t} + \frac{\partial\tau}{\partial t'}\frac{\partial t'}{\partial t} = -v\frac{\partial\tau}{\partial\xi}$$

The last relation is due to the fact that $\partial\tau/\partial t' = 0$, because in the new coordinate system moving with the heat source, the temperature does not change with time. In the new coordinate system Equation [1] takes the form

$$\frac{d^2\tau}{d\eta^2} + \frac{2\pi rv}{\alpha}\frac{d\tau}{d\eta} - \frac{4\pi^2r^2\sigma e}{sk}\tau^4 = -\frac{4\pi^2r^2q}{sk} \qquad [3]$$

where $\alpha = k/\rho C_0$. The value of q is given by Lambert's law

$$q = aK_s\cos^+ 2\pi\eta$$

where $\cos^+ 2\pi\eta$ stands for a rectified cosine function as represented in Fig. 2.

The differential equation for the temperature distribution is then

$$\frac{d^2\tau}{d\eta^2} + \frac{2\pi r}{\alpha}\frac{d\tau}{d\eta} - \frac{4\pi^2r^2\sigma e}{sk}\tau^4 = -\frac{4\pi^2r^2aK_s}{sk}\cos^+ 2\pi\eta \qquad [4]$$

This equation is nonlinear. In order to facilitate the analysis it will be assumed that the fractional temperature fluctuation $\hat{T}$, as defined in the following, is small compared to unity

$$\tau = T_0(1 + \hat{T})$$

This assumption permits the approximation

$$\tau^4 \approx T_0^4(1 + 4\hat{T}) = 4T_0^4(\hat{T} + 1/4) \qquad [5]$$

Introducing the notation

$$\hat{T} + 1/4 = T \qquad \tau = (3/4 + T) \qquad \tau \approx 4T_0T \qquad [6]$$

Equation [4] is replaced by the approximating equation

$$\frac{d^2\bar{T}}{d\eta^2} + b\frac{d\bar{T}}{d\eta} - c\bar{T} = -A_0\cos^+ 2\pi\eta \qquad [7]$$

where

$b = 2\pi rv/\alpha$

$c = (16\pi^2r^2\sigma e/sk)T_0^3$

$A_0 = -4\pi^2r^2aK_s/skT_0$

The $\bar{T}$ which solves [7] is thereby an approximation of T and yields an approximate value of the temperature

$$\bar{\tau} = (3/4 + \bar{T})\,T_0 \approx \tau$$

Average Temperature

The temperature of the cylinder at any point is represented as

$$\tau = T_0(1 + \hat{T})$$

where

T_0 = reference temperature
$\hat{T}$ = nondimensional temperature parameter, determining the temperature fluctuation

Let us choose T_0 to be the average temperature of the cylinder

$$T_0 = \int_0^1 \tau(\eta)d\eta$$

Then

$$T_0 = \int_0^1 T_0(1 + \hat{T})d\eta = \int_0^1 T_0 d\eta + T_0\int_0^1 \hat{T}d\eta = T_0 + T_0\int_0^1 \hat{T}d\eta$$

It follows that the average value of $\hat{T}$ as given by $\int_0^1 \hat{T}d\eta$ must be equal to zero.

Consider the equality of heat received by the cylinder and heat reradiated. The total heat received is

$$Q_1 = 2raK_s$$

The heat reradiated is

$$dQ_2 = \sigma e\tau^4 rd(2\pi\eta) = 2\pi r\sigma e\tau^4 d\eta$$

Introducing Equation [5] into the last equation yields

$$Q_2 = 2\pi r\sigma eT_0^4\left(\int_0^1 d\eta + 4\int_0^1 \hat{T}d\eta\right) = 2\pi r\sigma T_0^4$$

Equating $Q_1 = Q_2$ results in

$$T_0 = \sqrt[4]{aK_s/\pi e\sigma} \qquad [8]$$

Introduction of this relation into Equation [7] results in

$$\frac{d^2\bar{T}}{d\eta^2} + b\frac{d\bar{T}}{d\eta} - c\bar{T} = A_0\cos^+ 2\pi\eta \qquad [9a]$$

$$b = (2\pi r/\alpha)v \qquad [9b]$$

$$c = 16\pi r^2aK_s/skT_0 \qquad [9c]$$

$$A_0 = -(\pi/4)c \qquad [9d]$$

The solution of Equation [9a] with the boundary condition requiring periodicity

$$\bar{T}(0) = \bar{T}(1) \qquad \frac{d\bar{T}}{d\eta}(0) = \frac{d\bar{T}}{d\eta}(1) \qquad [9e]$$

will yield the temperature distribution along the circumference of the cylinder.

Equation [9a] is already in dimensionless form, but the interpretation of the solution and the meaning of the coefficients of the equation can be enhanced by the introduction of the following parameters:

Thermal radius

$$R = \sqrt{skT_0/16\pi aK_s} \qquad [10]$$

Dimensionless radius

$$\rho_0 = r/R = \sqrt{c} \qquad [11]$$

Thermal velocity

$$v^* = \alpha/\pi R \qquad [12]$$

Dimensionless velocity

$$v_0 = \frac{v}{v^*} = \frac{b}{2\sqrt{c}} \qquad [13]$$

Introduction of Equations [10 to 13] into Equation [9a] yields

$$\frac{d^2\bar{T}}{d\eta^2} + 2v_0\rho_0\frac{d\bar{T}}{d\eta} - \rho_0^2\bar{T} = -\frac{\pi}{4}\rho_0^2\cos^+ 2\pi\eta \qquad [14]$$

Solution of the Linearized Temperature Distribution Equation

Consider first the homogeneous part of Equation [14]. The two solutions of this equation are

$$V = e^{\nu_1 \eta} \qquad W = e^{\nu_2 \eta} \tag{15}$$

where

$$\nu_1 = v_0\rho_0\left(-1 + \sqrt{1 + 1/v_0^2}\right)$$
$$\nu_2 = v_0\rho_0\left(-1 - \sqrt{1 + 1/v_0^2}\right)$$
$$\dots\dots\dots\dots\dots\dots\dots\dots\dots\dots\dots\dots \tag{16}$$

In order to solve Equation [9a], it is advantageous to write it in the form

$$(e^{b\eta}\bar{T}_\eta)_\eta - ce^{b\eta}\bar{T} = e^{b\eta} A_0 \cos^+ 2\pi\eta \tag{17}$$

where the subscript η indicates the differentiation with respect to η.

Green's function for Equation [17] has to satisfy the equation

$$[p(\eta)g_\eta]_\eta - ce^{b\eta}g = -\delta(\eta - t) \tag{18}$$

subject to the boundary conditions of periodicity in the interval 0 to 1

$$g(0, t) = g(1, t) \qquad g_\eta(0, t) = g_\eta(1, t) \tag{19}$$

The solution of Equation [9a] is then

$$\bar{T}(\eta) = -\int_0^1 A_0 e^{bt} \cos^+ 2\pi t g(\eta, t) dt$$

or

$$\bar{T}(\eta) = \frac{A_0}{V_1 - \nu_2} \int_0^1 \left[\frac{e^{\nu_1\eta + \nu_2 t}}{1 - e^{\nu_1}} - \frac{e^{\nu_2\eta + \nu_1 t}}{1 - e^{\nu_2}} - \right.$$
$$\left. e^{\nu_1\eta + \nu_2 t} H(t - \eta) - e^{\nu_2\eta + \nu_1 t} H(\eta - t)\right] e^{bt} \cos^+ 2\pi t dt \tag{22}$$

$A_0/(\nu_1 - \nu_2)$ can be expressed in terms of v_0 and ρ_0

$$\frac{A_0}{\nu_1 - \nu_2} = -\frac{\pi}{8} \frac{\rho_0}{\sqrt{v_0^2 + 1}} \tag{23}$$

Because of the form of $\cos^+ 2\pi\eta$, the solution for $\bar{T}$ is different for the three regions:

Region I, $0 < \eta < \frac{1}{4}$
Region II, $\frac{1}{4} < \eta < \frac{3}{4}$
Region III, $\frac{3}{4} < \eta < 1$

The temperature fluctuation $\bar{T}$ in the three regions is, respectively

$$\bar{T}_{\mathrm{I}} = \frac{1}{16} \frac{\rho_0}{\sqrt{v_0^2 + 1}} \left\{\frac{1}{(\nu_1/2\pi)^2 + 1} \frac{e^{\nu_1\eta}}{e^{(1/4)\nu_1} - e^{-(1/4)\nu_1}} - \frac{1}{(\nu_2/2\pi)^2 + 1} \frac{e^{\nu_2\eta}}{e^{(1/4)\nu_2} - e^{-(1/4)\nu_2}} - \right.$$
$$\left. \left[\frac{1}{(\nu_1/2\pi)^2 + 1} - \frac{1}{(\nu_2/2\pi)^2 + 1}\right] \sin 2\pi\eta + \left[\frac{\nu_1/2\pi}{(\nu_1/2\pi)^2 + 1} - \frac{\nu_2/2\pi}{(\nu_2/2\pi)^2 + 1}\right] \cos 2\pi\eta \right\} \tag{24a}$$

$$\bar{T}_{\mathrm{II}} = \frac{1}{16} \frac{\rho_0}{\sqrt{v_0^2 + 1}} \left\{\frac{1}{(\nu_1/2\pi)^2 + 1} \frac{e^{\nu_1(\eta - 1/2)}}{e^{(1/4)\nu_1} - e^{-(1/4)\nu_1}} - \frac{1}{(\nu_2/2\pi)^2 + 1} \frac{e^{\nu_2(\eta - 1/2)}}{e^{(1/4)\nu_2} - e^{-(1/4)\nu_2}}\right\} \tag{24b}$$

$$\bar{T}_{\mathrm{III}} = \frac{1}{16} \frac{\rho_0}{\sqrt{v_0^2 + 1}} \left\{\frac{1}{(\nu_1/2\pi)^2 + 1} \frac{e^{\nu_1(\eta - 1)}}{e^{(1/4)\nu_1} - e^{-(1/4)\nu_1}} - \frac{1}{(\nu_2/2\pi)^2 + 1} \frac{e^{\nu_2(\eta - 1)}}{e^{(1/4)\nu_2} - e^{-(1/4)\nu_2}} - \right.$$
$$\left. \left[\frac{1}{(\nu_1/2\pi)^2 + 1} - \frac{1}{(\nu_2/2\pi)^2 + 1}\right] \sin 2\pi\eta + \left[\frac{\nu_1/2\pi}{(\nu_1/2\pi)^2 + 1} \frac{\nu_2/2\pi}{(\nu_2/2\pi)^2 + 1}\right] \cos 2\pi\eta \right\} \tag{24c}$$

where

$p(\eta) = e^{b\eta}$
δ = Dirac's function

The general solution of Equation [18], as described by Friedman (9) is

$$g(\eta, t) = AV(\eta) + BW(\eta) +$$
$$\frac{V(\eta)W(t)H(t - \eta) + W(\eta)V(t)H(\eta - t)}{J(W, V)} \tag{20}$$

where

A, B = constants to be determined from the boundary conditions [19]
V, W = two independent solutions of the homogeneous form of Equation [9a]
H = Heaviside unit function
$J(W, V) = -p(t)[W_t(t)V(t) - V_t(t)W(t)]$

Substitution of computed values of A, B and $J(W, V)$ into Equation [20] results in

$$g(\eta, t) = \frac{1}{\nu_1 - \nu_2}\left[-\frac{e^{\nu_1\eta} + e^{\nu_2 t}}{1 - e^{\nu_1}} + \frac{e^{\nu_2} e^{\nu_2\eta + \nu_1 t}}{1 - e^{\nu_2}} + \right.$$
$$\left. e^{\nu_1\eta + \nu_2 t} H(t - \eta) + e^{\nu_2\eta + \nu_1 t} H(\eta - t)\right] \tag{21}$$

where ρ_0, v_0, ν_1 and ν_2 are defined by Equations [10, 12, 13 and 16].

Discussion of the Temperature Distribution

The solution of the temperature distribution will be discussed for three cases: Stationary cylinder, cylinder moving at very high speed, and rotating at intermediate speeds.

Stationary Cylinder

When the rotational velocity is zero, the dimensionless velocity also becomes zero

$$v = 0 \qquad v_0 = 0 \qquad \nu_1 = -\nu_2 = \rho_0$$

The equation for the temperature distribution is then reduced to

$$\bar{\tau}_{\mathrm{I}} = T_0 \left\{\frac{3}{4} + \frac{1}{8} \frac{\rho_0}{(\rho_0/2\pi)^2 + 1} \left[\frac{\cosh \rho_0\eta}{e^{(1/4)\rho_0} - e^{-(1/4)\rho_0}} + \right.\right.$$
$$\left.\left. \frac{\rho_0}{2\pi} \cos 2\pi\eta \right]\right\} \tag{25a}$$

$$\bar{\tau}_{\mathrm{II}} = T_0 \left\{\frac{3}{4} + \frac{1}{8} \frac{\rho_0}{(\rho_0/2\pi)^2 + 1} \left[\frac{\cosh \rho_0(\eta - 1/2)}{e^{(1/4)\rho_0} - e^{-(1/4)\rho_0}}\right]\right\} \tag{25b}$$

$$\bar{\tau}_{\text{III}} = T_0 \left\{\frac{3}{4} + \frac{1}{8}\frac{\rho_0}{(\rho_0/2\pi)^2 + 1}\left[\frac{\cosh \rho_0(\eta - 1)}{e^{(1/4)\rho_0} - e^{-(1/4)\rho_0}} + \frac{\rho_0}{2\pi}\cos 2\pi\eta\right]\right\} \quad [25c]$$

The maximum temperature occurs at $\eta = 0$ (the line on the cylinder facing the heat source)

$$\bar{\tau}_{\max} = T_0 \left\{\frac{3}{4} + \frac{1}{8}\frac{\rho_0}{(\rho_0/2\pi)^2 + 1}\left[\frac{1}{e^{(1/4)\rho_0} - e^{-(1/4)\rho_0}} + \frac{\rho_0}{2\pi}\right]\right\}$$

The minimum temperature occurs at $\eta = \frac{1}{2}$ (the line on the cylinder on the far side from the heat source)

$$\bar{\tau}_{\min} = T_0 \left\{\frac{3}{4} + \frac{1}{8}\frac{\rho_0}{(\rho_0/2\pi) + 1}\left[\frac{1}{e^{(1/4)\rho_0} - e^{-(1/4)\rho_0}}\right]\right\}$$

The largest temperature difference is

$$\bar{\tau}_{\max} - \bar{\tau}_{\min} = T_0 \frac{\pi}{4}\frac{(\rho_0/2\pi)^2}{(\rho_0/2\pi)^2 + 1}$$

The temperature distribution is symmetrical with respect to η and can be easily computed for a given value of ρ_0.

Numerical example

Consider an aluminum alloy cylinder of:

radius	r	$= 1$ ft
wall thickness	s	$= 1/200$ ft
thermal conductivity	k	$= 100$ Btu/ft hr R
thermal diffusivity	α	$= 3$ ft^2/hr
solar constant	K_s	$= 442$ Btu/ft^2 hr
radiation constant	σ	$= 0.1717.10^{-8}$ Btu/ft^2 hr(R)^4

Assume the surface of the vehicle painted black and therefore $a \approx e \approx 1$. This assumption was chosen to maximize the radiation effects.

The average temperature T_0 can be computed

$$T_0 = \sqrt[4]{aK_s/\pi e\sigma} = 534.25 \text{ R}$$
$$R = \sqrt{skT_0/16\pi aK_s} = 0.1096 \text{ ft}$$
$$\rho_0 = 9.12$$
$$v^* = \alpha/\pi R = 8.71 \text{ ft/hr}$$

For the stationary cylinder

$$v_0 = 0$$
$$\bar{\tau}_{\max} = 705.48 \text{ R}$$
$$\bar{\tau}_{\min} = 420.94 \text{ R}$$
$$\bar{\tau}_{\max} - \bar{\tau}_{\min} = 284.54 \text{ R}$$

The temperature distribution is shown in Table 1.

The error in the energy balance for the case of the stationary cylinder was computed because the linearization of Equation [4] introduces the largest error in this particular case.

Employing the computed temperature distribution $\bar{\tau}$ obtained from the linearized equation, the reradiated heat (on the basis of this approximation) is $\int_0^1 \sigma\bar{\tau}^4\, er2\pi d\eta$. The heat received from the heat source is $2ra\, K_s$. Let the error in the energy balance be denoted by ϵ_Q

$$(1 - \epsilon_Q)\int_0^1 \sigma\bar{\tau}^4\, er2\pi d\eta = 2raK_s$$

The integration of this equation was performed numerically for the case of the stationary cylinder, resulting in $\epsilon_Q = 0.185$. To obtain an estimate of the error in the temperature distribution one can write

$$\bar{\tau} = \tau[1 + \epsilon_T(\eta)]$$

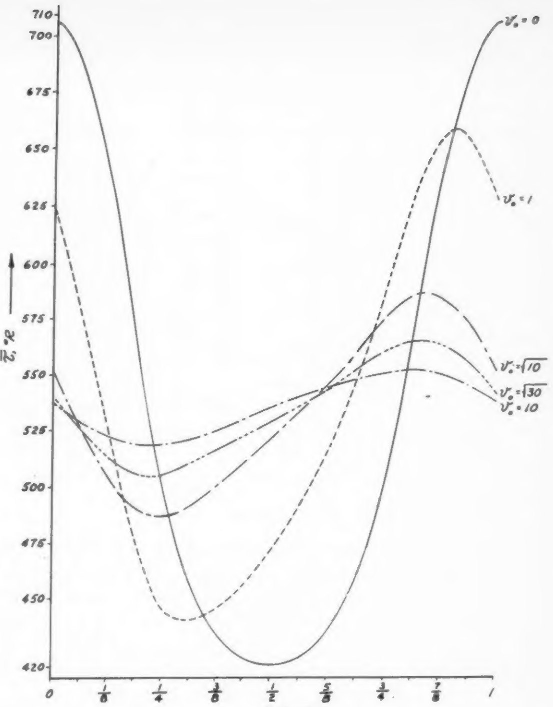

Fig. 4 Temperature distribution along the wall of a rotating cylinder for several nondimensional surface velocities

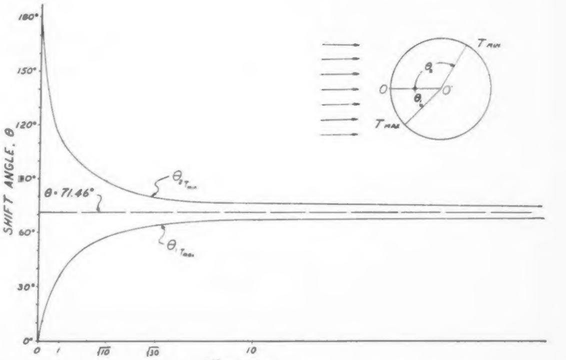

Fig. 5 Position of minimum and maximum temperature for a rotating cylinder as function of nondimensional velocity, as measured from the line 0–0′

where

τ = solution of the original Equation [4]
$\epsilon_T(\eta)$ = temperature error

The heat balance equation can be then rewritten as

$$(1 - \epsilon_Q)\int_0^1 \sigma[1 + 4\epsilon_T(\eta)]\tau^4 e\, 2\pi d\eta \approx 2aK_s = \int_0^1 \sigma\tau^4 e\, 2\pi d\eta$$

It follows that

$$\bar{\epsilon}_T \int_0^1 T^4 d\eta = \int_0^1 \epsilon_T(\eta)\tau^4 d\eta \approx \frac{1}{4}\frac{\epsilon_Q}{1 - \epsilon_Q}\int_0^1 \tau^4 d\eta$$

$$\bar{\epsilon}_T \approx \frac{1}{4}\frac{\epsilon_Q}{1 - \epsilon_Q}$$

where, by the mean value theorem, $\bar{\epsilon}_T$ lies between ϵ_T mini-

Table 1 Temperature distribution on the surface of a rotating cylinder for various nondimensional velocities

	$\eta = 0$	$\eta = \frac{1}{16}$	$\eta = \frac{1}{8}$	$\eta = \frac{3}{16}$	$\eta = \frac{1}{4}$	$\eta = \frac{5}{16}$	$\eta = \frac{3}{8}$	$\eta = \frac{7}{16}$
$v_0 = 0$	705.48	687.05	636.83	567.43	500.81	458.49	435.63	424.30
$v_0 = 1$	625.55	579.29	524.37	475.64	445.35	440.54	447.27	458.28
$v_0 = \sqrt{10}$	551.62	527.52	505.38	490.51	487.30	494.16	502.73	512.12
$v_0 = \sqrt{30}$	540.45	526.03	513.51	506.08	506.14	511.50	517.35	523.52
$v_0 = 10$	537.46	529.44	523.30	519.29	519.83	521.43	526.77	530.51
	$\eta = \frac{1}{2}$	$\eta = \frac{9}{16}$	$\eta = \frac{5}{8}$	$\eta = \frac{11}{16}$	$\eta = \frac{3}{4}$	$\eta = \frac{13}{16}$	$\eta = \frac{7}{8}$	$\eta = \frac{15}{16}$
$v_0 = 0$	420.94	424.94	435.63	458.49	500.81	567.43	636.83	687.05
$v_0 = 1$	473.67	493.27	517.37	548.67	587.30	629.83	655.04	652.91
$v_0 = \sqrt{10}$	522.37	533.57	545.79	559.14	573.71	585.15	584.50	572.20
$v_0 = \sqrt{30}$	530.01	536.90	597.46	551.61	559.75	565.02	562.64	553.68
$v_0 = 10$	534.25	537.99	542.26	546.00	550.28	552.41	550.28	544.94

mum and ϵ_T maximum. In this particular numerical example $\bar{\epsilon}_T \approx 5.7$ per cent.

Cylinder Rotating at High Speed

High speed is defined by the following conditions: $v_0^2 \gg 1$, and $v_0\rho_0 \gg \pi^2$. Under these restrictive conditions, the equation of the temperature distribution can be simplified by power series development and by neglecting terms $1/v_0^2$ and $\pi^2/v_0\rho_0$ as compared to unity.

The following equations are obtained

$$\bar{\tau}_{\text{I}} = T_0\left\{1 + \frac{\rho_0}{16v_0}\left[2\eta + \frac{\rho_0}{2v_0} \times \eta^2 - \sin(2\pi\eta - \phi)\right]\right\} \qquad [26a]$$

$$\bar{\tau}_{\text{II}} = T_0\left\{1 + \frac{\rho_0}{16v_0}\left[2\left(\eta - \frac{1}{2}\right) + \frac{\rho_0}{2v_0}\left(\eta + \frac{1}{2}\right)^2\right]\right\} \qquad [26b]$$

$$\bar{\tau}_{\text{III}} = T_0\left\{1 + \frac{\rho_0}{16v_0}\left[2(\eta - 1) + \frac{\rho_0}{2v_0}(\eta - 1)^2 - \sin(2\pi\eta - \phi)\right]\right\} \qquad [26c]$$

where

$$\tan\phi = \frac{1}{2}\,\frac{(\rho_0/2\pi)^2 + 1}{v_0(\rho_0/2\pi)}$$

The maximum temperature will occur in the fourth quadrant where $\partial\bar{\tau}_{\text{III}}/\partial\eta = 0$.

Using the same numerical example as in the previous section $\rho_0 = 9.12$, and selecting

$$v_0 = 10 \qquad v = 87.1 \text{ ft/hr} = 0.0242 \text{ fps}$$

or 0.232 rpm, it follows

$$\tan\phi = 0.107 \qquad \eta_{\max} = 0.814$$

The maximum temperature occurs at a point on the cylinder shifted in the direction of rotation, 66.96 deg away from the point facing the heat source.

Increasing the rotational speed to $v = 871$ ft/hr $= 0.242$ fps or 2.32 rpm corresponding to $v_0 = 100$, shifts the point of maximum temperature within a fraction of a degree to $\cos^{-1}(1/\pi)$, and the maximum temperature can be approximated by

$$\bar{\tau}_{\max} = T_0(1 + 0.084\,\rho_0/v_0)$$

Table 2 Positions of maximum temperature

v_0	0	$\frac{1}{4}$	1	$\sqrt{10}$	$\sqrt{30}$	10	∞
$\eta_{T\max}$	0	0.97	0.902	0.840	0.824	0.814	0.8015
$\theta_{T\max}$	0	10.8°	35.3°	57.6°	63.4°	67°	71.46°

$\bar{\tau}_{\max}$ is 1.008 T_0 for the particular case considered.

For $v_0 = 1000$ corresponding to 23.2 rpm with $\rho_0 = 9.12$ and the data otherwise unchanged, the temperature fluctuation is approximately 0.1 per cent of T_0.

Temperature Distribution for Intermediate Values of v_0

In these cases, the temperature distribution can be calculated from Equations [24]. These calculations were performed for $v_0 = 1$, $\sqrt{10}$, $\sqrt{30}$ and 10, and the values are presented in Table 1 and Fig. 4.

General Observations

The largest temperature fluctuations occur at zero velocity. Because these fluctuations are of considerable magnitude, the error in the values of the temperature due to the process of linearization is of the order of 5.7 per cent for the numerical example chosen.

As the speed increases, the temperature fluctuations become smaller. In this case the linearization of the differential equation is fully justified, and the result can be considered to be accurate.

Also in this case, the position of highest temperature is shifted in the direction of rotation. This shift is denoted by θ. At very high speeds θ approaches $\cos^{-1}(1/\pi)$ approximately 71.46 deg, and the fluctuations vanish. The position of the maximum temperature was computed for $\rho_0 = 9.12$ and a series of values of v_0, by solution of differentiated Equation [24c] set equal to zero. The values of $\bar{\tau}_{\max}$ and the corresponding angle of shift θ are presented in Table 2 and Fig. 5.

The minimum temperature occurs at zero speed on the far side of the cylinder, and, as the speed increases, the position shifts in the direction of rotation until at infinite speed the value of $\eta_{\min}$, at which $\bar{\tau}$ minimum is attained, moves to $\cos^{-1} 1/\pi$.

References

1 Schmidt, C. M. and Hanawalt, A. J., "Skin Temperatures of a Satelite," Jet Propulsion, vol. 27, Oct. 1957, pp. 1079–1083.

2 Seavery, M. H., "The Temperature of an Object Above the Earth's Atmosphere," Geophysics Research Directorate, Research Notes no. 5, March 1959.

3 Hibbs, A. R., "The Temperature of an Orbiting Missile," Progress Rep. no. 20-294, Jet Propulsion Laboratory, Calif. Inst. of Tech., Pasadena, March 28, 1956.

4 Haas, G. H. and Drummeter, L. F., Jr., "Temperature Stabilization of Vanguard Satellites—Theory and Practice," presented at Infrared Information Symposium, Boston, Sept. 1958, sponsored by Physics Branch, ONR, Washington, D. C.

5 Drummeter, L. and Schach, M., "Satellite Temperature Control," presented at IGY Conference, Nat. Acad. Sci., Washington, D. C., Oct. 1957.

6 Hanel, R. A., "Thermostatic Temperature Control of Satellites and Space Vehicles," ARS Journal, vol. 29, no. 5, May 1959, pp. 358–361.

7 Sandorff, P. E. and Prigge, J. S., Jr., "Thermal Control in a Space Vehicle," *J. Astron.*, vol. 3, no. 1, Spring 1956, pp. 4–8, 26.

8 Rosenthal, D., "The Theory of Moving Sources of Heat and Its Application to Metal Treatments," Trans. ASME, vol. 68, 1946.

9 Friedman, B., "Principles and Techniques of Applied Mathematics," John Wiley & Sons, Inc., N. Y., chap. 3, 1956.

Technical Notes

Solar-Lunar Perturbations of the Orbit of an Earth Satellite

MILDRED M. MOE[1]

Space Technology Laboratories, Inc., Los Angeles, Calif.

THE GRAVITATIONAL fields of the sun and moon can produce significant perturbations of the orbit of a highly eccentric Earth satellite. The importance of their effect on the lifetime of 1959 delta (Explorer VI) has been pointed out by Kozai (1),[2] who has made a study (2) of solar-lunar perturbations of Earth satellites. The purpose of this note is to treat these perturbations by a different method, based on some simplifying assumptions. It is assumed that the angular velocity of the disturbing body (sun or moon) is small enough compared to the angular velocity of the satellite that we may consider the disturbing body fixed during one revolution of the satellite. This simplification makes possible the integration of the instantaneous rate of change of the orbital elements over one revolution of the satellite to obtain the change in orbital elements per revolution. The magnitude of the error made by holding the disturbing body fixed is estimated. This leads to an evaluation of the effect of the motion of the disturbing body on the semimajor axis (hence energy) of the satellite orbit. The importance of the solar-lunar perturbations of orbits with high eccentricity is illustrated by computing the perturbations of the perigee distance of 1959 delta.

Perturbations of the Orbital Elements

The analysis of the perturbations is simplified if we choose a geocentric coordinate system having its z axis along the orbital angular momentum vector of the disturbing body. The orbit of the satellite is described by the instantaneous osculating ellipse (3) which has a semimajor axis a, an eccentricity e, an inclination i (with respect to the orbital plane of the disturbing body), an argument of perigee ω, and a longitude of the ascending node Ω (see Fig. 1). If there were no perturbing forces, these orbital elements would remain constant (assuming that our coordinate system is fixed in inertial space), and the orbit would be a Kepler orbit (4). If there is a perturbing acceleration having a radial component R, a transverse component S (measured in the plane of the instantaneous osculating ellipse and taken positive when making an angle less than 90 deg with the velocity vector), and a normal component W (normal to the plane of the instantaneous osculating ellipse and taken positive when making an angle less than 90 deg with the z axis), the orbital elements change at the rates (5)

$$\frac{da}{dt} = \frac{2e \sin v}{n\sqrt{1 - e^2}} R + \frac{2a\sqrt{1 - e^2}}{nr} S$$

$$\frac{de}{dt} = \frac{\sqrt{1 - e^2} \sin v}{na} R + \frac{\sqrt{1 - e^2}}{na^2e} \left[\frac{a^2(1 - e^2)}{r} - r\right] S$$

$$\frac{di}{dt} = \frac{r \cos (\omega + v)}{na^2\sqrt{1 - e^2}} W$$

$$\frac{d\Omega}{dt} = \frac{r \sin (\omega + v)}{na^2\sqrt{1 - e^2} \sin i} W$$

$$\frac{d\omega}{dt} = - \cos i \frac{d\Omega}{dt} - \frac{\sqrt{1 - e^2}}{nae} \times \left[R \cos v - \left(\frac{2 + e \cos v}{1 + e \cos v}\right) S \sin v\right] \qquad [1]$$

where

n = satellite's mean angular motion
r = radial distance of the satellite from Earth center
v = true anomaly (the angular distance of the satellite from perigee)

The rate of change of perigee distance q can be found from its relationship to a and e

$$q = a(1 - e)$$

The components R, S and W are given by Moulton (6). If r is always small compared to the distance a_d of the disturbing body from Earth's center, these components may be expanded in powers of r/a_d. Keeping only the first-order term, one obtains

$$R = K_d r (1 + 3 \cos 2\phi)$$

$$S = -6K_d r [\cos \gamma \sin (\omega + v) - \sin \gamma \cos (\omega + v) \cos i] \cos \phi$$

$$W = -6K_d r \cos \phi \sin i \sin \gamma$$

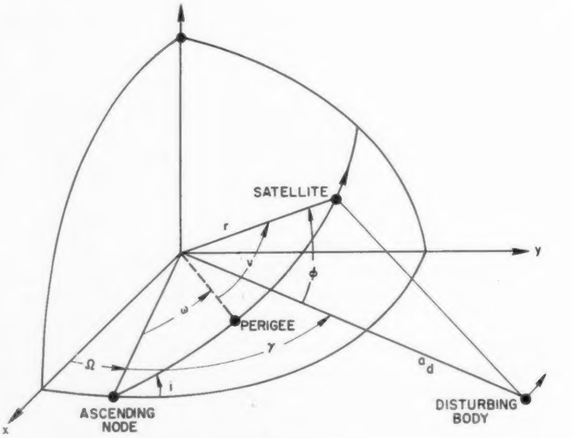

Fig. 1 Satellite orbit

EDITOR'S NOTE: The Technical Notes and Technical Comments sections of ARS JOURNAL are open to short manuscripts describing new developments or offering comments on papers previously published. Such manuscripts are usually published without editorial review within a few months of the date of receipt. Requirements as to style are the same as for regular contributions (see masthead page).

Received Dec. 11, 1959.

[1] Member of the Technical Staff.

[2] Numbers in parentheses indicate References at end of paper.

where

$K_d = GM_d/2a_d^3$
G = universal gravitational constant
M_d = the mass of the disturbing body
ϕ = angle between r and a_d
γ = angle from the line of nodes to a_d

We make an additional simplification by taking a_d constant.

Letting ϵ stand for any orbital element and $\Delta\epsilon$ for the change in that element after one revolution of the satellite (from perigee to perigee), we have

$$\Delta\epsilon = \int_{t=0}^{t=2\pi/n} \frac{d\epsilon}{dt}\, dt = \int_{v=0}^{2\pi} \frac{d\epsilon}{dt}\frac{dt}{dv}\, dv \qquad [2]$$

where t is time measured from perigee passage of the satellite. Since $\Delta\epsilon$ is supposed to be small compared to ϵ, it is permissible to approximate all variables in the expressions [1] for $d\epsilon/dt$ by the values they would have in the unperturbed orbit, and to approximate dt/dv by its relationship to the conservation of angular momentum h

$$\frac{dt}{dv} = \frac{r^2}{h}$$

where $h = na^2\sqrt{1 - e^2}$ is assumed constant. Since the angular velocity of the satellite is usually large compared to the angular velocity of the disturbing body, we may assume that γ is constant during the time the satellite takes to complete one revolution. Then integrals of the type [2] can be evaluated easily. The results are

$$\Delta a = 0 \qquad [3]$$

$$\Delta q = \frac{15K_d a\pi e\sqrt{1 - e^2}}{n^2} \times \{\sin 2\gamma \cos 2\omega \cos i - [\cos^2\gamma - \sin^2\gamma \cos^2 i] \sin 2\omega\} \qquad [4]$$

$$\Delta e = -(1/a)\Delta q \qquad [5]$$

$$\Delta i = \frac{-6K_d\pi \sin i \sin\gamma}{n^2\sqrt{1 - e^2}} \times \left\{\frac{5}{2} e^2 \sin 2\omega \sin\gamma \cos i + [1 - e^2(1 - 5\cos^2\omega)] \cos\gamma\right\} \qquad [6]$$

$$\Delta\Omega = \frac{-6K_d\pi \sin\gamma}{n^2\sqrt{1 - e^2}} \times \left\{\frac{5}{2} e^2 \sin 2\omega \cos\gamma + [1 + 4e^2 - 5e^2\cos^2\omega] \cos i \sin\gamma\right\} \qquad [7]$$

$$\Delta\omega = -\Delta\Omega \cos i - \frac{6K_d\pi\sqrt{1 - e^2}}{n^2}\left[1 - 3\sin^2\gamma\cos^2 i - \frac{5}{2}\sin 2\gamma \sin 2\omega \cos i + (1 - 5\cos^2\omega)(\cos^2\gamma - \sin^2\gamma\cos^2 i)\right] \qquad [8]$$

If, now, we let γ take values from zero to 2π, we see how the orbital elements change as a function of the time of month or year.

Error Due to Neglecting the Motion of the Disturbing Body

To estimate the error we have made by taking γ constant, let us consider the special case of co-planar motion of the satellite and the disturbing body ($i = 0$) and set $\omega = 0$. Then Equation [4] for the change in perigee per revolution becomes simply

$$\Delta q_0 = [(15K_d a\pi e\sqrt{1 - e^2})/n^2] \sin 2\gamma_0 \qquad [9]$$

where we have used the subscript zero to indicate that the disturbing body is held fixed. Now let us evaluate Δq when the disturbing body is moving, by taking $\gamma = \gamma_0 + n_d t$ where n_d is the angular velocity of the disturbing body. Equation [2] for Δq will contain integrals of the form

$$I = \int_0^{2\pi} f(\cos v, \sin v, \cos 2\gamma, \sin 2\gamma)\, dv \qquad [10]$$

where f stands for some function. We replace $\cos 2\gamma$ and $\sin 2\gamma$ by their Taylor expansions

$$\cos 2\gamma = \cos 2\gamma_0 - 2n_d t \sin 2\gamma_0 + \ldots$$

$$\sin 2\gamma = \sin 2\gamma_0 + 2n_d t \cos 2\gamma_0 + \ldots$$

and retain only the first two terms. Our integral now contains both v and t as variables of integration. These may be related to the eccentric anomaly E via the relations

$$t = (E - e\sin E)/n$$

$$\sin v = (\sqrt{1 - e^2}\sin E)/(1 - e\cos E)$$

$$\cos v = (\cos E - e)/(1 - e\cos E)$$

Equation [10] now takes the form

$$I = \int_0^{2\pi} F(\gamma_0, E, \sin E, \cos E)\, dE \qquad [11]$$

where F stands for the new function. This type of integral can be readily evaluated, and yields for Δq

$$\Delta q = \frac{15K_d a\pi e\sqrt{1 - e^2}}{n^2}\sin 2\gamma_0 \times \left\{1 + \frac{n_d}{n}\left[2\cot 2\gamma_0 + \frac{(1 - e)(4 + 45e + 58e^2 + 17e^3)}{15e(1 + e)\sqrt{1 - e^2}}\right]\right\} \qquad [12]$$

which shows that the additional term, contributed by the motion of the disturbing body, is of the order n_d/n which is usually less than 0.03.

It is also of interest to find how much the semimajor axis is perturbed, and this can be found only by considering the motion of the disturbing body. We return to the three-dimensional problem ($i \neq 0$) and find, by a procedure similar to that used to obtain Equation [12], that

$$\Delta a = (4K_d a\pi n_d/n^3)\{(4 - 6e - 5e^2)[\sin 2\omega \cos 2\gamma_0 \cos i - (1 + \cos^2 i)\sin 2\gamma_0 \cos^2\omega] + [2(1 - e^2) + (2 - 6e - 3e^2)\cos^2 i]\sin 2\gamma_0\}$$

Example

To illustrate the size of the perturbations, let us compute their effect on the perigee distance of 1959 delta (Explorer VI). Considering first the lunar perturbation and assuming that the orbital elements do not change significantly over the first few weeks of the satellite's life, we may average Equation [4] over one lunar month to obtain for the average value of Δq

$$\overline{\Delta q_m} = \frac{-15K_m a\pi e\sqrt{1 - e^2}}{2n^2}\sin 2\omega_m \sin^2 i_m \qquad [13]$$

where the subscript m indicates that the disturbing body is the moon. For 1959 delta the initial values of the orbital elements were approximately a = 15,000 nautical miles, e = 0.76, i_m = 41.5 deg and ω_m = 10.4 deg. With these values, we obtain $\bar{\Delta}q_m = -0.06$ nautical mile per revolution. Remembering that the satellite made about two revolutions a day, we see that the moon's perturbation can lead to a nonnegligible lowering of perigee.

The sun's influence, on the other hand, tends to raise perigee at first. Relative to the sun's plane (or ecliptic), the argument of perigee started at 2.7 deg, the orbital inclination was 40.3 deg, and γ_s was about 48 deg. The initial change in perigee, determined from Equation [4], is therefore $\Delta q_s = 0.26$ nautical mile per revolution. At the end of one month $\Delta q_s = 0.14$ nautical mile per revolution. Eventually the sun moves to such an angular position that Δq_s becomes negative. Then the combined solar-lunar forces produce an important lowering of perigee with the consequent reduction of lifetime. To obtain accurate results, one must evaluate Equation [4] for each revolution, taking into account the changing values of i_s, i_m, ω_s, ω_m, etc., dependent on all perturbations including those caused by Earth's oblateness and atmosphere.

Acknowledgments

The writer is indebted to Dr. Leon Blitzer for helpful discussions and suggestions for evaluating integrals and to Silvia Marcus for valuable conversations on astronomical language.

References

1 Kozai, Y., private communication.
2 Kozai, Y., "On the Effects of the Sun and Moon Upon the Motion of a Close Earth Satellite," Smithsonian Institution Astrophysical Observatory, Research in Space Science, Special Rep. no. 22.
3 Moulton, F. R., "An Introduction to Celestial Mechanics," Macmillan Co., N. Y., 1956, second ed., p. 322.
4 *Ibid.*, pp. 82–83.
5 *Ibid.*, pp. 404–405.
6 *Ibid.*, p. 340.

Jet Flows With Shocks

MILDRED M. MOE[1] and B. ANDREAS TROESCH[1]

Space Technology Laboratories, Inc., Los Angeles, Calif.

THE INVESTIGATION of supersonic jet flows from nozzles is of considerable interest in rocket technology. A knowledge of the jet flow field furnishes important information for problems of radiation, heat transfer and the attenuation of electromagnetic waves by exhaust gases.

In this note we use a method for computing the flow field (including shocks) of an axially symmetric supersonic jet expanding from a nozzle. The nozzle is assumed to be in still air (the case of ambient pressure) or to move through the surrounding air at supersonic speed. The latter case is illustrated in Fig. 1. The gas properties at the exit plane of the nozzle are assumed known. For an underexpanded nozzle, the initial slope of the jet boundary is determined by matching the shock equations in the air and the Prandtl-Meyer relations in the jet. Downstream from the exit plane the boundary turns inward, causing a compression resulting in the formation of a shock within the jet. The problem is to compute the entire flow field by the method of characteristics supplemented by the Rankine-Hugoniot relations for the shocks inside the jet flow and in the surrounding air. The present method cannot be used in regions where the flow becomes subsonic, e.g., behind the Mach disk.

Basic Equations

The computation is based on the equations governing the steady-state flow of a compressible, ideal gas. Viscous effects are neglected, and it is assumed that the changes in gas properties occur through adiabatic processes; i.e., no heat transfer takes place. Furthermore it is assumed that the air and gas obey the entropic equation of state (1).[2] It can be shown (1) that these equations represent, for supersonic flow, a system of hyperbolic partial differential equations. Therefore an integration can be carried out along the characteristic curves (or Mach lines) of the flow. For numerical integration it has proved convenient (2) to introduce as dependent variables the Mach number M, the angle θ between the streamline and symmetry axis, and the entropy S. Then the equations for the directions of the characteristic curves are

$$dr/dz = \tan(\theta - \mu) \text{ (right running characteristic)} \qquad [1]$$

$$dr/dz = \tan(\theta + \mu) \text{ (left running characteristic)} \qquad [2]$$

where

r = distance from nozzle axis
z = distance along the nozzle axis
μ = Mach angle, $\sin^{-1}(1/M)$

The corresponding characteristic relations turn out to be

$$d\theta = \mp \frac{\sqrt{M^2 - 1}}{M\{1 + [(\gamma - 1)/2]M^2\}}\, dM \pm \frac{dz}{\left(\sqrt{M^2 - 1}\cot\theta \pm 1\right)r} \mp \frac{\sqrt{M^2 - 1}}{c_p(\gamma - 1)M^2}\, dS \qquad [3]$$

where

γ = ratio of specific heats
c_p = specific heat at constant pressure

The upper sign refers to the right running characteristic and the lower sign to the left running characteristic. It should be noted that pressure and density do not appear in these formulas, but may be computed from the Mach number and entropy.

Numerical Procedure

The computation consists of several distinct parts (see Fig. 1): The determination of the flow at the nozzle edge, involving the Prandtl-Meyer expansion and the exterior shock; the determination of the points on this attached shock; the points on the interior shock; the boundary points; and all the interior points.

The computation of interior points is performed by the usual finite difference procedure (3,4), and all formulas are iterated. On the axis, instead of Equations [1 to 3], slightly modified formulas must be used (5,6).

At the boundary between jet and air, which represents a contact discontinuity, the pressures and streamline angles θ must be equal on both sides. The boundary point 7 (see Fig. 2) can be determined by satisfying these conditions along with the characteristic relations [3] for the left running characteristic through the fixed point 6 and the right running characteristic through point 5, which is interpolated between its neighbors and changes its position during the iteration process.

At the first boundary point (point 3 in Fig. 2), a slightly special treatment is necessary. We assume that the attached shock has constant strength up to point 2, where the right running characteristic extended backward from the boundary

Received Dec. 16, 1959.

---

[1] Member of the Technical Staff.

[2] Numbers in parentheses indicate References at end of paper.

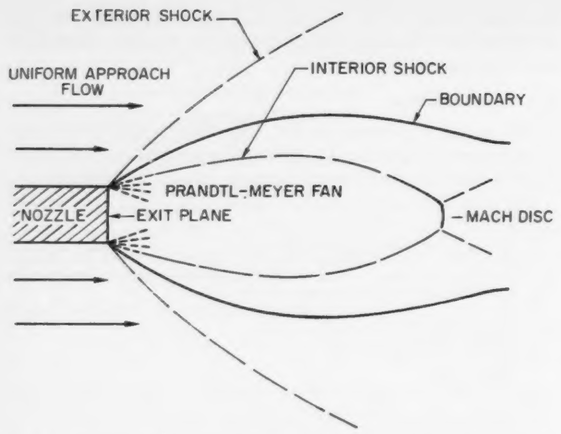

Fig. 1 Flow pattern of a supersonic jet in a supersonic stream

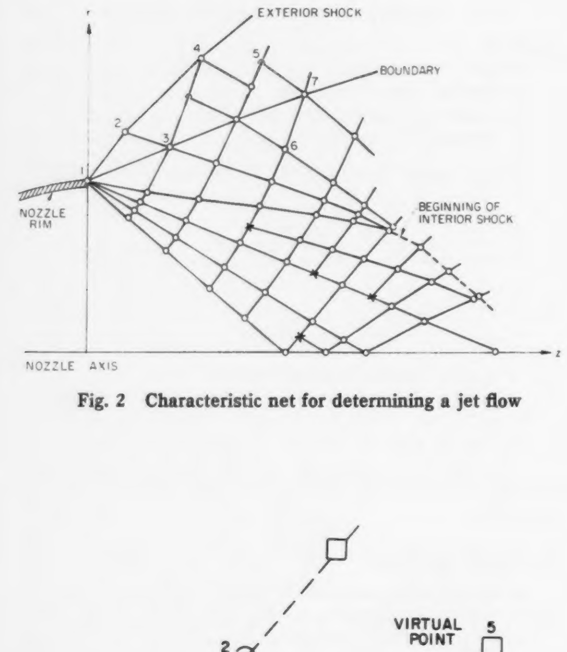

Fig. 2 Characteristic net for determining a jet flow

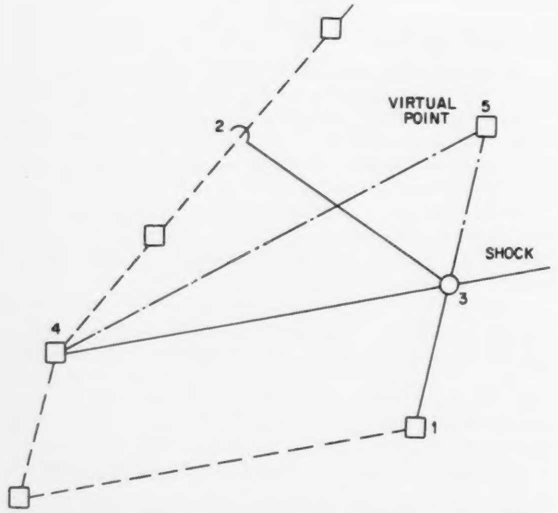

Fig. 3 Computation of a typical shock point. (Points denoted by squares have fixed positions and properties in the course of the iterations)

point 3 intersects the shock. This simple treatment is permissible because, in actual computations, the first left running characteristic is chosen especially close to the nozzle edge.

The succeeding points on the attached shock are determined by using the shock equations and Equation [3] along a left running characteristic. For example, in Fig. 2, the left running characteristic from point 3 intersects the shock at point 4 where the Rankine-Hugoniot shock conditions (1,3), relating the Mach numbers, flow angles and entropies on the two sides of the shock, are applied.

Turning next to the interior shock, we note that the computation of this shock is more involved, since the approach flow is not uniform and the starting point of the shock is more difficult to locate. The determination of the shock position and the properties on both sides is, therefore, the most complicated part of the method [(4), p. 675]. A sketch of the points involved in a typical computation is given in Fig. 3; the overall picture of the converging right running characteristics leading to the shock is shown in Fig. 2. Given the shock point 4 in Fig. 3, the next shock point 3 is determined by first computing an auxiliary or virtual point 5. This is the point determined as the interior point from 1 and 4 under the assumption that there is no shock present. It is used to obtain the upstream properties at 3 by interpolation between points 1 and 5. Although the position of point 3 and the shock angle there are not known, they may be determined by satisfying simultaneously Equation [3] along the right running characteristic from 2 to 3, along the left running characteristic from 1 to 3, and the shock equations. Additional information is given by the slope of the shock at point 4.

In a finite difference approach, the first point on the interior shock is taken as the point where two like characteristics first intersect. It can easily be shown that for shocks in jets it is sufficient to test the distance from the axis of two consecutive points on a left running characteristic and insert a shock when this distance decreases, i.e., when a foldback occurs.

The elements of the computational procedure described in the preceding paragraphs are combined into a complete program in a way easily explained by referring to Fig. 2. The flow properties given at the nozzle exit are stored on an initial line, either at the first Prandtl-Meyer characteristic for a bell-shaped nozzle, or a circular arc for a conical nozzle. The integration proceeds along a left running characteristic, from the initial line toward the boundary and exterior shock, then back to the initial line or axis for the next characteristic. When two right running characteristics intersect, the interior shock computation is started. The integration continues until eventually a normal shock (7) must be inserted, and, therefore, a subsonic region appears.

It is important that the program be able to insert new characteristic curves whenever the characteristics diverge rapidly. This situation is illustrated in Fig. 2 by the spreading of the left running characteristics originating on the axis. The insertions (designated by crosses in Fig. 2) are made whenever the test for maximum allowable mesh size is not met.

The procedure outlined here applies to the determination of a supersonic jet in a supersonic stream, but, with the appropriate simplifications, can be used for jet flows expanding to ambient pressure. The details of the numerical method are described in (8).

Results

The numerical procedure has been used to compute many jet shapes, three of which are shown in Figs. 4, 5 and 6. The first of these is an example of a jet expanding to a constant pressure boundary and the second is an example of a supersonic jet in a supersonic stream. They should be compared with Figs. 4 and 10 of (2) which show the same jets as computed by the method of characteristics without the shock conditions. Since the position and strength of the interior shocks have been determined in our computations, a greater portion of

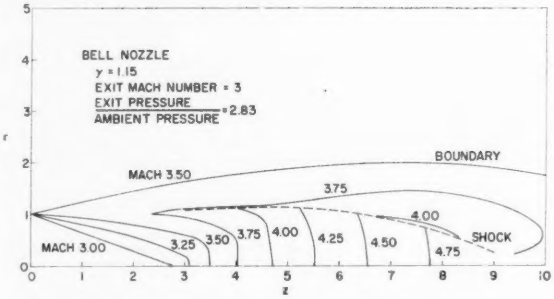

Fig. 4 Jet flow from a bell nozzle into still air

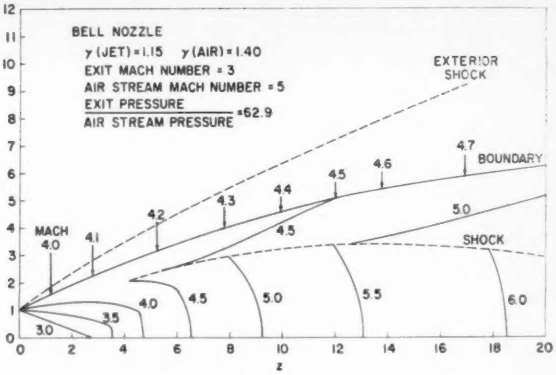

Fig. 5 Jet flow from a bell nozzle into supersonic airstream

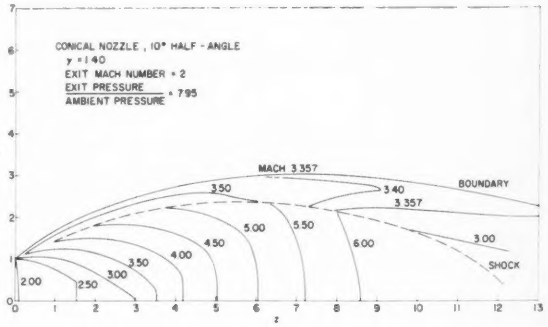

Fig. 6 Jet flow from a conical nozzle into still air

the jet flow field has been found. At first the shocks are very weak, but they become stronger as they bend toward the axis. For example, in Fig. 4 the pressure ratio across the shock increases from 1.6 at $z = 4.0$ to 4.6 at $z = 8.8$. In Fig. 5, it increases from 1.3 at $z = 5.2$ to 3.5 at $z = 19.4$. Fig. 6 is another case of a jet expanding to ambient pressure. It shows good agreement with the photograph of a jet (7) having the same exit and boundary conditions.

Acknowledgments

The authors are indebted to C. J. Wang, J. B. Peterson, H. M. Lieberstein and R. Kramer for valuable discussions. Of particular help on the treatment of the shocks were the discussions with J. M. Boyer (Convair, Astronautics, San Diego), who explained his method to us in full detail. W. A. Sassaman carried out the programming, joined in the final stage of the work by M. N. Perry and L. Stoller.

References

1 Courant, R. and Friedrichs, K. O., "Supersonic Flow and Shock Waves," Interscience Publishers, Inc., N. Y., 1948.

2 Wang, C. J. and Peterson, J. B., "Spreading of Supersonic Jets from Axially Symmetric Nozzles," Jet Propulsion, vol. 28, no. 5, May 1958, p. 321.

3 Ferri, A., "Elements of Aerodynamics of Supersonic Flows," MacMillan Co., N. Y., 1949.

4 "General Theory of High Speed Aerodynamics," W. R. Sears, Ed., Vol. VI of "High Speed Aerodynamics and Jet Propulsion," Princeton Univ. Press, 1954.

5 Schäfer, M., "Flows of Compressible Fluids, Steady Supersonic Flows," Ministry of Aircraft Production Völkenrode, Reports and Translations no. 995, p. 9, April 15, 1948. Obtainable from Central Air Documents Office, Wright-Patterson Air Force Base.

6 Ehlers, F. E., "The Method of Characteristics for Isoenergetic Supersonic Flows Adapted to High Speed Digital Computers," *J. Soc. Ind. Appl. Math.*, vol. 7, no. 1, March 1959, p. 85.

7 Adamson, T. C., Jr. and Nicholls, J. A., "On the Structure of Jets from Highly Underexpanded Nozzles into Still Air," *J. Aero/Space Sci.*, vol. 26, no. 1, 1959, p. 16.

8 Moe, M. M. and Troesch, B. A., "The Computation of Jet Flows with Shocks," Space Technology Laboratories, Inc., TR-59-0000-00661, 1959.

Specific Impulse Nomograph

WILLIAM L. SENN Jr.[1] **and RONALD V. REPETTI**[2]

U. S. Air Force, Wright-Patterson AFB, Ohio

A graphical method is presented which makes possible the rapid determination of specific impulse once the various parameters of a rocket propellant system are known.

THE EVALUATION of propellant systems often requires the calculation of specific impulse from the various system parameters. Frequently, it is of interest to examine the dependence of specific impulse upon each parameter, which necessitates the repetition of a rather laborious computation. A method of performing these calculations quickly and accurately is therefore highly desirable. A graphical method satisfying these conditions has been devised which facilitates the rapid solution of the following equation

$$I_{sp} = \frac{1}{g}\sqrt{2gR \cdot \frac{k}{k-1} \cdot \frac{T}{M} \cdot \left[1 - \left(\frac{P_2}{P_1}\right)^{(k-1)/k}\right]} \quad [1]$$

where

I_{sp} = specific impulse, sec
g = acceleration due to gravity, 32.2 fps^2
R = universal gas constant, 1544 lb-ft/lb mole-R
k = average specific heat ratio of exhaust gases, c_p/c_v
T = chamber temperature, R
M = average molecular weight of exhaust gases, lb/lb mole
P_1, P_2 = chamber pressure and exhaust pressure, respectively, consistent units

---

Received Dec. 8, 1959.

[1] Chemist. Present address, Esso Research Laboratories, Baton Rouge, La.

[2] Chemical Engineer. Member ARS.

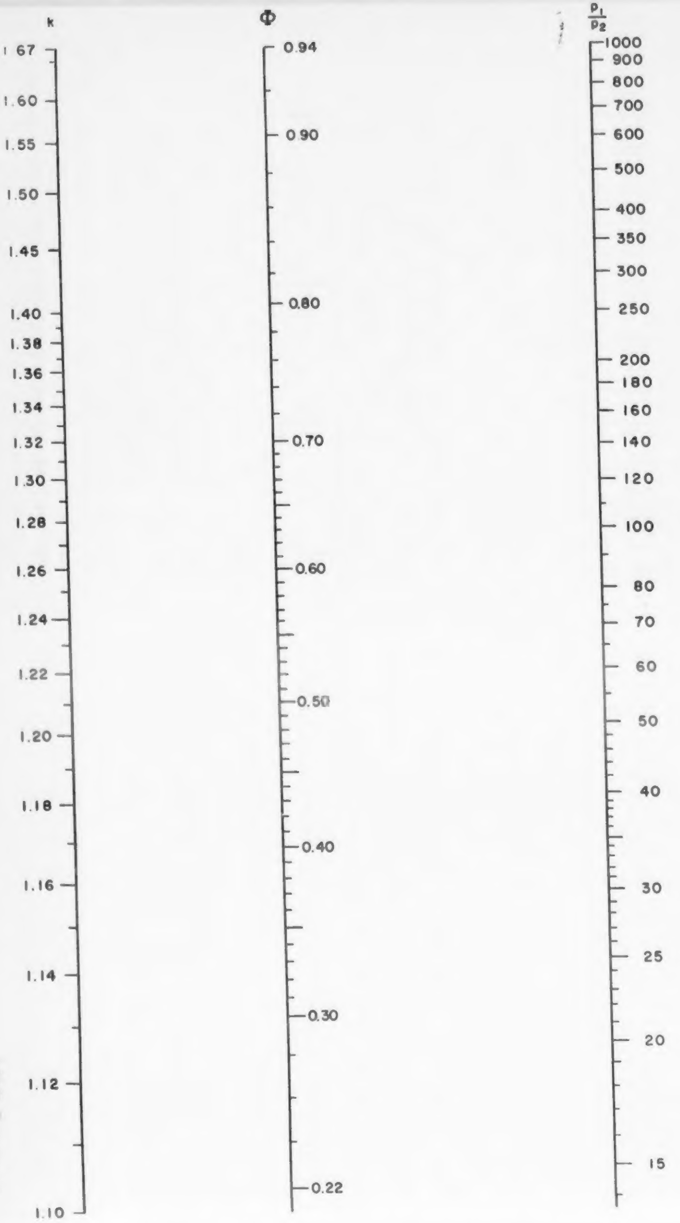

Fig. 1 Solution of $\Phi = [1 - (P_1/P_2)^{(1-k)/k}]$

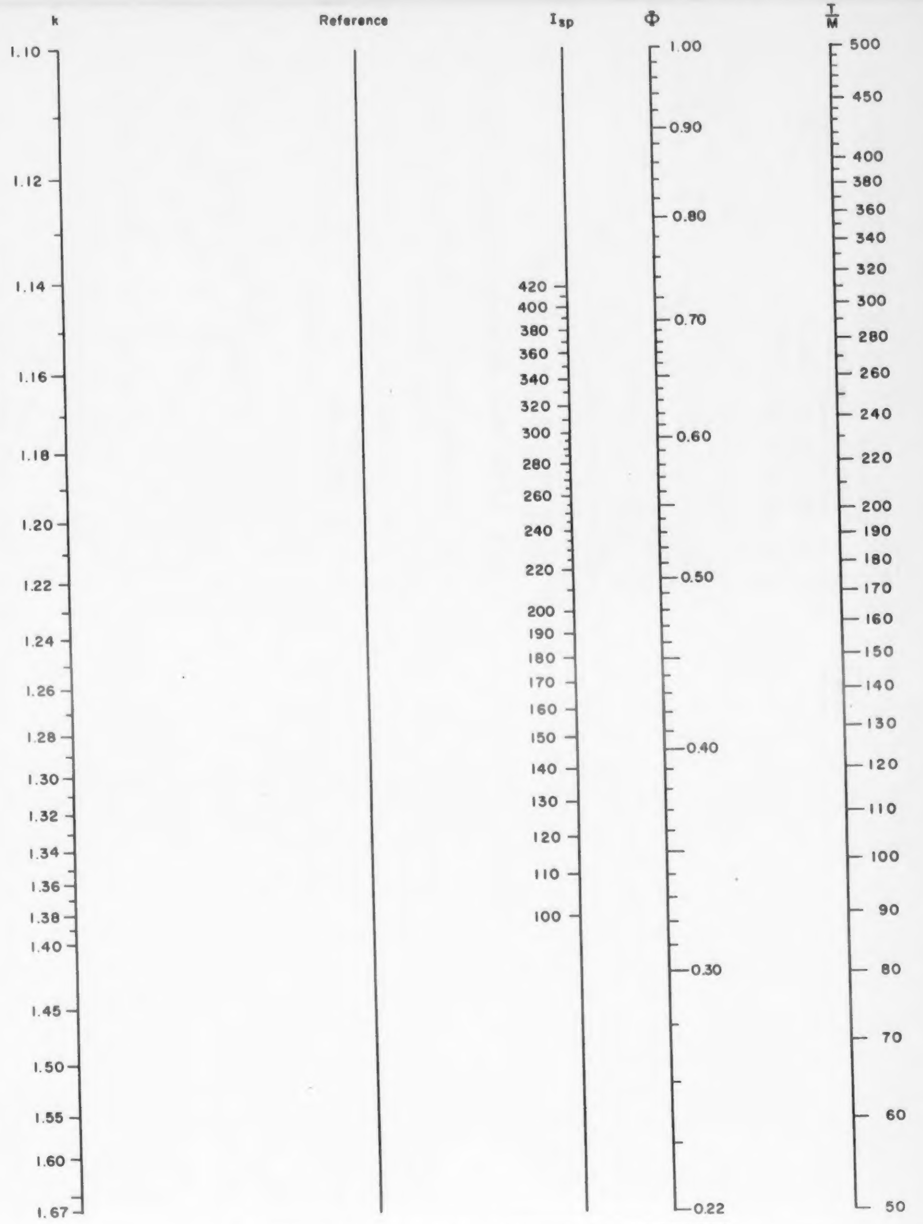

Fig. 2 Solution of $I_{sp} = (1/g)\sqrt{2gR \cdot k/(k-1) \cdot T/M} \cdot \Phi$

Fig. 2 Solution of $I_{sp} = (1/g)\sqrt{2gR \cdot k/(k-1) \cdot T/M} \cdot \Phi$

Fig. 1 Solution of $\Phi = [1 - (P_1/P_2)^{(1-k)/k}]$

Because of certain restrictions imposed by Equation [1], the method presented here involves the use of two nomographs. One graph uses the known parameters k and P_1/P_2 in order to solve the expression

$$\Phi = 1 - (P_1/P_2)^{(1-k)/k} \qquad [2]$$

The quantity Φ will be recognized as being equal to the ideal cycle efficiency of a constant pressure engine cycle operating between the pressures P_1 and P_2. Once the value of Φ has been determined, the second graph is used to compute I_{sp}, using as input data: k, Φ and T/M.

The error involved in solving Equation [1] by these nomographs is less than 1 per cent of the computed value.

The procedure for calculating I_{sp} by this method is as follows:

1 Fig. 1: Connect k with P_1/P_2; read off value of Φ.

2 Fig. 2: Connect k with Φ found above and mark intersection with reference line; connect reference line point with T/M; read off value of I_{sp}.

Initial Azimuths and Times for Ballistic Lunar Impact Trajectories

W. C. RIDDELL[1]
Convair (Astronautics Div.), San Diego, Calif.

Analytic expressions have been derived that show approximately the launch azimuths and launch times for which a ballistic missile will hit the moon. Also shown are the conditions producing the smallest angle of intersection between the missile plane and the lunar plane, and those giving an optimum launch azimuth. The formulas are applicable to missions other than lunar impact.

THE PURPOSE of this paper is to indicate the time of launch and initial azimuth for which an Earth launched missile will intersect the moon. The contact is a function of other parameters. However, they are, in turn, functions of the two specified parameters.

The formulas derived here are approximate and are necessary for the determination of refined values for operational purposes. They may be used with slight modification for the formulation of missions other than the moon intersection. For example, the missile might be asked to contact a space station, in which case the formulas will give the time of launch and azimuth for such an event to occur.

The derived formulas are the consequence of a simplified version of the complex physical structure. This system consists of the Earth-moon space and a ballistic body under the influence only of a potential field due to a spherical Earth.

Such a model may appear to be oversimplified. However, digital computer simulation in the complex environment gives results for a moon contact compatible with analytic solutions in the simple model. If, then, first approximations are desired, the simplified version of this paper is adequate.

The first part of the paper gives the pertinent usable formulas, with brief discussion. The Appendix gives the derivation of these formulas. Where multivalued functions are encountered, the proper or desired values are to be used. For definiteness, the launch site is considered to be in the northern hemisphere.

Pertinent Formulas

Roman numeral I refers to case I: $l > i_e$. Roman numeral II refers to case II: $l \leqq i_e$

$$\cos\theta = \sin\alpha \sin i_e \cos H' + \cos\alpha\,(\sin i_e \sin l \sin H' + \cos i_e \cos l) \qquad [1]$$

Minimum θ for an assigned H' or an assigned α

$$\cot\alpha = \sin l \tan H' + (\cos l \cot i_e/\cos H') \qquad [1a]$$

$$\tan H' = \cot\alpha \sin l \qquad [1b]$$

Absolute θ minimum

$$H' = 90\ \text{deg} \quad \alpha = 0\ \text{deg} \quad \theta = l - i_e \qquad \text{I} \quad [1c]$$

$$\sin H' = \frac{\tan l}{\tan i_e} \quad \cos\alpha = \frac{\cos i_e}{\cos l} \quad \theta = 0\ \text{deg} \qquad \text{II} \quad [1d]$$

$$\cos\theta = \frac{\sin i_e}{\sin\phi}(\cos H' \cos l \sin\delta - \cos A' \sin l \cos\delta) + \frac{\cos i_e}{\sin\phi}\sin A'' \cos l \cos\delta \qquad [2]$$

Minimum θ for a given target point

$$H' = 90\ \text{deg}$$

$$\cos\theta = \cos\alpha \cos(l - i_e)$$

$$\cos\alpha = \sqrt{\cos^2(l - i_e) - \cos^2\phi}/\cos(l - i_e)\sin\phi$$

$$\cos\alpha = \frac{\sin A''}{\{1 + \cos^2 A''[\cos^2 l \tan^2(i_e - l) - 2\cos l \sin l \tan i_e]\}^{1/2}} \quad \cdots\cdots \text{I} \quad [2a]$$

$$\sin H' = \tan l/\tan i_e \qquad \cos\alpha = \cos i_e/\cos l \qquad \theta = 0\ \text{deg} \qquad \text{II} \quad [2b]$$

$$\cos\alpha = \cos\delta(\sin A''/\sin\phi) \qquad [3]$$

$$\cos\phi = \cos A'' \cos l \cos\delta + \sin l \sin\delta \qquad [3a]$$

$$\sin A' = \cot i_e \tan\delta \qquad [3b]$$

$$H' = A' - A'' \qquad [3c]$$

Minimum $|\alpha|$

$$|\cos\phi| \leq \left|\frac{\sin i_e}{\sin l}\right| \qquad \sin\delta = \sin l \cos\phi \qquad \alpha = 0\ \text{deg} \qquad \text{I} \quad [3d]$$

$$\left|\frac{\sin i_e}{\sin l}\right| \leqq |\cos\phi| \leqq |\cos(l - i_e)|$$

$$\delta = -i_e$$

$$0 \geqq |\alpha| \leqq 90\ \text{deg} \quad \cdots\cdots \text{I} \quad [3e]$$

$$\sin\delta = \sin l \cos\phi \qquad \alpha = 0\ \text{deg} \qquad \text{II} \quad [3f]$$

$$|\cos A''| \leqq \left|\frac{\tan i_e}{\tan l}\right| \qquad \tan\delta = \tan l \cos A'' \qquad \alpha = 0\ \text{deg} \qquad \text{I} \quad [3g]$$

Received Nov. 23, 1959.

[1] Flight Performance and Guidance Analyst.

$$\left|\frac{\tan i_e}{\tan l}\right| \leqq |\cos A''| \leqq 1 \qquad \delta = -i_e$$

$$0 \leqq |\alpha| \leqq 90 \text{ deg}$$

$$\dots\dots\dots\dots\dots\dots\text{I} \quad [3h]$$

$$\tan\delta = \tan l \cos A'' \quad \alpha = 0 \text{ deg} \qquad \text{II} \quad [3i]$$

Discussion

Case I

The launch site never coincides with the lunar plane. The least angle of intersection is always produced by launching at a time when the launch site is closest to the lunar plane. The least possible angle is given by the conditions of I in Equation [1c]. These apply when entering a parking orbit. The direct shot conditions are given by I in Equation [2a]. The target point is defined by ϕ or A''. Either of these parameters, especially ϕ, also partially defines the missile orbit.

The conditions for nearest due east launch are given by I in Equation [3d], I in Equation [3e] or by I in Equation [3g], I in Equation [3h]. The launch azimuth and launch time are found by substituting into the general equations [3 to 3c]. The intersection angle is found by substituting into Equation [1] or [2].

Case II

The launch site passes through the lunar plane. A coplanar launch may always be made. The conditions are given by the identical sets II in Equation [1d] and II in Equation [2b]. Under the ideal condition of $l = i_e$, the launch is due east.

A due east launch may always be made under the conditions of II in Equation [3f], or II [3i]. The launch time is obtained from Equations [3a, 3b and 3c], and the intersection angle from Equation [1] or [2].

Appendix: Derivation of Formulas

The unit position vector of the launch site is, in equatorial coordinates

$$1_L = \begin{pmatrix} \cos H' \cos l \\ \sin H' \cos l \\ \sin l \end{pmatrix} \qquad [A\text{-}1]$$

The orthogonal north and east vectors are

$$1_{LN} = \begin{pmatrix} -\cos H' \sin l \\ -\sin H' \sin l \\ \cos l \end{pmatrix} \qquad [A\text{-}2]$$

$$1_{LE} = \begin{pmatrix} -\sin H' \\ \cos H' \\ 0 \end{pmatrix} \qquad [A\text{-}3]$$

From these the azimuth vector is formed

$$1_\alpha = \begin{pmatrix} -\cos H' \sin l \sin\alpha - \sin H' \cos\alpha \\ -\sin H' \sin l \sin\alpha + \cos H' \cos\alpha \\ \cos l \sin\alpha \end{pmatrix} \qquad [A\text{-}4]$$

This with Equation [A-1] determines the missile orbital plane

$$1_m = 1_L \cdot 1_\alpha = \begin{pmatrix} \sin\alpha \sin H' - \cos\alpha \sin l \cos H' \\ -(\sin\alpha \cos H' + \cos\alpha \sin l \sin H') \\ \cos\alpha \cos l \end{pmatrix} \quad [A\text{-}5]$$

The plane of the moon is defined by its normal

$$1_M = \begin{pmatrix} 0 \\ -\sin i_e \\ \cos i_e \end{pmatrix} \qquad [A\text{-}6]$$

The angle of intersection between the planes is given by

$$1_m \cdot 1_M = \cos\theta = \sin\alpha \sin i_e \cos H' +$$

$$\cos\alpha\,(\sin i_e \sin l \sin H' + \cos i_e \cos l) \quad [A\text{-}7]$$

A stationary value of this function will give a minimum value of $|\theta|$.

Setting the partial derivative with respect to α equal to zero results in

$$\cot\alpha = \sin l \tan H' + (\cot i_e \cos l/\cos H') \qquad [A\text{-}8]$$

This gives the optimum α for an assigned H'.

In like manner we obtain

$$\tan H' = \sin l \cot\alpha \qquad [A\text{-}9]$$

Solving Equations [A-8 and A-9] simultaneously gives, for the absolute minimum

$$\cos\alpha = \cos i_e/\cos l \qquad \sin H' = \tan l/\tan i_e \qquad [A\text{-}10]$$

If $l > i_e$, these solutions are imaginary. But a geometric consideration verifies that then the optimum remains the same as for $l = i_e$. That is

$$\alpha = 0 \qquad H' = 90 \text{ deg} \qquad [A\text{-}11]$$

The unit position vector of the target is

$$1_T = \begin{pmatrix} \cos A' \cos\delta \\ \sin A' \cos\delta \\ \sin\delta \end{pmatrix} \qquad [A\text{-}12]$$

This with Equation [A-1] gives the missile orbital plane in terms of launch position and target position

$$1_m = \frac{1_L \cdot 1_T}{\sin\phi} =$$

$$\frac{1}{\sin\phi}\begin{pmatrix} \sin H' \cos l \sin\delta - \sin A' \sin l \cos\delta \\ \cos A' \sin l \cos\delta - \cos H' \cos l \sin\delta \\ \sin A'' \cos l \cos\delta \end{pmatrix} \qquad [A\text{-}13]$$

If this is to be identical with Equation [A-5], then it is identical component by component. Equating the z components gives a relationship between the launch azimuth and the target point

$$\cos\alpha = (\sin A''/\sin\phi)\cos\delta \qquad [A\text{-}14]$$

A'' and ϕ are related through δ, as is found by taking

$$1_L \cdot 1_T = \cos\phi = \cos A'' \cos l \cos\delta + \sin l \sin\delta \qquad [A\text{-}15]$$

so that [A-14] may be rewritten

$$\cos\alpha = \sqrt{\cos^2 l \cos^2\delta - (\cos\phi - \sin l \sin\delta)^2}/\sin\phi \cos l \qquad [A\text{-}16]$$

or

$$\cos\alpha = \cos\delta \sin A''/\sqrt{1 - (\cos A'' \cos l \cos\delta + \sin l \sin\delta)^2} \qquad [A\text{-}17]$$

The target position is defined by δ. Its connection with A' is, from spherical trigonometry

$$\sin A' = \cot i_e \tan\delta \qquad [A\text{-}18]$$

It is logical to inquire as to what target position, for a given ϕ or A'', gives a minimum $|\alpha|$. This is found by setting the partial derivation of Equation [A-16] or [A-17], with respect to δ, equal to zero. The conditions are, respectively

$$\sin\delta = \sin l \cos\phi \qquad [A\text{-}19]$$

$$\tan\delta = \tan l \cos A'' \qquad [A\text{-}20]$$

In case $l > i_e$, there are obvious restrictions on the values of $\cos\phi$ and $\cos A''$ for which the equations can be fulfilled. When the equations cannot be applied exactly, the value of δ coming nearest to giving equality is to be used. This will be for ϕ and A'' close to 180 deg and is $\delta = -i_e$.

The intersection angle in terms of target position is obtained from Equations [A-6 and A-13]

$$1_m \cdot 1_M = \cos\theta = \frac{\sin i_e}{\sin\phi}(\cos H' \cos l \sin\delta - \cos A' \sin l \cos\delta) + \frac{\cos i_e}{\sin\phi} \sin A'' \cos l \cos\delta \qquad [A\text{-}21]$$

This equation is difficult to use in minimizing θ, since H', A', A'', ϕ and δ are all interdependent. A simple form that can be analyzed by inspection is obtained by using lunar-Earth system coordinates. These are defined in the Nomenclature. In this system

$$1_L = \begin{pmatrix} \cos u' \cos\lambda \\ \sin u' \cos\lambda \\ \sin\lambda \end{pmatrix} \qquad [A\text{-}22]$$

$$1_T = \begin{pmatrix} \cos u \\ \sin u \\ 0 \end{pmatrix} \qquad [A\text{-}23]$$

$$1_M = \begin{pmatrix} 0 \\ 0 \\ 1 \end{pmatrix} \qquad [A\text{-}24]$$

$$1_m = 1_L \cdot 1_T = \frac{1}{\sin\phi} \begin{pmatrix} -\sin u \sin\lambda \\ \cos u \sin\lambda \\ \sin u'' \cos\lambda \end{pmatrix} \qquad [A\text{-}25]$$

$$1_L \cdot 1_T = \cos\phi = \cos u'' \cos\lambda \qquad [A\text{-}26]$$

$$1_m \cdot 1_M = \cos\theta = \sin u'' \cos\lambda / \sin\phi \qquad [A\text{-}27]$$

$$\cos\theta = \sqrt{\cos^2\lambda - \cos^2\phi}/\sin\phi \qquad [A\text{-}28]$$

By inspection it is evident that the smallest $|\theta|$ is given by the smallest $|\lambda|$. Sin ϕ cannot equal zero unless $\cos^2\lambda = 1$, in which case $\cos^2\theta = 1$.

The restriction is imposed of

$$\cos^2\phi \leqq \cos^2\lambda \qquad [A\text{-}29]$$

If Equation [A-1] is rotated into the lunar-Earth system, we have

$$1_L = \begin{pmatrix} \cos H' \cos l \\ \sin H' \cos l \cos i_e + \sin l \sin i_e \\ -\sin H' \cos l \sin i_e + \sin l \cos i_e \end{pmatrix} \qquad [A\text{-}30]$$

Comparison with Equation [A-22] shows that

$$\sin\lambda = -\sin H' \cos l \sin i_e + \sin l \cos i_e \qquad [A\text{-}31]$$

Thus λ varies from $l - i_e$ to $l + i_e$ as $\sin H'$ varies from 1 to -1. It is the $H' = 90$ deg, $\lambda = l - i_e$ condition that is of interest when $l > i_e$, and the $\lambda = 0$, $\sin H' = \tan l \cot i_e$ condition otherwise.

Nomenclature

A = right ascension of the target
H = sidereal hour angle of the launch site
A' = $A - \Omega_e$, right ascension of the target, measured from the ascending lunar equatorial node
H' = $H - \Omega_e$
A'' = $A' - H' = A - H$, arc of the Equator intercepted by the meridian planes of the launch site and target point. It is also the negative of the hour angle of the target from the launch site
i_e = inclination of date of the lunar plane to the equatorial plane
l = latitude of the launch site
L = launch site
M = moon or referring to moon
m = missile
T = target, the point on the moon's orbit intersected by the missile plane
u = angular position or the target measured in the lunar plane from Ω_e
u' = launch site coordinate measured as above
u'' = $u - u'$
α = launch azimuth, relative to a nonrotating Earth, measured from due east, positive to north
δ = declination of the target
ϕ = angle between the launch site position vector and the target position vector
λ = launch site angular elevation from the lunar plane
θ = angle of intersection between the plane of the missile and the plane of the moon
Ω_e = ascending equatorial node of the moon

Evaluation of Preflight Risks by Means of Very High Speed Digital System Simulation

JESSE R. BRINKERHOFF[1]

Boeing Airplane Co., Seattle, Wash.

This paper gives a brief description of the mathematical and programming techniques employed in using a comprehensive digital computer simulation of a complex system to provide, in a short time, accurate data on the chance of successful operation of the system in a specific test. A mathematical model of the system is obtained by writing equations and logical relations specifying the behavior of each part of the system as a function of the states of the other parts and parameters determined by external factors. These equations are then programmed on a computer and after setting parameter values and starting conditions, the equations are solved and the solution is checked against an applicable criterion to determine whether performance is satisfactory. In practice, this procedure may become extremely complicated, and it is often abandoned in favor of other methods which analyze the various parts of the system separately or which make broad simplifying assumptions and generalizations to enable simple analytical treatment of the system.

THE SUBJECT of this paper is work done at the Boeing Airplane Co. in designing a simulation tool and using it for predicting the results of some individual test flights of the BOMARC interceptor.

Performance of the BOMARC system is strongly dependent on the setting of guidance and control parameters, and final optimization of many of these parameter values was not complete for much of the flight testing schedule. Performance is also dependent on the conditions of the test, many of which could not be controlled in a tactical situation, but are subject to control in a flight test. Further uncertainties arose in early flight tests when performance of some parts of the system was temporarily restricted. Under these conditions, a

---

Presented at the ARS Flight Testing Conference, Daytona Beach, Fla., March 23–25, 1959.

[1] Systems Performance Unit, Weapon System Staff.

method of accurately predicting the chance of success for a particular test was desired for use in making decisions on parameter settings and test conditions. This tool was especially needed since tests were contemplated with conditions which were near or beyond the nominally expected performance limits of the system.

For this purpose, and for use in parameter optimization studies and analysis of overall system performance in the composite tactical situation, a digital computer simulation, the BUG (BOMARC Univac AN/GPA-35), was designed. It was programmed in machine language for the Remington Rand Univac Scientific 1103-A computer, and AN/GPA-35 is the type designation of the weapon control equipment utilized in the flight test program. The simulation had to satisfy two basic requirements: The system representation had to be complete and detailed enough so that results obtained would be accurate and dependable; it had to be fast enough to allow generation of statistically significant quantities of data on short notice.

The following paragraphs enumerate some of the major difficulties which were met in attempting to satisfy both requirements, the techniques which were utilized, the manner in which this simulation was used, and the type of results which were obtained.

Development of the Model

The BOMARC system can be roughly separated into three parts:

1 Search radar and tracking.
2 Guidance calculation and ground control.
3 The missile, including homing guidance.

The characteristics of each of these parts can be described, to a close approximation, by elementary mathematical equations. However, the equations for one part depend on those of the other parts, and in many cases this interdependence is not simple. For example, there are some roughly periodic occurrences in each of the parts, e.g., rotation of the search radar, transmission of successive command signals and searching operation of the missile's homing guidance device. The phase relationships between these quasi-periodic functions may be quite important, and the only information available about them is that they are probably random at some starting point of time and are determined thereafter by the relations between the quasi-periods of these occurrences. In the development of the model, these phase relationships are so represented. Two more random items appear in the search radar and tracking simulation. The fact that each time the radar beam passes the target a return may or may not be obtained is taken into account in the model by requiring the specification of the nominal blip-to-scan ratio as an external parameter and making a random test each time to determine whether a return is obtained. In the same way, parameters are required for the standard deviation of radar noise, and a random noise error is ascribed to each return accordingly.

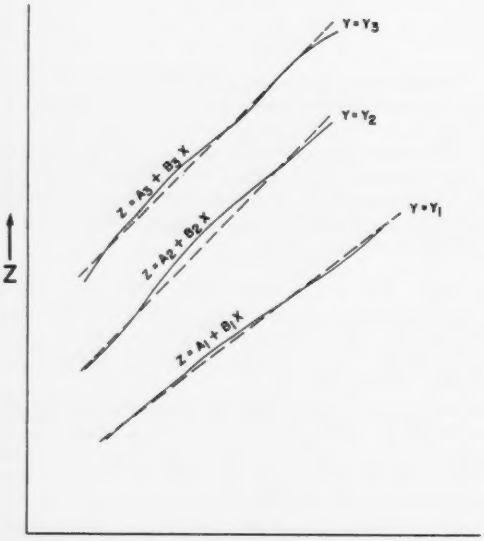

Fig. 1 Curve fits of Z against first variable, X

Representation of the random processes in this manner poses the requirement that a statistically significant sample of runs is needed for a single set of input conditions in order to determine the probability of successful performance. However, the estimate attained in this manner should accurately represent the actual probability.

With the exception of the random sampling problems noted, the development of the model for the search radar and tracking, and guidance calculation and ground control, sections of the system presented no major problems. With the missile model, however, two major problems appeared.

The equations of this section were mainly the differential equations needed to specify the missile path as a function of time and of the operation of the airborne guidance and control system. These had to be integrated numerically. For the greatest accuracy, a complex iterative integration scheme would be suggested, with a small mesh size. However, because of the computer speed needed, the iterative integration scheme could be used only with a large mesh size, and it was decided to use a very simple integration scheme (Euler's method) with a fairly small mesh size. This provided an integration error smaller than the random errors in the system, and the greater accuracy which would be provided by a more complex integration method was not necessary. The small mesh size also proved advantageous in successfully representing the relatively fine grained effects near the end of the intercept while the missile is under homing guidance.

Another problem in developing the missile model was the fact that some quantities, for example, the thrust of the ramjet engines, were given in graphical form and could be represented mathematically only as arbitrary functions of several variables. One possible method of representing these functions in the computer would be to enter tables, and program a table read routine rather than a function evaluation routine. However, the tables needed would be too large for the high speed computer storage, and in order to achieve the computing speed required, the program had to operate almost exclusively from the high speed magnetic core storage.

To alleviate this difficulty, a curve fitting process was developed to provide simple polynomial approximations to these arbitrary data. Intuitively, the process appears somewhat unsound, and examples can be made up where it fails completely, but in experience with actual data it seems that the process is remarkably versatile. It should be stated that the author's experience with this process has been mainly with functions of only two variables. Although the extension of the method to functions of more than two variables is simple, it is not clear that the accuracy obtained would be satisfactory. An explanation of the procedure will be given here for a function Z of two variables X and Y.

Suppose the function Z is given on a graph of the form shown in Fig. 1. The first step in obtaining a polynomial approximation to the function is to find a first-degree (as shown) or second-degree (if more accuracy is needed) curve fit for each curve where Y equals constant. These curve fits are shown as dashed lines in Fig. 1, and have the equations shown there in terms of A_i and B_i, the curve fit coefficients.

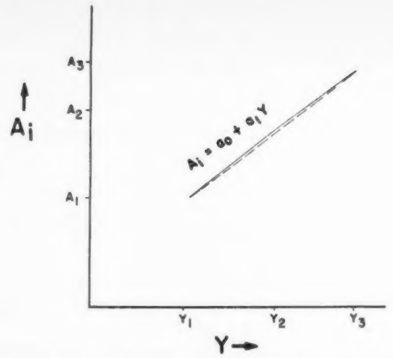

Fig. 2 Curve fits of zero-degree coefficients against second variable, Y

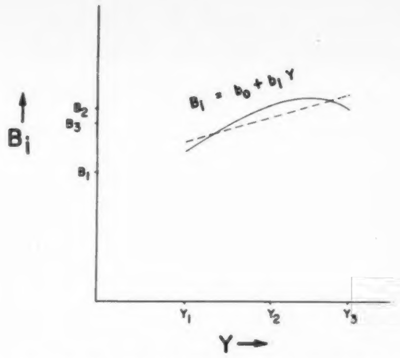

Fig. 3 Curve fits of first-degree coefficients against second variable, Y

This curve fitting can be done by least squares or any other method.

The next step is to plot the zero-degree curve fit coefficients A_i against the variable Y, as shown in Fig. 2. As before, a first- or second-degree curve fit is obtained for this curve, shown as the dashed line in Fig. 2, and its equation is given in terms of a_i, the curve fit coefficients.

In the same manner, the first-degree coefficients B_i are plotted against the variable Y, as shown in Fig. 3, and the curve fit coefficients b_i are obtained. The polynomial approximation for Z is now completely specified, as

$$Z = \overbrace{(a_0 + a_1Y)}^{A_i} + \overbrace{(b_0 + b_1Y)}^{B_i}x$$

In this explanatory example, first-degree curve fits were used throughout, but in the simulation problems both first- and second-degree fits were used. They can be intermixed at each stage of the process, and higher degree curve fits can be used if desired. If the process does not work too well, it may be improved by inverting the order of curve fitting, fitting first against the variable Y and then against X. In particularly bad cases the data may be broken into two or more classes, according to the value of one or both variables.

As an example of the applicability of this method, the actual data shown in Fig. 4 were successfully represented in three sections with only first- and second-degree fits.

Even with these simplifications, the missile model takes a large proportion of the machine time, but the simulation is fast enough to enable a complete interception to be simulated in about 30 seconds. In contrast, the only BOMARC simulation available previously, programmed by Boeing on the IBM 701, required about 30 min for the same job.

The missile model developed for the BUG simulation has been used in essentially the same form for all the comprehensive digital simulations of the BOMARC IM-99A system which have been written to date. Useful data were obtained from the BUG simulation as early as June 1957.

Use of Simulation for Preflight Risk Analysis

To find the probability of success for specific test, the target paths, guidance and control parameters, and noise and blip-to-scan ratio parameters are inserted into the simulation. Then a number of runs are made, with only the random quantities varying from run to run. The number of runs needed is difficult to determine, and it varies with conditions. For example, if the target is performing a periodic maneuver, the phase of the maneuver is an additional random variable, and more runs are needed. It has been determined from experience that 20 or 30 runs will give a good estimate for a nonmaneuvering target.

After all the runs are obtained, the probability of success is just the ratio of the number of successful runs to the total number.

Much additional data are provided by the simulation. Data are given from which correlation can be estimated between system performance and many variables of the system which can be controlled by adjusting parameters.

Conclusions

By using the technique described, it was possible to obtain a very high speed digital simulation as a tool for accurately evaluating the chance of success or failure of a flight test under particular conditions on short notice. This procedure was very useful in providing information for preflight decisions on test conditions and parameter settings.

Acknowledgments

The work described here was done by the group currently known as the Systems Performance Unit of the Weapon System Staff, Pilotless Aircraft Division of the Boeing Airplane Co., supervised at that time by W. J. Nemerever.

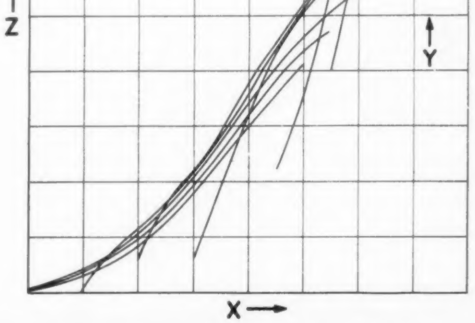

Fig. 4 Sample of data successfully fitted

Prediction of Peak Temperature for Satellite Entries With Lift

R. H. EDWARDS[1] and G. S. CAMPBELL[2]

Hughes Aircraft Co., Culver City, Calif.

A LARGE share of the present understanding of lifting re-entry technique is based on numerical calculation. In order to avoid the necessity of repeating such computations with every change of parameters, it seems desirable to have a simple but accurate method of trajectory prediction. The approximations obtained might also be useful for developing, at a later time, lift programs to minimize equilibrium surface temperatures.

The method used in the present note is essentially an extension of the skip trajectory analysis of (1).[3] The formulas obtained give surface temperature, altitude and velocity at the bottom of the first skip for satellite entry at constant lift. Results of the approximate method are compared with IBM calculations from a design study reported in (2).

Analysis

The problem is to obtain, for given initial conditions at the edge of the atmosphere, an accurate estimate of the peak temperature during the first skip of a lifting satellite entry. Lift and drag coefficients are constant, and the flight path angle is assumed small.

First approximation

As a first approximation, velocity is constant and weight is balanced by centrifugal force, as in (1)

$$-V\dot{\gamma} = (C_L S/m)q \qquad [1]$$

The usual relations between density, altitude and flight path angle are assumed

$$\rho = \bar{\rho}_0 e^{-\beta y} \qquad [2]$$

$$\dot{y} = -V\gamma \qquad [3]$$

For constant velocity, the solution of these equations is

$$\gamma = -\lambda_0 \tanh T$$

$$y - y_0 = \frac{2}{\beta} \log \frac{\cosh T}{\cosh T_0}$$

where

$$T = \lambda_0 \frac{\beta V_0}{2} t - \tanh^{-1} \frac{\gamma_0}{\lambda_0}$$

$$\lambda_0^2 = \gamma_0^2 + \frac{\rho_0 C_L S}{\beta m}$$

Quantities with subscript zero denote initial values at $t=0$. After linearizing the relation for λ_0, these equations are simplified

$$\gamma = -\gamma_0 \tanh T \qquad [4]$$

$$y - y_0 = \frac{2}{\beta} \log \frac{\cosh T}{\cosh T_0} \qquad [5]$$

$$\frac{\rho}{\rho_0} = \frac{q}{q_0} = \frac{1}{2\epsilon} \operatorname{sech}^2 T \qquad [6]$$

$$2T = \gamma_0 \beta V_0 t + \log (\epsilon/2) \qquad [7]$$

$$\epsilon = \rho_0 C_L S / 2\beta m \gamma_0^2 \qquad [8]$$

The next approximation to the first skip trajectory requires an estimate of the velocity variation, which is obtained from the drag equation

$$\dot{V} = g\gamma - (C_D S/m)q \qquad [9]$$

This equation may be integrated by substituting Equations [4 and 6] to give

$$w = (V - V_0)/V_0 \qquad [10]$$

$$w = -\gamma_0 \frac{C_D}{C_L} (1 + \tanh T) - \frac{g(y - y_0)}{V_0^2} \qquad [11]$$

The first term on the right is the drag contribution to slowdown and is the only term in the skip analysis of (1). The remaining term represents the component of gravity in the drag direction.

Second approximation

The necessity for a higher approximation may be shown from the relation for equilibrium surface temperature given in (3)

$$T_W = K\rho^{1/8} V^{3/4} \qquad [12]$$

The peak temperature is achieved at the bottom of the skip at altitude $(y_{1_m} + h_m)$, where y_{1_m} is the first approximation to minimum altitude and h_m is a small correction. Peak density is therefore

$$\rho_m = (\beta m \gamma_0^2 / C_L S)(1 - \beta h_m)$$

from Equation [6] with $T = 0$. This relation, along with Equation [10], gives the approximate maximum equilibrium temperature

$$T_W = K \left(\frac{\beta m}{C_L S}\right)^{1/8} \gamma_0^{1/4} V_0^{3/4} \left[1 - \frac{1}{8} \beta h_m + \frac{3}{4} w_m\right] \qquad [13]$$

The constant K can be readily evaluated from (3), for example.

For representative satellite entry conditions, the secondary terms in Equation [13] provide temperature reductions up to 200 F. The necessary corrections are the first-order velocity term (Eq. [11] with $T = 0$) and the second approximation to the minimum altitude. Development of the relation for βh_m follows.

The complete lift equation, for small flight path inclinations, is

$$-V\dot{\gamma} = \frac{C_L S}{m} q + \left(\frac{V^2}{r} - g\right) \qquad [14]$$

The integral of this equation is, for the exponential atmosphere

$$\gamma^2 = \gamma_0^2 - \frac{C_L S \bar{\rho}_0}{\beta m} (e^{-\beta y} - e^{-\beta y_0}) + 2 \int_{y_0}^{y} \left(\frac{1}{r} - \frac{g}{V^2}\right) dy \qquad [15]$$

In the first approximation, denoted by subscript 1, the last term was neglected. The relation for the altitude correction h_m is obtained by putting $\gamma = 0$ in Equation [15], subtracting the first approximation, and assuming βh_m small

$$\frac{\gamma_0^2}{2} \beta h_m = -\int_{y_0}^{y_m} \left(\frac{1}{r} - \frac{g}{V^2}\right) dy \qquad [16]$$

Entry altitudes are a small fraction of Earth's radius, and so the gravity and radius variations may be linearized. For entry at velocities close to surface circular satellite velocity $\sqrt{g_e r_e}$ let

$$u = (V_0 - \sqrt{g_e r_e})/V_0 \qquad [17]$$

Received Dec. 8, 1959.

[1] Member of the Technical Staff.

[2] Member of the Technical Staff. Member ARS.

[3] Numbers in parentheses indicate References at end of paper.

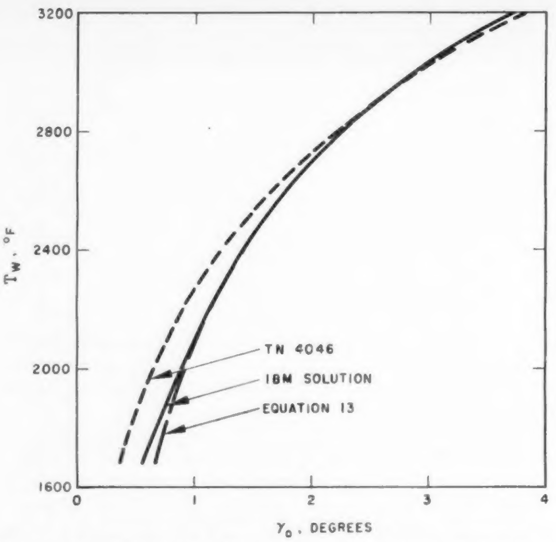

Fig. 1 Maximum stagnation surface temperature during first skip of a lifting entry from 60 nautical miles.
$C_L = 0.54, C_D = 0.52, W/S = 15$ lb/ft²

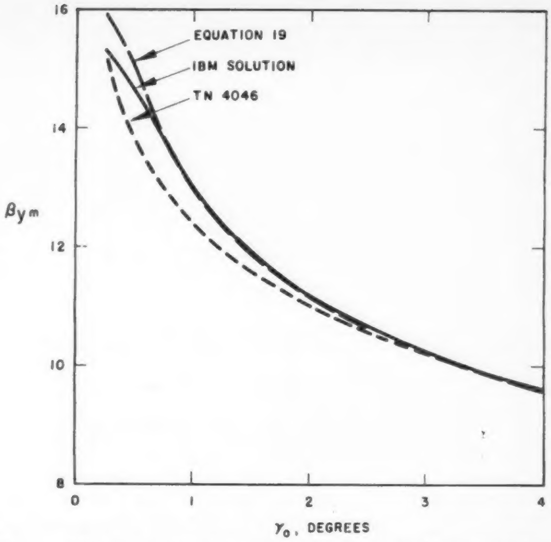

Fig. 2 Minimum altitude reached during first skip of a lifting entry from 60 nautical miles.
$C_L = 0.54, C_D = 0.52, W/S = 15$ lb/ft²

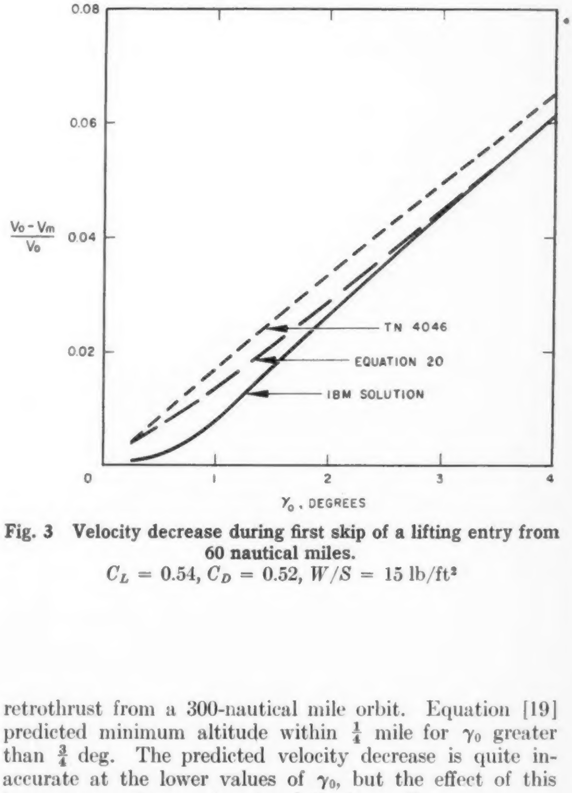

Fig. 3 Velocity decrease during first skip of a lifting entry from 60 nautical miles.
$C_L = 0.54, C_D = 0.52, W/S = 15$ lb/ft²

The integrand of Equation [16] finally becomes

$$\frac{1}{r} - \frac{g}{V^2} = \frac{1}{r_e}\left[\frac{y}{r_e} + 2u + 2w\right]$$

Comparison with exact numerical results has shown that the integration of Equation [16] may be carried out by replacing y and y_m by their first approximations. The resulting expression for the altitude correction is

$$\beta h_m = \frac{-2}{\gamma_0\, \beta r_e}\left[2\,\frac{C_D}{C_L}\left(2 + \log\frac{\epsilon}{2}\right) + \frac{1}{\gamma_0}\left(\frac{y_0}{r_e} - 2\,\frac{C_D}{C_L}\,\gamma_0 + 2u\right)\log 2\epsilon\right] \qquad [18]$$

The difference between y_0/r_e and $(y_{1m} + y_0)/2r_e$ was neglected in obtaining Equation [18]. The altitude at the bottom of the skip is the sum of y_{1m} and h_m, so that

$$\beta y_m = \beta y_0 + \log 2\epsilon + \beta h_m \qquad [19]$$

The velocity decrease to the bottom of the skip is

$$w_m = -\frac{\gamma_0 C_D}{C_L} - \frac{g_e}{\beta V_0^2}\log 2\epsilon \qquad [20]$$

Maximum stagnation temperature is calculated from Equation [13] with the proper values of h_m and w_m.

Results

The formulas from the preceding section have been used to compute peak temperatures during lifting satellite entries for a range of initial flight path angles. The results of the calculations are compared in Fig. 1 with IBM solutions obtained during the design study of (2). For entry angles above 1 deg, Equation [13] predicts peak temperature within 10 F of the IBM solutions. An earlier method for peak skip temperature prediction (1) is subject to 180 F inaccuracy, and so a marked improvement is shown.

The minimum altitude for the first skip is shown in Fig. 2, and velocity decrease is given in Fig. 3. Initial flight velocity V_0 varied from 26,155 to 25,717 fps over the 0 to 4 deg range of γ_0 because the initial conditions were established by single retrothrust from a 300-nautical mile orbit. Equation [19] predicted minimum altitude within $\frac{1}{4}$ mile for γ_0 greater than $\frac{3}{4}$ deg. The predicted velocity decrease is quite inaccurate at the lower values of γ_0, but the effect of this inaccuracy on temperature is relatively small.

One of the primary uses for the approximate skip trajectory equations is to estimate the effects of small parameter changes on temperature, dynamic pressure, etc. For example, differentiation of Equation [13] gives the effect of initial over-velocity on peak temperature

$$\frac{\partial T_W}{\partial V_0} = \frac{T_W}{V_0}\left(\frac{\log 2\epsilon}{\beta r_e\, \gamma_0^2} + \frac{3}{4}\right) \qquad [21]$$

This formula confirms the numerical results of (2): That velocities *greater* than local satellite velocity *can* cause decreased stagnation temperatures. This effect is caused by increased centrifugal force with higher velocity. However, it is seen from Equation [21] that for entry angles greater than 3 or 4 deg, depending on initial weight to lift ratio, stagnation temperature is *increased* by initial overvelocities.

References

1 Eggers, A. J., Jr., Allen, H. J. and Neice, S. E., "A Comparative Analysis of the Performance of Long-Range Hypervelocity Vehicles," NACA Technical Note 4046, Oct. 1957.

2 Stalony-Dobrzanski, J., "Effect of Re-Entry Technique on the Design of a Space Vehicle," American Astronautical Society Preprint no. 59-17. Aug. 1959.

3 Chapman, D. R., "An Approximate Analytical Method for Studying Entry Into Planetary Atmospheres," NACA Technical Note 4276, May 1958.

Polymerization of Solid Propellants[1]

W. H. GROETZINGER III[2]

Rohm and Haas Co., Huntsville, Ala.

NEGLECTING internal heat transfer by convection, the problem of coupled heat transfer and polymerization during curing in simple, one-dimensional, solid propellant grains with constant thermal properties can be stated as

$$\frac{\partial T(s,t)}{\partial t} = G\frac{\alpha}{s}\frac{\partial T(s,t)}{\partial s} + \alpha\frac{\partial^2 T(s,t)}{\partial s^2} + \frac{Q}{c}f(T,P)$$

$$a < s < b,\ t > 0$$

$$\frac{\partial P(s,t)}{\partial t} = f(T,P) \qquad a \le s \le b,\ t \ge 0$$

with appropriate initial and boundary conditions, where

G = geometric factor (0, 1 and 2 for slabs, cylinders and spheres, respectively)
T = temperature
P = polymer fraction (fraction of monomer converted to polymer)
t = time
s = distance from reference (centerline for cylinders, center for spheres and arbitrary for slabs)
a = distance from reference to inside propellant surface (inside radius for hollow cylinders and hollow spheres, zero for solid cylinders and solid spheres, arbitrary for slabs)
b = distance from reference to outside propellant surface (outside radius for cylinders and spheres and arbitrary for slabs)
α = propellant thermal diffusivity
c = propellant specific heat
f = propellant rate of polymerization function
Q = total heat of polymerization per unit mass of propellant

This problem has been studied previously by investigators at Aerojet-General Corp. (1)[3] and Jet Propulsion Laboratory (3)[4] for solid cylindrical geometries. The Aerojet investigators solved the problem numerically on a card calculator using explicit finite difference equations, whereas the JPL investigators solved the problem numerically on a differential analyzer using difference-differential equations. The interest of these investigators was apparently temperature oriented. Results were reported principally in terms of centerline temperature.

This problem was studied recently at Rohm and Haas Co. (7); the solution was achieved numerically on an electronic digital computer using explicit finite difference methods. Attention was given to polymer fraction as well as to temperature. The nature of the polymer fraction distribution is discussed in this note.

As an illustration, consider the typical problem of a hollow circular cylinder with an inside radius of 7 in. and an outside radius of 18 in. (11-in. web, 0.85 loading fraction) initially filled with an unpolymerized propellant ($P = 0$) at 150 F, having a thermal diffusivity of $6(10^{-3})$ ft^2/hr. The ratio of heat of polymerization to specific heat Q/c is taken to be 50 F, and the polymerization is assumed to progress at the rate

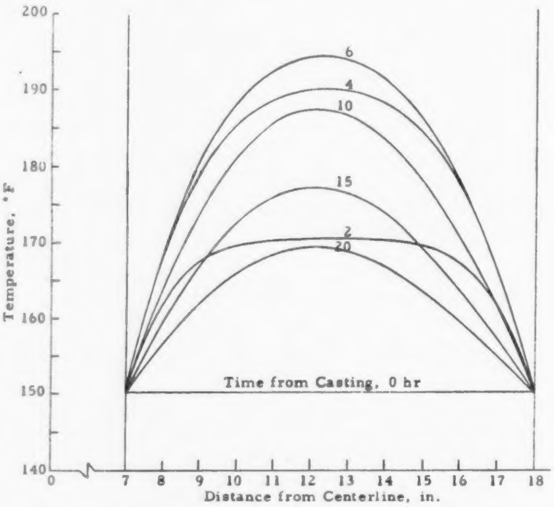

Fig. 1 Radial temperature distribution. Standard case

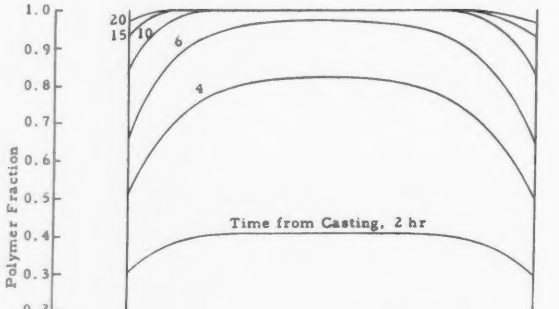

Fig. 2 Radial polymer fraction distribution. Standard case

Received Dec. 23, 1959.

[1] This work was sponsored by the Army Ordnance Corps under Contract no. DA-01-021-ORD5135.

[2] Head, Engineering Research Group, Redstone Arsenal Research Div.

[3] Numbers in parentheses indicate References at end of paper.

[4] This is the principal Jet Propulsion Laboratory report. The work has been reported elsewhere with modifications and extensions (2,4,5,6).

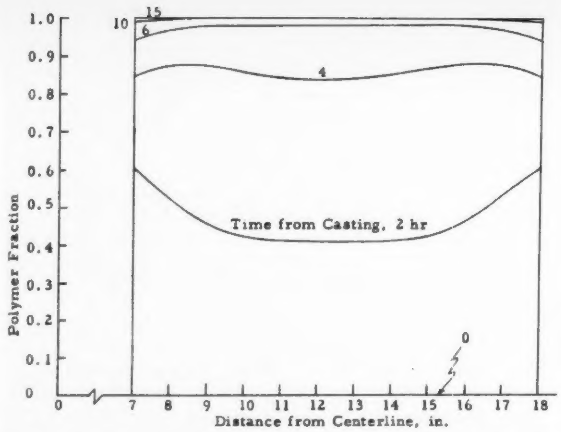

Fig. 3 Radial polymer fraction distribution. Hotter surfaces

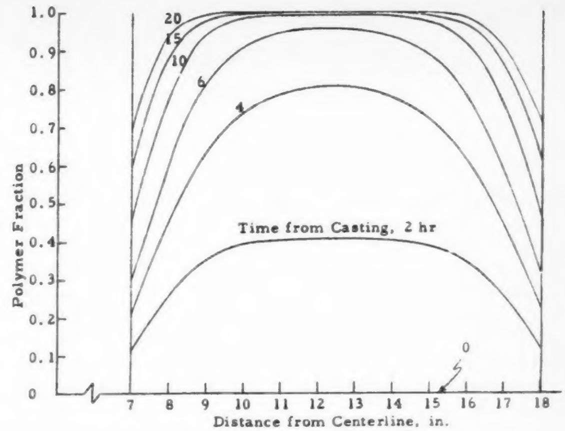

Fig. 4 Radial polymer fraction distribution. Colder surfaces

$f(T, P) = B(1 - P) \exp(-A/RT)$, where the frequency factor B is 10^{10}/hr and the activation energy A is $3(10^4)$ Btu/lb mole. The boundaries are assumed to be held constant at 150 F.

The solution to this problem is shown in Figs. 1 and 2 which give the resulting temperature and polymer fraction distributions, respectively.

Taking this problem as a standard, the effect on the polymer fraction distribution of changes in wall temperature, ratio of heat of polymerization to specific heat, and temperature sensitivity of the polymerization rate can be examined. Fig. 3 shows the effect of increasing the wall temperature 25 F, Fig. 4 the effect of a similar decrease. Fig. 5 shows the effect of increasing the ratio of the heat of polymerization to specific heat by 25 F. Fig. 6 shows the effect of increasing the temperature sensitivity of the polymerization rate [achieved by increasing the activation energy from $3(10^4)$ to $4(10^4)$ Btu/lb mole while simultaneously increasing the frequency factor from 10^{10} to $3.85\ (10^{13})$/hr to keep the polymerization time approximately the same].

The effect of temperature and polymer fraction distribution during curing on the quality of the finished grain is of importance to the propellant producer. The effect of temperature gradients as well as the effects of thermal contraction and polymerization shrinkage on the stress-strain distribution in the grain-case combination under the assumptions of uniform polymer fraction distribution and of elastic response upon the initiation of polymerization has been studied previously (8,9). However the effect of nonuniform polymer fraction distributions, such as those illustrated here, on the stress-strain distribution both during curing and after the completion of curing presents an aspect not previously investigated. Also, the nonuniform polymer fraction distributions presumably affect the strength properties of the polymerized propellant in critical areas, such as at the case bond and at the highly stressed inside propellant surface.

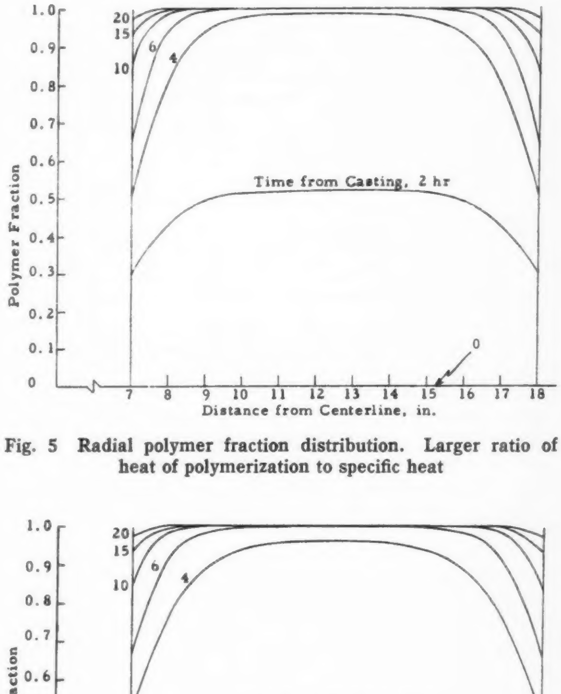

Fig. 5 Radial polymer fraction distribution. Larger ratio of heat of polymerization to specific heat

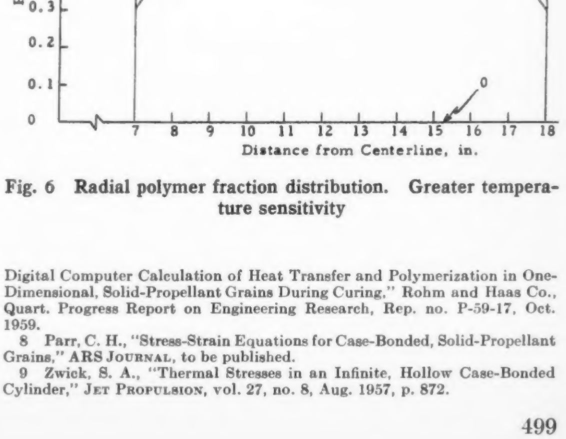

Fig. 6 Radial polymer fraction distribution. Greater temperature sensitivity

References

1 Kirchner, W. R., Lawrence, R. W. and Hepner, F. R., "Aeroplex Propellent Evaluation and Curing Studies," Aerojet-General Corp., Rep. no. 498 (Final Summary), March 1951.

2 Nichols, P. L., Jr. and Presson, A. G., "The Problem of Heat Release in Solid Propellant Curing," Bull. 8th Meeting JANAF Solid Propellant Group, vol. I, 1952, p. 391. (*Confidential.*)

3 Nichols, P. L., Jr. and Presson, A. G., "Heat-Transfer Calculations Related to Solid-Propellant Curing," Jet Propulsion Laboratory, Rep. no. 20–68, Sept. 1953.

4 Nichols, P. L., Jr. and Presson, A. G., "Heat Conduction in an Infinite Cylindrical Medium with Heat Generated by a Chemical Reaction," *J. Appl. Phys.*, vol. 25, no. 12, Dec. 1954, p. 1469.

5 Nichols, P. L., Jr., "Control of Chemical and Physical Factors in the Application of Casting Resins," *Soc. Plastics Eng. J.*, vol. 12, no. 11, Nov. 1956, p. 26.

6 Nichols, P. L., Jr. and Schieler, L., "Heat Transfer in a Solid Medium Heated by Chemical Reaction," Jet Propulsion Laboratory, External Publication no. 458, March 1958.

7 Groetzinger, W. H., III, "On a Generalized Program for the Electronic Digital Computer Calculation of Heat Transfer and Polymerization in One-Dimensional, Solid-Propellant Grains During Curing," Rohm and Haas Co., Quart. Progress Report on Engineering Research, Rep. no. P-59-17, Oct. 1959.

8 Parr, C. H., "Stress-Strain Equations for Case-Bonded, Solid-Propellant Grains," ARS JOURNAL, to be published.

9 Zwick, S. A., "Thermal Stresses in an Infinite, Hollow Case-Bonded Cylinder," JET PROPULSION, vol. 27, no. 8, Aug. 1957, p. 872.

Real-Time Analysis, New Approach in Flight Testing

GUENTHER HINTZE[1]

White Sands Missile Range, N. Mex.

The possibility of increasing the information contents of flight records through controlled exercise of missiles during firing tests is discussed. The discussion is based on a brief description of an experiment which is presently being planned at White Sands Missile Range for the accurate determination of aerodynamic coefficients under controlled and trimmed flight conditions. The best solutions for the analysis equations will be obtained when the exciting fin deflection and the corresponding angle of attack are approximately 90 deg out of phase. This leads to the requirement to exercise the missile with a frequency close to its natural frequency. The basic relations of natural frequency and damping ratio as functions of missile velocity and altitude are derived, and typical trends of natural frequency with altitude for different Mach numbers, as obtained from flight simulation studies, are presented. Firing tests can be made into experiments yielding more information concerning the in-flight component and missile behavior when through the real-time analysis of flight data exercises of the missile can be introduced which are adapted to the momentary flight condition.

As THE first practical problem in connection with the development of real-time flight analysis and control at White Sands Missile Range, the measurement and determination of certain aerodynamic coefficients have been chosen. The aerodynamic problem requires a minimum of change to the existing flight test program. The quality of present telemetered data appears to be adequate for the proposed problem. The only special instrumentation required is an angle of attack meter and a triple linear potentiometer for sensing the fin position. Both of these have been used in Engineer-User (E-U) flights.

Presently, so-called aerodynamic rounds are flown to determine aerodynamic coefficients by flight tests whereby the missile is made to respond to pre-programmed commands with the guidance system kept inactive. However, this method does not exercise a closer control of the missile, keeping certain variables such as bank angle and undesired motion in several planes to a minimum. Real-time connection with the flight will control the missile into aerodynamic conditions which enhance the measurement of specific aerodynamic coefficients by determining the type of maneuvers the missile must perform to obtain the most useful data and by momentarily minimizing the effect of other interfering parameters. For the planned experiment a two-dimensional problem was chosen to simplify initial setup procedures and problem solution.

Analysis Equations

The experiment shall find a solution with respect to Mach number of the normal force coefficient

$$C_N = C_{N_\alpha}\alpha + C_{N\delta}\delta \qquad [1]$$

where

α = angle of attack
δ = fin deflection

For simplicity the analysis is being restricted to the computation of the aerodynamic coefficients from the linearized normal force equation

$$C_{N_\alpha}\alpha + C_{N\delta}\delta = \frac{m(a - l\dot{Q})}{qS} \equiv N \qquad [2]$$

where

m = mass of the missile
a = normal acceleration determined by an accelerometer
l = distance from the missile c.g. to the accelerometer
$\dot{Q}$ = pitch angular acceleration
q = dynamic pressure
S = reference area

In Equation [2] all quantities except $C_{N\alpha}$ and $C_{N\delta}$ can be observed directly or deduced from observed data. Thus, two sets of data observed at judicious times, t_1 and t_2, close enough to assume that Mach number has remained unchanged, will yield corresponding values of $C_{N\alpha}$ and $C_{N\delta}$ by solving the equations

$$\begin{aligned} C_{N_\alpha}\alpha_1 + C_{N\delta}\delta_1 &= N_1 \\ C_{N_\alpha}\alpha_2 + C_{N\delta}\delta_2 &= N_2 \end{aligned} \qquad \ldots\ldots [3]$$

The solution for the unknowns $C_{N\alpha}$ and $C_{N\delta}$ is found by Cramer's rule

$$C_{N\alpha} = \frac{\begin{vmatrix} N_1\delta_1 \\ N_2\delta_2 \end{vmatrix}}{\Delta} \qquad C_{N\delta} = \frac{\begin{vmatrix} \alpha_1 N_1 \\ \alpha_1 N_2 \end{vmatrix}}{\Delta} \qquad \Delta = \begin{vmatrix} \alpha_1\delta_1 \\ \alpha_2\delta_2 \end{vmatrix} \qquad [4]$$

From Equations [4] it can be seen that good solutions for the two unknowns $C_{N\alpha}$ and $C_{N\delta}$ are obtained when the values for α and δ have markedly changed between the observations at times t_1 and t_2, and when, in addition, α and δ are offset by a distinct phase shift. Otherwise the determinant Δ may tend toward zero, resulting in singularity or near singularity of the matrix. On the other hand, it has been stated that the observations at t_1 and t_2 must be close enough to justify the assumption of a constant Mach number.

The element of possible control in the experiment offers the opportunity for achieving data sets which will satisfy the above conditions. Real-time analysis of flight data provides the basis for a controlled exercise of the missile as compared with missiles which go into larger exercises only when some malfunctions occur.

Derivation of Excitation Commands

The excitation could be done either by step inputs or by a sinusoidal input for the commands on the fin deflection δ. Sinusoidal excitation has been chosen for several reasons. A step command introduces transients in the missile response which probably do not settle out in $\frac{1}{2}$ sec for the missile under investigation, making very questionable the filtering process by which the values of the variables are averaged over the period for which the step command is being held. Sinusoidal signals can be more easily and accurately smoothed to remove their noise content. In addition, the computation for transient response is more involved than the corresponding computation of the response of a linear system to steady-state sinusoidal excitation. With a sinusoidal input for δ and assuming a linear system, the quantities α, a and $\dot{Q}$ will also vary sinusoidally with the information of interest contained in their respective amplitudes and phases.

In order to keep the controlled excitation as simple as possible in this experiment, the missile will be exercised in climb only with the command

$$G_c = G_0 + G_1 \sin \omega_n t \qquad [5]$$

where

G_0 = $+0.5g$ is a fixed command to keep the missile on a long high trajectory
G_1 = amplitude
ω_n = frequency of the sinusoidal excitation

Additional safeguards will be provided in the real-time analysis experiment with the live missile, in case the planned exercise has to be changed back to normal missile control (1).[2]

Presented at the ARS Flight Testing Conference, March 23–25, 1959, Daytona Beach, Fla.

[1] Chief, Flight Simulation Laboratory.

[2] Numbers in parentheses indicate References at end of paper.

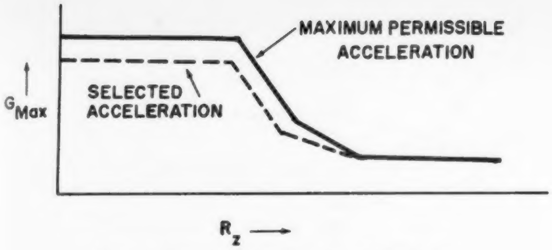

Fig. 1 Acceleration G_{max} vs. altitude R_z

For best resolution of the measured data the amplitude of the excitation should be maintained during the flight at the maximum permissible level. For the test vehicle with which the experiment is being planned, the lateral acceleration is not allowed to go beyond a fixed number of G's, determined by the altitude according to a curve acceleration G_{max} vs. altitude R_z as shown in Fig. 1.

With the exception of the rightmost segment, the computer is programmed to select the total climb command G_c according to the dotted line. This allows a small amount of reserve in the command value so that the missile is not strained to its limits. The difference between solid and dotted line varies from zero to about $\frac{1}{2}\,g$. From the total command G_c, determined in this way, the constant upward command G_0 which compensates for gravity has to be subtracted in order to obtain the size of the sinusoidal exercising acceleration command $G_1 \sin \omega_n t$.

The next step is the determination of the excitation frequency ω_n. It has been stated that good solutions for Equations [4] are obtained when the fin deflection δ and the angle of attack α are clearly out of phase, the most desirable situation being a phase shift of 90 deg between δ and α. For a second- order linear system, which can be assumed with sufficient accuracy for the tested missile, oscillations with the natural frequency ω_n will cause δ and α to be 90 deg out of phase, with the sharpness of resonance determined by the damping ratio ζ of the oscillating body. A universal chart which is applicable to any system with persistent oscillation, illustrating these conditions (2), is shown in Fig. 2.

Natural Frequency and Damping Ratio of Missile

The natural frequency and damping ratio of a missile are determined by the moment equations describing the oscillatory motion of the missile around its center of gravity. With the missile motion restricted to a vertical plane and considering the oscillation around the pitch axis only, the respective moment equation is as follows

$$Ip\ddot{\theta} \cong qSc\left(c_{m_\alpha}\cdot\alpha + c_{m_{c\dot{\theta}/2V}}\cdot\frac{c\dot{\theta}}{2V}\right) \qquad [6]$$

where, in addition to the previously defined quantities

θ = missile body attitude in pitch
Ip = moment of inertia around pitch axis
c = reference length
c_{m_α} = aerodynamic moment coefficient with respect to α
$c_{m_{c\dot{\theta}/2V}}$ = aerodynamic moment coefficient with respect to $c\dot{\theta}/2V$
V = total missile velocity relative to air

Taking the Laplace transform and assuming for the momentarily considered oscillation a constant velocity V and initial conditions to be zero, Equation [6] can be written

$$s^2\theta(s) = \frac{qSc}{Ip}\left[c_{m_\alpha}\cdot L(\alpha) + c_{m_{c\dot{\theta}/2V}}\cdot\frac{cs\theta(s)}{2V}\right] \qquad [7]$$

In order to obtain an oscillatory equation in θ only, the term $L(\alpha)$ has to be replaced by an expression in θ. This expression can be derived from the normal force equation

$$qSc_{N_\alpha}\cdot\alpha = m(\dot{w} - u\dot{\theta}) \qquad [8]$$

where no fin deflection is assumed, and

$\dot{w}$ = lateral acceleration in vertical plane
u = longitudinal velocity component $\approx V$

For small angles the angle of attack α can be expressed by the ratio$(-w/V)$; with this and collecting the terms with w, Equation [8] is rearranged

$$\dot{w} + \frac{qS}{mV}\,c_{N_\alpha}\cdot w = V\dot{\theta} \qquad [9]$$

Taking the Laplace transform

$$[s + (qS/mV)\,c_{N_\alpha}]\,w(s) = Vs\theta(s) \qquad [10]$$

or

$$L(\alpha) \approx L\left(\frac{w}{V}\right) \approx \frac{s\theta(s)}{s + (qS/mV)\,c_{N_\alpha}} \qquad [11]$$

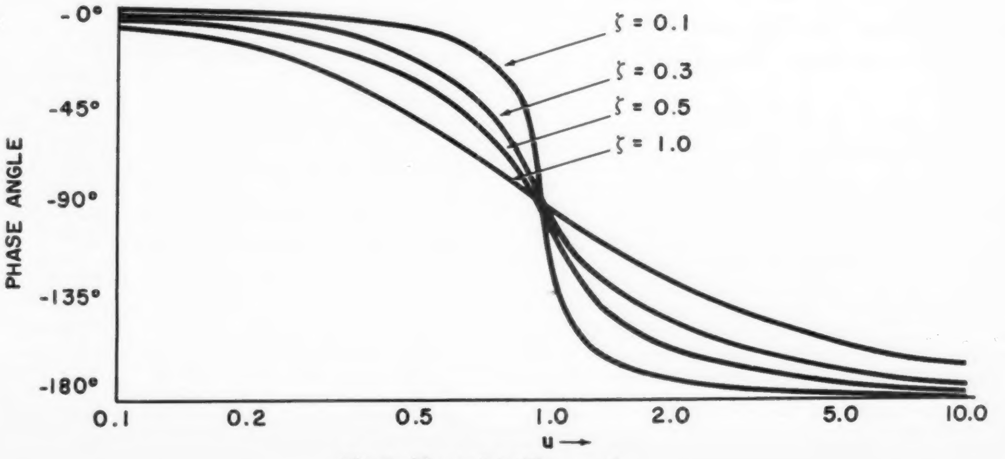

Fig. 2 Phase plot with $u = \omega/\omega_n$

Substituting this in Equation [7] gives

$$s^2\theta(s) = \frac{qSc}{Ip}\left[\frac{c_{m\alpha}\cdot s\theta(s)}{s + (qS/mV)c_{N\alpha}} + c_{m_{c\dot{\theta}/2V}}\cdot\frac{cs\theta(s)}{2V}\right] \qquad [12]$$

Now letting

$$-\frac{qSc}{Ip}c_{m_\alpha} = \bar{a} \qquad \frac{qS}{mV}c_{N\alpha} = \bar{b} \qquad -\frac{qSc^2}{2IpV}c_{m_{c\dot{\theta}/2V}} = \bar{c} \qquad [13]$$

the oscillatory equation for θ is obtained as follows

$$s^2\theta + (\bar{b} + \bar{c})s\theta + (\bar{a} + \bar{b}\bar{c})\theta = 0 \qquad [14]$$

with the natural frequency

$$\omega_n = \sqrt{\bar{a} + \bar{b}\bar{c}} = \sqrt{\frac{qSc}{Ip}c_{m_\alpha} + \left(\frac{qS}{mV}c_{N\alpha}\right)\left(\frac{qSc^2}{2IpV}c_{m_{c\dot{\theta}/2V}}\right)} \qquad [15]$$

and the damping ratio

$$\zeta = \frac{\bar{b} + \bar{c}}{2\omega_n} \qquad [16]$$

From Equations [15 and 16] it can be seen that ω_n and ζ are mainly functions of the dynamic pressure q and missile velocity V; that means, since $q = \frac{1}{2}\rho V^2$, the natural frequency and the damping ratio of the missile vary with velocity and air density as a function of altitude. Typical trends of the variation of the natural frequency ω_n with altitude as obtained from a series of flight simulation studies are shown in Fig. 3.

The curves can be expressed as powers of e. For easier computer solution the e-functions can be approximated by a power series for which only the first two terms have to be considered when the curve is divided in small enough segments along the altitude scale. For each interval correction factors are predetermined and stored together with the known center values of altitude, Mach number and frequency for the interval. With these data, prepared in advance, it is easy to compute in real-time the natural frequency corresponding to the actual altitude and Mach number (3).

Utilization of Real-Time Data

The preceeding discussion brings out several points for the need of flight data analyzed in real-time. In order to obtain flight records with a high information content, missiles have to be exercised in flight. This excitation has to be done according to the momentary flight condition when it shall render a maximum of useful information without upsetting the flight.

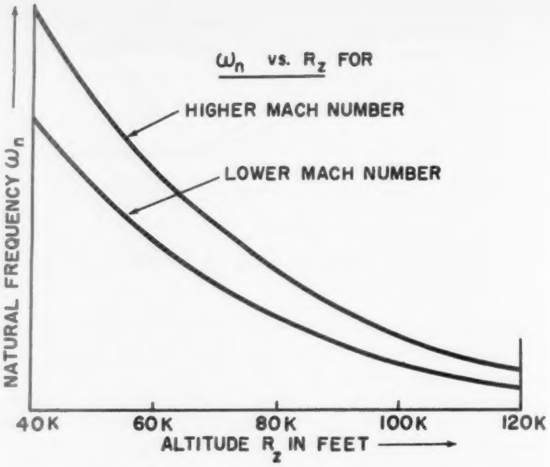

Fig. 3 Natural frequency ω_n vs. altitude R_z

Since missiles have a relative low damping ratio the phase shift around the natural frequency will be very steep, as shown in Fig. 2. Therefore, in order to obtain close to 90 deg phase shift between excitation and response it is necessary to excite the missile with a frequency very near to the natural frequency. According to Fig. 3 the natural frequency changes considerably with altitude, and a satisfactory phase shift cannot be obtained for all altitude and Mach number conditions using a single excitation frequency.

Flight data, analyzed and displayed in real-time, will not only provide an immediate knowledge of the events and the behavior of the missile in flight, but they will also furnish automatically the proper inputs to adaptive excitation programmers when such programs are being executed.

References

1 McCool, W. A., "Simplified N-H Missile Control for RT-I," Flight Simulation memo no. 53, White Sands Missile Range, N. Mex., Sept. 21, 1959.

2 Nixon, F. E., "Principles of Automatic Controls," Prentice-Hall Elec. Engrg. Series, N. Y., 1953.

3 Dalton, O. N., "General Description of the Real-Time Experiment with the HADC Computer Facility," Real-Time Project Data Rep. no. 4, Flight Simulation Laboratory, White Sands Missile Range, N. Mex., Jan. 1960.

Ballistic Effect of Pyrolyzed Liner in Solid Propellant Motor Firings

L. J. GORDON[1]

Aerojet-General Corp., Sacramento, Calif.

Any combustion chamber liner material lost during burning of a solid propellant motor contributes to the momentum of the exhaust even though it adds no energy to the stream. A relationship yielding the true propellant specific impulse from the measured thrust-time integral, the propellant weight and the weight of liner lost in a static test firing is derived. A relationship between vehicle burnout velocity and these parameters is also given.

Static Test Firings

IN MANY cases the weight loss upon test firing of solid propellant motors is found to be greater than the weight of the propellant alone; the additional loss is due to pyrolysis or erosion of liner. It is necessary, however, to determine the specific impulse of the propellant from the experimental data even though some liner is lost. This discussion will show that the specific impulse of the propellant itself may be nearly correctly calculated from the experimentally obtained thrust-time integral and the weight loss by

$$I_{s_0} = \int FdT/[W_p(W_p + W_L)]^{1/2} \qquad [1]$$

where

W_L = weight of liner lost upon firing
W_p = propellant weight

This result is first derived for a mathematically simplified case, and then a discussion of possibly more accurate methods of data reduction are discussed.

Received Dec. 18, 1959.

[1] Senior Engineer, Thermodynamics Section, Solid Propellant R&D Laboratory. Member ARS.

Assume for the simple case that:

1 The liner is pyrolyzed at a uniform rate throughout the firing;

2 the specific heat and molecular weight of the propellant combustion products are equal to those of the liner decomposition products and are constant;

3 there is no pressure drop during the pyrolysis and complete mixing of gases.

A heat and material balance then yields

$$W_pC_p(T_1 - T_2) = W_Lq + W_LC_p(T_2 - T_L) \qquad [2]$$

where

C_p = specific heat of combustion products
q = heat required for pyrolysis of unit weight of liner
T_1 = combustion temperature of propellant
T_L = initial temperature of liner
T_2 = resultant temperature upon mixing of propellant and liner decomposition products

Solving for T_2 yields

$$T_2 = \frac{W_pT_1 + W_LT_L - (W_Lq/C_p)}{W_p + W_L} \qquad [3]$$

And since there has been no change in pressure, molecular weight, or in C_p

$$\frac{I_s}{I_{s_0}} = \left(\frac{T_2}{T_1}\right)^{1/2} = \left[\frac{W_p + W_L(T_L/T_1) - (W_Lq/C_pT_1)}{W_p + W_L}\right]^{1/2} \qquad [4]$$

where

I_{s_0} = specific impulse of propellant
I_s = specific impulse of mixed gases as expanded through nozzle

This expression can be simplified by two approximations:

1 Since $W_L < W_p$ and $T_L < T_1$, then $W_L(T_L/T_1) \ll W_p$ so that $W_p(T_L/T_1)$ can be neglected.

2 If the heat of pyrolysis and interaction can be ignored

$$\frac{I_s}{I_{s_0}} = \left(\frac{W_p}{W_p + W_L}\right)^{1/2} \qquad [5]$$

Experimentally one finds

$$\int FdT = (W_p + W_L)I_s \qquad [6]$$

and solving Equations [5 and 6] for the desired I_{s0} yields Equation [1]. For small values of W_L/W_p, Equation [1] may be written

$$I_{s0} = \int FdT/[W_p + (W_L/2)] \qquad [7]$$

Equation [1] may also be derived from simple energy-momentum considerations by realizing that addition of mass to the exhaust stream increases the momentum of the stream, although the total kinetic energy remains constant. By neglecting any heat of pyrolysis or interaction, a kinetic energy balance yields

$$\frac{W_pV_1^2}{2g} = (W_p + W_L)\,\frac{V_2^2}{2g} \qquad [8]$$

where

V_1 = velocity that the propellant combustion products would have at the nozzle exhaust plane if no liner were pyrolyzed
V_2 = velocity the mixed products would have if the liner decomposition products obtained their velocity at the energy expense of the propellant gases

One may then solve for I_{s0} as follows (using the same nomenclature as in Equations [1 to 7])

$$\frac{V_1}{V_2} = \left(\frac{W_p + W_L}{W_p}\right)^{1/2} \qquad [9]$$

$$I_s = \int FdT/(W_p + W_L) \qquad [10]$$

$$I_{s0} = \frac{V_1}{V_2}\,I_s = \left(\frac{W_p + W_L}{W_p}\right)^{1/2} \times \frac{\int FdT}{(W_p + W_L)} = \frac{\int FdT}{[W_p(W_p + W_L)]^{1/2}} \qquad [11]$$

and Equation [11] is recognized to be identical to Equation [1].

It may be shown that this result is independent of the time period during which the liner is pyrolyzed. Assume, as a simple example, that the liner is pyrolyzed uniformly during the second half of the burning only, and that the propellant burns uniformly throughout. Applying Equation [1] to the second period and the normal thrust relationship to the first period

$$\int_0^T FdT = \int_0^{T/2} FdT + \int_{T/2}^T FdT = \left(\frac{W_p}{2}\right)I_{s0} + \left(\frac{W_p}{2} + \frac{W_L}{2}\right)I_{s0} = \left(W_p + \frac{W_L}{2}\right)I_{s0} \qquad [12]$$

and this result is identical to that in Equation [8]. It is then obvious that whatever the pyrolysis-time relationship, it can be broken into such periods.

The only reasonable way to include the heat of pyrolysis when estimating the effect of pyrolyzed liner on a measured thrust is to assume that the decomposition products of the liner, which is of the same material as the propellant binder, come to equilibrium with the propellant combustion products. The gases that flow out the nozzle may then be considered to be identical to the combustion products of a composite propellant having a greater binder proportion than the base propellant. The heats of pyrolysis and interaction are therefore included in the specific impulse calculated for this composite propellant. In order to obtain the specific impulse of the base propellant from the thrust time integral obtained for the composite propellant, one must know the relative theoretical specific impulse and the combustion efficiencies of the base and composite propellants. For similar propellants, one generally expects combustion efficiencies for a given motor to be independent of propellant composition so that

$$\frac{I_{s0}}{I_s} = \frac{I_{s0}'}{I_s'} \qquad [13]$$

where the primed numbers are theoretical values, and the unprimed numbers are experimental values. This yields the relationship

$$I_{s0} = \frac{I_{s0}'}{I_s'} \cdot \frac{\int FdT}{(W_p + W_L)} \qquad [14]$$

Vehicle Burnout Velocity

It is seen from the previous discussion that the usual expression

$$V_b = I_{s0} \ln \frac{1}{1 - \lambda_0} - gt$$

where λ_0, the propellant weight fraction in the loaded vehicle, need only be modified to

$$V_b = I_{s0}\left(\frac{W_p}{W_p + W_L}\right)^{1/2} \ln\left(\frac{1}{1 - \lambda}\right) - gt = I_{s0}\left(\frac{\lambda_0}{\lambda}\right)^{1/2} \ln\left(\frac{1}{1 - \lambda}\right) - gt$$

where λ is the weight fraction expelled as liner and propellant.

Heating Penalty Associated With Modulated Entry Into Earth's Atmosphere

JOHN V. BECKER[1]

Langley Research Center, NASA, Langley Field, Va.

AN INTERESTING recent paper by Lees, Hartwig and Cohen (1)[2] discusses the use of modulated aerodynamic lift to reduce the peak resultant force experienced by a space vehicle entering the atmosphere. By reducing only the lift force in the low drag region of the force polar (Fig. 1) they obtained an attenuation factor ($G/G_{\text{fixed }L/D}$) of about $\frac{1}{2}$ for a vehicle capable of a lift-drag ratio of 3. It is unfortunate that this mode of operation leads to difficult, if not impractical, heating problems for the relatively low drag vehicles required to achieve large attenuation factors. Since both the peak heat rate and the total convective heat load in laminar flow tend to increase as $1/\sqrt{\bar{C}_D}$ (where $\bar{C}_D$ is the average effective drag coefficient), the problem encountered in this low-drag type of modulated entry is not readily dealt with by either the radiation cooled or heat absorbing structural approaches. A recent study by Chapman (2) leads to this same conclusion.

Grant (3, 4) has investigated the modulation of both aerodynamic lift and drag according to realistic schedules corresponding to operation in various regions of the force polar. He finds that maximum attenuation is achieved by an entry starting at $C_{L_{\max}}$ and extending down the force polar into the low lift, low drag region (Fig. 1). The maximum attenuation ratio achieved with this schedule is considerably greater than for the "lift-only" mode, being about $\frac{1}{5}$ for a body capable of a lift-drag ratio of 3. If the region of the polar below maximum lift-drag ratio is ruled out because of the heating difficulties, it is still possible to achieve an attenuation factor of about $\frac{1}{3}$ by a schedule extending from $C_{L_{\max}}$ to $(L/D)_{\max}$. The heating penalties associated with such a schedule are the subject of the remainder of this note.

We consider first the case where force modulation is used to permit steeper entry path angles for a specific resultant force limitation of 10 g. It is assumed that all of the entries have the same initial velocity and the same velocity decrement in the pull-up maneuver. Using an unmodulated entry at $L/D = 1$ for reference, we obtain the comparisons for the total convective (laminar) heat load increment (ΔQ) given in Table 1.

It is seen that the heat load penalty associated with modulation in the entry in which the low drag region of the polar is avoided is only about one quarter of the penalty found for the low drag entry.

The increased heat flux rate in these modulated entries will, in general, cause no difficulty if the ablation technique is employed to absorb the heat pulse. However, if the heat pulse is absorbed by an internal coolant the increased heat rate may be an important factor in design.

The guidance corridor widths corresponding to these various types of entry are shown in Fig. 2. (The "corridor" width Δh is defined as the difference in miles between the highest possible perigee for a single-pass entry at $C_{L_{\max}} = -0.7$ and the perigee of the approach trajectory corresponding to the 10 g entry.) It is evident that the modulation according to Grant (3) yields a corridor some three times wider than the fixed L/D entry, at the expense of some 60 per cent in the pull-up heat load. As indicated previously the "lift-only" modulation is less effective in widening the corridor and much more costly from the heating standpoint.

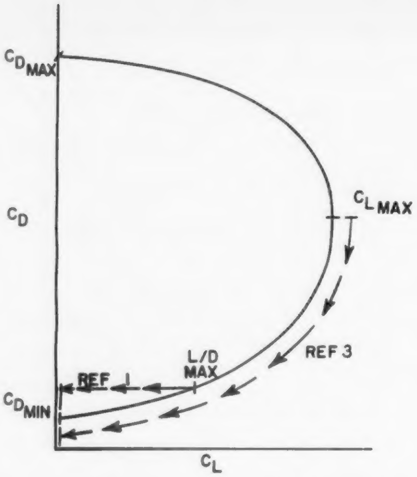

Fig. 1 Regions of force polar considered in modulated entry studies of (1 and 3)

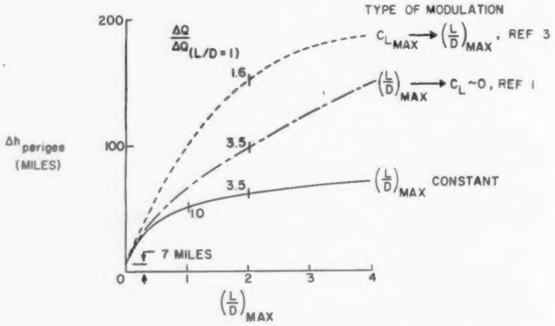

Fig. 2 Guidance corridor widths for various modes of entry at parabolic velocity. $G_{\max} = 10$

Table 1

Type of modulation	$\Delta Q/\Delta Q_{(L/D=1)}$
fixed $L/D = 1$	1.0
variable lift (1)	
$(L/D)_{\max} \rightarrow C_L = 0$	3.5
variable lift and drag (3)	
$C_{L_{\max}} \rightarrow (L/D)_{\max}$	1.6

Table 2

Type of entry	$G_{\max}$	$\Delta Q_n/\Delta Q_{n_{(L/D=1)}}$
fixed $L/D = 1$	5.6 g	1.0
variable lift and drag (3), $C_{L_{\max}} \rightarrow (L/D)_{\max}$	2.0 g	1.5

Received Jan. 8, 1960.

[1] Aeronautical Research Engineer.

[2] Numbers in parentheses indicate References at end of paper.

A second comparison has been made holding the entry angle as well as the other initial entry conditions constant, i.e., utilizing modulation to reduce the resultant force rather than to permit a steeper entry. In this study the vehicle surface was assumed to have a peak allowable temperature of 2500 F, and an emissivity of 0.9. The net laminar heat load (ΔQ_n) which would have to be absorbed by the vehicle to hold the surface temperature at 2500 F was evaluated. The assumed entry conditions are: Velocity, 25,500 fps, entry angle -6 deg and altitude 400,000 ft. The vehicle had a flat-bottomed 70-deg swept delta wing with a blunt leading edge. Appropriate allowances were made for changes in distribution of the heating rates with angle of attack. The results obtained are shown in Table 2.

The penalty in net heat load increments associated with modulation is seen to be about 50 per cent, or, relatively, the same moderate penalty as found in the previous example. The net heat load for the modulated entry in this case, in absolute terms, is only about 50 Btu per lb of vehicle weight for a vehicle in the 5000-lb class. It thus appears that modulated entries, properly executed, will not involve prohibitive heating penalties.

References

1 Lees, L., Hartwig, F. W. and Cohen, C. B., "Use of Aerodynamic Lift During Entry Into the Earth's Atmosphere," ARS JOURNAL, vol. 29, no. 9, 1959, pp. 633–641.

2 Chapman, D. R., "An Analysis of the Corridor and Guidance Requirements for Supercircular Entry Into Planetary Atmospheres," NASA TN D-136, 1959.

3 Grant, F. C., "Importance of the Variation of Drag with Lift in Minimization of Satellite Entry Acceleration," NASA TN D-120, Oct. 1959.

4 Grant, F. C., "Analysis of Low-Acceleration Lifting Entry from Escape Speed," NASA TN D-249, 1960.

Electrically Charged Missile in Vertical Descent

MARVIN H. HEWITT[1]

The Martin Co., Denver, Colo.

The Lorentz deflection of an electrically charged missile in vertical descent from low altitude is determined and compared in nature with the Coriolis displacement in the northern hemisphere. It is found that a 10^2 kg missile having an initial altitude of 10 km at latitude 60 deg N and an initial speed of Mach 10 is negligibly displaced.

RECENT work[2] has indicated that small electrically charged missiles moving in the Earth's magnetic field are perturbed and afford a small measure of control over the trajectory. Most work of this nature has necessitated machine computation or numerical methods. It will be shown here that perturbed vertical descent at low altitude can be determined without resort to a computer. The high Mach numbers now attainable and the fact that the Lorentz force is velocity-dependent elicit an interest in ascertaining how effective this force is in producing deflection of a fast, relatively low altitude missile.

The equation of motion governing the motion of a negatively charged missile in vertical descent over a rotating Earth with magnetic field is, neglecting drag

$$m\vec{a} = m\vec{g} - 2m\vec{\omega} \times \vec{v} - Q\vec{v} \times \vec{B} \qquad [1]$$

where

m = mass of missile

Q = charge on missile in electromagnetic units

$\vec{v}$ = vertical velocity

$\vec{B}$ = magnetic field strength due to terrestrial dipole

$\vec{g}$ = gravitational acceleration

$\vec{a}$ = apparent acceleration of missile relative to Earth

$\vec{\omega}$ = Earth's rotational velocity, directed from south to north (dipole situated at Earth's center)

The terrestrial field as treated here has components in a spherical coordinate system (r, θ, λ)

$$B_r = B_p \sin\theta \qquad [2]$$

$$B_\theta = -(1/2)B_p \cos\theta \qquad [3]$$

$$B_\lambda = 0 \qquad [4]$$

$$B_p = 2M/r^3 \qquad [5]$$

where

M = dipole moment = 8.1×10^{25} gauss-cm^3

θ = latitude

r = distance from Earth's center to center of charged missile

and

$$B = \sqrt{B_r^2 + B_\theta^2 + B_\lambda^2} = M\phi/r^3 \qquad [6]$$

where

$$\phi = \sqrt{1 + 3\sin^2\theta} \qquad [7]$$

A magnetic line of force has the equation

$$r = r_0 \cos^2\theta \qquad \lambda = \text{constant} \qquad [8]$$

where r_0 is the distance from the dipole center to where the line of force intersects the equatorial plane ($\theta = 0$). The angle between the line of force and the radius vector is given by

$$\sin\alpha = \cos\theta/\phi \qquad [9]$$

The direction of the velocity is at all times nearly downward. Consequently, the angle α can be treated as a constant. Because of its special interest, consider impact in the northern hemisphere where the Coriolis force gives an eastward deflection. Equation [1] becomes

$$\overrightarrow{ma} = \overrightarrow{mg} + 2m\omega v \cos\theta \hat{X} - \frac{QMv\cos\theta}{r^3}\hat{X} \qquad [10]$$

where $\hat{X}$ is a unit coordinate vector in the eastward direction. We see that the magnetic field causes a westward deflection of the missile in the northern hemisphere, for the velocity we have chosen. To a sufficient degree of approximation, the velocity is equal to the product of the gravitational acceleration by the time t during which the missile has been falling, increased by the initial velocity v_0. We can now write the differential equation for the total deflection

$$\frac{d^2x}{dt^2} = 2\omega(gt + v_0)\cos\theta - \frac{QM(gt + v_0)\cos\theta}{mr^3} \qquad [11]$$

Received Dec. 3, 1959.

[1] Design Engineer, Applied Research Section. Member ARS.

[2] Fain, W. W. and Greer, B. J., "Electrically Charged Bodies Moving in the Earth's Magnetic Field," ARS JOURNAL, vol. 29, no. 6, June 1959, pp. 451–453.

The height through which the body has fallen is very closely $h = (1/2)gt^2$; consequently

$$r \cong r_e + h - (1/2)gt^2 \qquad [12]$$

where r_e is the mean Earth radius taken equal to 6371.221 km. We consider those cases where r can be well approximated by r_e. Then,

$$\frac{d^2x}{dt^2} = \left[2g\omega \cos\theta - \frac{QMg \cos\theta}{mr_e^3}\right] t + \left[2\omega v_0 \cos\theta - \frac{QMv_0 \cos\theta}{mr_e^3}\right] \qquad [13]$$

Integrating Equation [13], we obtain the deflection

$$x = \left[\frac{g\omega \cos\theta}{3} - \frac{QMg \cos\theta}{6mr_e^3}\right] t^3 + \left[\omega v_0 \cos\theta - \frac{QMv_0 \cos\theta}{2mr_e^3}\right] t^2 \qquad [14]$$

We recall that $t = \sqrt{2h/g}$ and therefore

$$x = \frac{\omega}{3}\left(\frac{8h^3}{g}\right)^{1/2} \cos\theta - \frac{QM}{6mr_e^3}\left(\frac{8h^3}{g}\right)^{1/2} \cos\theta + \omega v_0 \left(\frac{2h}{g}\right) - \frac{QMv_0}{2mr_e^3}\left(\frac{2h}{g}\right) \qquad [15]$$

The westward deflection is

$$\Delta = \left[\frac{QM}{6mr_e^3}\left(\frac{8h^3}{g}\right)^{1/2} + \frac{QMv_0}{2mr_e^3}\left(\frac{2h}{g}\right)\right] \cos\theta \qquad [16]$$

To illustrate the magnitude of Δ, choose a missile with a mass of 10^2 kg, an initial height of 10 km, at latitude 60 deg N, and an initial velocity of Mach 10 with an eastward Coriolis deflection. We find that Δ is less than a centimeter and therefore of no importance.

It is interesting to note that the Lorentz deflection is latitude-dependent in the same way as the Coriolis deflection. It differs from the Coriolis displacement in being mass- and charge-dependent, and, in the magnetic model assumed here, is independent of Earth's rotation. In addition, the Lorentz deflection is in an opposite direction, for negatively charged bodies, to the Coriolis displacement.

Acknowledgment

The author expresses his gratitude to D. E. Muir for information concerning the problem.

ROCKETRY LETTER SYMBOLS NOW AVAILABLE

The American Society of Mechanical Engineers has just published the new American Standard Letter Symbols for Rocket Propulsion, ASA Y10.14–1959, approved last September by the American Standards Assn. Sponsored by ASME, in collaboration with the AMERICAN ROCKET SOCIETY and the Institute of the Aeronautical Sciences, the standard letter symbols are available from the American Society of Mechanical Engineers, 29 West 39th St., New York 18, N.Y., at a price of $2 per copy, with quantity discounts available.

New Patents

George F. McLaughlin, *Contributor*

Sampling device (2,906,125). F. B. Jewett Jr., New Canaan, Conn., assignor to the U. S. Navy.

Deflated bag carried aloft by a balloon. The top of the bag is held open so the sample will enter and inflate the bag as it ascends.

Nozzle (2,907,527). R. L. Cummings, Berea, Ohio, assignor to Thompson Ramo Wooldridge, Inc.

Swirl-type fuel nozzle for directing a jet of pressurized fuel vapor through a chamber and flow orifice, to atomize and disperse the liquid fuel into a finely divided spray.

Magnetic torque motor (2,908,171). L. Biberman, China Lake, Calif., assignor to the U. S. Navy.

Means for processing a gyroscope in a given direction at a predetermined rate. A hollow dome of magnetic material is mounted on the inner gimbal. Pairs of electromagnets produce a torque on the dome.

Surface cooling means for aircraft (2,908,455). H. H. Hoadley, Manchester, Conn., assignor to United Aircraft Corp.

Porous surface exposed to an airstream of high supersonic Mach numbers subjecting it to high temperatures. Cooling material exuded through the surface has high heat absorption characteristics.

Guidance system (2,922,600). J. B. Craft, Los Angeles, Calif.

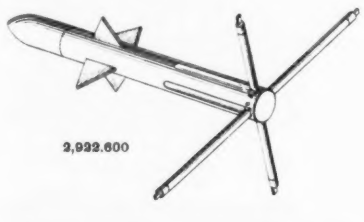

2,922.600

Sensing elements responsive to the electrical conductivity of the surrounding air to control electrically operated controls. During movement of the vehicle, the elements are disposed radially outward.

Rocket motor (2,913,983). A. L. Lytle, Pacoima, Calif.

Projectile with a releasable cover at one end, and a rocket motor in the other end. A partition plug carries pins to engage rifling in a gun barrel when launching.

Safety and arming device (2,913,984). J. M. Meek, H. B. Smith Jr. and E. T. Winston, Falls Church, Va., assignors to the U. S. Army.

Remotely located rotor actuating means for use in a missile. A coil spring between a movable unit and the rotor holds apart mating slots when there is no acceleration.

Editor's Note: Patents listed above were selected from the Official Gazette of the U. S. Patent Office. Printed copies of patents may be obtained from the Commissioner of Patents, Washington 25, D. C., at a cost of 25 cents each; design patents, 10 cents.

Low noise electron gun (2,914,699). M. R. Currie, Beverly Hills, Calif., assignor to Hughes Aircraft Co.

Profile-shaping electrode at a potential positive with respect to an accelerating electrode. Emitted electrons are constrained by a magnetic field to flow in a selected direction.

Propyl nitrate monofuel (2,914,910). C. H. King Jr. (Member ARS), Jupiter, Fla., assignor to United Aircraft Corp.

Method for decomposing monopropellant in a jet engine by adding a nickel salt soluble in propyl nitrate outside of the combustion chamber, converting the salt into finely divided particles.

Controlling the effective thrust produced by ramjet units or athodyds (2,914,911). G. Richter, Nievre, France, assignor to SNECMA Co.

Fuel valve responsive to the position of the inlet shock wave formed when the unit travels at supersonic speeds. Two static pressure taps in the intake are spaced at both sides of a selected location of the wave, and a third tap at a location where it is not affected by the wave.

Apparatus for jet propulsion through water (2,914,913). Dr. F. Zwicky (Member ARS), Pasadena, Calif., assignor to Aerojet-General Corp.

Internally streamlined channel housing a propellant injector into which pressurized water reactive propellant is released.

Three-dimensional variable exhaust nozzle (2,914,914). C. E. Vandenberg, Fullerton, Calif., assignor to North American Aviation, Inc.

Forward and aft elongated members pivotally mounted at one of their ends to form a jet engine exhaust tube. The other ends may be moved radially inward and outward when rotated. A longitudinal gap is caused between forward and aft members.

Radiantly cooled inlet (2,914,915). E. A. Sziklas and C. M. Banas, Manchester, Conn., assignors to United Aircraft Corp.

Opening and throat for conducting fluid at high supersonic velocities. A plurality of surfaces of the inner wall are parallel to the flow axis; alternating portions are at an angle to the axis. One set of surfaces of high emissivity faces toward the opening for radiating heat in that direction.

Control of fluid flow (2,914,916). P. Gelin and M. Kadosch, Paris, France, assignors to SNECMA Co.

Two opposite auxiliary nozzles opening toward the interior of a jet propulsive nozzle and supplying pressure fluid transversely into the stream to form a partial obstruction to the flow and deflection of the thrust.

Rotary jet engine (2,914,920). E. J. Paradiso, Valley Stream, N. Y.

Fuel and ignition carried by a fixed shaft to the combustion chamber within an elongated casing. Spaced nozzles project from the casing and open into the combustion chamber for receiving exhaust gases to rotate the casing.

Rotating flame spreader (2,914,921). W. D. Pouchot (Member ARS), Media, Pa., assignor to Westinghouse Electric Corp.

Blades moving in a direction transverse to the flow direction of high velocity air under pressure in a combustion chamber. Portions of blades are movable into and out of the wake of a stationary flameholder.

High speed wind tunnel (2,914,941). O. Frenzl, Dammarie-les-Lys, France, assignor to SNECMA Co.

Ejection-type tunnel. An accumulator contains water at a temperature greater than its boiling point at atmospheric pressure, and under a pressure sufficient to prevent boiling. The water passing through a nozzle partially vaporizes, expands, and forms a fine spray.

Variable sweepback airplane (2,922,601). B. N. Wallis, Effingham, England, assignor to Vickers-Armstrongs (Aircraft) Ltd.

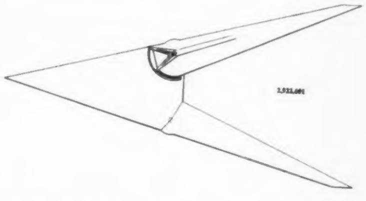

2,922,601

Delta fore-wing with tapered cantilever main wings pivotally connected at the rear. Means for driving main wings along an arc to permit their movement in sweep during flight.

Aerodyne with wings having variable sweepback (2,915,261). B. N. Wallis, Effingham, England.

Fore-wing of delta-shaped plan. Two pivoted main wings extending from the base ends are adjustable in sweep during supersonic and low subsonic flight.

Rocket head design (186,798). L. Y. Booharin, San Francisco, Calif.

Disk-like shroud below a conical head, and provided with four exhaust nozzles near its edge for imparting rotary motion to the vehicle.

Supersonic airfoil (2,916,230). W. R. Nial, Troy, N. Y., assignor to General Electric Co.

Airfoil having an upper and lower portion with opposing surfaces defining a diffusion channel. In the downstream direction, the channel has an inlet, a supersonic section of decreasing flow area, a throat section of minimum flow area, and a subsonic flow section of increasing flow area.

Propellant powder (2,916,775). J. J. O'Neill (Member ARS), Alton, Ill., assignor to Olin Mathieson Chemical Co.

Pourable paste made by mixing particles of gelatinized nitrocellulose propellant and a liquid plasticizer. The composition is maintained at atmospheric pressure until the nitrocellulose is dissolved and the mass has solidified.

Rocket powder grain (2,916,776). J. J. O'Neill (Member ARS) and C. E. Silk, Alton, Ill., assignor to Olin Mathieson Chemical Co.

Plastic molding material subjected to changing temperature while confined in one dimension by a solid plastic sheath, and in the transverse dimension by a solid plastic member. All have the same thermal expansion coefficient.

Book Reviews

Ali Bulent Cambel, Northwestern University, *Associate Editor*

High Temperature Materials, edited by R. F. Hehemann and G. M. Ault, John Wiley and Sons, New York, 1959, xvi + 544 pp. $17.50.

Reviewed by Leon Green Jr.
Aeronutronic Division, Ford Motor Co.

This book is a collection of papers presented at an AIME Symposium in 1957. Part I, Cobalt and Nickel-Base Alloys, contains the chapters "Status and Future of Nickel-Base Alloys" by F. L. Ver Snyder; "Investigation of High-Temperature Properties of Nickel-Base Alloys Using Balanced-Experiment Designs" by T. L. Robertshaw; "Evaluation of a Cast Nickel-Base Alloy for Use as a Bucket Material at 1650° F" by R. A. Signorelli, J. R. Johnston and J. W. Weeton; "W545—A New Higher-Temperature Turbine Disk Alloy" by J. T. Brown and J. Bulina; "History, Status, and Future of Cobalt Alloys" by G. A. Fritzlen; "ML—1700 Cast Turbine Bucket Alloy" by R. J. Morris and "Temperature Dependence of the Hardness of Secondary Phases Common in Turbine Bucket Alloys" by J. H. Westbrook.

Part II, Cermets and Intermetallics, contains the chapters, "Cermets and Bonded Hard Metals" by J. T. Norton; "Recent Developments in Sintered Titanium Carbide Compositions" by J. Wambold and J. C. Redmond; "Recent Advances in Infiltrated Titanium Carbides" by H. W. Lavendel and C. G. Goetzel; "Wettability and Microstructure Studies in Liquid-Phase Sintering" by N. M. Parikh and M. Humenik Jr.; "Modes of Fracture and Slip in Cemented Carbides" by N. M. Parikh; "Materials Based on Intermetallic Compounds" by R. Steinitz and "The Use of Cermets as Gas-Turbine Blading," by G. C. Deutsch.

Part III, Refractory Metals, contains the chapters "Chromium-Base Alloys for High-Temperature Applications" by R. W. Fountain and M. Korchynsky; "Transition Temperatures of Chromium and Chromium-Base Alloys" by E. P. Abrahamson II and N. J. Grant; "Molybdenum, Its Alloys and Its Protection" by J. J. Harwood and M. Semchyshen; "Processing and Properties of Selected Experimental Molybdenum-Base Alloys" by T. K. Redden and "Refractory Metals: Tungsten, Tantalum, Columbium, and Rhenium" by J. W. Pugh.

Part IV, Strengthening by Dispersion of Insoluble Particles, contains the chapters "Observation of SAP and Present Theories for Its Remarkable High-Temperature Strength" by F. V. Lenel and "The Development of SAP-Type Structures in Titanium for Elevated Temperature Service by Powder Metallurgical Techniques" by R. W. Jech, A. D. Schwope and E. P. Weber.

Part V, Vacuum Melting and Its Effects on Properties, contains the chapters "Effects of Vacuum Melting on Gas Content and Metal Structure of Cast Nickel-Base Alloys" by C. M. Hammond and R. A. Flinn; "Evaluation of Vacuum-Melted Vacuum-Investment-Cast Nickel-Base Alloys" by P. W. Beamer and J. J. Eisenhauer; "Consumable - Electrode Vacuum Remelting of High-Temperature Alloys" by R. K. Pitler, E. E. Reynolds and W. W. Dyrkacz; "Relations of High-Temperature Properties of a Nickel-Base Precipitation-Hardening Alloy to Contamination by Crucibles" by R. F. Decker, J. P. Rowe and J. W. Freeman and "The Effect of Vacuum Melting on the High-Temperature Properties of Nickel-Base Superalloys" by F. M. Richmond.

Part VI, Effect of Testing Environment on Properties, contains the chapters "The Effect of Environment on High-Temperature Creep Properties of Metals and Alloys" by D. A. Douglas; "A Comparison of the Creep-Rupture Properties of Nickel in Air and in Vacuum" by P. Shaninian and M. R. Achter; "Effect of Environments of Sodium Hydroxide, Air, and Argon on the Stress-Rupture Properties of Nickel at 1500° F" by H. T. McHenry and H. B. Probst and "The Effect of Testing Atmospheres on the Creep-Rupture Properties of Molybdenum-Base Alloys at 1800° F" by D. D. Lawthers and M. J. Manjoine.

Part VII, Oxidation Resistance, contains the chapters "Oxidation Resistance of Binary Chromium-Base Alloys" by E. P. Abrahamson II and N. J. Grant; "The Oxidation of Tungsten and Molybdenum from 1800 to 2500° F" by J. W. Semmel Jr. and "High-Temperature Oxidation of Gas-Turbine Alloys" by J. F. Radvich.

As is evident from the contents, the symposium was concerned with materials for a specific application, namely, aircraft gas turbines, and a large part of the book consists of a collection of metallurgical and engineering data of use to turbine designers. This information on specific alloys or cermets usable up to about 2000 F will be of interest to readers in the rocket field who are concerned with the design of turbine drives for propellant pumps, auxiliary power supplies and the like. To readers concerned with thermal protection against re-entry heating or with the design of nozzles and controls for large solid propellant rockets, on the other hand, the title of this book will appear much too general. In this sense the title is doubly misleading, since in general (with the exception of the chapter by Pugh and possibly that by Harwood and Semchyshen) the temperature levels involved might more properly be classed as "intermediate," and since the refractory nonmetals were not considered except as constituents in cermets or dispersion-hardened metals.

Despite these shortcomings, the book will be of general interest because of the presence of chapters which are general or basic in character, treating principles which may guide the development of new high temperature materials. The discussions by Westbrook, Norton, Parikh and Humenik, Parikh and Lenel are of this nature. Also, the interpretations by Douglas of specific data on Inconel may have general validity. It is believed that this book will be desired by institutional libraries as a reference work, but because of its high price, its appearance in personal libraries will probably be limited.

Soviet Space Science, by Ari Shternfeld (translated from the Russian by the Technical Documents Liaison Office, WPAFB), Basic Books, Inc., New York, 1959, xviii + 349 pp. $6.

Reviewed by C. C. Miesse
Armour Research Foundation

This book, recently translated from the Russian by the United States Air Force, provides a broad general summary of international progress in space technology for the novice, and a compendium of astronautical facts and figures for the lecturer. The author displays his mathematical genius for the calculation of orbits, orbital periods and trajectories, and the reader is presented with a magnificent display of mathematical space-gems which illustrate the unexpected phenomena associated with optimal trajectories. Although repeated reference is made to the characteristics and problems associated with the first two Sputniki, and a revealing review of recent Russian achievements in space technology is presented to the reader, no undue emphasis is placed on Soviet plans or progress. Hence, the title ascribed to the translated edition is somewhat misleading, and should probably be replaced by a direct translation of the original Russian title: "Artificial Satellites."

The opening chapters present the laws of celestial mechanics as applied to artificial satellites. There follows next a description of the rocket propulsion system and launching procedures, liberally augmented by the mathematical details of rocket staging and optimum launching characteristics. Brief discussions of satellite construction and the survival problems to be encountered by the first cosmonauts are followed by careful analyses of the observations possible from a satellite platform, and of the mechanics of re-entry and nongeocentric satellites. After several chapters on the problems of communication, and the utilization of artificial satellites, the author concludes with some consideration of international cooperation and space law.

Perhaps the best critique of the treatise is provided by the author himself, in his Preface to the Second Soviet Edition: "Within the scope of this book it has not been possible to discuss the entire complex of questions connected with artificial satellites. We have given major space to questions of celestial mechanics and

Multi-Use Automated Maintenance

MPTE

The recent demonstration of multi-purpose test equipment (MPTE), developed by RCA under a series of Army Ordnance contracts, highlights *a new dimension in automated multi-use systems support* and culminates a long-term RCA effort in this field. This General Evaluation Equipment is an automated, transistorized, dynamic checkout system. It contains a completely modularized array of electronic and mechanical evaluation equipment, capable of checking a variety of electromechanical devices, ranging from radar subassemblies to missile guidance computers. MPTE provides the stimuli, programming, control, measurement and test functions for the NIKE AJAX, NIKE HERCULES, LACROSSE, HAWK and CORPORAL missile systems and has been extended to other weapons systems related to our defense efforts.

RCA Tmk(s)®

RADIO CORPORATION of AMERICA

DEFENSE ELECTRONIC PRODUCTS
CAMDEN, NEW JERSEY

CONTRACT RESEARCH, DEVELOPMENT, FABRICATION

Specializing in the fields of

- Rocket and Satellite Instrumentation
- Payload Systems
- Solar and Stellar Pointing Systems
- Guidance and Control Systems

WRITE FOR BROCHURE

Prime Contractors to the NASA, Air Force, Navy

Employment Opportunities Available for Scientists and Engineers with Above Average Abilities

BALL BROTHERS RESEARCH CORP.
INDUSTRIAL PARK BOULDER, COLORADO
Hillcrest 2-2966

rocketry, as the basic elements of the road toward realization of artificial satellites, and have relegated to secondary place questions such as remote control, radio communications, and physiology. This book presents not only a discussion of propositions already known but also results of the author's own research."

Explosions, Detonations, Flammability and Ignition, AGARDograph 31, by B. P. Mullins and S. S. Penner, Pergamon Press, London, 1959, 287 pp. $10.

Reviewed by Robert A. Gross
University of California

This single volume really comprises two books. The first, by Penner, is a 107-page summary of the current analytical understanding of aerothermochemistry. The second, by Mullins, is a 162-page summary of experimental findings in the area of flammability, ignition and explosion. There is, unfortunately, little interaction between the two parts other than that they are examining, from different viewpoints, the same subject. This is not surprising since it is indicative of the state of affairs in this complex subject and, indeed, is one of the values of the book. The subject matter treated concerns advances in the subject made recently, but prior to 1958. The reader is expected to be familiar with the classic treatments and to have access to or previous knowledge of AGARDographs on related subjects.

In Part I are presented the fundamentals of aerothermochemistry, explosion limit theory for premixed gases with and without wall effects, detonation theory, flammability, quenching, ignition and single droplet burning theory. As befits analysis, the problems are simplified and models are frequently employed. The list of references is very good and includes some of the important Russian progress in this field.

In Part II data on flammability and ignition are critically reviewed and correlated. This is done using a simple thermal approach with no chain reaction concepts employed. Thus, limiting combustion phenomena are thought to occur when the rate of heat developed by chemical transformation equals the rate of heat lost to the surroundings. This simple concept frequently (but not always) gives good correlation for flammability limits of homogeneous and heterogeneous fuel oxidizer mixtures, spark ignition, and spontaneous ignition phenomena. Finally, two very good and welcome chapters are presented on explosion prevention with particular emphasis on techniques used in large engine development test facilities. These final chapters will be helpful to those persons who are responsible for the running and safety of large test facilities.

Unfortunately the authors do not give a separate listing of symbols and for this subject, which contains so many disciplines, the notation is often complex and confusing. Since this book will serve primarily as a reference rather than a text book (to be studied from cover to cover), this lack of a listing of notation is particularly annoying. It struck this reviewer as surprising that, in this subject which is so concerned with rate phenomena, there is no mention made, either theoretically or experimentally, of collision cross sections. Neither is there mention made of the microscopic point of view to aid in understanding the macroscopic events. In general this book will appeal to, and be used by, persons active in this type of research or those who wish to apply the results of such research.

Handbook of Supersonic Aerodynamics, Vol. 3, Section 6, Two-Dimensional Airfoils, prepared by the Applied Physics Laboratory, Johns Hopkins University and the Defense Research Laboratory, University of Texas. NavOrd Report 1488 (Vol. 3), 1957, iv + 96 pp. $1.50.

Reviewed by ARTHUR A. KOVITZ
Northwestern University

This section is another in the impressive series, published under cognizance of the Department of the Navy, Bureau of Ordnance, titled Handbook of Supersonic Aerodynamics.

The object of Section 6 is to provide the designer with data pertaining to certain two-dimensional airfoils. Included are data in graphical form for double symmetrical sharp edge airfoil sections of double wedge, flattened double wedge and biconvex types. Additional data are provided for modification of the types mentioned, including the effects of camber and position of maximum thickness. Finally, data for estimating the effect of viscosity on drag coefficients are also presented.

As a background for the data the theories applicable to these airfoils are given in short résumé. Comparison of the theories with available experimental data is also presented in graphical form.

This section is designed to serve as an introduction to Section 7, Three-Dimensional Airfoils, which treats more practical design considerations. As such the reviewer feels it has done its job very well. The theoretical resume has sufficient detail to adequately review and renew the reader's knowledge of two-dimensional supersonic flow. At the same time it is not so lengthy as to cloud the main purpose of the section, i.e., presentation of data.

The data is presented on clearly labeled graphs that can stand apart from the text. This adds greatly to the usefulness of the section.

This reviewer finds it a source of comfort to know that at his fingertips is a readily accessible, easily readable handbook of two-dimensional supersonic airfoil theory.

Book Notices

Magnetic and Electrical Fundamentals (Franklinian Approach), by Alexander Efron, John F. Rider, Publisher, Inc., New York, 1959, 132 pp. $2.50.

This booklet is written for the high school and the junior college level. It is profusely illustrated and descriptive in nature.

The Philosophy of Space and Time, by Hans Reichenbach, translated by M. Reichenbach and J. Freund, Dover Publications, New York, 1958, 295 pp. $2.

This is the English translation from the German of "Philosophie der Raum-Zeit Lehre."

Fuels and Lubricants, by M. Popovich and C. Hering, John Wiley & Sons, New York, 1959, 312 pp. $8.50.

This volume constitutes a compilation of multifareous types of information concerning fuels and lubricants.

Technical Literature Digest

M. H. Smith, *Associate Editor*
The James Forrestal Research Center, Princeton University

Fluid Dynamics, Heat Transfer and MHD

A Discussion of Methods for Reducing Aerodynamic Heating in Supersonic Flight, by A. J. Eggers Jr., *NACA RM* A55F21a, Sept. 1955, 16 pp.

A Method for Simulating the Atmospheric Entry of Long-range Ballistic Missiles, by A. J. Eggers Jr., *NACA Rep.* 1378, 1958, 7 pp. (Supersedes *NACA RM* A55I15.)

The Transitional Aerodynamic Drag of Meteorites, by R. M. L. Baker Jr., *Astrophys. J.*, vol. 129, no. 3, May 1959, pp. 826–831.

Slip-flow Heat Transfer from Cylinders in Subsonic Airstreams, by L. V. Baldwin, *NACA TN* 4369, Sept. 1958, 39 pp.

The Effect of Helium Injection at an Axially Symmetric Stagnation Point, by H. Hoshizaki and H. J. Smith, *J. Aero/Space Sci.*, vol. 26, no. 6, June 1959, pp. 399–400.

Mass Transfer in the Laminar Boundary Layer Along a Flat Plate Calculated by Means of the Integral Method, by H. J. Merk, *Appl. Sci. Res.*, Sec. A, vol. 8, no. 4, 1959, pp. 261–277.

Mass Transfer in Laminar Boundary Layers Calculated by Means of a Perturbation Method, by H. J. Merk, *Appl. Sci. Res.*, Sec. A, vol. 8, no. 4, 1959, pp. 237–260.

Rate of Heat-transfer Near the Stagnation Point of a Blunt Body of Revolution in the Presence of a Magnetic Field, by Rudolf X. Meyer, *Space Tech. Labs., Inc., Phys. Res. Lab.*, March 14, 1958, 59 pp.

A Survey and Correlation of Data on Heat Transfer by Forced Convection at Supersonic Speeds, by R. J. Monaghan, *Gt. Brit., Aeron. Res. Council, Rep. & Mem.* 3033, 1958, 43 pp.

Turbulent Heat Transfer Through a Highly Cooled, Partially Dissociated Boundary Layer, by P. H. Rose, R. F. Probstein and M. C. Adams, *J. Aero/Space Sci.*, vol. 25, no. 12, Dec. 1958, pp. 751–760.

Steady-state Surface Temperatures in Dissociated High-speed Gas Flows, by D. E. Rosner, *J. Aero/Space Sci.*, vol. 26, no. 6, June 1959, pp. 384–385.

Hypersonic Stagnation Point Heat Transfer to Surfaces Having Finite Catalytic Efficiency, by Sinclaire M. Scala, *Proc., 3d U.S. Nat. Congr. Appl. Mech., ASME*, New York, 1958, pp. 99–106.

Combined Forced and Free Convection in a Boundary Layer Flow, by E. M. Sparrow, R. Eichhorn and J. L. Gregg, *Phys. Fluids*, vol. 2, no. 3, May-June 1959, pp. 319–324.

Effect of a Nonisothermal Free Stream on Boundary-layer Heat Transfer, by E. M. Sparrow and J. L. Gregg, *J. Appl. Mech.*, vol. 26, no. 2, Series E, June 1959, pp. 161–165.

Turbulent Heat Transfer on Blunt-nosed Bodies in Two-dimensional and General Three-dimensional Hypersonic Flow, by R. Vaglio-Laurin, *Wright Air Dev. Center TN* 58-301, Sept. 1958, 41 pp. (*ASTIA AD* 206,050.)

Boiling Burnout with Water in Vortex Flow, by W. R. Gambill and N. D. Greene, *Chem. Engng. Progr.*, vol. 54, no. 10, pp. 68–76.

Third Compilation of Current Work on Transient Boiling—Report #3 (Enclosure A), by S. K. Hellman, S. Kaminsky and R. W. Kupp, *Vitro Engng. Co., Bettis Plant, WAPD-V(FBE)*-226, 17 pp.

An Approximate Analysis of Unsteady Vaporization Near the Stagnation Point of Blunt Bodies, by Leonard Roberts, *NASA TN* D-41, Sept. 1959, 31 pp.

Hydrodynamic Aspects of Boiling Heat Transfer, by Novak Zuber, *Univ. Calif., Los Angeles*, June 1959, 196 pp. (Dissertation, Ph.D.)

Analysis of Turbulent Flow and Heat Transfer in Noncircular Passages, by R. G. Deissler and M. F. Taylor, *NACA TN* 4384, Sept. 1958, 35 pp.

EDITOR'S NOTE: Contributions from Professors E. R. G. Eckert, J. P. Hartnett, T. F. Irvine Jr. and P. J. Schneider of the Heat Transfer Laboratory, University of Minnesota, are gratefully acknowledged.

Laminar Steady-state Magnetohydrodynamic Flow in an Annular Channel, by Samuel Globe, *Phys. Fluids*, vol. 2, no. 4, July, Aug. 1959, pp. 404–407.

Heat Transfer in a Liquid Metal Flowing Turbulently Through a Channel with a Step Function Boundary Temperature, by H. F. Poppendiek, *NASA Memo* 2-5-59W, March 1959, 64 pp.

Thermal Entrance Region of a Circular Tube Under Transient Heating Conditions, by E. M. Sparrow and R. Siegel, *Proc., 3d U.S. Nat. Congr. Appl. Mech., June 1958, ASME*, 1958, pp. 817–826.

A Variational Method for Fully Developed Laminar Heat Transfer in Ducts, by E. M. Sparrow and R. Siegel, *J. Heat Transfer*, vol. 81, Series C, no. 2, pp. 157–167.

Further Developments of New Methods in Heat-flow Analysis, by M. A. Biot, *J. Aero/Space Sci.*, vol. 26, no. 6, June 1959, pp. 367–381.

The Heating of Slabs with Arbitrary Heat Inputs, by T. R. Goodman, *Allied Res. Assoc., Inc., Rep* (*AFOSR TN* 58-524), May 1958, 17 pp.

Thermal Analysis of Stagnation Regions with Emphasis of Heat-sustaining Nose Shapes at Hypersonic Speeds, by A. J. Hanawalt, A. J. Blessing and C. M. Schmidt, *J. Aero/Space Sci.*, vol. 26, May 1959, pp. 257–263.

On Heat Transfer in Slip Flow, by S. H. Maslen, *J. Aero/Space Sci.*, vol. 26, no. 6, June 1958, pp. 400–401.

Viscous Aerodynamic Characteristics in Hypersonic Rarefied Gas Flow, by Ronald F. Probstein and Nelson H. Kemp, *AVCO Res. Lab., Res. Rep.* 48, March 1959, 64 pp.

Temperature Errors Introduced by Temperature-measuring Probes, by I. G. Donaldson, *Brit. J. Appl. Phys.*, vol. 10, no. 6, June 1959, pp. 252–255.

A Total Temperature Probe for High-temperature Boundary-layer Measurements, by M. Sibulkin, *J. Aero/Space Sci.*, vol. 26, no. 7, July 1959, pp. 458–459.

On the Calculation of Eddy Viscosity and Heat Transfer in a Turbulent Boundary Layer Near a Rapidly Rotating Disk, by D. R. Davis, *Quart. J. Mech. & Appl. Math.*, vol. 12, Part 2, May 1959, pp. 211–221.

The Effect of High Intensity Stationary and Progressive Sound Fields on Free Convection from a Horizontal Cylinder, by R. M. Fand and J. Kaye, *Wright Air Dev. Center, WADC TN* 59-18 (*ASTIA Doc. AD* 209532), March 1959, 124 pp.

The Effect of High Constant Pressure Sound Fields on Free Convection Heat Transfer from a Horizontal Cylinder, by Jack P. Holman and Tipton P. Mott-Smith, *U.S. Air Force, Wright Dev. Center, WADC TN* 58-352, Dec. 1958, 54 pp.

Transient Heat Convection Within a Spherical Film, by I. G. Sevruk, *PMM: Appl. Math. & Mech.*, vol. 22, no. 3, 1958, pp. 587–593.

Heat and Mass Transfer from a Rotating Disk, by F. Kreith, J. H. Taylor and J. P. Chang, *Trans., ASME*, Series C., *J. Heat Transfer*, vol. 81, no. 2, May 1959, pp. 95–105.

Radiative Transport Within an Ablating Body, by Leo P. Kadanoff, *AVCO Everett Res. Lab., Res. Rep.* 61, July 1959, 37 pp.

Experimental Verification of Theoretical Relations Between Total Gas Absorptivities and Total Gas Emissivities for CO, by U. P. Oppenheim, *J. Appl. Phys.*, vol. 30, no. 6, June 1959, pp. 803–807.

The Effects of Radiative Transfer on Turbulent Flow of a Stratified Fluid, by A. A. Townsend, *J. Fluid Mech.*, vol. 4, no. 4, Aug. 1958, pp. 361–375.

The Effect of Pressure Fluctuations in a Gas Flow upon Convective Heat Exchange, by S. I. Kosterin, I. A. Kozhinor and A. I. Leontiev, *Teploenergetika*, vol. 6, no. 3, March 1959, pp. 66–72. (In Russian.)

An Experimental and Theoretical Study of Quartz Ablation at the Stagnation Point, by Mac C. Adams, William E. Powers and Steven Georgiev, *AVCO Everett Res. Lab., Res. Rep.* 57, June 1959, 28 pp.

Aerodynamic Ablation of Melting Bodies, by Theodore R. Goodman, *Proc., 3d U.S. Nat. Congr. Appl. Mech., ASME*, New York, 1958, pp. 735–745.

Mass Transfer Cooling in a Laminar Boundary Layer in Steady Two-dimensional Stagnation Flow, by A. A. Hayday, *Univ. Minnesota, Inst. Tech., Heat Transfer Lab., TN* 19 (*AFOSR TN* 58-337; *ASTIA AD* 154-241), April 1958, 17 pp.

Solutions of the Laminar Compressible Boundary-layer Equations with Transpiration Which Are Applicable to the Stagnation Regions of Axisymmetric Blunt Bodies, by John T. Howe and William A. Mersman, *NASA TN* D-12, Aug. 1959, 73 pp.

Experimental Investigation of Air Film Cooling Applied to an Adiabatic Wall by Means of an Axially Discharging Slot, by S. Stephen Papell and Arthur M. Trout, *NASA TN* D-9, Aug. 1959, 67 pp.

A Method of Reducing Heat Transfer to Blunt Bodies by Air Injection, by Jackson R. Stalder and Mamoru Inouye, *NACA RM* A56B27a, May 1956, 18 pp.

A Comparison of Several Approximate Theories of Melting Ablation, by G. W. Sutton, *J. Aero/Space Sci.*, vol. 26, no. 6, June 1959, pp. 397–398.

Effects of Mach Number and Wall-temperature Ratio on Turbulent Heat Transfer at Mach Numbers from 3 to 5, by Thorval Tendeland, *NASA Tech. Rep.* R-16, 1959, 15 pp.

Survey of Heat Transfer Literature, by Milton Levy, *Aberdeen Proving Ground, Coating & Chem. Lab., Rep.* CCL 24, June 1959, 51 pp.

A Graphical Solution of Shock Equations, by Charles E. Treanor and Marcia J. Williams, *Cornell Aeron. Lab., Inc., Rep.* AD-1118-A-4, Nov. 1959, 32 pp.

Turbulent Flow and Heat Transfer Rates in Non-Newtonian Fluids, by A. B. Metzner, *Univ. Delaware, Chem. Engng. Dept., Final Rep.*, Dec. 1959, 12 pp.

Compressible Flow Tables k = 1.20; Isentropic Process, by C. Hoebich, *Army Rocket & Guided Missile Agency, Ord. Missile Labs., Redstone Arsenal, Alabama, ARGMA TN* 1H1N-6, Dec. 1959, 89 pp.

Bibliography on Plasma Physics and Magnetohydrodynamics and Their Applications to Controlled Thermonuclear Reactions, by James D. Ramer, College Park, Md., *Univ. Maryland, Engng. & Sciences Library*, 1959, 105 pp.

Spectroscopic Investigation of Hydrogen Plasma Produced by an Impulsive Discharge, by Manabu Yamamoto, *J. Phys. Soc. Japan*, vol. 14, Dec. 1959, pp. 1739–1745.

Ion-electron Relaxation of Plasmas in a Strong Magnetic Field, by Taro Kihara, *J. Phys. Soc. Japan*, vol. 14, Dec. 1959, pp. 1751–1754.

Nonlinear Alfven Waves in a Cold Ionized Gas, by David Montgomery, *Phys. Fluids*, vol. 2, Nov.-Dec. 1959, pp. 585–588.

Akademiia Nauk, SSSR, Institute Atomnoi Energii, **Physics of Plasmas and Problems of Controlled Thermonuclear Reactions,** Moscow, Akademiia Nauk, 1958, 4 vol. (in Russian). *Vol. 1:*

Investigations of the Heating of Hydrogen Plasma in Small Toroidal Systems, by A. M. Andrianov, O. A. Bazilevskaia, S. Yu. Lukianov, S. M. Osovets, Yu. F. Petrov, I. M. Podgornii and N. A. Yavlinskii, pp. 42–65 (1951).

The Influence of the Vibrations of the Plasma on Its Electrical and Thermal Conductivity, by B. I. Davydov, pp. 77–88 (1951).

Ignition of an Electrodeless Discharge, by B. I. Davydov, pp. 89–94 (1951).

Theory and Experiments on the Ignition of an Electrodeless Discharge in a Magnetic Field, by A. M. Andrianov and S. M. Osovets, pp. 95–106 (1951).

Forces Acting on a Linear Current Which Is Within Conducting Cylindrical Tubes, by M. A. Leontovich, pp. 110–114 (1951).

Compression of a Plasma Under the Action of Its Own Magnetic Field, by S. I. Braginskii, pp. 115–121 (1951).

The Betatron Method of Heating Plasma to High Temperatures, by G. I. Budker, pp. 122–129 (1951).

The Velocity of Equilibration of the Temperatures of Charged Particles in a Plasma, by V. I. Kogan, pp. 130–137 (1951).

Theory of the Temperature Jump at the Boundary of a Plasma in a Magnetic Field, by D. N. Zubarev and V. N. Klimov, pp. 138–160 (1951).

Dielectric Constant of a High Temperature Magnetized Plasma and the Evaluation of the Radiant Heat Conductivity, by V. M. Galitskii and A. B. Migdal, pp. 161–171 (1951).

The Electron Temperature Dependence of the Spectrum of the Bremsstrahlung of a Plasma, by V. I. Kogan and A. B. Midgal, pp. 172–177 (1951).

The Flow of Particles and Heat Across a Strong Magnetic Field in a Completely Ionized Two-temperature Plasma, by S. I. Braginskii, pp. 178–185 (1951).

The Physical Phenomena in the Process of the Ignition of a Discharge for Incomplete Ionization, by S. I. Braginskii and G. I. Budker, pp. 186–206 (1952).

The Stability of a Flexible Conductor in a Longitudinal Magnetic Field, by M. A. Leontovich and V. D. Shafranov, pp. 207–213 (1952).

An Electrical Breakdown in a Gas in the Presence of a Strong External Magnetic Field Variable in Time, by G. I. Budker, pp. 214–221 (1952).

The Magnetic Field of a Linear Current Surrounded by an Ideally Conducting Cylinder with a Cut, by M. A. Leontovich, pp. 222–228 (1952).

Investigation of the Axial Region of a Plasma Pinch, by S. I. Braginskii, pp. 229–233 (1952).

A Piezo-electric Method of Investigating a Strong Gas Discharge, by V. S. Komel'kov and V. I. Sinitsyn, pp. 234–242 (1952).

Thermonuclear Reaction in a Potential Hole of a Negative Charge, by G. I. Budker, pp. 243–249 (1952).

The Instability of a Plasma Cylinder, by B. A. Trubnikov, pp. 289–298 (1952).

Vol. 2 (356 pp.):

The Plasma Pinch with Heat Loss at the Electrodes, by S. I. Braginskii and V. D. Shafranov, pp. 3–19 (1953).

The Processes in a Plasma Column with Rapid Increase of Current, by S. I. Braginskii and A. B. Migdal, pp. 20–25 (1951).

Passing of Large Currents Through a Plasma in the Presence of a Longitudinal Magnetic Field, by L. A. Artsimovich, pp. 81–86 (1953).

Magnetic Current in a Compressing Cylinder, by L. A. Artsimovich, pp. 87–100 (1953).

Analysis of the Equations of the Compression of the Pinch in the Presence of an External Magnetic Field, by L. A. Artsimovich, pp. 101–108 (1954).

The Yield of Thermonuclear Reactions, by V. I. Kogan, pp. 109–129 (1953).

Stability of a Plasma Pinch in the Presence of a Longitudinal Magnetic Field and a Conducting Envelope, by V. D. Shafranov, pp. 130–143 (1953).

The Stability of a Plasma Cylinder in an External Magnetic Field, by T. F. Volkov, pp. 144–149 (1953).

Distribution of the Intensity of the Neutron Radiation Along the Axis of a Straight Tube for a Strong Pulse Discharge in Deuterium, by N. A. Borzunov and D. V. Orlinskii, pp. 150–164 (1954).

Mechanism of the Observed Neutron Emission, by S. M. Osovets, pp. 165–169 (1954).

Investigation of a Powerful Electric Discharge in Deuterium, by V. S. Komel'kov, T. I. Morozova and Yu. V. Skvortsov, pp. 170–184 (1954).

Investigations of a Pulse Discharge in Gases for Current Strength of 500 KA, by A. N. Andrianov, O. A. Bazilevskaya and Yu. G. Prokhorov, pp. 185–211 (1956).

Measurement of the Conductivity of the Plasma for the Passage of Current for a Long Time, by V. D. Kirilov, pp. 212–225 (1954).

The Theory of Bremsstrahlung for Nonrelativistic Radiation, by V. V. Babikov, pp. 226–237 (1954).

A Plasma Discharge in an Electromagnetic Field, by S. M. Osovets, pp. 238–241 (1953).

Investigation of a Gas Discharge in a Uni-connected Region, by S. M. Osovets Yu. F. Petrov and N. I. Shchedrin, pp. 242–263 (1955).

Investigation of a Ring Gas Discharge in a Transverse Magnetic Field, by Yu. F. Nasedkin, pp. 264–282 (1955).

Relativistic Plasma in Variable Field, by S. T. Belyaev and G. I. Budker, pp. 283–329 (1953).

Kinetic Equation for an Electron Gas for Rare Collisions, by G. I. Budker and S. T. Belyaev, pp. 330–354 (1954).

Vol. 3 (363 pp.):

Several Problems Associated with Spatial Stability of a Ring Current in Plasma, by G. I. Budker, pp. 32–40 (1951).

Multi-quanta Recombinations in an Ionized Gas, by S. T. Belyaev and G. I. Budker, pp. 41–49 (1955).

Kinetic Equations for Dilute Gases in Strong Fields, by S. T. Belyaev, pp. 50–65 (1955).

The Kinetics of an Ionized Gas in a Strong Magnetic Field, by S. T. Belyaev, pp. 66–85 (1955).

Radiant Heat Losses of a Dense High Temperature Plasma, by V. V. Babikov and V. I. Kogan, pp. 86–98 (1955).

Recombination Radiation of a Hydrogen Plasma, by V. I. Kogan, pp. 99–103 (1956).

SYSTEMS ENGINEERS AND SCIENTISTS

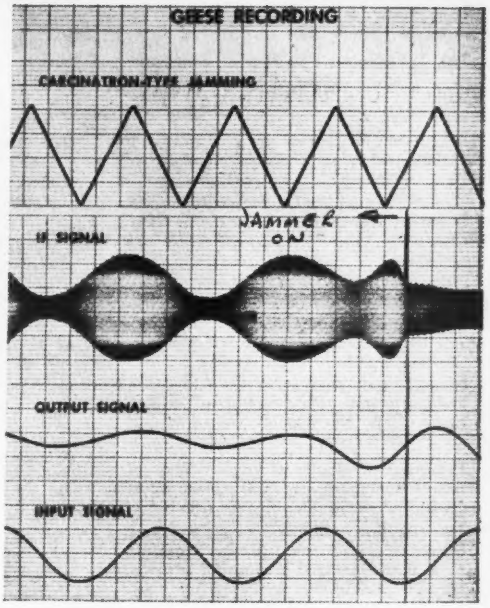

Almost any conceivable signal can be generated on GEESE; these signals can be carefully controlled in frequency, phase and amplitude, and their instantaneous relationship can be recorded. GEESE has the flexibility to fully evaluate advance radar, communications and guidance systems and the effects of various jamming and anti-jamming techniques.

EVOLVING LARGE-SCALE SYSTEMS CONCEPTS

AND DEVELOPING THE TOOLS THAT SPEED THEIR DESIGN CYCLE

Defense Systems Department is directing its technical capabilities toward the development of large-scale electronic systems. Inherent within this work program is the recognition, definition and solution of problems in every aspect of the systems technology.

To accomplish this ambitious task, a growing number of studies are being directed toward the development of unique tools that will aid in the design of superior systems in less time, at lower cost.

A recent contribution by Defense Systems Department in this technological area is GEESE (General Electric's Electronic System Evaluator). Utilizing advance computer techniques, it enables systems engineers to accurately predict, optimize and synthesize system performance prior to design.

GEESE is indicative of the scope of Defense Systems Department's involvement in the systems technology. Many programs offer systems-oriented engineers and scientists an opportunity to participate in new areas of long-term importance.

Senior members of our technical staff would welcome the occasion to discuss personally and in detail the career positions available with this growing organization. Address your inquiries in professional confidence to Mr. E. A. Smith, Box 35ME.

DSD DEFENSE SYSTEMS DEPARTMENT
A Department of the Defense Electronics Division

GENERAL ELECTRIC

Northern Lights Office Building, Syracuse, New York

Electromagnetic Waves in a Relativistic Plasma in the Presence of a Magnetic Field, by B. A. Trubnikov, pp. 104–113 (1956).

The Distributed Function of Electrons in a Plasma Situated in a Magnetic Field, by V. S. Kudryavtsev, pp. 114–120 (1956).

Magnetic Emission of a Layer of Plasma, by B. A. Trubnikov and A. E. Bazhanova, pp. 121–147 (1957).

The Problem of the Decomposition of an Arbitrary Shock in a Continuous Medium, by T. F. Volkov, pp. 148–152 (1956).

High Frequency Heating of Plasma, by L. I. Rudakov and R. Z. Sagdeev, pp. 153–164 (1956).

Theory of Rapid Processes, by S. M. Osovets, pp. 165–181 (1957).

Investigation of a Powerful Ring Gas Discharge in the Presence of an Equilibrium Orbit, by Yu. F. Nasedkin and S. M. Osovets, pp. 182–195 (1956).

Plasma Turbulence in the Presence of Active Resistance, by S. M. Osovets and N. I. Shchedrin, pp. 196–213 (1957).

Investigation of the Pressures in a Powerful Gas Discharge with the Help of a Piezo-electric Measuring Device, by N. V. Philippov, pp. 231–249 (1956).

The Behavior of Rapid Electrons in an Electron Model of a Trap with Magnetic Mirrors, by G. M. Antropov, V. A. Belyaev and M. K. Komanovskii, pp. 250–258 (1957).

The Repulsion of Charged Particles from Regions of Strong Magnetic Fields, by O. B. Firsov, pp. 259–267 (1956).

A Quasi-hydrodynamic Description of a Dilute Plasma in a Magnetic Field, by L. I. Rudakov and R. Z. Sagdeev, pp. 268–277 (1957).

Some Properties of the Plasma with Anisotropic Distribution of the Velocities of Ions in the Magnetic Field, by A. A. Vedenov and R. Z. Sagdeev, pp. 278–284 (1957).

Magnetic Traps with "Gofrirovanoe" Field, by B. B. Kadomtsev, pp. 285–299 (1956).

Stabilization of Plasma with the Help of Shielding Conductors, by S. I. Braginskii and B. B. Kadomtsev, pp. 300–326 (1957).

Plasma in "Magnetic Net," by O. B. Firsov, pp. 327–335 (1957).

Stationary Distribution of the Density of the Plasma in an Electro-magnetic Field, by T. F. Volkov, pp. 336–345 (1957).

Containment of the Plasma by the Pressure of a Standing Electro-magnetic Wave, by R. Z. Sagdeev, pp. 346–361 (1957).

Vol. 4 (440 pp.):

Containment of a Plasma by Traveling Magnetic Field, by S. M. Osovets, pp. 3–15 (1957).

Hydrodynamics of a Plasma of Low Pressure, by B. B. Kadomtsev, pp. 16–23 (1957).

Magneto Hydrodynamic Waves in a Dilute Plasma, by S. I. Braginskii and A. P. Kazantsev, pp. 24–31 (1958).

The Motion of Charged Particles in a Magnetic Trap, by L. S. Solov'ev, pp. 32–41 (1957).

The Motion of a Charged Particle in the Rapidly Alternating Electro-magnetic Fields, by A. A. Vedenov and L. I. Rudakov, pp. 43–48 (1958).

Stabilization of a Plasma with the Help of a System of Rods, by D. V. Orlinskii, pp. 49–53 (1958).

Investigation of the Stability of a Cylindrical Plasma Column by Methods of Kinetic Equations, by L. I. Rudakov and R. Z. Sagdeev, pp. 54–60 (1958).

Stability of a Plasma Column with a Distributed Current, by V. D. Shafranov, pp. 61–69 (1958).

Calculation of Quasi-stationary Electromagnetic Field in a System with Toroidal Symmetry, by N. M. Polievktov-Nikolaidze, pp. 70–80 (1958).

Investigation of the Neutron Emission Arising in a Gaseous Discharge with a Current of 160 KA, by V. F. Demichev and Yu. G. Prokhorov, pp. 81–86 (1957).

A Possible Mechanism of the Neutron Effect at Massive Pulse Discharges in Deuterium, by B. A. Trubnikov, pp. 87–97 (1958).

The Influence of a High Frequency Electro-magnetic Field on the Vibrations of a Plasma, by T. F. Volkov, pp. 98–108 (1958).

The Vibration and Stability of the Surface Plasma in the Field of a Traveling Electro-magnetic Wave, by T. F. Volkov, pp. 109–115 (1958).

The Electrodeless Discharge with High Current in a Toroidal Chamber with a Longitudinal Magnetic Field, by A. L. Bezbatchenko, I. N. Golovin, P. I. Kozlov, V. S. Strelkov and N. A. Yavlinskii, pp. 116–133 (1957).

The Measurement of the Electron Temperature and Ion Concentration by a Double Floating Probe in an Electrodeless Discharge, by V. I. Pistunovich, pp. 134–155 (1957).

Investigation of the Radiation of an Electrodeless Discharge in Deuterium, by V. S. Strelkov, pp. 156–169 (1958).

Powerful Gas Discharge in Chambers with Conducting Walls, by D. P. Petrov, N. V. Filippov, T. I. Filippova and V. A. Khrabrov, pp. 170–181 (1957).

Investigation of the Pulse Discharge in Deuterium for Velocities of Current Rise of up to 10^{12} Amp/sec and Potentials to 120 kv, by A. M. Andrianov, O. A. Bazilevskaya and Yu. G. Prokhorov, pp. 182–220 (1958).

The Theory of the Compression and Pulsation of a Plasma Column in a Strong Pulse Discharge, by S. I. Braginskii, I. M. Gel'fand and R. P. Fedorenko, pp. 201–221 (1958).

Investigation of the Process of Electrodynamic Acceleration of Clumps of Plasma, by I. M. Podgornyi, S. A. Chuvatin, G. A. Bykov and V. D. Pis'mennyi, pp. 222–234 (1957).

The Radial Distribution of Potential in a Cylindrical Magnetic Trap Using a Magnetron Method of Ion Injection, by E. E. Yushmanov, pp. 235–257 (1957).

The Widening of Spectral Lines in a High Temperature Plasma, by V. I. Kogan, pp. 258–304 (1957).

The Relation Between the Coefficients of Absorption and Emission of Plasma Radiation Present in a Magnetic Field, by B. A. Trubnikov, pp. 305–308 (1957).

The Behavior of Plasma in a Rapidly Varying Magnetic Field, by B. A. Trubnokov, pp. 309–330 (1957).

Cherenkov Generation of Magneto-acoustical Waves, by A. I. Morozov, pp. 331–352 (1958).

Magnetic Traps for Plasma, by B. B. Kadomtsev, pp. 353–363 (1957).

The Instability of Plasma in a Magnetic Field in the Presence of Ionic Beams, by B. B. Kadomtsev, pp. 364–369 (1958).

The Dynamics of Plasma in a Strong Magnetic Field, by B. B. Kadomtsev, pp. 370–379 (1958).

The Convective Instability of a Plasma, by B. B. Kadomtsev, pp. 380–383 (1958).

Non-linear Motions of a Diluted Plasma in a Magnetic Field, by R. Z. Sagdeev, pp. 384–390 (1958).

The Quenching of Vibrations of a Plasma Column, by A. I. Morozov and L. S. Solov'ev, pp. 391–415 (1958).

Deduction of the Tensor of Dielectric Permeability of a Plasma, by V. D. Shafranov, pp. 416–421 (1958).

Absorption of Electro-magnetic Waves Propagating Along a Constant Magnetic Field in a Plasma, by R. Z. Sagdeev, pp. 422–425 (1958).

The Index of Refraction of a Plasma in a Magnetic Field in the Region of the Ion Cyclotron Resonance, by V. D. Shafranov, pp. 426–429 (1958).

The Vibrations of a Plasma Column with Consideration of the Heat Motion of the Ions, by R. Z. Sagdeev and V. D. Shafranov, pp. 430–435 (1958).

High-Speed Shock Waves in a Magnetic Annular Shock Tube, by Richard M. Patrick, *Phys. Fluids*, vol. 2, Nov.-Dec. 1959, pp. 589–598.

Theory of the Flow in the Magnetic Annular Shock Tube, by Nelson H. Kemp and Harry E. Petschek, *Phys. Fluids*, vol. 2, Nov.-Dec. 1959, pp. 599–608.

Moving Magnetic Field Behind a Strong Deuterium Shock, by F. R. Scott and R. F. Wenzel, *Phys. Fluids*, vol. 2, Nov.-Dec. 1959, pp. 609–613.

Thermal and Electrical Properties of an Argon Plasma, by H. N. Olsen, *Phys. Fluids*, vol. 2, Nov.-Dec. 1959, pp. 614–623.

Some Interior Problems of Hydromagnetics, by J. D. Cole and J. H. Huth, *Phys. Fluids*, vol. 2, Nov.-Dec. 1959, pp. 624–626.

Flow of an Incompressible Fluid in a Hydromagnetic Capacitor, by C. C. Chang and T. S. Lundgren, *Phys. Fluids*, Nov.-Dec. 1959, pp. 627–632.

Magnetohydrodynamic Waves in Wave Guides, by Ryszard Gajewski, *Phys. Fluids*, vol. 2, Nov.-Dec. 1959, pp. 633–641.

Instability of Certain Electrohydrodynamic Systems, by Otmar M. Stuetzer, *Phys. Fluids*, Nov.-Dec. 1959, pp. 642–648.

Electrostatic Field About an Ion Moving Slowly in a Plasma, by S. Rand, *Phys. Fluids*, vol. 2, Nov.-Dec. 1959, pp. 649–652.

Dynamic Instability of Accelerated Fluids, by C. T. Chang, *Phys. Fluids*, vol. 2, Nov.-Dec. 1959, pp. 656–663.

Turbulent Boundary Layer Measurements at Mach Numbers from 8 to 10, by F. K. Hill, *Phys. Fluids*, vol. 2, Nov.-Dec. 1959, pp. 668–679.

Simple Wave Flow in Ducts, by Roy Gunderson, *Phys. Fluids*, vol. 2, Nov.-Dec. 1959, pp. 680–687.

Transport Properties of High-temperature Multicomponent Gas Mixtures, by Edward A. Mason, Joseph T. Vanderslice and Jerrold M. Yos, *Phys. Fluids*, vol. 2, Nov.-Dec. 1959, pp. 688–694.

Electro-hydromagnetic Waves in a Fully Ionized Gas, I, by K. D. Cole, *Planetary & Space Sci.*, vol. 1, Sept. 1959, pp. 319–324.

The Behaviour of an Axially Symmetric Sonic Jet Near to the Sonic Plane, by M. C. Smith, *Quart. J. Mech. & Appl.*

Math., vol. 12, Aug. 1959, pp. 287–297.

Shock Waves with Discontinuous Gas Conductivity Situated in an Electromagnetic Field, by G. A. Lyubimov, *Soviet Phys.-Doklady*, vol. 4, no. 3, Dec. 1959, pp. 510–513.

On the Phenomenon of Magnetic "Detachment" of the Flow of a Conducting Medium, by V. N. Zhigulev, *Soviet Phys.-Doklady*, vol. 4, no. 3, Dec. 1959, pp. 514–516.

On the Calculation of Shock Waves in Magnetohydrodynamics, by M. I. Kiselev, *Soviet Phys.-Doklady*, vol. 4, no. 3, Dec. 1959, pp. 517–520.

Shape-preserving, Exact Solutions of the Equations of Magnetohydrodynamics, by N. N. Kochina, *Soviet Phys.-Doklady*, vol. 4, no. 3, Dec. 1959, pp. 521–525.

Stationary Flow of a Ideally Conducting Gas Around a Corner, by G. A. Lyubimov, *Soviet Phys.-Doklady*, vol. 4, no. 3, Dec. 1959, pp. 529–531.

On the Approximation Method in Investigation of Plane Rotational Flow in Magnetohydrodynamics, by I. I. Nochevkina, *Soviet Phys.-Doklady*, vol. 4, no. 3, Dec. 1959, pp. 549–553.

Some Exact Solutions of the Equations of Magneto-Gas Dynamics with Internal Gravitational Forces Present and with a Zero Temperature Gradient, by E. V. Ryazanov, *Soviet Phys.-Doklady*, vol. 4, no. 3, Dec. 1959, pp. 554–557.

Flight Mechanics

Nearly Circular Transfer Trajectories for Descending Satellites, by George M. Low, *NASA TR* R-3, 1959, 17 pp.

Experimental Results of the U. S. Rocket Program for the International Geophysical Year to 1 July 1958, *IGY World Data Center, A. Rockets and Satellites, IGY Rocket Report Series* no. 1, July 30, 1958, 236 pp.

Flight Summaries for the U. S. Rocketry Program for the International Geophysical Year, Part 1, July 5, 1956–June 30, 1958; Part 2, May 23–Dec. 31, 1958, *IGY World Data Center, A. Rockets and Satellites, IGY Rocket Report Series* no. 2, March 1, 1959, 193 pp.; and no. 3, Sept. 30, 1959, 129 pp.

Processed Observational Data for USSR Satellites 1957 Alpha and 1957 Beta, *IGY World Data Center, A. Rockets and Satellites, IGY Satellite Report Series* no. 1, March 1, 1958, 120 pp.

Status Reports on Optical Observations of Satellites 1958 Alpha and 1958 Beta, *IGY World Data Center, A. Rockets and Satellites, IGY Satellite Report Series* no. 2, April 30, 1958, 41 pp.

Radio Observations of Soviet Satellites 1957 Alpha 2 and 1957 Beta 1, *IGY World Data Center, A. Rockets and Satellites, IGY Satellite Report Series* no. 5, July 30, 1958, 50 pp.

Simplified Satellite Prediction from Modified Orbital Elements, *IGY World Data Center, A. Rockets and Satellites, IGY Satellite Report Series* no. 7, Jan. 1, 1959, 54 pp.

Some Preliminary Reports of Experiments in Satellites 1958 Alpha and 1958 Gamma, *IGY World Data Center, A. Rockets and Satellites, IGY Satellite Report Series* no. 3, May 1, 1958, 92 pp.:

Status Reports on Optical Observations of Satellites 1958 Alpha and 1958 Beta, by G. F. Schilling, pp. 1–16.

The Determination of the Orbit of 1958 Alpha at the Vanguard Computing Center, by Joseph W. Siry, pp. 17–24.

Reports and Analyses of Satellite Observations, *IGY World Data Center, A. Rockets and Satellites, IGY Satellite Report Series* no. 6, Aug. 15, 1958, 60 pp.

Moonwatch Catalogue—May Through June 1958, by E. P. Bullis and L. Campbell, pp. 1–21.

Preliminary Note on the Mass-area Ratios of Satellites 1958 Delta 1 and 1958 Delta 2, by G. F. Schilling, C. A. Whitney and B. M. Folkart, pp. 22–24.

The Descent of Satellite 1957 Beta 1, by L. G. Jacchia, pp. 25–38.

Positions of Satellite 1957 Beta 1 During the First 100 Revolutions, by R. M. Adams, R. E. Briggs and E. K. L. Upton, pp. 39–60.

Ephemeris of Satellite 1957 Alpha 2 and Collected Reports on Satellite Observations, *IGY World Data Center, A. Rockets and Satellites, IGY Satellite Report Series* no. 8, June 15, 1959, 122 pp.:

Orbital Acceleration of Satellite 1958 Beta Two, by L. G. Jacchia and R. E. Briggs, pp. 67–70.

The Diurnal Effect in the Orbital Acceleration of Satellite 1957 Beta One, by L. G. Jacchia, pp. 71–74.

On the Effects of the Sun and the Moon upon the Motion of a Close Earth Satellite, by Yoshihide Kozai, pp. 85–88.

An Empirical Formula for Satellite Ephemerides Near the End of Their Lifetime, by L. G. Jacchia, pp. 89–92.

RESEARCH SCIENTISTS

ARMOUR RESEARCH FOUNDATION has professionally challenging openings for high calibre research engineers and scientists to do theoretical and experimental research in the fields of:

Shock and Detonation Wave Phenomena
Hypersonic Flow
Rarefied Gas Phenomena
Transport Phenomena

The Foundation encourages original research and publication of papers. These positions offer stimulating associations with other leading scientists in these fields.

Applicants must have an M.S. or Ph.D. degree in Engineering or Science, and have experience in one or more of these areas. In addition to the many cultural opportunities in Chicago, we offer the advantage of being located on a university campus. We have an excellent benefit program which includes a liberal vacation policy of up to four weeks each year.

We invite you to send your resume to:

E. P. Bloch
ARMOUR RESEARCH FOUNDATION
of Illinois Institute of Technology
10 West 35th Street
Chicago 16, Illinois

SOUTHWEST
"Monoball"®
SELF-ALIGNING BEARINGS

EXT.
INT.
PLAIN TYPES
ROD END TYPES
PATENTED U. S. A.
World Rights Reserved

CHARACTERISTICS

ANALYSIS	RECOMMENDED USE
① Stainless Steel Ball and Race	For types operating under high temperature (800-1200 degrees F.).
② Chrome Alloy Steel Ball and Race	For types operating under high radial ultimate loads (3000-893,000 lbs.).
③ Bronze Race and Chrome Steel Ball	For types operating under normal loads with minimum friction requirements.

Thousands in use. Backed by years of service life. Wide variety of Plain Types in bore sizes 3/16" to 6" Dia. Rod end types in similar size range with externally or internally threaded shanks. Our Engineers welcome an opportunity of studying individual requirements and prescribing a type or types which will serve under your demanding conditions. Southwest can design special types to fit individual specifications. As a result of thorough study of different operating conditions, various steel alloys have been used to meet specific needs. Write for Engineering Manual No. 551. Address Dept. ARS-60.

SOUTHWEST PRODUCTS CO.
1705 SO. MOUNTAIN AVE., MONROVIA, CALIFORNIA

Honeycomb, a critical assembly device, is one of many research tools developed through the cooperation of Los Alamos scientists and engineers to enhance the Laboratory's constant quest for knowledge.

For employment information write:
Personnel Director
Division 60-41

los alamos
scientific laboratory
OF THE UNIVERSITY OF CALIFORNIA
LOS ALAMOS, NEW MEXICO

Index to Advertisers

AEROJET-GENERAL CORP. . . . . Back cover
D'Arcy Advertising Co., Los Angeles, Calif.

ARMOUR RESEARCH FOUNDATION OF ILLINOIS INSTITUTE OF TECHNOLOGY 515

BALL BROTHERS RESEARCH CORP. 510
Walter L. Schump Advertising, Denver, Colo.

GENERAL ELECTRIC CO., DEFENSE SYSTEMS DEPT. 513
Deutsch & Shea, Inc., New York, N.Y.

LOS ALAMOS SCIENTIFIC LABORATORY 516
Ward Hicks Advertising, Albuquerque, N. Mex.

THE MARTIN CO., DENVER DIV. . . . . Second cover
E. M. Halvorson Co., Denver, Colo.

RADIO CORP. OF AMERICA, DEFENSE ELECTRONIC PRODUCTS 509
Al Paul Lefton Co., Inc., Philadelphia, Pa.

RAMO-WOOLDRIDGE, DIV. OF THOMPSON RAMO WOOLDRIDGE INC. 442
The McCarty Co., Los Angeles, Calif.

SOUTHWEST PRODUCTS CO. . . . 515
O. K. Fagan Advertising Agency, Los Angeles, Calif.

SPACE TECHNOLOGY LABORATORIES 439
Gaynor & Ducas, Inc., Beverly Hills, Calif.

THIOKOL CHEMICAL CORP. . 440–441
Brown & Butcher, Inc., New York, N.Y.

UNITED AIRCRAFT CORP., RESEARCH LABORATORIES. 437
B. E. Burrell & Associates, Hartford, Conn.

WYMAN GORDON CO. . . . Third cover
The Davis Press, Inc., Worcester, Mass.